



## VIABILITY ASSESSMENT OF TRANSMISSION LINE MODELS IN TIME AND FREQUENCY DOMAINS

Mirko Mashenko Yanque Tomasevich

Tese de Doutorado apresentada ao Programa de Pós-graduação em Engenharia Elétrica, COPPE, da Universidade Federal do Rio de Janeiro, como parte dos requisitos necessários à obtenção do título de Doutor em Engenharia Elétrica.

Orientador: Antonio Carlos Siqueira de Lima

Rio de Janeiro

Abril de 2015

VIABILITY ASSESSMENT OF TRANSMISSION LINE MODELS IN TIME AND  
FREQUENCY DOMAINS

Mirko Mashenko Yanque Tomasevich

TESE SUBMETIDA AO CORPO DOCENTE DO INSTITUTO ALBERTO LUIZ  
COIMBRA DE PÓS-GRADUAÇÃO E PESQUISA DE ENGENHARIA (COPPE)  
DA UNIVERSIDADE FEDERAL DO RIO DE JANEIRO COMO PARTE DOS  
REQUISITOS NECESSÁRIOS PARA A OBTENÇÃO DO GRAU DE DOUTOR EM  
CIÊNCIAS EM ENGENHARIA ELÉTRICA.

Examinada por:

---

Prof. Antonio Carlos Siqueira de Lima, D.Sc.

---

Prof. Washington Luiz Araujo Neves, Ph.D.

---

Prof. Sandoval Carneiro Jr., Ph.D.

---

Prof. João Clavio Salari Filho, D.Sc.

---

Prof. Robson Francisco da Silva Dias, D.Sc.

RIO DE JANEIRO, RJ – BRASIL

ABRIL DE 2015

Yanque Tomasevich, Mirko Mashenko

Viability assessment of transmission line models in Time and Frequency Domains/Mirko Mashenko Yanque Tomasevich. – Rio de Janeiro: UFRJ/COPPE, 2015.

XIII, 147 p.: il.; 29,7cm.

Orientador: Antonio Carlos Siqueira de Lima

Tese (doutorado) – UFRJ/COPPE/Programa de Engenharia Elétrica, 2015.

Referências Bibliográficas: p. 126 – 136.

1. Electromagnetic Transients. 2. Frequency Domain synthesis. 3. Full-wave. 4. Idempotent decomposition. 5. Images Method. 6. Numerical stability. 7. Quasi-TEM. 8. Time Domain analysis. 9. Transmission Line modeling. 10. Transmission Line theory. I. Lima, Antonio Carlos Siqueira de. II. Universidade Federal do Rio de Janeiro, COPPE, Programa de Engenharia Elétrica. III. Título.

*In memory of Prof. Carlos Manuel  
de Jesus Cruz de Medeiros Portela,  
for believing in me and accepting  
me as his Master student.*

# Acknowledgement

To God for giving me the strength of soul to surmount the difficulties of the PhD. course, in first place. And to everyone who cooperated, contributed or helped me in any way in the development of the present work. A special mention is in order to the following persons and institutions:

- The PEE/COPPE/UFRJ, for giving me the chance to develop a Doctorate course in Brazil.
- The “Conselho Nacional de Desenvolvimento Científico e Tecnológico”–CNPq, “Coordenação de Aperfeiçoamento de Pessoal de Nível Superior”–CAPES, “Instituto Nacional de Energia Elétrica”–INERGE and FAPEMIG, for supporting directly or indirectly the present work.
- My research supervisor professor, Antonio Carlos Siqueira de Lima, for his complete support, teachings and dedication that helped me to finish this work.
- Hans Hoidalén for providing a running test case of a ULM approach using Models in ATP.
- João Salari Filho, for helping me in the past with useful information and tips.
- My parents: Justo Yanque and Liliana Tomasevich, and my brother: Ivanko Yanque Tomasevich, for their invaluable and unconditional support.
- The personal working in the Academic Department and the LASPOT laboratory, specially to the secretaries Daniele Cristina Oliveira, Aline Zimmermann and Marcia Coelho de Oliveira, for helping me during all these years.
- The friends and colleagues: Cristiano, David, Douglas, João, Tunico and Thassiana, for their friendship and constant support.

Resumo da Tese apresentada à COPPE/UFRJ como parte dos requisitos necessários para a obtenção do grau de Doutor em Ciências (D.Sc.)

## AVALIAÇÃO DA VIABILIDADE DOS MODELOS DE LINHAS DE TRANSMISSÃO NOS DOMÍNIOS DO TEMPO E DA FREQUÊNCIA

Mirko Mashenko Yanque Tomasevich

Abril/2015

Orientador: Antonio Carlos Siqueira de Lima

Programa: Engenharia Elétrica

O presente trabalho avalia o uso do modelo de linha Idempotente implementado com um esquema de ajuste alternativo para a modelagem no domínio do tempo por coordenadas de fase de linhas de transmissão aéreas e cabos subterrâneos, usando o Método das Características, evitando respostas instáveis no domínio do tempo quando a aproximação racional da função de propagação contem razões grandes entre resíduos e polos.

Embora simulações estáveis foram obtidas para cabos subterrâneos, foi encontrado que para linhas aéreas a precisão do ajuste das matrizes idempotentes diminui ao crescer o número de fases do sistema.

Para pesquisar se as causas dos problemas mencionados estão inerentemente relacionadas à precisão do cálculo da função de propagação, avaliamos os parâmetros da linha usando um solo geral com perdas numa ampla banda de frequência, i.e., considerando tanto as correntes de condução como as correntes de deslocamento.

Respostas no domínio do tempo baseadas na Transformada Numérica de Laplace e no Método das Características foram usadas para investigar a precisão dos modelos de linha acima mencionados.

Encontramos que o uso de expressões fechadas aproximadas por Imagens para o cálculo dos parâmetros de linha por unidade de comprimento pode originar instabilidades numéricas devido a violações na passividade quando uma grande faixa de frequência é considerada e o solo é assumido com perdas, modelado seja com parâmetros constantes ou dependentes da frequência. Uma formulação quasi-TEM foi usada para comparar estes resultados. Não foram encontradas violações na passividade nos casos de linha monofásica e multifásica. Algumas técnicas de mitigação foram também propostas.

Finalmente, baseados nesta pesquisa, temas de investigação futuros são propostos.

Abstract of Thesis presented to COPPE/UFRJ as a partial fulfillment of the requirements for the degree of Doctor of Science (D.Sc.)

## VIABILITY ASSESSMENT OF TRANSMISSION LINE MODELS IN TIME AND FREQUENCY DOMAINS

Mirko Mashenko Yanque Tomasevich

April/2015

Advisor: Antonio Carlos Siqueira de Lima

Department: Electrical Engineering

This work evaluates the use of the Idempotent line model implemented using an alternative fitting scheme for the phase coordinate time domain modeling of overhead lines and underground cables with the Method of Characteristics, avoiding unstable time-domain responses when the rational approximation of the propagation function contains large residue-pole ratios.

Although stable time-domain simulations were attained for underground cables, it was found that for transmission lines that the fitting accuracy of the idempotent matrices decreases as the total number of phases of the system increases.

To investigate whether the causes of the aforementioned issues are inherently related to the calculation accuracy of the propagation function, we evaluated the line parameters using a general lossy ground in a wide frequency range, i.e., considering both ground conduction currents and displacement currents.

Time-domain responses based on the Numerical Laplace Transform and the Method of Characteristics were used to assess the accuracy of the aforementioned lines models.

We found that the use of Images approximation closed-form expressions for per-unit-length line parameters may lead to numerical instabilities due to passivity violations when a wide frequency range is considered and the ground is assumed lossy, modeled either with constant or frequency-dependent parameters. A quasi-TEM formulation was used to compare these results. No passivity violations were found in both the single-phase and multi-phase line cases. Some mitigation techniques were also proposed.

Finally, based on this investigation, further research themes are proposed.

# Contents

<b>List of Figures</b>	<b>x</b>
<b>List of Tables</b>	<b>xiii</b>
<b>1 Introduction</b>	<b>1</b>
1.1 Important Considerations . . . . .	1
1.2 Motivation . . . . .	4
1.3 Objectives . . . . .	5
1.4 Document organization . . . . .	6
<b>2 Transmission Line models by using Idempotent Decomposition</b>	<b>7</b>
2.1 Introduction . . . . .	8
2.2 Phase Coordinates Transmission Line Modeling . . . . .	9
2.3 ULM modeling . . . . .	10
2.4 Time-delay Identification . . . . .	12
2.5 Interpolation scheme . . . . .	14
2.6 Idempotent Decomposition . . . . .	15
2.6.1 Conventional Approach (Id-Line) . . . . .	15
2.6.2 Idempotent Grouping (Id-Line-gr) . . . . .	16
2.7 Test cases . . . . .	16
2.7.1 Fitting of $\overline{\mathbf{M}}_i$ and composition of $\mathbf{H}$ . . . . .	18
2.7.2 Time-domain simulation . . . . .	34
2.8 Discussion . . . . .	41
<b>3 Numerical Issues in Single-Phase Line Models</b>	<b>42</b>
3.1 Introduction . . . . .	44
3.2 Identification of the Propagation Constant . . . . .	44
3.3 Evaluation of the Line Parameters . . . . .	49
3.4 Numerical Stability of a Single-phase Line Model . . . . .	54
3.5 Time and Frequency Domains Evaluation . . . . .	59
3.6 Causes of the Passivity violations . . . . .	63



3.7	Conclusions . . . . .	66
<b>4</b>	<b>Numerical Issues in Multi-Phase Line Models</b>	<b>68</b>
4.1	Introduction . . . . .	69
4.2	Formulation of the Line Parameters . . . . .	69
4.2.1	Quasi-TEM Formulation . . . . .	71
4.2.2	Image Approximation . . . . .	71
4.3	Inclusion of frequency dependent soil models . . . . .	72
4.4	Numerical stability of a multiphase line model . . . . .	74
4.5	Test Cases . . . . .	75
4.5.1	Constant ground parameters soil models . . . . .	76
4.5.2	Frequency dependent ground parameters soil models . . . . .	85
4.6	Time and Frequency Domain Evaluation . . . . .	97
4.6.1	Constant ground parameters soil models . . . . .	98
4.6.2	Frequency dependent ground parameters soil models . . . . .	98
4.7	Mitigation Techniques . . . . .	101
4.8	Assessment of Idempotent Decomposition improvement by the use of a quasi-TEM formulation . . . . .	108
4.8.1	System Geometry and data . . . . .	109
4.8.2	Fitting of $\bar{\mathbf{M}}_i$ . . . . .	110
4.9	Discussion . . . . .	121
<b>5</b>	<b>Conclusions</b>	<b>122</b>
5.1	Final Conclusions . . . . .	122
5.2	Future Research . . . . .	124
	<b>Bibliography</b>	<b>126</b>
<b>A</b>	<b>State Space Formulation of Overhead Lines and Underground Cable Parameters</b>	<b>137</b>
<b>B</b>	<b>Numerical Laplace Transform</b>	<b>139</b>
<b>C</b>	<b>Formulation of Modal Equation Using Hertz Vectors</b>	<b>142</b>
<b>D</b>	<b>Numerical Integration</b>	<b>144</b>
<b>E</b>	<b>Formulation of Modal Equation Using Magnetic and Electric Vector Potentials</b>	<b>146</b>

# List of Figures

1.1	General overview - Frequency Dependent Line Models. . . . .	2
1.2	General overview - Frequency Dependent Line calculation approaches. . .	3
1.3	Frequency Dependent soil models studied. . . . .	3
2.1	Multiconductor line. . . . .	9
2.2	Norton equivalent of a transmission system Frequency-domain approach.	10
2.3	Norton equivalent of a transmission system Time-domain approach. . . .	11
2.4	Single-Phase conductor over a lossy ground. . . . .	13
2.5	Identification of time-delay for different fitting orders of $h \exp(s\tau)$ . . . .	13
2.6	Comparison of one-segment and two-segment interpolation schemes. . . .	14
2.7	Norton equivalent of a transmission system Time-domain Id. Line approach.	16
2.8	System geometry of each case. . . . .	17
2.9	Rational Fitting of $\bar{\mathbf{M}}_1, \bar{\mathbf{M}}_2$ and $\bar{\mathbf{M}}_3$ for #1. . . . .	21
2.10	Rational Fitting of $\bar{\mathbf{M}}_4, \bar{\mathbf{M}}_5$ and $\bar{\mathbf{M}}_6$ for #1. . . . .	22
2.11	Rational Fitting of $\bar{\mathbf{M}}_1, \bar{\mathbf{M}}_2$ and $\bar{\mathbf{M}}_3$ for #2. . . . .	23
2.12	Rational Fitting of $\bar{\mathbf{M}}_1, \bar{\mathbf{M}}_2$ and $\bar{\mathbf{M}}_3$ for #3. . . . .	24
2.13	Rational Fitting of $\bar{\mathbf{M}}_4, \bar{\mathbf{M}}_5$ and $\bar{\mathbf{M}}_6$ for #3. . . . .	25
2.14	Rational Fitting of $\bar{\mathbf{M}}_1, \bar{\mathbf{M}}_2$ and $\bar{\mathbf{M}}_3$ for #4. . . . .	26
2.15	Rational Fitting of $\bar{\mathbf{M}}_4, \bar{\mathbf{M}}_5$ and $\bar{\mathbf{M}}_6$ for #4. . . . .	27
2.16	Rational Fitting of $\bar{\mathbf{M}}_7, \bar{\mathbf{M}}_8$ and $\bar{\mathbf{M}}_9$ for #4. . . . .	28
2.17	Rational Fitting of $\bar{\mathbf{M}}_{10}, \bar{\mathbf{M}}_{11}$ and $\bar{\mathbf{M}}_{12}$ for #4. . . . .	29
2.18	Rational Fitting of $\bar{\mathbf{M}}_{13}, \bar{\mathbf{M}}_{14}$ and $\bar{\mathbf{M}}_{15}$ for #4. . . . .	30
2.19	Rational Fitting of $\bar{\mathbf{M}}_{16}, \bar{\mathbf{M}}_{17}$ and $\bar{\mathbf{M}}_{18}$ for #4. . . . .	31
2.20	Rational approximations for $\mathbf{H}_{id}$ - Test cases #1 and #2. . . . .	32
2.21	Rational approximations for $\mathbf{H}_{id}$ - Test cases #3 and #4. . . . .	33
2.22	Circuits for the evaluation of the time responses for test cases #1 and #2. .	34
2.23	Circuits for the evaluation of the time responses for test cases #3 and #4. .	35
2.24	#1 - Time-domain simulations and error of the Idempotent Decomposition.	36
2.25	#2 - Time domain simulations and error of the Idempotent Decomposition.	37
2.26	#3 - Time domain simulations and error of the Idempotent Decomposition.	38
2.27	#4 - Time-domain simulations and error of the Idempotent Decomposition.	39

3.1	Single-phase conductor arrangement. . . . .	45
3.2	Behavior of $\gamma$ for distinct approaches. . . . .	48
3.3	Accuracy comparison of closed-form $T$ . . . . .	52
3.4	Passivity violations in $\mathbf{Y}$ using different closed-forms of $T$ . . . . .	53
3.5	Behavior of $Y_c$ for the three distinct approaches. . . . .	56
3.6	Behavior of $H$ for the three distinct approaches. . . . .	57
3.7	Passivity violations in $\lambda_1$ and $\lambda_2$ . . . . .	58
3.8	Single-phase circuit for time-domain test. . . . .	60
3.9	Impulse voltage response using NLT. . . . .	60
3.10	Fitting error of $Y_c$ for the three distinct approaches. . . . .	61
3.11	Fitting error of $H$ for the three distinct approaches. . . . .	62
3.12	Impulse voltage response using MoC. . . . .	62
3.13	Sensitivity assessment of variables in $Z$ and $Y$ . . . . .	64
3.14	Deviation of quasi-TEM vs Image approximations. . . . .	65
4.1	Multiphase conductor arrangement. . . . .	70
4.2	Test cases configurations. . . . .	75
4.3	Passivity violations of the 138 kV circuit - Constant ground parameters. . . . .	79
4.4	Passivity violations of the 230 kV circuit - Constant ground parameters. . . . .	80
4.5	Passivity violations of the 500 kV circuit - Constant ground parameters. . . . .	81
4.6	Rational fitting of $\mathbf{Y}_c$ and $\mathbf{H}$ - 138 kV circuit. . . . .	82
4.7	Absolute fitting error of $\mathbf{Y}_c$ and $h_i$ - 138 kV circuit. . . . .	83
4.8	Passivity violations in $\mathbf{Y}_n$ - 138 kV circuit. . . . .	84
4.9	Passivity violations of the 138 kV circuit - Frequency dependent soils. . . . .	86
4.10	Passivity violations of the 230 kV circuit - Frequency dependent soils. . . . .	87
4.11	Passivity violations of the 500 kV circuit - Frequency dependent soils. . . . .	88
4.12	Rational fitting of $\mathbf{Y}_c$ - 138 kV circuit. . . . .	91
4.13	Rational fitting of $\mathbf{H}$ - 138 kV circuit. . . . .	92
4.14	Absolute fitting error of $\mathbf{Y}_c$ - 138 kV circuit. . . . .	93
4.15	Absolute fitting error of $h_i$ - 138 kV circuit. . . . .	94
4.16	Passivity violations in $\mathbf{Y}_n$ from original data - 138 kV circuit. . . . .	95
4.17	Passivity violations in $\mathbf{Y}_n$ from fitted $\mathbf{Y}_c$ and $\mathbf{H}$ - 138 kV circuit. . . . .	96
4.18	Multiphase circuit for time-domain test. . . . .	97
4.19	Time-domain results in 138 kV circuit - Constant ground parameters. . . . .	99
4.20	Time-domain results in 138 kV circuit - Frequency dependent soils. . . . .	100
4.21	Rational fitting of $\mathbf{Y}_c$ and $\mathbf{H}$ for 138 kV circuit - scalar potential definition . . . . .	102
4.22	Passivity violations for 138 kV circuit - scalar potential definition . . . . .	103
4.23	Time-domain results in 138 kV circuit - scalar potential definition . . . . .	104
4.24	Fitting of $\mathbf{Y}_c$ and $\mathbf{H}$ for 138 kV circuit - scalar potential definition ( $\eta = \gamma_2$ ) . . . . .	105

4.25	Passivity violations for 138 kV circuit - scalar potential definition ( $\eta = \gamma_2$ )	106
4.26	Time responses for 138 kV circuit - scalar potential definition ( $\eta = \gamma_2$ ) . .	107
4.27	System geometry of each case. . . . .	109
4.28	Rational Fitting of $\bar{\mathbf{M}}_1$ , $\bar{\mathbf{M}}_2$ and $\bar{\mathbf{M}}_3$ for #1. . . . .	110
4.29	Rational Fitting of $\bar{\mathbf{M}}_1$ , $\bar{\mathbf{M}}_2$ and $\bar{\mathbf{M}}_3$ for #2. . . . .	111
4.30	Rational Fitting of $\bar{\mathbf{M}}_1$ , $\bar{\mathbf{M}}_2$ and $\bar{\mathbf{M}}_3$ for #3. . . . .	112
4.31	Rational Fitting of $\bar{\mathbf{M}}_4$ , $\bar{\mathbf{M}}_5$ and $\bar{\mathbf{M}}_6$ for #3. . . . .	113
4.32	Rational Fitting of $\bar{\mathbf{M}}_1$ , $\bar{\mathbf{M}}_2$ and $\bar{\mathbf{M}}_3$ for #4. . . . .	114
4.33	Rational Fitting of $\bar{\mathbf{M}}_4$ , $\bar{\mathbf{M}}_5$ and $\bar{\mathbf{M}}_6$ for #4. . . . .	115
4.34	Rational Fitting of $\bar{\mathbf{M}}_7$ , $\bar{\mathbf{M}}_8$ and $\bar{\mathbf{M}}_9$ for #4. . . . .	116
4.35	Rational Fitting of $\bar{\mathbf{M}}_{10}$ , $\bar{\mathbf{M}}_{11}$ and $\bar{\mathbf{M}}_{12}$ for #4. . . . .	117
4.36	Rational Fitting of $\bar{\mathbf{M}}_{13}$ , $\bar{\mathbf{M}}_{14}$ and $\bar{\mathbf{M}}_{15}$ for #4. . . . .	118
4.37	Rational Fitting of $\bar{\mathbf{M}}_{16}$ , $\bar{\mathbf{M}}_{17}$ and $\bar{\mathbf{M}}_{18}$ for #4. . . . .	119

# List of Tables

2.1	Poles from the rational approximation of the line parameters. . . . .	18
2.2	Calculated and Lumped time delays. . . . .	18
2.3	Maximum fitting deviation of $\mathbf{H}$ - Idempotent modeling . . . . .	19
2.4	Absolute fitting error of the Idempotent Matrices. . . . .	19
2.5	Residue-pole ratios of the propagation matrix $\mathbf{H}$ . . . . .	40
2.6	Total simulation time for Id-Line and ULM modeling. . . . .	40
3.1	Passivity violations and minima of $\lambda_1$ and $\lambda_2$ . . . . .	55
3.2	Passivity violations as a function of $h$ . . . . .	59
3.3	Passivity violations as a function of $r$ . . . . .	59
3.4	Passivity violations as a function of $\ell$ . . . . .	59
4.1	Frequency dependent soil model characteristics. . . . .	73
4.2	Coefficients $a_i$ for the Smith-Longmire soil model. . . . .	73
4.3	Computational processing times of quasi-TEM and image approximations. . . . .	76
4.4	Frequency of largest passivity violations and minima of $\lambda$ for $\ell = 300$ m. . . . .	77
4.5	Passivity violations and minima of $\lambda$ for a line length of $\ell = 300$ m. . . . .	85
4.6	Minimum line length $\ell$ for test cases (m). . . . .	89

# Chapter 1

## Introduction

### 1.1 Important Considerations

Power Systems worldwide are becoming increasingly complex. The network expansion together with environmental constraints demand more complex and asymmetrical transmission system configurations. A new circuit may share the same tower of an existing one and the coupling effect cannot be neglected.

The first transient studies with more detailed transmission line models were completely solved in the frequency domain [1]. Later, simulation tools such as the Electromagnetic Transient Programs (EMTPs) allowed the transient analysis of multiple components in an electrical network using a time-domain solution [2–4].

As non-linear elements and phenomena are frequently found in nowadays system topologies, i.e., corona effect and surge arresters just to mention a few, the use of time-domain analysis to model the electrical network is preferred. This is due to its capability to accurately simulate fast and very fast transients phenomena using a recursive convolution scheme which allows the inclusion of certain frequency dependent elements through the use of rational approximations.

Purposely, in relation to the simulation of transmission lines and underground cables, an essentially free distribution program which is widely extended use in the electrical and academic sectors throughout the world is the EMTP-ATP. This program includes three frequency-dependent line models: the Semlyen model [5], the JMarti model [6] and the Taku Noda model [7]. The JMarti model relies in the use of modal decomposition [8, 9] assuming a real frequency independent modal transformation matrix [5, 6, 10, 11]. This line model is the most widely used among the aforementioned three, due to its best performance and simpler interface when compared to the former two models [12, 13].

However, in the case of non-symmetric line configurations, a model with a frequency dependent transformation matrix is expected along with the interaction between different time-delays. To overcome these limitations, the modeling of transmission lines without

resorting to modal decomposition, i.e., using phase coordinates, has been studied [7, 14–21]. Two of these models were later implemented in EMTP-type programs: the Auto-Regressive Moving Average (ARMA) model [7] based on a Z-domain rational fitting was implemented in the EMTP-ATP while the Universal Line Model (ULM) [20] based on the frequency domain rational fitting of parameters was implemented in the PSCAD/EMTDC and the EMTP-RV.

Purposely, a method for the rational fitting of parameters in the frequency domain known as “Vector Fitting”, based in a Sanathanan-Koerner iteration scheme, has recently gained popularity in the scientific community. Due to its simplicity and solid performance [22–28], its computational routines have been implemented in MATLAB and are free-to-use [29].

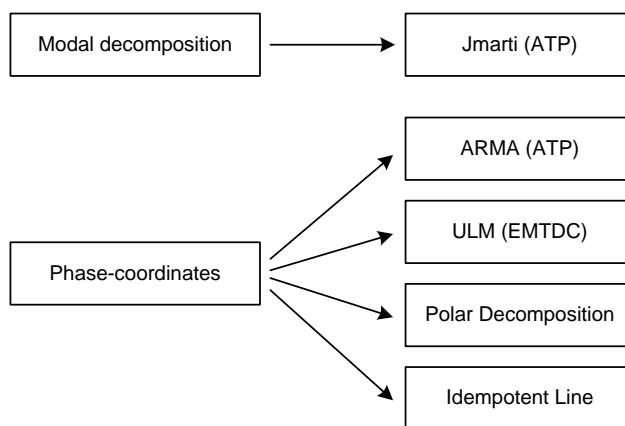


**Figure 1.1:** *General overview - Frequency Dependent Line Models.*

For the analysis of electromagnetic transients in overhead transmission lines or underground cables, the quasi-Transverse Electromagnetic (quasi-TEM) propagation is normally assumed. In power system studies the ground return expressions are developed assuming the ground as a good conductor, i.e., neglecting displacement currents associated with the ground permittivity. This implies the evaluation of the ground return impedance using either Carson’s or Pollaczek’s formulation [30–32] involving the solution of non-trivial infinite integrals traditionally expressed by simplified expressions [33–36]. For the ground return impedance, the inclusion of the ground permittivity  $\epsilon_s$  is essentially straight forward, as we only need to replace the ground conductivity  $\sigma_s$  by the complex value of  $\sigma_s + j\omega\epsilon_s$ .

One of the most successful approximations is based on the image approach [34, 37] which consists of a further simplification leading to a closed-form formula based on logarithms. These image approximations are also used in the calculation of the ground shunt admittance.

Therefore, for very high frequency phenomena, i.e., lightning, the inclusion of the ground permittivity in the calculation of the per-unit-length line parameters is necessary for the modeling of transmission circuits. The inclusion of the ground permittivity in

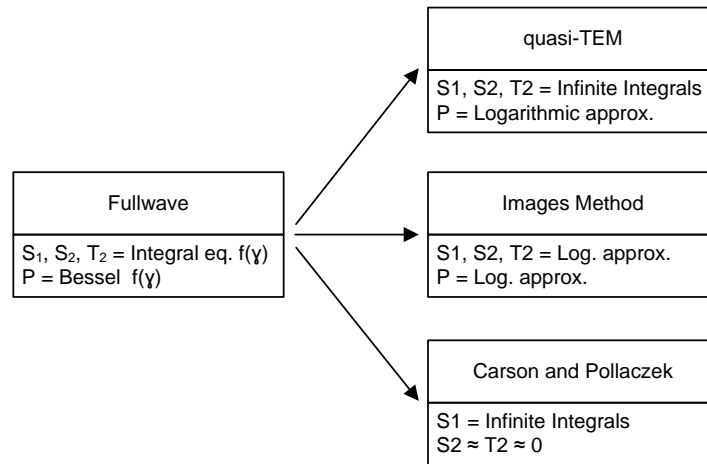


**Figure 1.2:** General overview - Frequency Dependent Line calculation approaches.

the series impedances and shunt admittance can be done through the calculation of the line parameters using a Fullwave model, a quasi-TEM formulation or Image approximations [38]. The impact of its inclusion in the time-domain line behavior when high frequency range excitations are considered has not been fully assessed and remains nowadays as an open research topic.

Another point of interest is the time-domain modeling of transmission lines for fast and very fast transients. The evaluation of lightning performance [39–41], might require to consider frequencies up to 10 MHz [20, 23, 42, 43] or 100 MHz [44, 45]. This large bandwidth is also involved in the improvement of frequency domain fitting, identification of time-delays, and to avoid frequencies with numerical instabilities. In these cases, it is important to include the ground permittivity, since ground displacement currents are no longer negligible due to the high frequencies involved, and the approximation of modeling a lossy ground as a pure conductor can render inaccurate results.

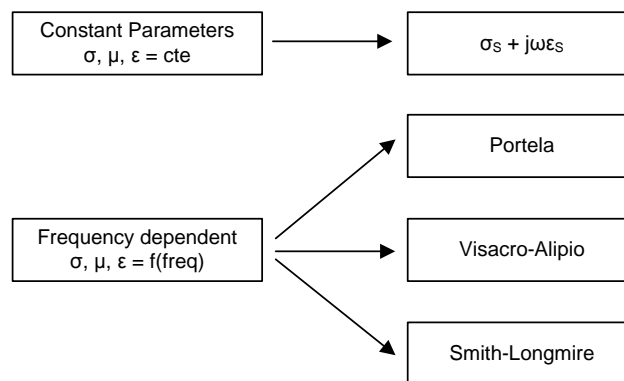


**Figure 1.3:** Frequency Dependent soil models studied.



## 1.2 Motivation

While rational fitting methods have facilitated the representation of electrical parameters in the frequency domain via partial fractions, their direct application in Electromagnetic Transient modeling can still present certain difficulties.

As an example, the ULM has received several improvements concerning the fitting accuracy of the propagation function [46], out of band passivity violations [43] and more recently related to its numerical stability [45, 47], where large residue-pole ratios cause the magnification of interpolation errors leading to unstable time-domain simulations [48]. Nonetheless, these improvements required to overcome certain shortcomings of the ULM, such as the the obtention of unstable time-domain simulations when a one-segment interpolation scheme is used, i.e., a 2-point interpolation approach. To surmount this limitation, an additional post-processing treatment of the transmission circuit parameters based on the usage of a two-segment interpolation scheme must be employed, i.e., a 3-point interpolation approach.

As pointed out in [45], a one-segment interpolation scheme is enough for modal decomposition models, where the absence of interaction between distinct modes avoids the magnification of interpolation errors, i.e., each mode has its own independent interpolation scheme. Therefore, if a line can be modeled on phase coordinates without interaction between distinct time-delays, some of the aforementioned instability issues might be waived. In the technical literature there are two phase coordinate models that fall into this category: the polar decomposition model [49] and the Idempotent line model [50, 51], being the latter a model left aside in the past due to accuracy issues in the method used for the rational fitting of the Idempotent Matrices. Although issues in the quality of the fitting of the Idempotent matrices were originally reported in [52], no specific details were given. These findings discouraged any further research on its viability as an alternative line model to the ULM approach.

For time-domain simulations using the Idempotent line model, the procedure is slightly different from the ULM approach. Since the propagation matrix is represented as a sum of several independent matrices, it is more efficient to represent both history current sources as a set of parallel current sources, i.e., each current source has its own interpolation scheme associated with a single idempotent matrix, and there are no interactions between different time-delays, which will allow for a more robust phase-domain simulation using a one-segment interpolation scheme.

Additional research is also required in the field of line modeling using the fullwave approach, the quasi-TEM formulation and image approximations for multiphase overhead lines including the effect of the ground admittance per-unit length. Approximated expressions have already been proposed to include its effect in the calculation of per-unit-length line parameters [53–56]. Nonetheless, there has not been neither an assessment of their

impact on the line behavior in the high frequency range, nor a synthesis of calculated line parameters using rational functions.

Furthermore, although recent research indicates the need to consider the frequency dependence in ground parameters [41, 57], its effect in multiphase overhead lines has only been studied for a simplified Carson or Pollaczek model of the ground return impedance, leaving as an open research topic field its impact in a Fullwave approach, which is the least simplified way to obtain the line parameters.

### 1.3 Objectives

The fundamental objectives of this work are:

- To continue a research started during the master dissertation of the author by studying the behavior of Transmission Line models with frequency dependent soil parameters and considering the effect of the displacement currents in time domain simulations. It is important to point out that the impact of displacement currents is usually disregarded.
- The assessment of the possibility to evaluate transmission circuits using the Idempotent Decomposition model [50, 51] with an improved fitting scheme to attain a low fitting order as an alternative to the traditional ULM approach.
- An investigation of the viability of the Idempotent Decomposition model using the Method of Characteristics to obtain time-domain results.
- The evaluation, in both frequency and time-domain, of the applicability, limitations, numerical stability and precision of rational fitting models.
- The study of alternative models for the representation of overhead transmission lines, especially in the high frequency domain and their limitations in the rational fitting of parameters. First, the fullwave approach, which is the least simplified way to obtain the line parameters by the iterative calculus of the propagation constant of the circuit, second, the quasi-TEM formulation, which includes simplified infinite integrals, and finally, the Image approximations, which employs closed-form expressions to consider the infinite integrals, and to study in each of the aforementioned procedures.
- The assessment of the effect of frequency-dependent soil parameters in the modeling of overhead transmission lines represented using the fullwave approach, the quasi-TEM formulation and image approximations.

## 1.4 Document organization

The present text is divided into 5 chapters. In the following paragraphs a brief description of each chapter is presented.

Chapter 1 includes the present introduction, which describes the principal considerations taken in the present research work, motivation, objectives and a description of the document organization.

Chapter 2 presents an application assessment of the Idempotent Decomposition in phase coordinates as an alternative to the ULM approach for modeling overhead lines and underground cables preserving the one-segment interpolation scheme used to calculate the convolution integrals in the time domain.

Chapter 3 studies the numerical issues related to both the line modeling and the rational fitting of the propagation function and characteristic admittance of a single phase line over a lossy ground using a fullwave, quasi-TEM and Image approaches. Comparative results of time-domain simulations for the quasi-TEM approach are presented.

Chapter 4 investigates the applicability and limitations of rational fitting applied to the multiphase line parameters using a quasi-TEM formulation and Image approximations with soil models using constant and frequency dependent parameters. The issues found in the fitting of the Idempotent matrices are assessed using a quasi-TEM formulation to recalculate the examples presented in the former chapters.

Finally, Chapter 5 treats the principal results of the present work and proposes some topics for future research.

## Chapter 2

# Transmission Line models by using Idempotent Decomposition

In the present chapter, we assess the application of the Idempotent Decomposition in phase-coordinates as an alternative to the ULM approach for modeling underground cables and overhead transmission lines in phase-coordinates. The Vector Fitting method (VF) [24]–[58] was used for the rational approximation of the Characteristic Admittance and Idempotent matrices instead of the asymptotic magnitude fit originally used in the Idempotent Line model [50, 51]. Time-domain responses obtained by the Method of Characteristics (MoC) were compared with results calculated using a frequency-domain algorithm based on the Numerical Laplace Transform (NLT) [59–61].

It was found that for the modeling of underground cables, the Idempotent Decomposition is a suitable solution presenting both a good quality fit of the Idempotent matrices and an accurate time-domain response. To the best of the authors' knowledge, the modeling of underground cables using Idempotent Decomposition as an alternative phase-domain method has not been presented before in the technical literature. However, for the modeling of overhead transmission lines, results indicate that there is a limitation to the number of phases an Idempotent Line model can accurately represent. In this case, as the number of phases increases, the accuracy of the rational fitting of the Idempotent matrices involved decrease. Issues in the quality of the fitting of the Idempotent matrices were originally reported in [52], although no specific details were given. A proposition to group Idempotent Matrices with similar associated time-delays based on the grouping routine used in the ULM approach to reduce the order of the rational functions which compose the propagation matrix was tested. Some speed gain was attained due to a lesser number of Idempotent matrices required for the simulations; however, no significant accuracy improvement in the fitting of the Idempotent matrices was obtained in the test cases considered here.

The chapter is organized as follows: An introduction to this chapter is presented in Section 2.1. A brief review of time-domain modeling of transmission lines is presented

in Section 2.2. The so-called ULM approach is reviewed in Section 2.3. The time-delay extraction procedure is briefly explained in Section 2.4. The interpolation principles used in time-domain simulations by the Method of Characteristics are explained in Section 2.5. The principles of idempotent decomposition modeling are shown in Section 2.6. Some test cases are evaluated in Section 2.7. Finally, the main conclusions are presented in Section 2.8.

## 2.1 Introduction

Power Systems worldwide are becoming increasingly complex. The network expansion together with environmental constraints have created more complex and asymmetrical configurations. A new circuit may share the same tower of an existing one and the coupling between circuits cannot be neglected. Furthermore, as new interconnections with longer transmission lines in HVDC and HVAC are established [62, 63], more precise simulation methods are required for the representation of multiphase transmission systems.

In the aforementioned line configurations, due to computational burden limitations, the simulation of transmission lines and underground cables in Electromagnetic Transients Programs (EMTP) originally relied on the use of modal decomposition [8, 9] and a one-segment interpolation scheme to evaluate the modal time-delays as they are not generally multiples of the time-step. Nonetheless, for more asymmetric configurations, the use of a frequency dependent transformation matrix is preferred, thus a phase-coordinates model seems more suitable as the assumption of a real frequency independent modal transformation matrix [5]–[11] loses validity.

To overcome the limitations associated with assuming a real and constant transformation matrix in the modeling of transmission lines, a large amount of research has been carried out using phase-coordinates [14]–[21]. Two of these models were latterly implemented in EMTP-type programs: the Universal Line Model (ULM) [20], included in both the PSCAD/EMTDC and EMTP-RV, and the IARMA model [7] in ATP. Since its proposal, the ULM has received several improvements related to fitting accuracy [46], out of band passivity violations [64] and, more recently, to its numerical stability [45, 47], as large residue-pole ratios caused magnifications of interpolation errors leading to unstable time-domain simulations.

As pointed out in [45], a one-segment interpolation scheme, i.e., a 2-point interpolation approach, is enough for modal decomposition models, where the absence of interaction between distinct modes avoids the magnification of interpolation errors, as each mode is interpolated independent separately. Therefore, if a line can be modeled on phase-coordinates without interaction between distinct time-delays, certain instability issues of the ULM reported in [45] might be avoided. In the technical literature there are two phase-

coordinate models which satisfy these requirements: the Polar Decomposition model [49] and the Idempotent Line model (id-Line) [50, 51]. While the Polar Decomposition test cases considered underground cables and overhead lines, the id-Line was tested only in overhead transmission lines.

## 2.2 Phase Coordinates Transmission Line Modeling

The distributed nature of transmission line impedances together with the skin effect in conductors and earth return path cause voltage and current distortions and attenuations. The behavior of voltages and currents in a transmission line is fully described by the following equations

$$\begin{aligned}\frac{d\mathbf{V}}{dx} &= -\mathbf{Z} \cdot \mathbf{I} \\ \frac{d\mathbf{I}}{dx} &= -\mathbf{Y} \cdot \mathbf{V}\end{aligned}\quad (2.1)$$

where  $\mathbf{V}$  is the phase to ground voltage vector,  $\mathbf{I}$  is the current vector,  $\mathbf{Z}$  is the series impedance matrix and  $\mathbf{Y}$  is the shunt admittance matrix, both in per-unit-length units. For a  $n$ -conductor system the matrices are  $n \times n$  while the vectors are  $n \times 1$ .

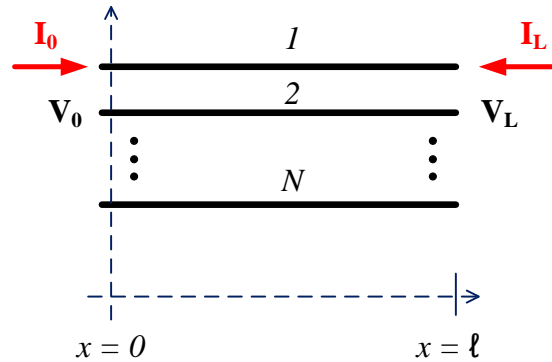


**Figure 2.1:** Multiconductor line.

For a transmission line with length  $\ell$  as the one depicted in Fig. 2.2, the voltages  $\mathbf{V}_0$ ,  $\mathbf{V}_L$  and currents  $\mathbf{I}_0$ ,  $\mathbf{I}_L$  at the terminals are related in the frequency-domain by (2.2),  $\mathbf{Y}_C = \mathbf{Z}^{-1}\sqrt{\mathbf{Z} \cdot \mathbf{Y}}$  is the characteristic admittance and  $\mathbf{H} = \exp\left(-\ell\sqrt{\mathbf{Y} \cdot \mathbf{Z}}\right)$  is the propagation function matrix.

$$\begin{aligned}\mathbf{I}_0 - \mathbf{Y}_C \mathbf{V}_0 &= -\mathbf{H}(\mathbf{I}_L + \mathbf{Y}_C \mathbf{V}_L) \\ \mathbf{I}_L - \mathbf{Y}_C \mathbf{V}_L &= -\mathbf{H}(\mathbf{I}_0 + \mathbf{Y}_C \mathbf{V}_0)\end{aligned}\quad (2.2)$$

Fig. 2.2 shows the equivalent circuit representation of the transmission system in the

frequency domain.

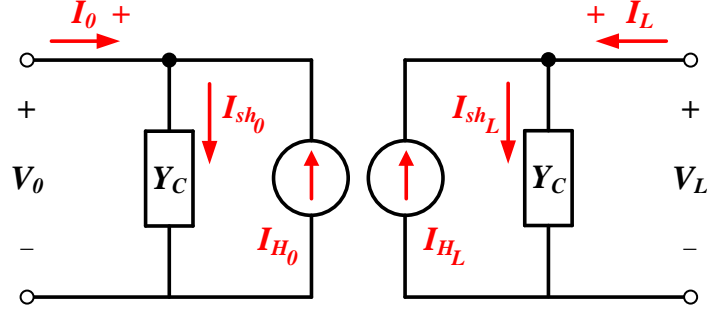


**Figure 2.2:** Norton equivalent of a transmission system  
Frequency-domain approach.

The time-domain counterpart of (2.2) is given by

$$\begin{aligned} \mathbf{i}_0 &= \mathbf{y}_c * \mathbf{v}_0 - \mathbf{h} * (\mathbf{i}_L + \mathbf{y}_c * \mathbf{v}_L) \\ \mathbf{i}_L &= \mathbf{y}_c * \mathbf{v}_L - \mathbf{h} * (\mathbf{i}_0 + \mathbf{y}_c * \mathbf{v}_0) \end{aligned} \quad (2.3)$$

as  $\mathbf{y}_c$  and  $\mathbf{h}$  are the unit impulse responses of  $\mathbf{Y}_C$  and  $\mathbf{H}$ ,  $\mathbf{v}_0$ ,  $\mathbf{v}_L$ ,  $\mathbf{i}_0$  and  $\mathbf{i}_L$  are the time-domain counterparts of frequency domain terminal voltages and injected currents and the symbol  $*$  indicates convolution. It is possible to rewrite  $\mathbf{i}_0$  as

$$\mathbf{i}_0 = \mathbf{i}_{sh_0} - \mathbf{i}_{H_0} \quad (2.4)$$

where

$$\begin{aligned} \mathbf{i}_{sh_0} &= \mathbf{y}_c * \mathbf{v}_0 = \mathbf{i}_{sh_0,aux} + \mathbf{G} * \mathbf{v}_0 \\ \mathbf{i}_{H_0} &= \mathbf{h} * (\mathbf{i}_L + \mathbf{y}_c * \mathbf{v}_L) = \mathbf{h} * \mathbf{i}_{fwL} \end{aligned} \quad (2.5)$$

and  $\mathbf{i}_{sh_0,aux}$  is an auxiliary shunt current source,  $\mathbf{i}_{fwL}$  a forward traveling current-wave vector and  $\mathbf{G}$  an equivalent conductance matrix. By exchanging the subindexes 0 and L in (2.4) and (2.5), the corresponding set of equations for  $\mathbf{i}_L$  can be obtained. Fig. 2.3 shows the equivalent circuit model of the transmission system. A rather efficient recursive formulation of the time-domain convolutions is possible if both  $\mathbf{Y}_C$  and  $\mathbf{H}$  are represented using rational approximations [5].

For underground cables the procedure is basically the same, only the frequency-domain behavior of the per-unit-length parameters will be different.

## 2.3 ULM modeling

For the rational approximation of the line parameters, a Vector Fitting (VF) implementation with a relaxation of the scaling function was used [25, 26]. See [65] for a detailed

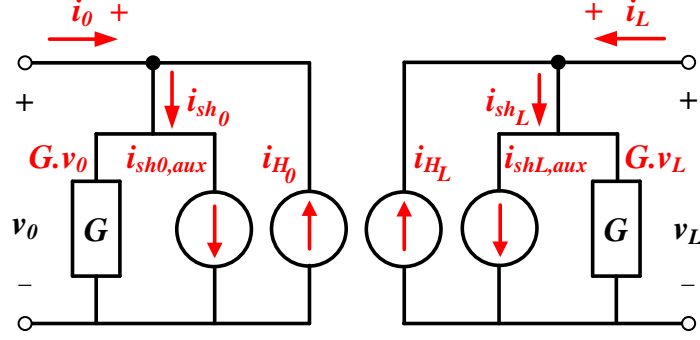


**Figure 2.3:** Norton equivalent of a transmission system  
Time-domain approach.

accuracy comparison of different vector fitting implementations.

A rational representation of  $\mathbf{Y}_C$  has the form:

$$\mathbf{Y}_C \approx \sum_{n=1}^K \frac{\mathbf{R}_n}{s - a_n} + \mathbf{D} \quad (2.6)$$

where  $a_n$  are the poles obtained from fitting the trace of the characteristic admittance,  $\mathbf{R}_n$  is the matrix of residues and  $\mathbf{D}$  is a constant matrix.

The rational fitting of the propagation matrix  $\mathbf{H}$  is slightly different. First, the modal propagation parameters are obtained by decomposing  $\mathbf{H}$  in its eigenvalues and eigenvectors, resulting in the product of a frequency dependent transformation matrix  $\mathbf{T}$ , a diagonal matrix of modes  $\mathbf{H}_m$  and the inverse matrix of  $\mathbf{T}$  given by

$$\mathbf{H} = \mathbf{T} \cdot \mathbf{H}_m \cdot \mathbf{T}^{-1} \quad (2.7)$$

Each mode  $h_i$  can be represented by a minimum phase-shift function  $p_i(s)$  and an exponential function of the time-delay  $\tau_i$  as:

$$h_i \approx p_i(s) \exp(-s\tau_i) = \left( \sum_{m=1}^{N_i} \frac{\hat{c}_{m,i}}{s + p_{m,i}} \right) \exp(-s\tau_i) \quad (2.8)$$

where  $N_i$  is the fitting order of the mode  $i$ ,  $p_{m,i}$  are the poles and  $\hat{c}_{m,i}$  are the residues of the rational approximation. After identifying each  $\tau_i$  [66, 67], the propagation matrix  $\mathbf{H}$  is fitted using the poles from the modes  $p_{m,i}$ , thus

$$\mathbf{H} \approx \mathbf{H}_{ULM-ug} = \sum_{i=1}^N \left( \sum_{m=1}^{N_i} \frac{\mathbf{R}_{m,i}}{s + p_{m,i}} \right) \exp(-s\tau_i) \quad (2.9)$$

where  $N$  is the number of modes,  $\mathbf{R}_{m,i}$  is the matrix of residues associated with mode  $i$ , and  $\mathbf{H}_{ULM-ug}$  stands for the rational approximation considering all the modes. If modes with nearly equal time-delays are grouped together we have the rational approximation of



the propagation function proposed in the ULM [20]

$$\mathbf{H} \approx \mathbf{H}_{ULM} = \sum_{k=1}^K \left( \sum_{m=1}^{N_k} \frac{\mathbf{R}_{m,k}}{s + p_{m,k}} \right) \exp(-s\tau_k) \quad (2.10)$$

where  $K$  is the number of grouped modes ( $K < N$ ),  $\tau_k$  is the collapsed time-delay,  $\mathbf{R}_{m,k}$  is the matrix of residues calculated for the corresponding poles  $p_{m,k}$  of the grouped mode and  $\mathbf{H}_{ULM}$  stands for the rational approximation of  $\mathbf{H}$  considering the grouped modes.

## 2.4 Time-delay Identification

From equation (2.8), we extract the time-delay of each mode  $h_i$  and we calculate a proper rational approximation.

$$h_i \exp(s\tau_i) \approx \sum_{n=1}^{N_i} \frac{\hat{c}_{i,n}}{s + p_{i,n}} \quad (2.11)$$

The expression (2.11) is a minimum-phase function multiplied by an exponential time-delay [10], then the poles and residues can be calculated using a rational fitting algorithm. To extract the time-delays  $\tau_i$  in a transmission circuit of length  $\ell$ , we can use the transit time of each mode from their respective velocities  $v_i$  at the highest frequency of interest  $\Omega$ . Each modal velocity  $v_i$  is given by

$$v_i = \frac{2\pi f(\Omega)}{\Im \left( \sqrt{Z_{i(\Omega)} Y_{i(\Omega)}} \right)} \quad (2.12)$$

$$\tau_i = \frac{\ell}{v_i}$$

Nonetheless, the calculated value of each time-delay is not necessarily the value which will render the best fitting. The time-delay used must be the one which presents the least RMS fitting error in the frequency band of interest.

It is possible to optimize the process limiting the minimum time-delay  $\tau_{min}$  and the maximum time-delay  $\tau_{max}$  values to the theoretical speed of light time  $\ell/c$  and the modal velocity  $\ell/v_i$  respectively

$$\frac{\ell}{c} \leq \tau_i \leq \frac{\ell}{v_i} \quad (2.13)$$

where  $c$  is the velocity of light.

To clarify this process in more detail, we present here a brief application example. Consider the time-delay identification of the transmission line presented in Fig. 2.4, with a single-phase conductor of 10 km length.

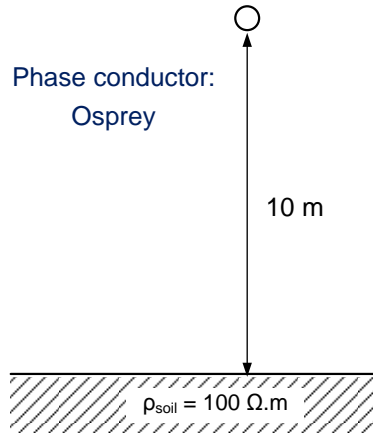


**Figure 2.4:** Single-Phase conductor over a lossy ground.

Figure 2.5 presents the search for the time-delay with the minimum RMS-Error for different fitting orders of the term  $h \exp(s\tau)$ , being  $\tau_{min}$  the time-delay of an ideal line, and  $\tau_{max}$  the time-delay of the mode with the highest frequency of interest [67].

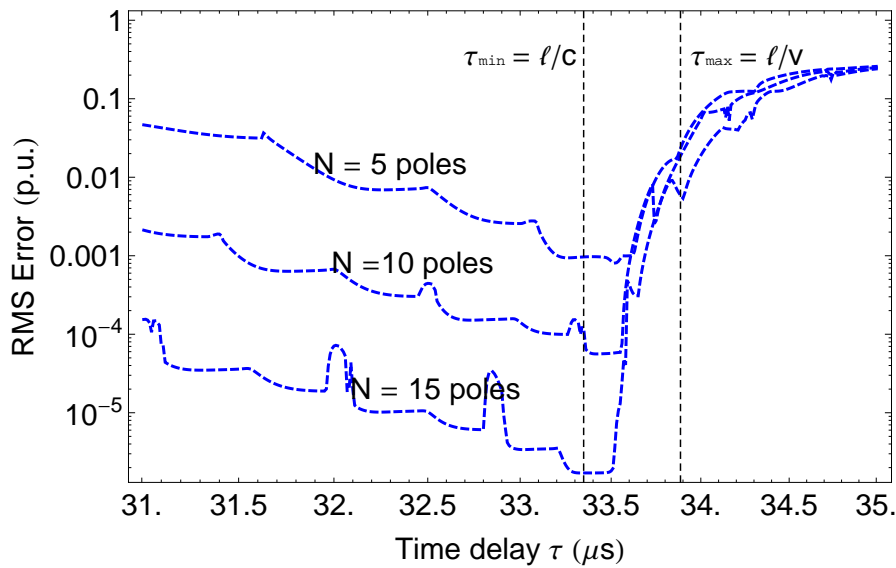


**Figure 2.5:** Identification of time-delay for different fitting orders of  $h \exp(s\tau)$ .

For this example, the minimum and maximum time-delays are respectively  $33,33 \mu s$  and  $33,90 \mu s$ , while the time-delays which present the minimum RMS-errors for the orders of  $N = 5, 10$  and  $15$  poles are respectively  $33,53 \mu s, 33,43 \mu s$  and  $\approx 33,33 \mu s$ , i.e., a time-delay slightly higher to the ideal time-delay of the line.

## 2.5 Interpolation scheme

For a time-delay  $T$ , consider the frequency-domain rational approximation form of  $h$  as follows

$$h(s) = \frac{r}{s-a} e^{-sT} \quad (2.14)$$

the integral solution of (2.14) is given by

$$y(t) = r \cdot e^{a\Delta t} y(t - \Delta t) + r \int_0^{\Delta t} e^{a\tau} u(t - \tau - T) d\tau \quad (2.15)$$

When the integral is performed over the one-segment line between  $u(t - \tau - T)$  and  $u(t - T)$ , it gives for

$$\begin{aligned} x(t) &= \alpha x(t - \Delta t) + \lambda u_{(t-(k+\xi)\Delta t)} + \mu u_{(t-(k+1+\xi)\Delta t)} \\ y(t) &= r \cdot x(n) \end{aligned} \quad (2.16)$$

Since the coefficient  $\xi$  is in general different for the different delay groups, the one-segment approximation of  $u(t)$  cumulatively perturbs the rational model, hence the ULM time-domain simulations become unstable with an increasing number of phases. Thus, a two-segment interpolation scheme is needed in the ULM to guarantee stable simulations.

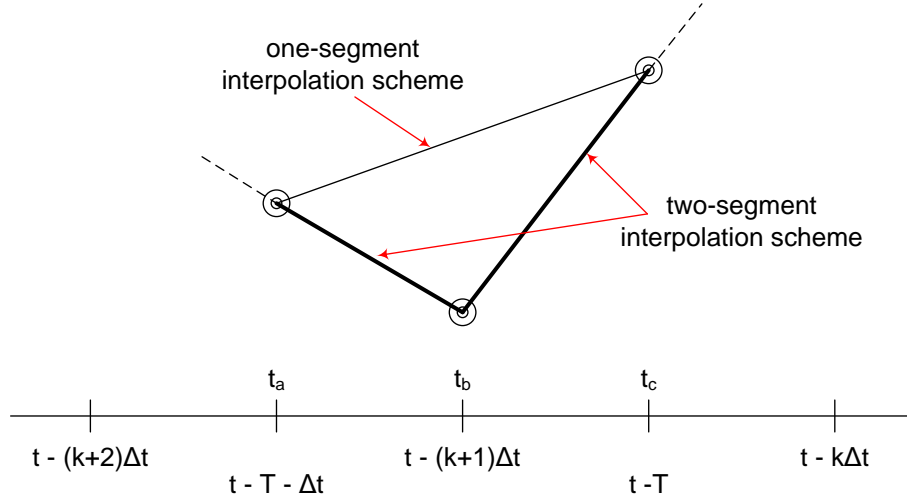


**Figure 2.6:** Comparison of one-segment and two-segment interpolation schemes.

The mathematical formulation is given by

$$\begin{aligned} x^*(t) &= \alpha_1 x(t - \Delta t) + \lambda_1 u_{(t_b)} + \mu_1 u_{(t_a)} \\ x(t) &= \alpha_2 x^*(t - \Delta t) + \lambda_2 u_{(t_c)} + \mu_2 u_{(t_b)} \\ y(t) &= r \cdot x(t) \end{aligned} \quad (2.17)$$

## 2.6 Idempotent Decomposition

For the Idempotent decomposition, the rational approximation of  $\mathbf{Y}_c$  is the same as in the previous section. Next, we present two possible approaches for the rational approximation of  $\mathbf{H}$ .

### 2.6.1 Conventional Approach (Id-Line)

Consider again the eigendecomposition of the propagation matrix  $\mathbf{H}$  presented in (2.7). Expanding  $\mathbf{T}$ ,  $\mathbf{H}_m$  and  $\mathbf{T}^{-1}$  we have

$$\mathbf{H} = \begin{bmatrix} \mathbf{T}_1 & \cdots & \mathbf{T}_N \end{bmatrix} \begin{bmatrix} h_1 & \cdots & 0 \\ \vdots & \ddots & \vdots \\ 0 & \cdots & h_N \end{bmatrix} \begin{bmatrix} \mathbf{S}_1 \\ \vdots \\ \mathbf{S}_N \end{bmatrix} = \sum_{i=1}^N \mathbf{M}_i h_i \quad (2.18)$$

where  $N$  is the number of modes,  $\mathbf{T}_i$  represents a column vector of  $\mathbf{T}$ ,  $\mathbf{S}_i$  is a row vector of  $\mathbf{T}^{-1}$  and  $\mathbf{M}_i = \mathbf{T}_i \cdot \mathbf{S}_i$  is an Idempotent matrix associated with mode  $i$ . If we write

$$\overline{\mathbf{M}}_i = \mathbf{T}_i \cdot \mathbf{S}_i p_i(s) \quad (2.19)$$

where  $p_i(s)$  is defined as in (2.8). Let  $\overline{\overline{\mathbf{M}}}_i$  be a rational approximation of  $\overline{\mathbf{M}}_i$ , then  $\mathbf{H}$  can be approximate as

$$\mathbf{H} \approx \mathbf{H}_{id} = \sum_{i=1}^N \overline{\overline{\mathbf{M}}}_i \exp(-s\tau_i) \quad . \quad (2.20)$$

Although a low order fit of  $h_i$  is generally possible, a high order value is expected for  $\overline{\mathbf{M}}_i$ , as both  $\mathbf{T}_i$  and  $\mathbf{S}_i$  present frequency dependent behavior. The following procedure is then adopted:

- We extract the time-delays in  $h_i$  and obtain a minimum phase-shift function  $p_i(s)$ .
- Second, we proceed to calculate each matrix  $\overline{\overline{\mathbf{M}}}_i$ .
- Finally, a fit of each one is done independently using VF to allow for pole relocation.

For time-domain simulations, the procedure is slightly different from the ULM approach. Since  $\mathbf{H}$  is now a sum of several independent matrices, it is more efficient to represent both history current sources  $\mathbf{i}_{\mathbf{H}_0}$  and  $\mathbf{i}_{\mathbf{H}_L}$  as a set of parallel current sources, i.e., each current source has its own interpolation scheme associated with a single idempotent matrix as depicted in Fig. 2.7, and there are no interactions between different time delays, which will allow for a more robust phase-domain simulation using a one-segment interpolation scheme.

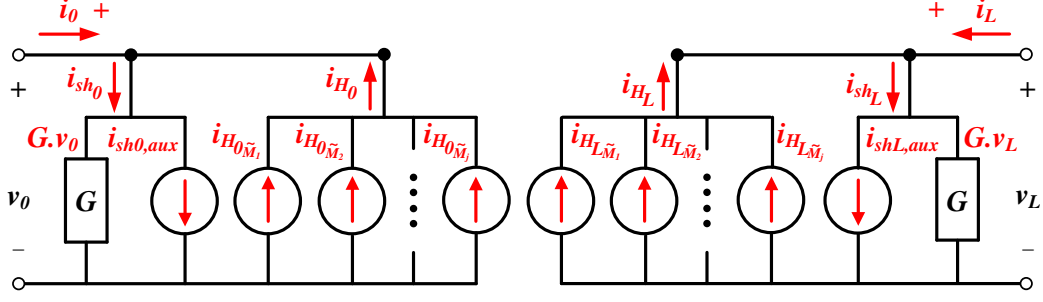


**Figure 2.7:** Norton equivalent of a transmission system  
Time-domain Id. Line approach.

## 2.6.2 Idempotent Grouping (Id-Line-gr)

A possibility found in the ULM approach consists into grouping the modes with similar time-delays to reduce the order of the rational functions which compose the propagation matrix. An analogue procedure such as follows is possible regarding the idempotent decomposition:

1. First, we compute the differences  $\Delta\tau$  between the modal time-delays of the transmission system.
2. Let  $\Omega$  be the highest frequency considered in the fitting. Time-delays that satisfy  $\Omega\Delta\tau < 2\pi \cdot 10/360$  are lumped together and approximated by a common time-delay  $\bar{\tau}$ , where  $\Delta\tau = \tau_i - \tau_j$ .
3. The common time-delay  $\bar{\tau}$  is chosen to be equal to the smallest of the individual lumped time-delays.
4. The grouping is done by fitting each sum of idempotent matrices using their corresponding  $\bar{\tau}$ .

This procedure may result in different idempotent matrix groups for a transmission system. The propagation matrix is approximated as

$$\mathbf{H} \approx \mathbf{H}_{id-gr} = \sum_{k=1}^K \overline{\overline{\mathbf{M}}}_i \exp(-s\tau_k) \quad (2.21)$$

where  $K$  is the number of lumped modes and  $\tau_k$  is the collapsed time-delay.

## 2.7 Test cases

For the assessment of the accuracy and numerical performance of the Idempotent Decomposition modeling, we have considered a set of four test cases, namely:

1. #1: an underground single-core (SC) cable system without armor, 1 km length.
2. #2: a 800 kV line with 2 ground wires with 3-phases, 50 km length.
3. #3: a 500 kV line in parallel to a 138 kV line with a total of 6-phases, 50 km length.
4. #4: a 230 kV line with 18-phases, 100 km length.

Test cases #1 and #4 present unstable time-domain responses using the ULM approach with a one-segment interpolation scheme [45]. Despite the rather unusual geometry of test #4, its analysis here is made to compare the Idempotent decomposition performance in a previously reported unstable example and to verify if the Idempotent grouping presents any actual computational gain or improved fitting accuracy. Fig. 4.27 depicts the geometries and data for the test cases. All the overhead line test cases assumed ground wires to be continuously grounded.

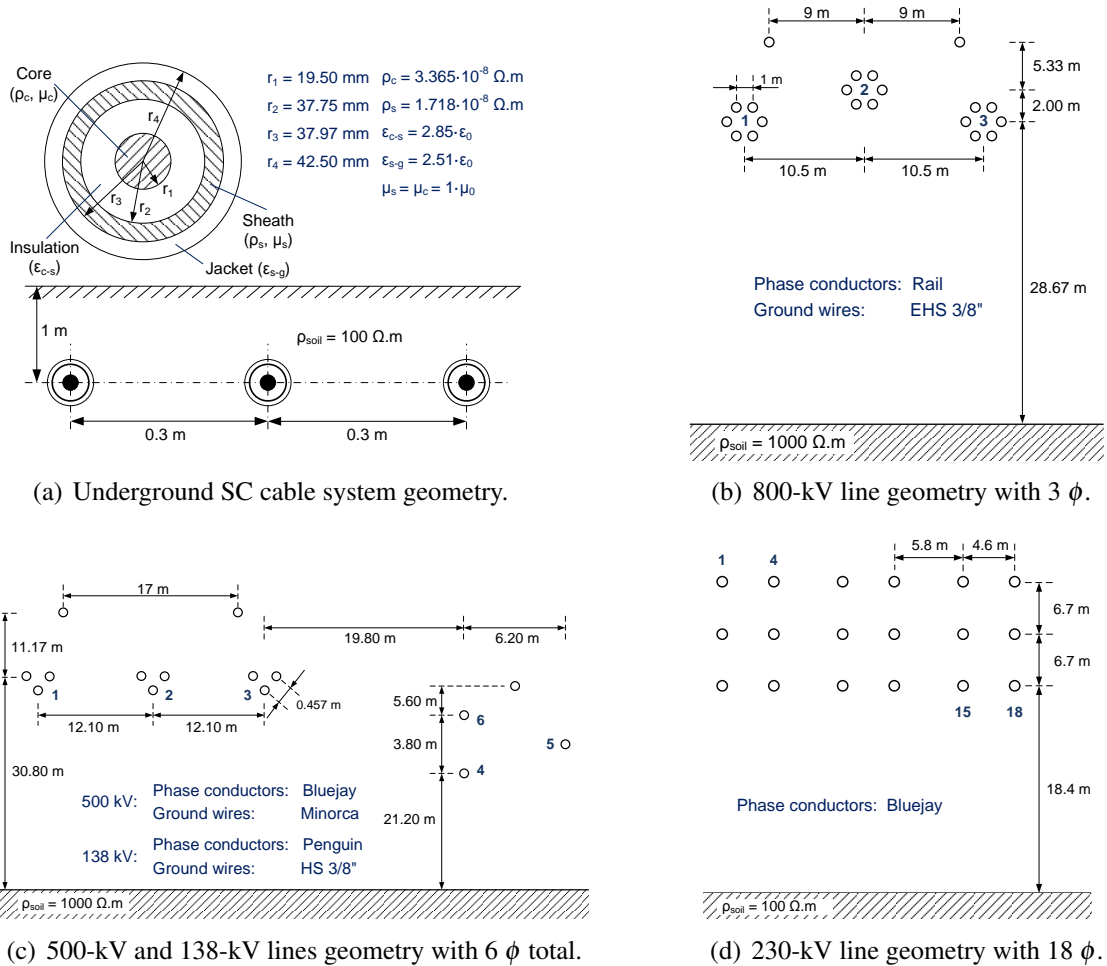


**Figure 2.8:** System geometry of each case.

In all cases, the influence of the fitting implementation over the accuracy of the rational approximation of the Idempotent Matrices and the Characteristic Admittance was negligible.

### 2.7.1 Fitting of $\bar{\mathbf{M}}_i$ and composition of $\mathbf{H}$

Tests #1 and #4 considered a frequency fitting band between 0.1 Hz to 100 MHz and between 0.1 Hz to 10 MHz as in [45]. The other two test cases considered a frequency fitting band between 0.1 Hz and 10 MHz. Table 2.1 shows the number of poles used for the rational approximation of  $h_i$ ,  $\mathbf{Y}_C$ ,  $\bar{\mathbf{M}}_i$ ,  $\mathbf{H}_{ULM-ug}$  (ULM without mode collapsing),  $\mathbf{H}_{ULM}$  (conventional ULM approach),  $\mathbf{H}_{id}$  (conventional idempotent modeling) and  $\mathbf{H}_{id-gr}$  (idempotent grouping). For the rational approximation of  $\bar{\mathbf{M}}_i$  and  $h_i$ , we must first extract the time-delays associated with each mode  $i$ . The procedure for obtaining the time-delays is described in Section 2.4.

**Table 2.1:** Poles from the rational approximation of the line parameters.

Test Case	Number of fitting poles						
	$h_i$	$\mathbf{Y}_C$	$\mathbf{M}_i$	$\mathbf{H}_{ULM}$	$\mathbf{H}_{ULM-gr}$	$\mathbf{H}_{id}$	$\mathbf{H}_{id-gr}$
# 1	16	12	20	96	80	120	100
# 2	6	12	20	36	—	60	—
# 3	6	12	20	72	60	120	100
# 4	14	12	20	216	60	360	100

Table 2.2 presents the time-delays associated to each mode even when mode collapsing is considered.

**Table 2.2:** Calculated and Lumped time delays.

Test Case	Mode	Time delay ( $\mu s$ )					
		1	2	3	4	5	6
# 1	Calculated	55.69	26.07	21.09	5.632	5.629	5.629
	Lumped	55.69	26.07	21.09	5.629	—	—
# 2	Calculated	175.84	166.78	167.02	—	—	—
	Lumped	175.84	166.78	167.02	—	—	—
# 3	Calculated	333.61	333.63	337.33	333.55	333.60	359.96
	Lumped	333.60	333.63	337.33	333.55	359.96	—
# 4	Calculated	333.569	333.569	333.568	333.568	333.568	333.567
		333.567	333.567	333.565	333.504	333.564	333.504
		333.563	333.564	333.560	333.906	336.796	400.539
	Lumped	333.560	333.504	333.906	336.796	400.539	—

The Id-Line-gr allowed a sensible reduction in the dimension of the rational approximation of  $\mathbf{H}$ . In #1, the coaxial modes were lumped reducing from 6 to 4 the number of time-delays. In #3, the reduction was from 6 to 5 and in #4 the reduction was from 18 to 5 time-delays. There was no lumping possible for test case #2, as 3 time-delays remained.

**Table 2.3:** Maximum fitting deviation of  $\mathbf{H}$  - Idempotent modeling

Test Case	Id-Line	Id-Line-gr
# 1	$2.89 \cdot 10^{-4}$	$3.88 \cdot 10^{-3}$
# 2	$2.09 \cdot 10^{-4}$	—
# 3	$1.98 \cdot 10^{-2}$	$4.94 \cdot 10^{-2}$
# 4	$3.48 \cdot 10^{-2}$	$5.72 \cdot 10^{-2}$

Despite the reduction found in 3 of the test cases, a higher number of poles was needed when using the id-Line-gr ( $\mathbf{H}_{id-gr}$ ) compared with the number of poles using ULM even without mode lumping. Furthermore, the idempotent grouping did not improve the overall accuracy in the rational approximation of  $\mathbf{H}$ .

Table 2.3 presents the absolute value of the maximum deviation found in the rational approximation of  $\mathbf{H}$  using conventional idempotent decomposition and considering idempotent grouping. The results indicated a slight increase in this deviation whenever idempotent grouping is considered. Furthermore, the idempotent grouping did not prevent the low frequencies oscillations found in the rational modeling of  $\mathbf{H}$  in some of the test cases as it will be shown next. For this reason, in the following figures we present only the results for the conventional idempotent modeling.

For the Rational Fitting of the Idempotent Matrices, Figures 2.9 to 2.19 present the results for test cases #1 to #4, respectively. Table 2.4 presents the absolute value of the maximum deviation found in the fitting of the Idempotent matrices.

**Table 2.4:** Absolute fitting error of the Idempotent Matrices.

Test Case	Absolute fitting error (p.u.)		
# 1	$47.20 \cdot 10^{-6}$	$1.64 \cdot 10^{-6}$	$141.60 \cdot 10^{-6}$
	$2.40 \cdot 10^{-3}$	$3.25 \cdot 10^{-6}$	$3.04 \cdot 10^{-3}$
# 2	$21.10 \cdot 10^{-6}$	$64.32 \cdot 10^{-6}$	$4.73 \cdot 10^{-7}$
# 3	0.12	0.12	0.60
	0.077	0.020	0.61
# 4	$6.68 \cdot 10^{-3}$	0.025	0.036
	0.058	0.067	0.191
	0.046	0.020	0.164
	0.068	0.111	0.270
	0.062	0.061	0.121
	0.128	0.146	0.053

Figures 2.20 and 2.21 present the rational fitting of  $\mathbf{H}$  using idempotent modeling for test cases #1 to #4.

For the test cases involving overhead lines (test cases #2 to #4), a shunt conductance was needed to be included in the data to avoid small low frequencies oscillations in the



rational approximation. In #2, a shunt conductance of  $3 \cdot 10^{-11}$  S/m was used. This value is slightly higher than the one proposed in [68] for the EMTP-type modeling of overhead lines.

The inclusion of a shunt conductance of  $3 \cdot 10^{-11}$  S/m did not prevent the small oscillations in the amplitude of the rational approximation of  $\mathbf{H}$  for #3. It was found that if a shunt conductance of  $3 \cdot 10^{-10}$  S/m or higher is considered, these oscillations in the fitted function cease to exist. However, this high conductance value, which is one order of magnitude higher than the one in #2, alters significantly the low frequency behavior of  $\mathbf{Y}_c$ .

The rational approximation of test case #4 presents the lowest accuracy. In this case, a shunt conductance equal to the one in #2 was considered. For this case, some of the rational approximations of  $\overline{\mathbf{M}}_i$  presented poor accuracy. However, its impact on the fitting of  $\mathbf{H}$  is less pronounced although small oscillations in the rational approximation of  $\mathbf{H}$  persisted.

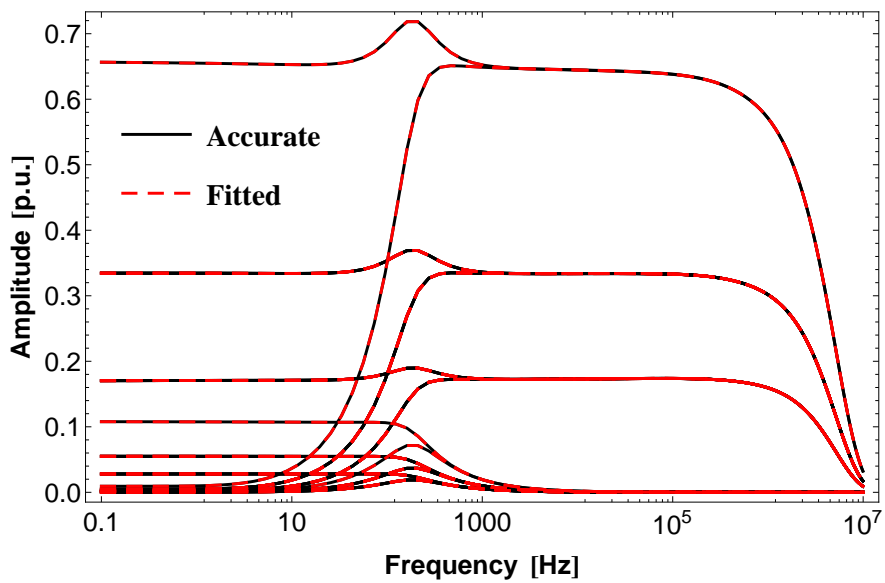
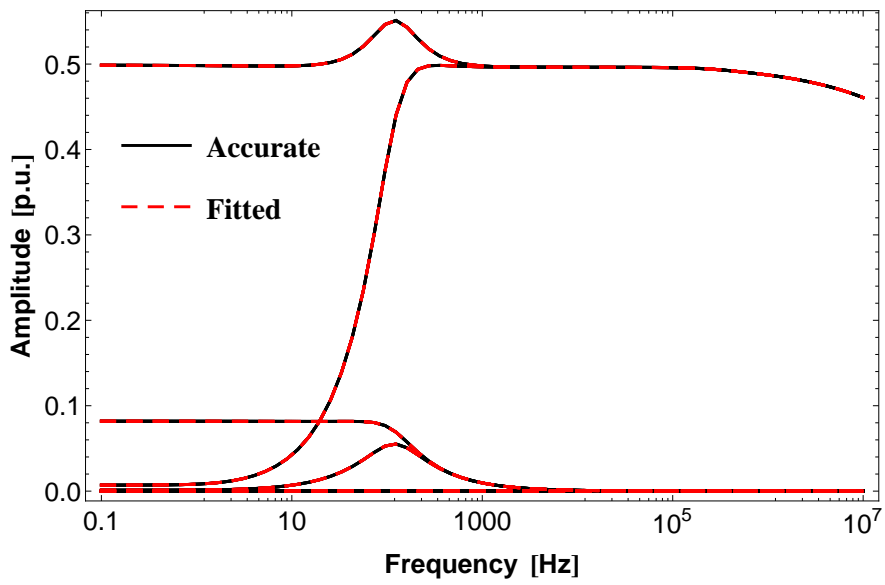
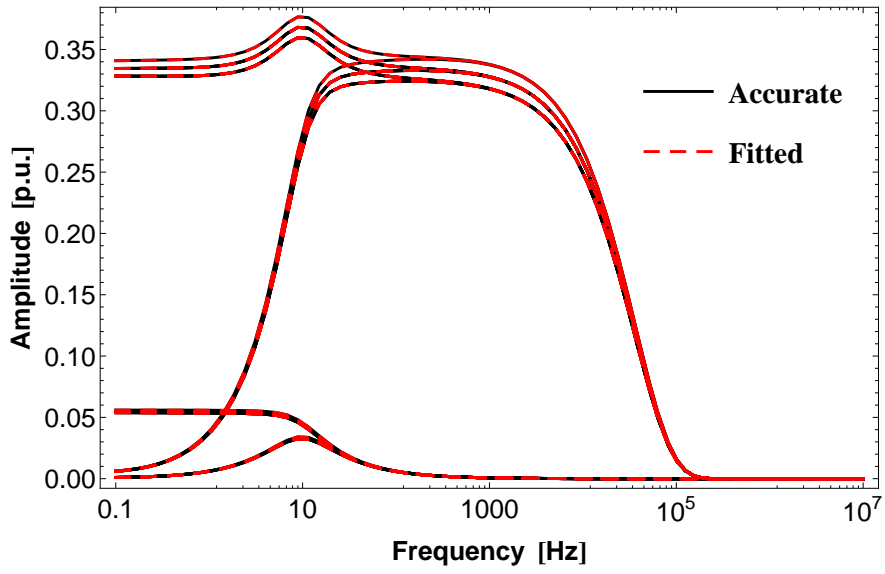


**Figure 2.9:** Rational Fitting of  $\bar{M}_1$ ,  $\bar{M}_2$  and  $\bar{M}_3$  for #1.

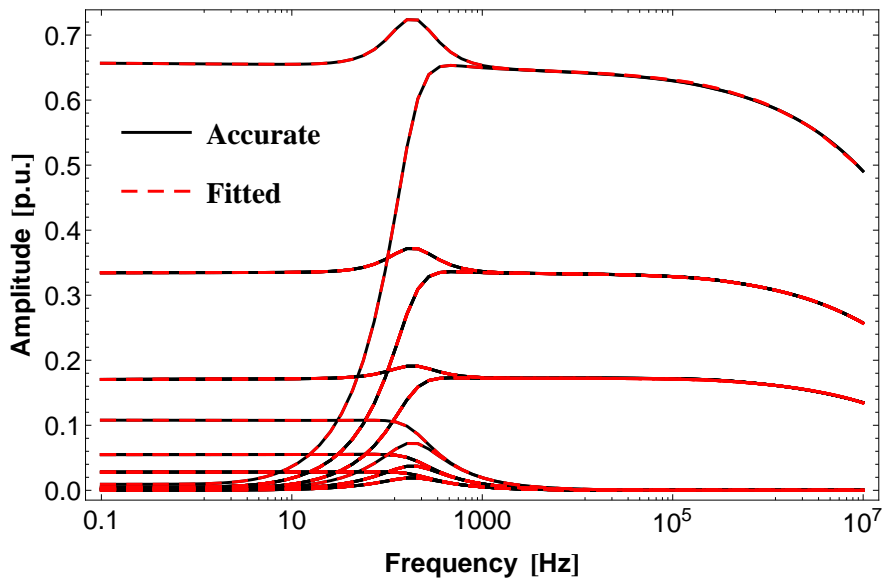
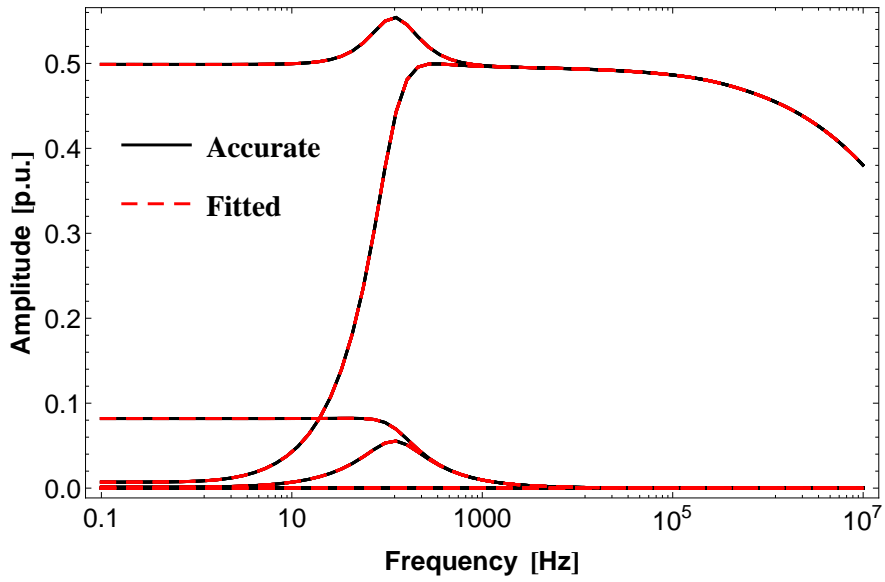
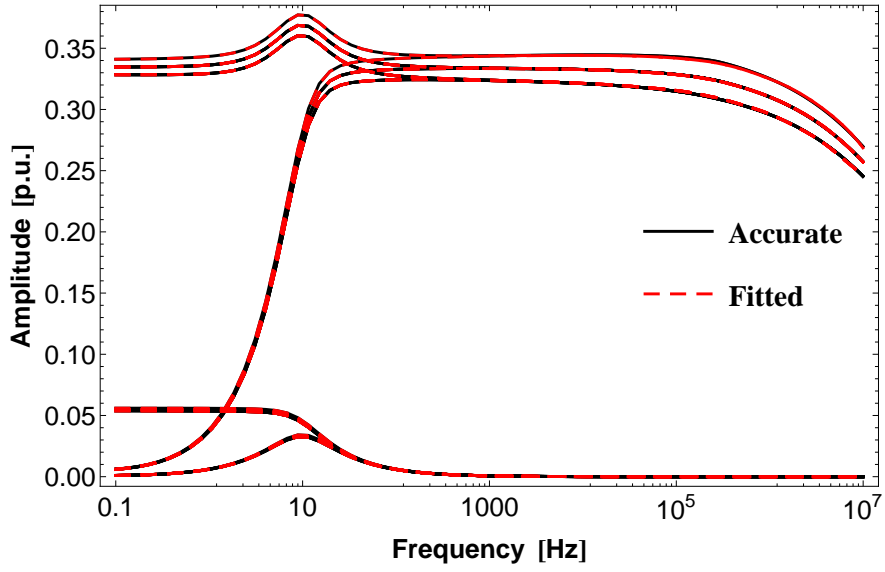
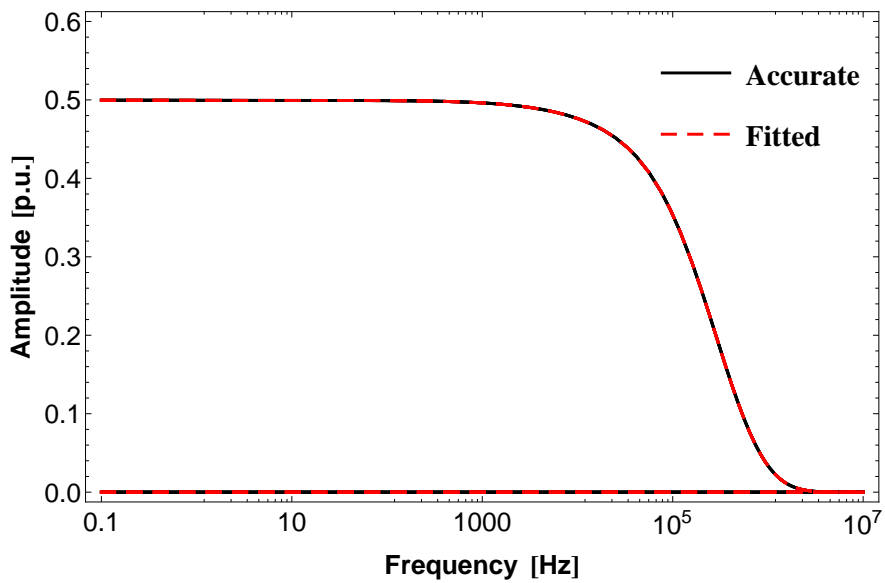
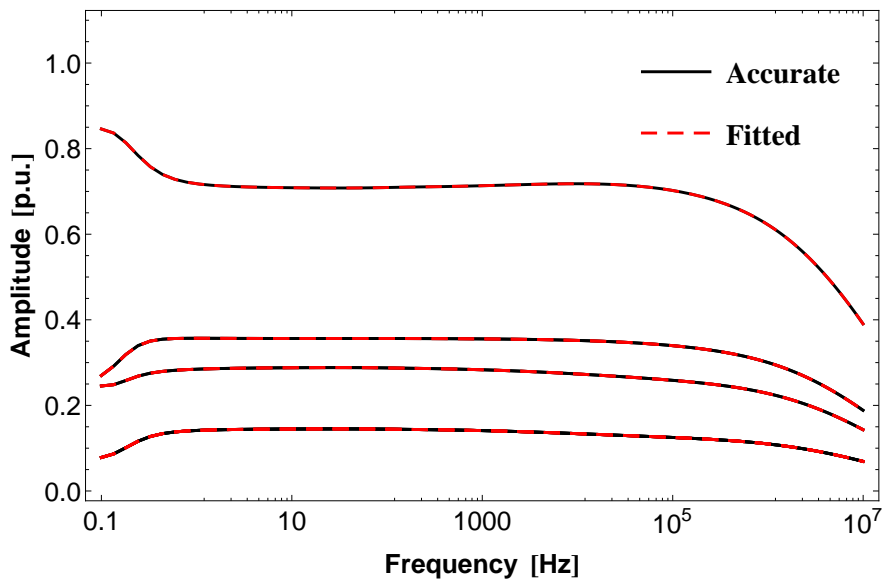
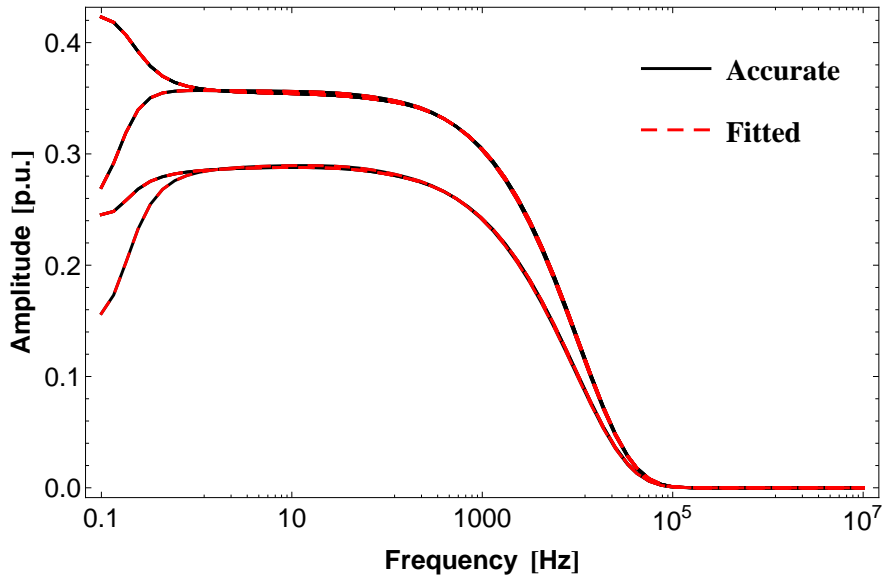
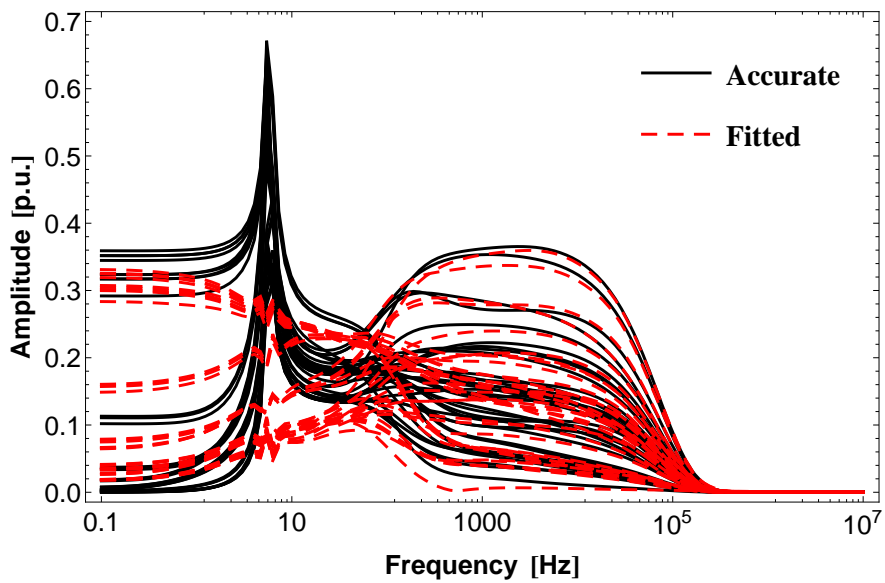
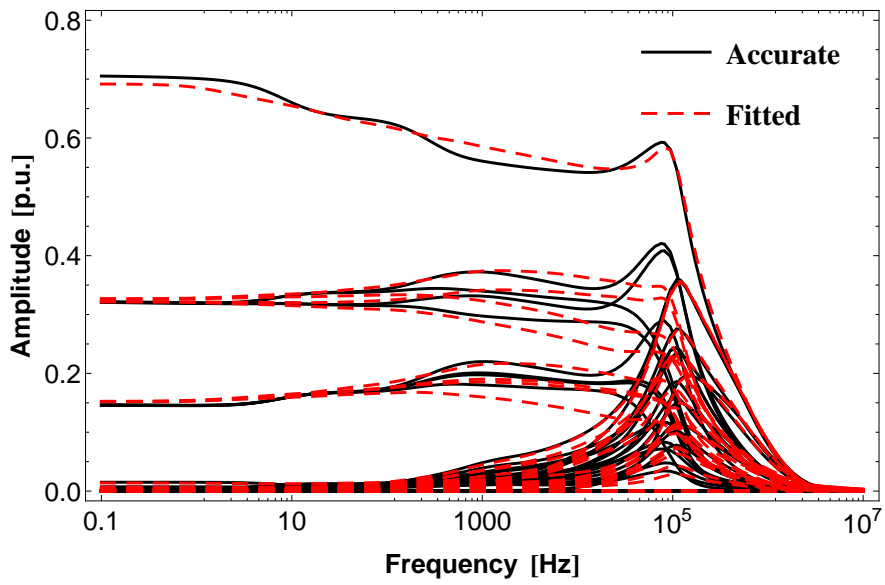
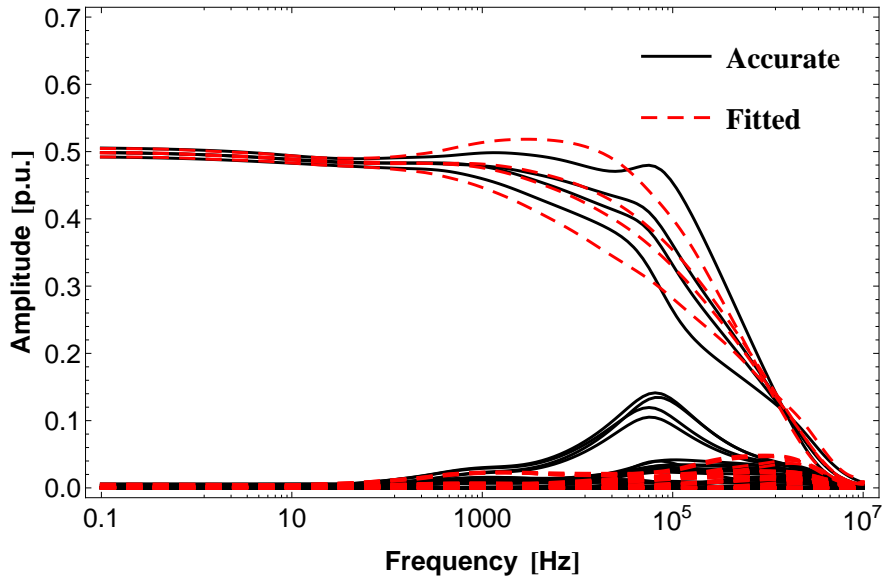


Figure 2.10: Rational Fitting of  $\bar{M}_4$ ,  $\bar{M}_5$  and  $\bar{M}_6$  for #1.



**Figure 2.11:** Rational Fitting of  $\bar{M}_1$ ,  $\bar{M}_2$  and  $\bar{M}_3$  for #2.



**Figure 2.12:** Rational Fitting of  $\bar{M}_1$ ,  $\bar{M}_2$  and  $\bar{M}_3$  for #3.

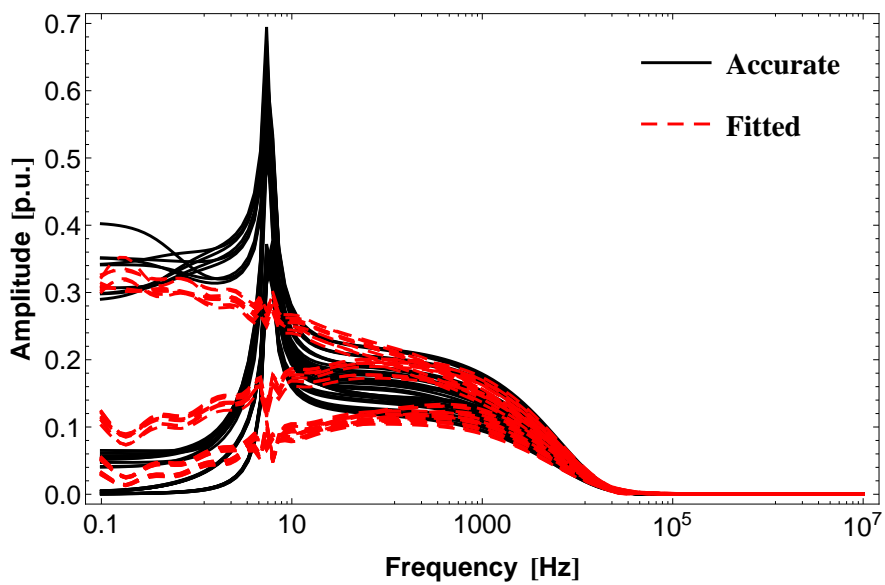
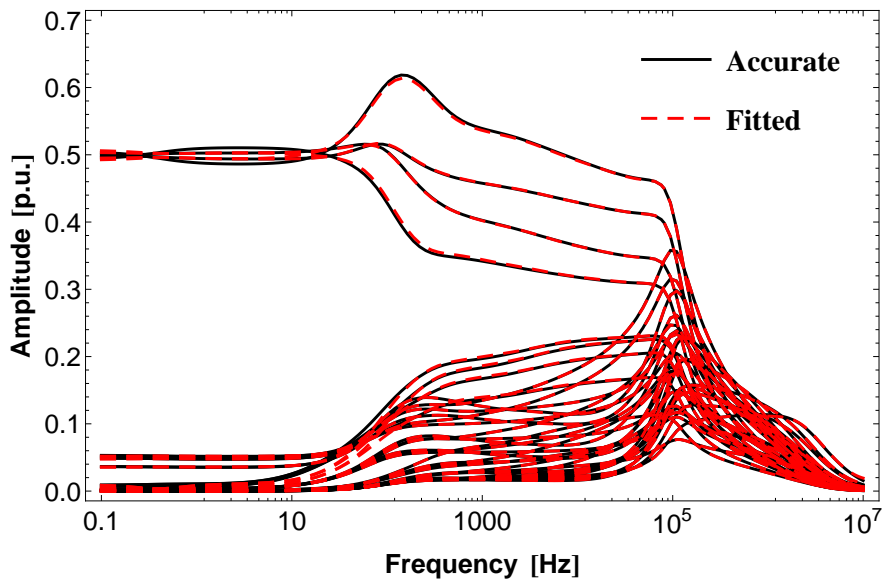
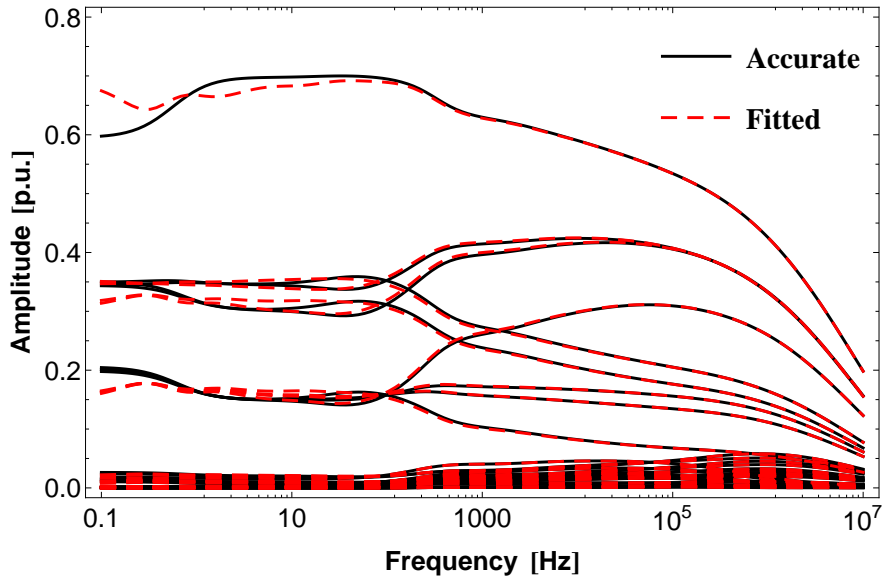


**Figure 2.13:** Rational Fitting of  $\bar{M}_4$ ,  $\bar{M}_5$  and  $\bar{M}_6$  for #3.

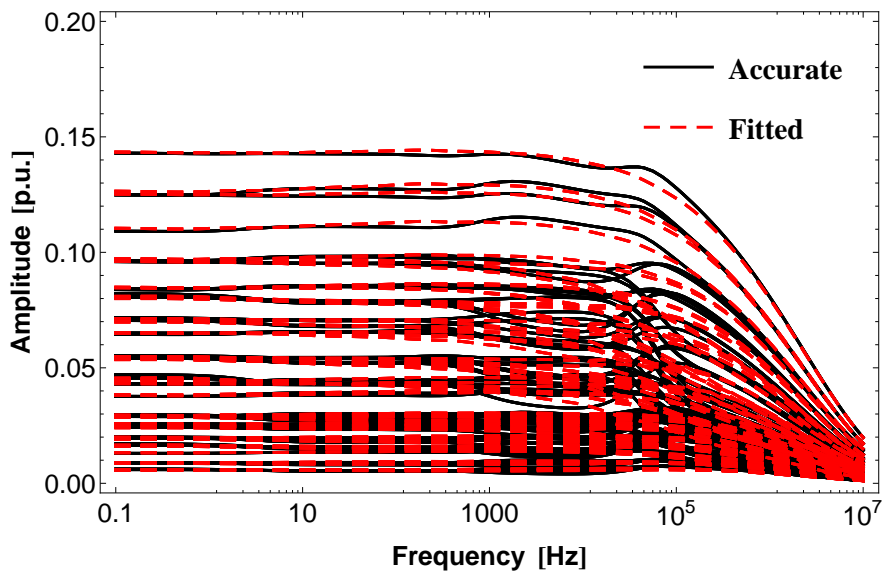
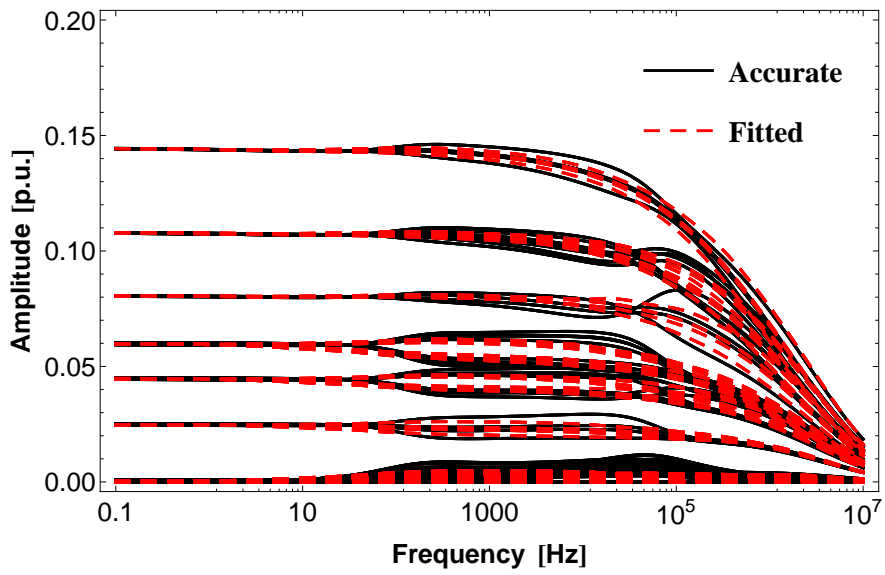
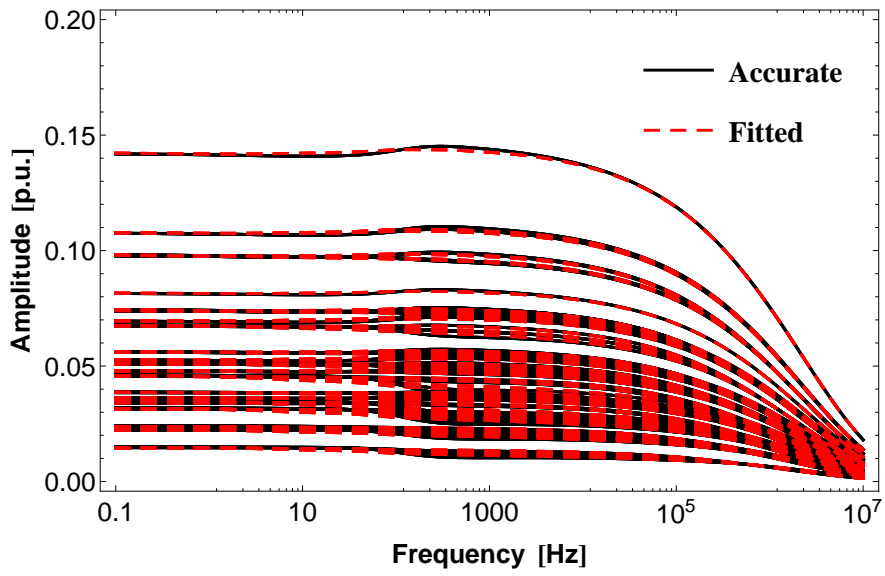


Figure 2.14: Rational Fitting of  $\bar{M}_1$ ,  $\bar{M}_2$  and  $\bar{M}_3$  for #4.

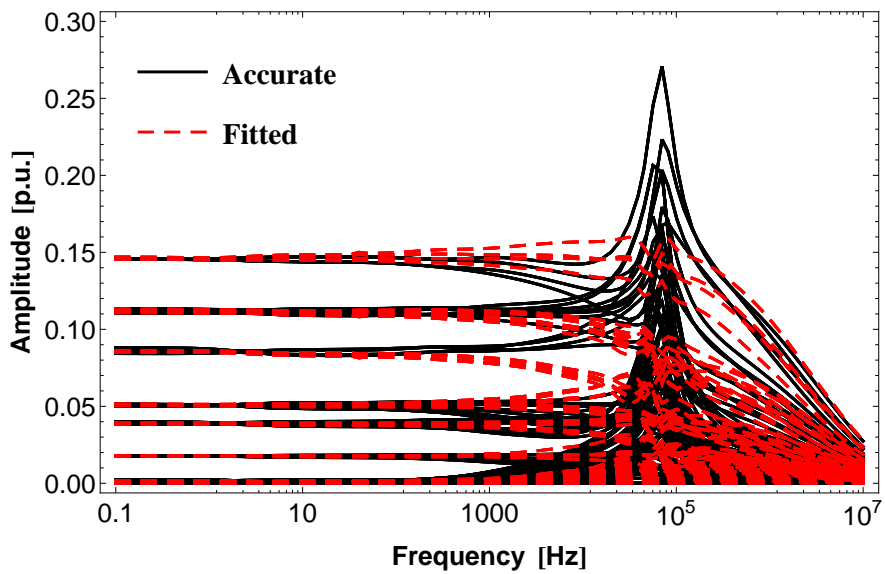
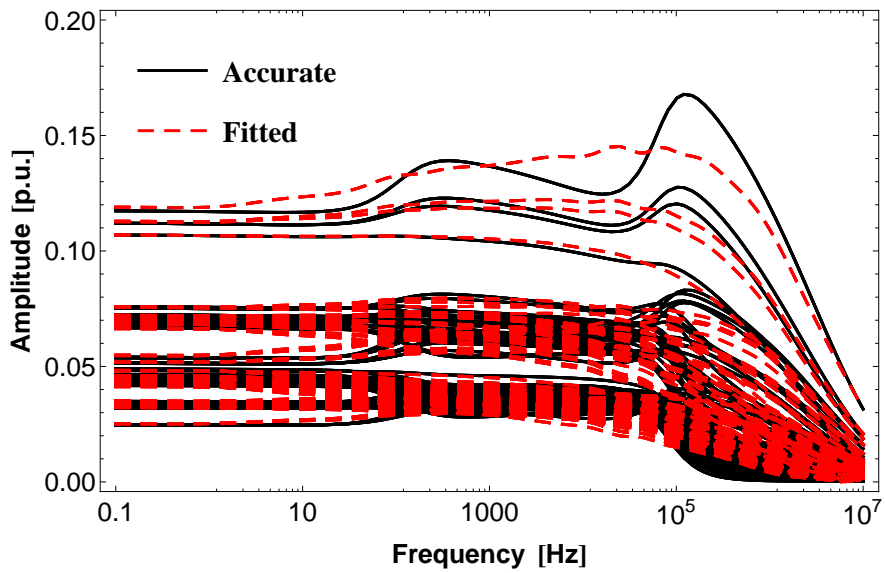
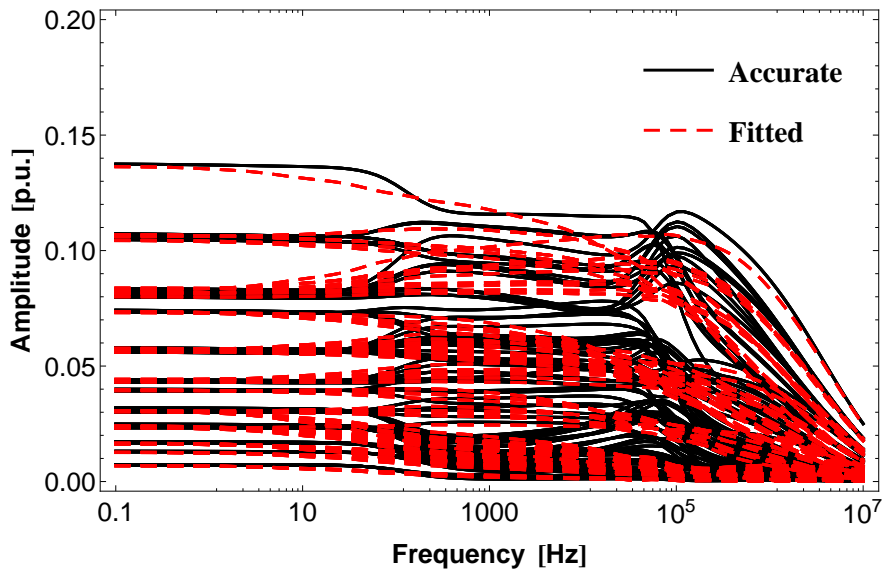


Figure 2.15: Rational Fitting of  $\bar{M}_4$ ,  $\bar{M}_5$  and  $\bar{M}_6$  for #4.



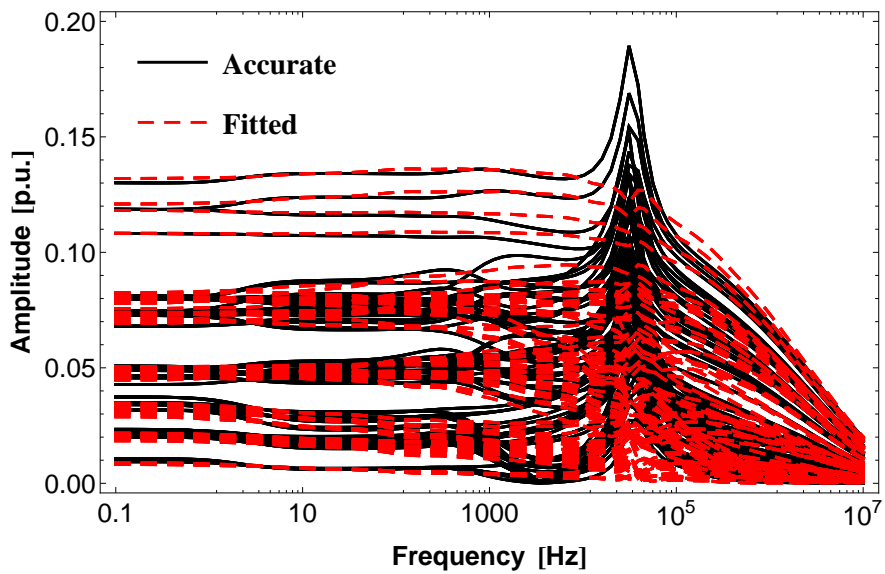
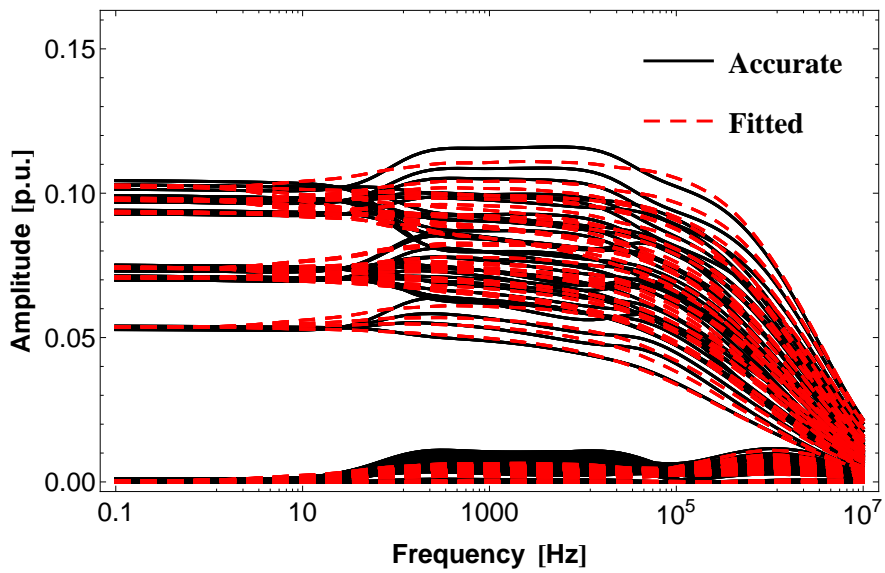
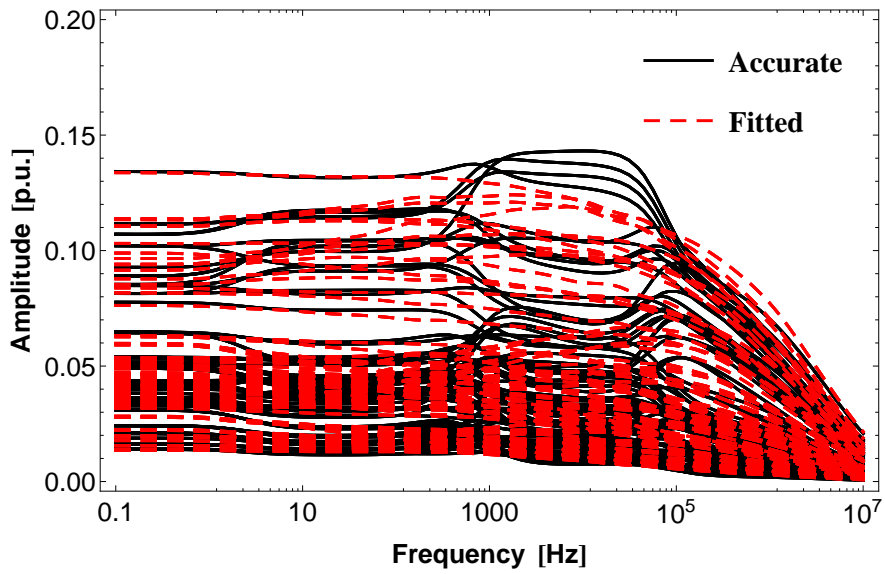
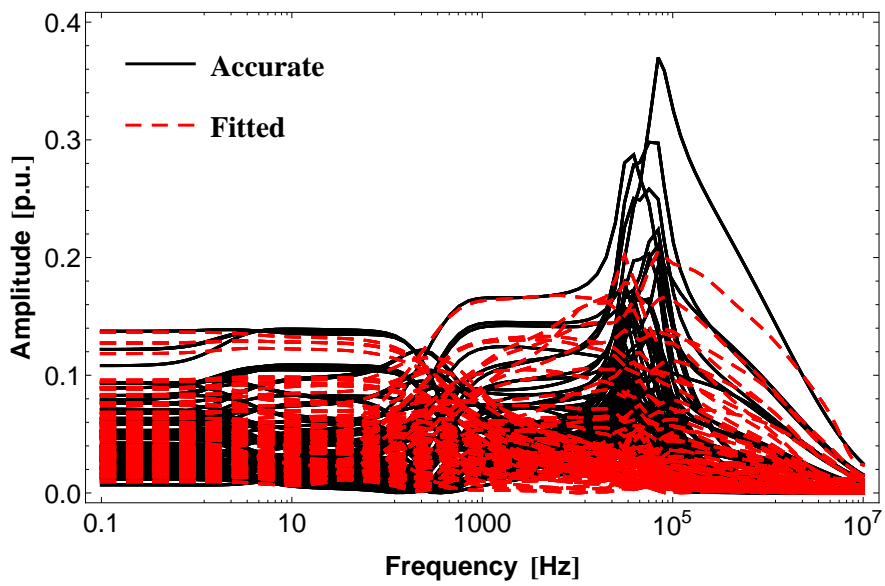
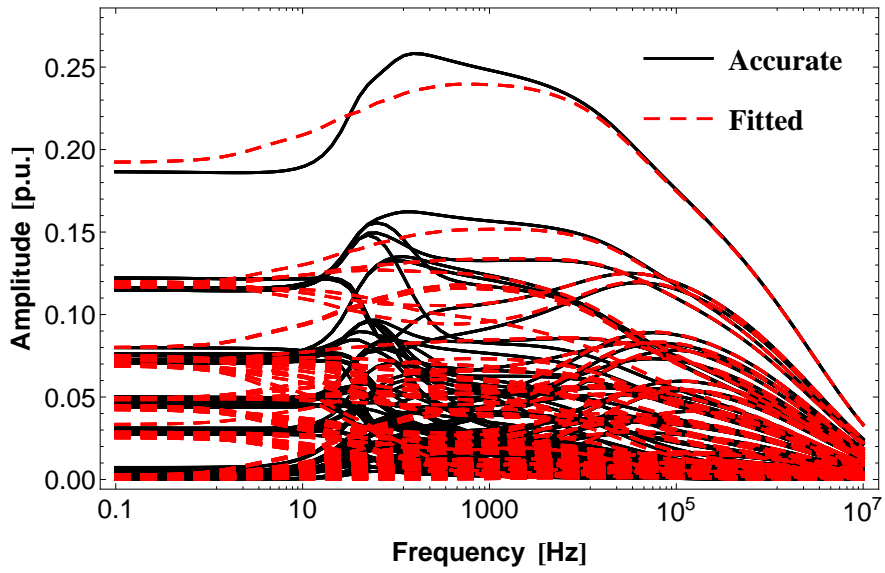
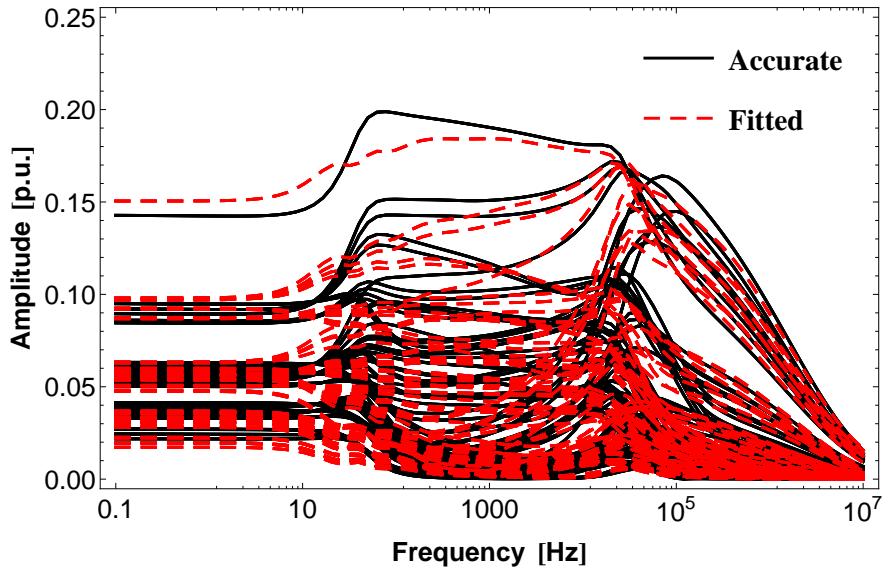


Figure 2.16: Rational Fitting of  $\bar{M}_7$ ,  $\bar{M}_8$  and  $\bar{M}_9$  for #4.



**Figure 2.17:** Rational Fitting of  $\bar{M}_{10}$ ,  $\bar{M}_{11}$  and  $\bar{M}_{12}$  for #4.

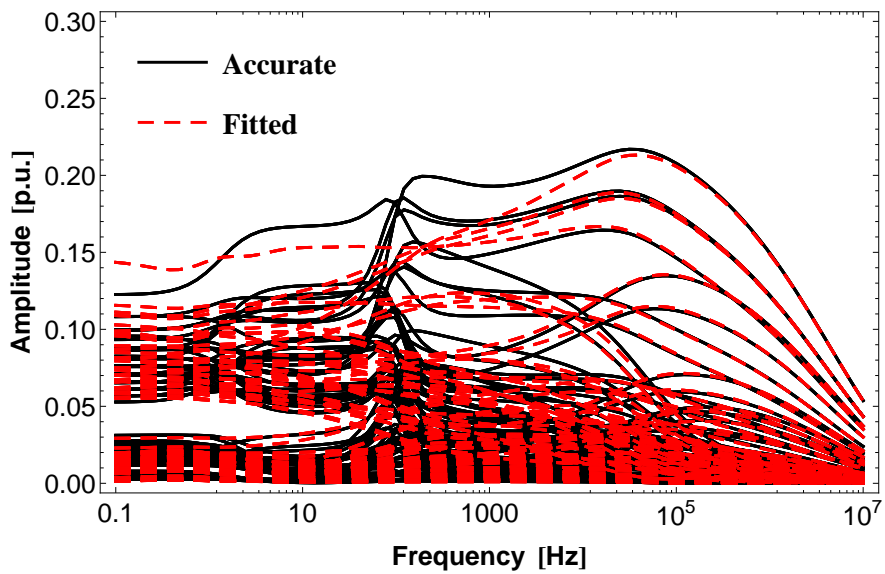
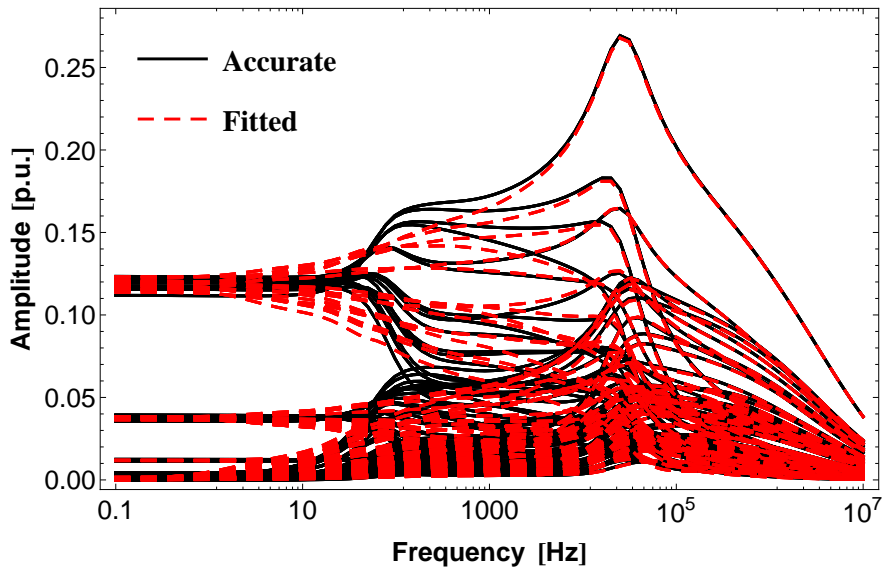
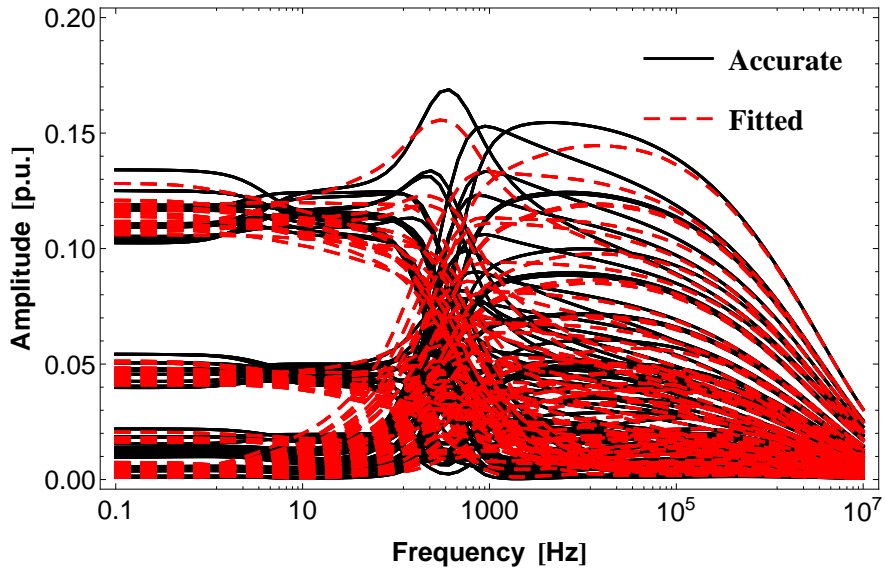
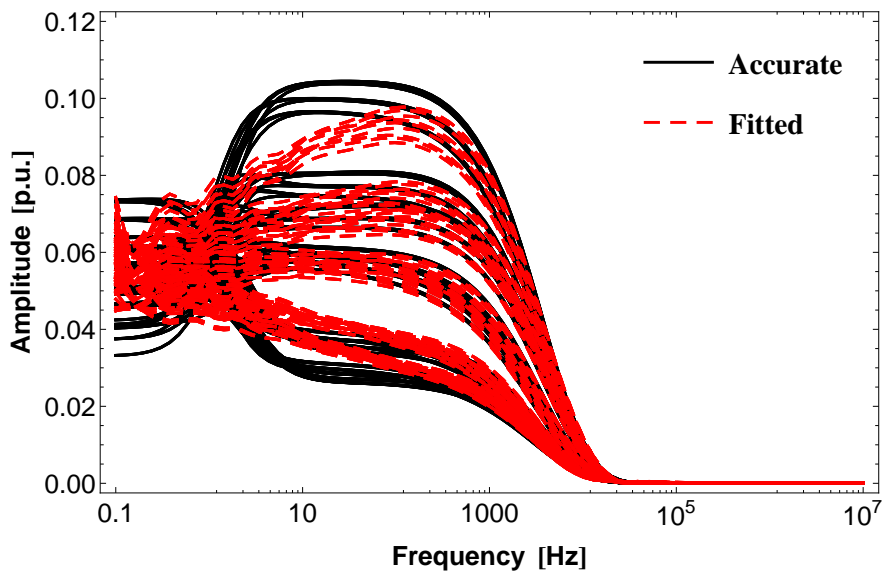
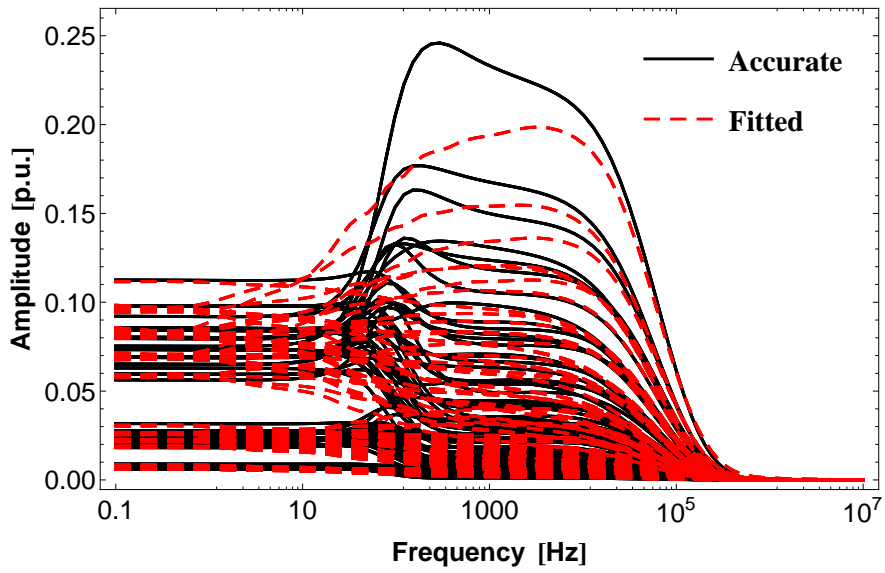
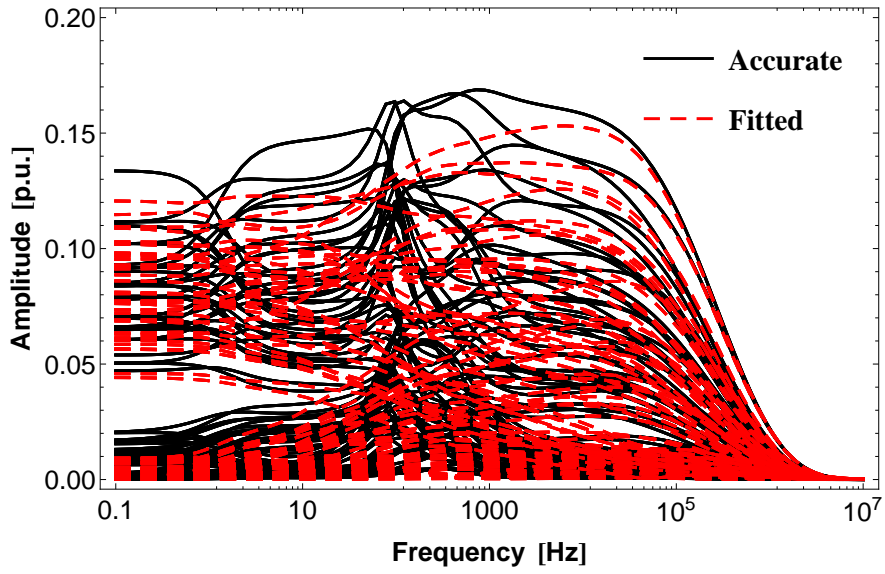
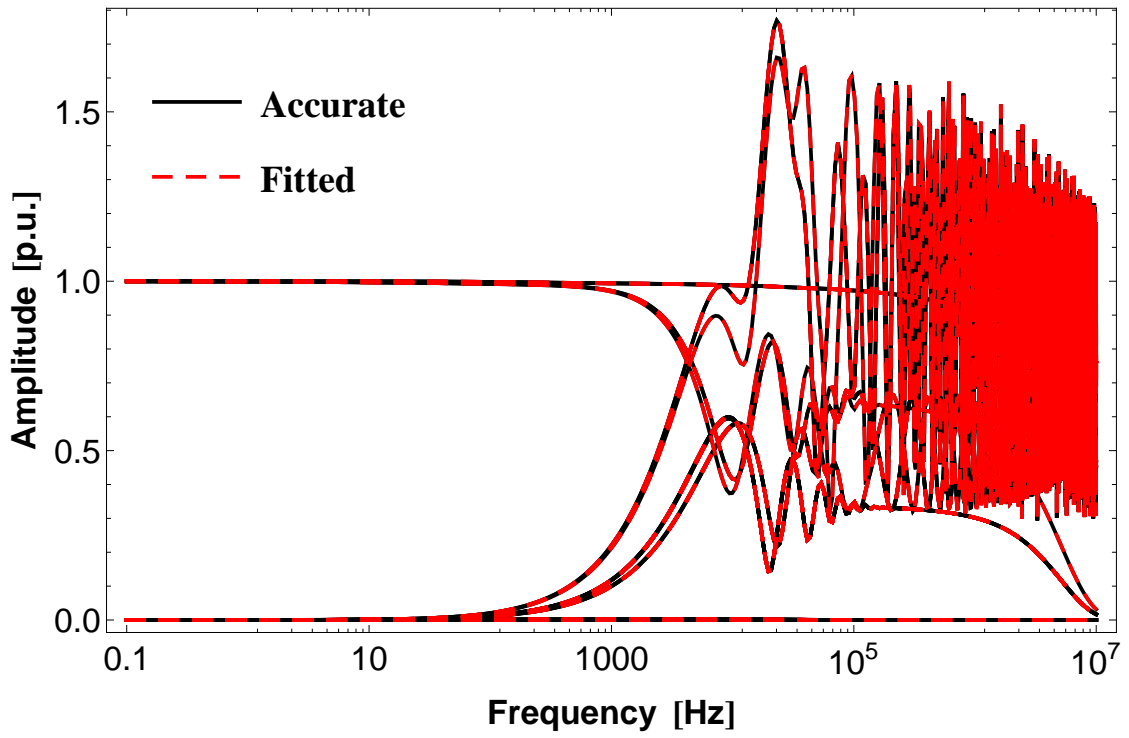


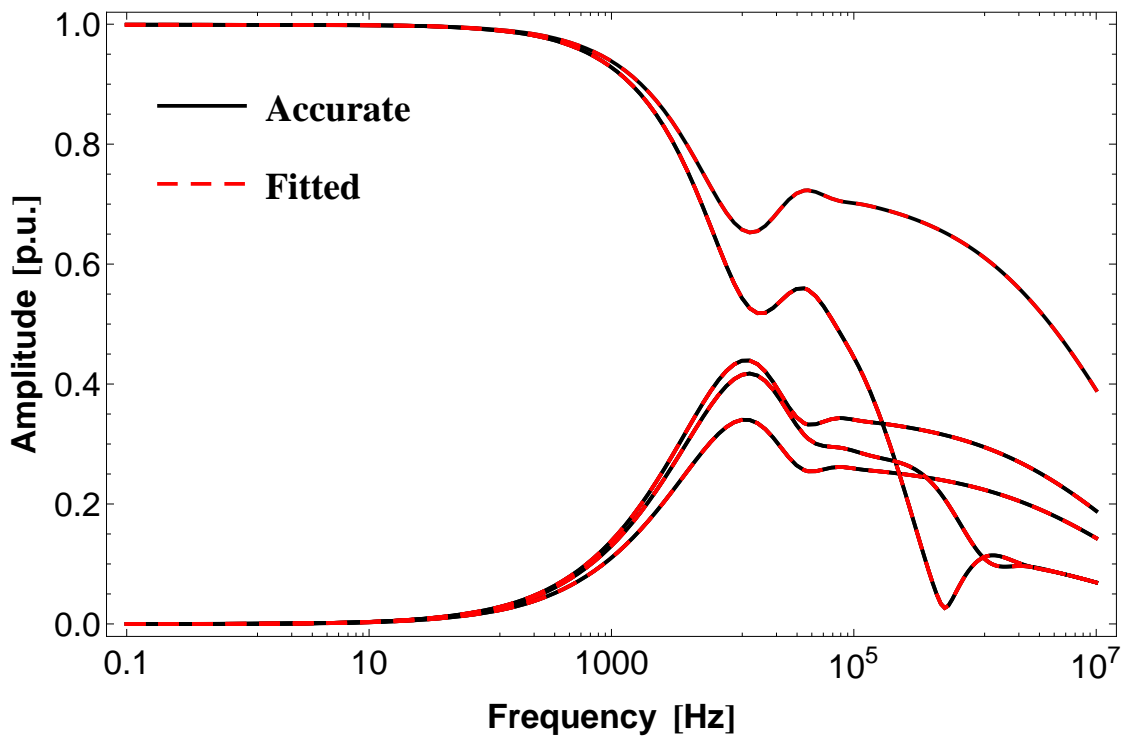
Figure 2.18: Rational Fitting of  $\bar{M}_{13}$ ,  $\bar{M}_{14}$  and  $\bar{M}_{15}$  for #4.



**Figure 2.19:** Rational Fitting of  $\bar{M}_{16}$ ,  $\bar{M}_{17}$  and  $\bar{M}_{18}$  for #4.

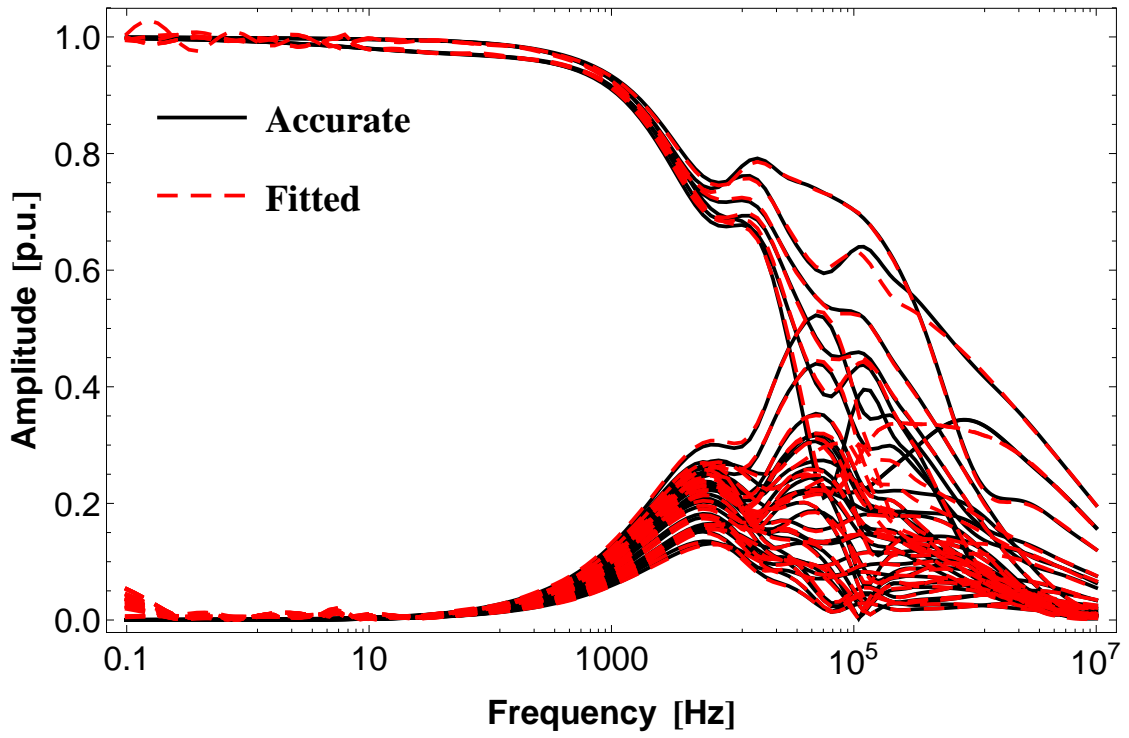


(a) #1.

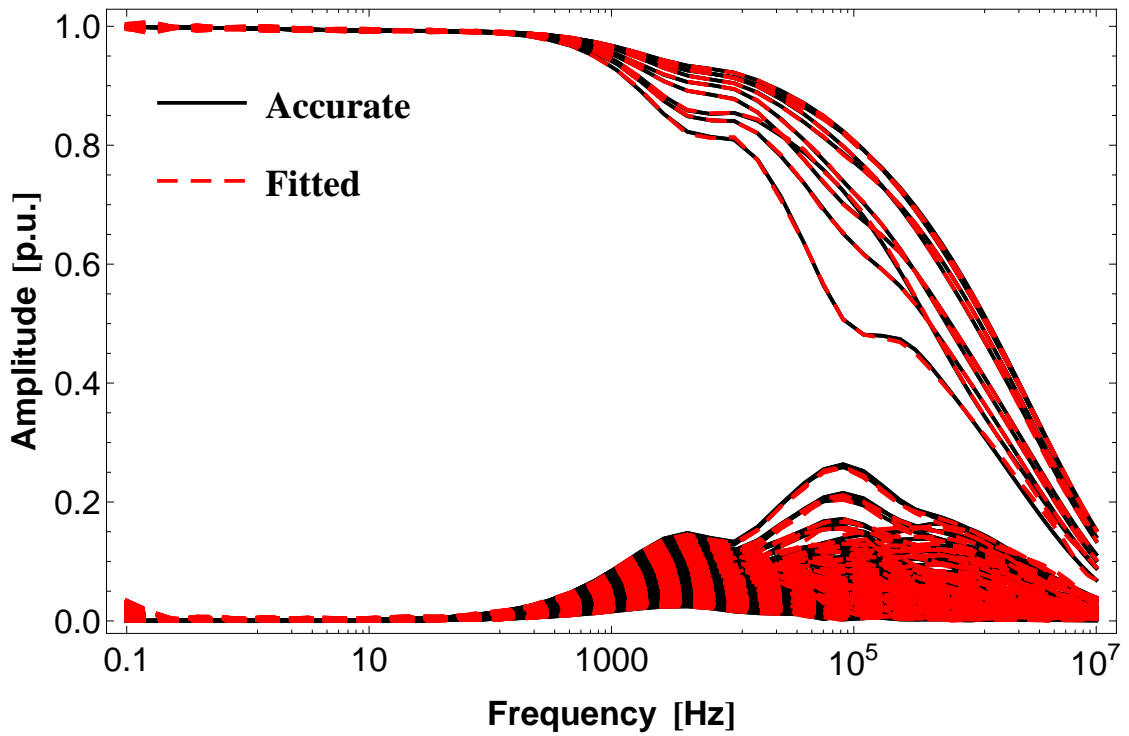


(b) #2.

**Figure 2.20:** Rational approximations for  $\mathbf{H}_{id}$  - Test cases #1 and #2.



(a) #3.



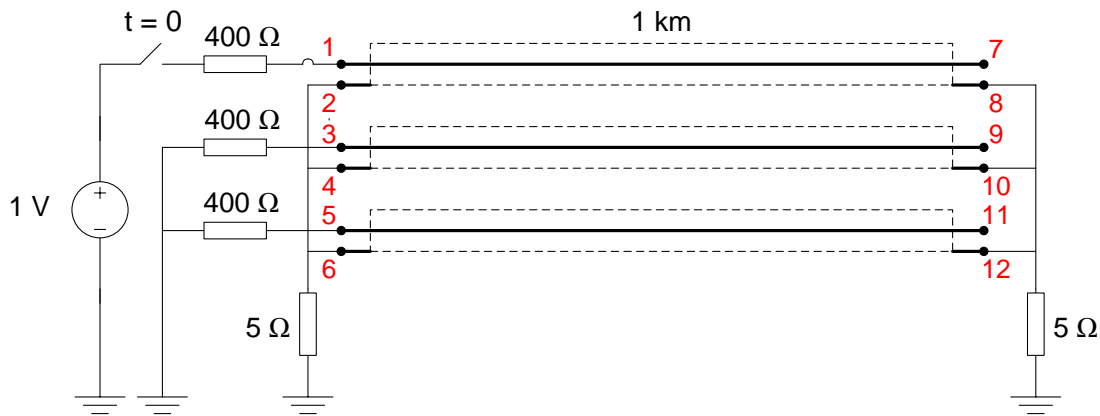
(b) #4.

**Figure 2.21:** Rational approximations for  $\mathbf{H}_{id}$  - Test cases #3 and #4.

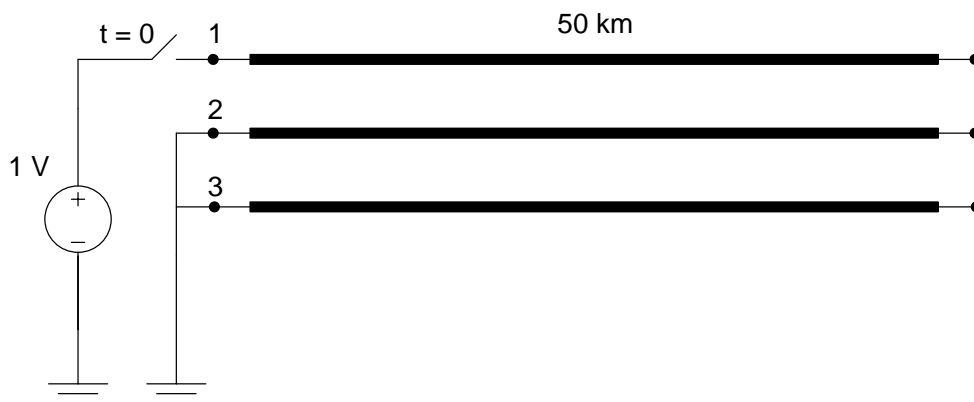
## 2.7.2 Time-domain simulation

To allow for the inclusion of circuital elements using a matrix formulation, a user defined routine was written for this purpose using the Modified Nodal Analysis in Wolfram MATHEMATICA [69] in a similar fashion as in the MatEMTP program described in [70]. For the idempotent decomposition we require to model multiple current sources that are implemented following the principles presented in Appendix A.

For the time-domain simulations in order to allow comparisons with the results in [45], a  $\Delta t = 0.5 \mu s$  was considered for test case #1, and a  $\Delta t = 10 \mu s$  was considered for #4. The other two test cases used a time-step of  $1 \mu s$ . A total simulation time of  $100 \mu s$  was considered for #1. The other three test cases employed a total simulation time of  $5000 \mu s$ . Figures 2.22 and 2.23 show the energization schemes of all the test cases. For test case #1, to simulate a cable connection with a simplified transmission line,  $400 \Omega$  resistors were used to represent each line phase. Also, for test case #1 and #2,  $5 \Omega$  and  $10 \Omega$  resistors were used to represent the resistance to earth of the grounding connected to the cable shield. In all the test cases, a unit voltage source ramped from  $0 V$  to  $1 V$  in  $5 \mu s$  connected to one of the phases was considered.

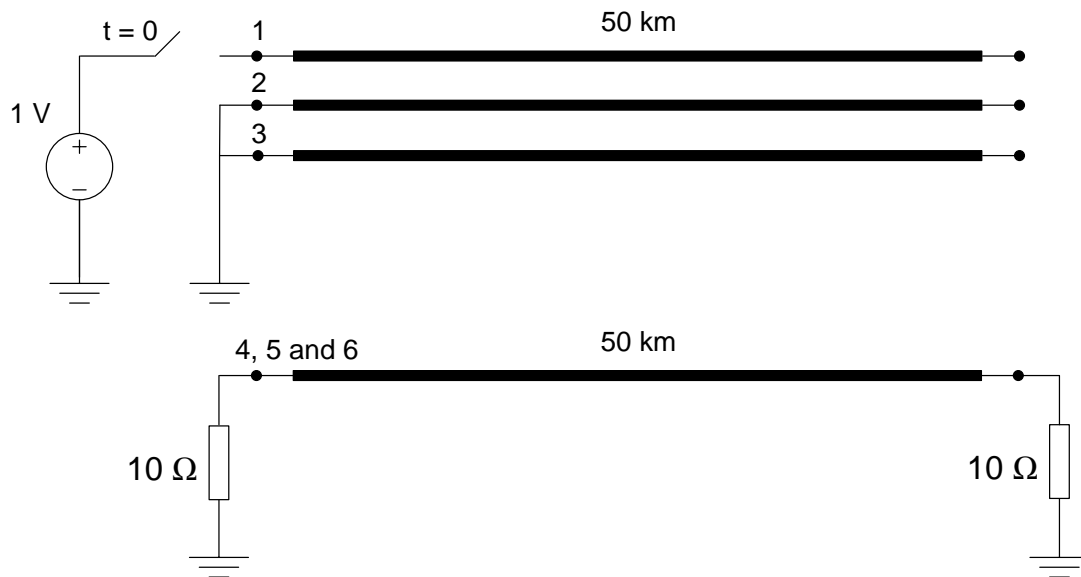


(a) #1.

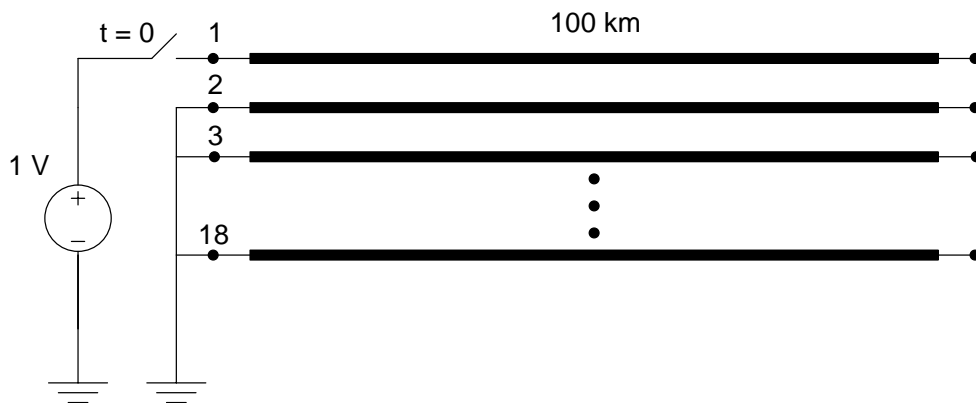


(b) #2.

**Figure 2.22:** Circuits for the evaluation of the time responses for test cases #1 and #2.



(a) #3.



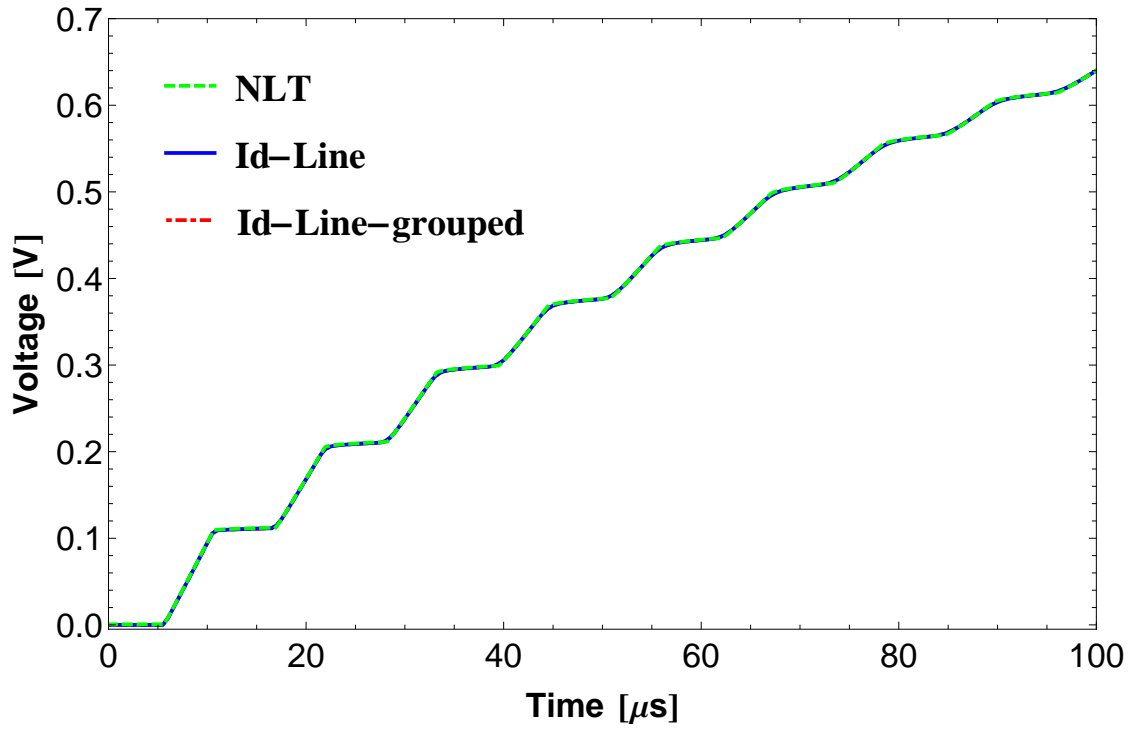
(b) #4.

**Figure 2.23:** Circuits for the evaluation of the time responses for test cases #3 and #4.

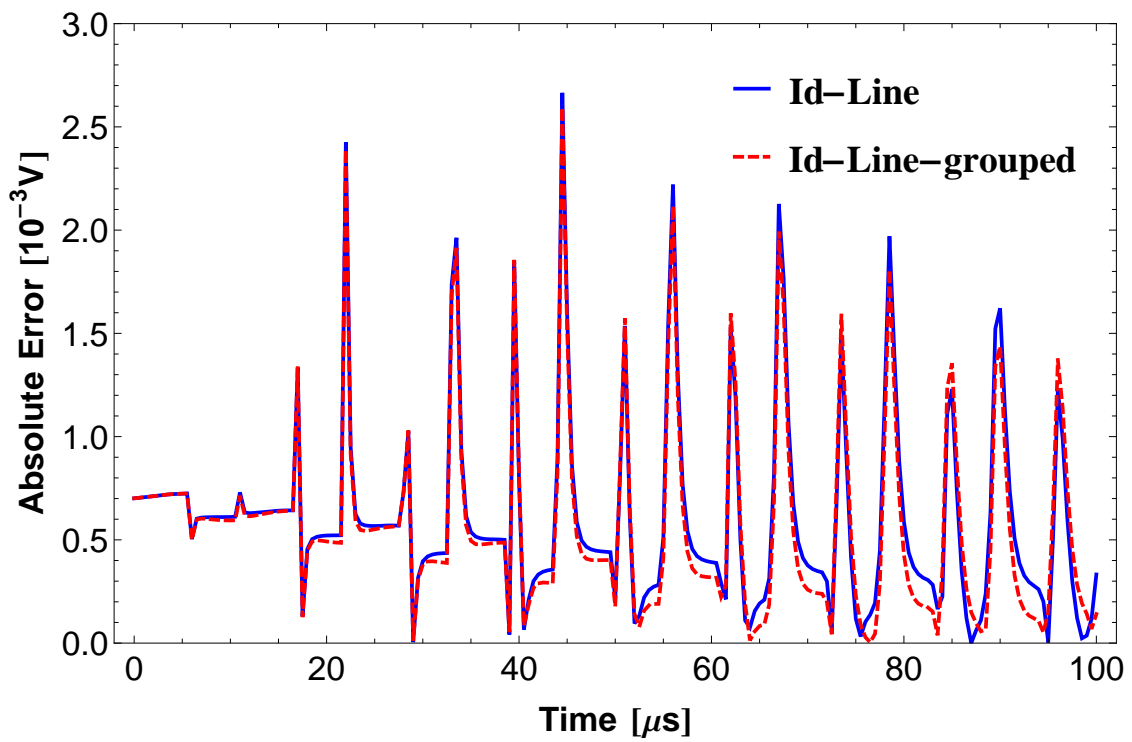
For the NLT simulations 4096 frequency samples were used, see Appendix B for details on the NLT implementation. As the time-step in NLT is not the same as the one found in the idempotent modeling, interpolations between consecutive samples were also used to allow a comparison with the results from the idempotent modeling.

Fig. 2.24 to Fig. 2.27 present the voltage responses on different receiving end conductors using the NLT [71]–[61], the Id-Line and Id-Line-gr. These figures also show the error of the idempotent modeling from the results obtained using the NLT.



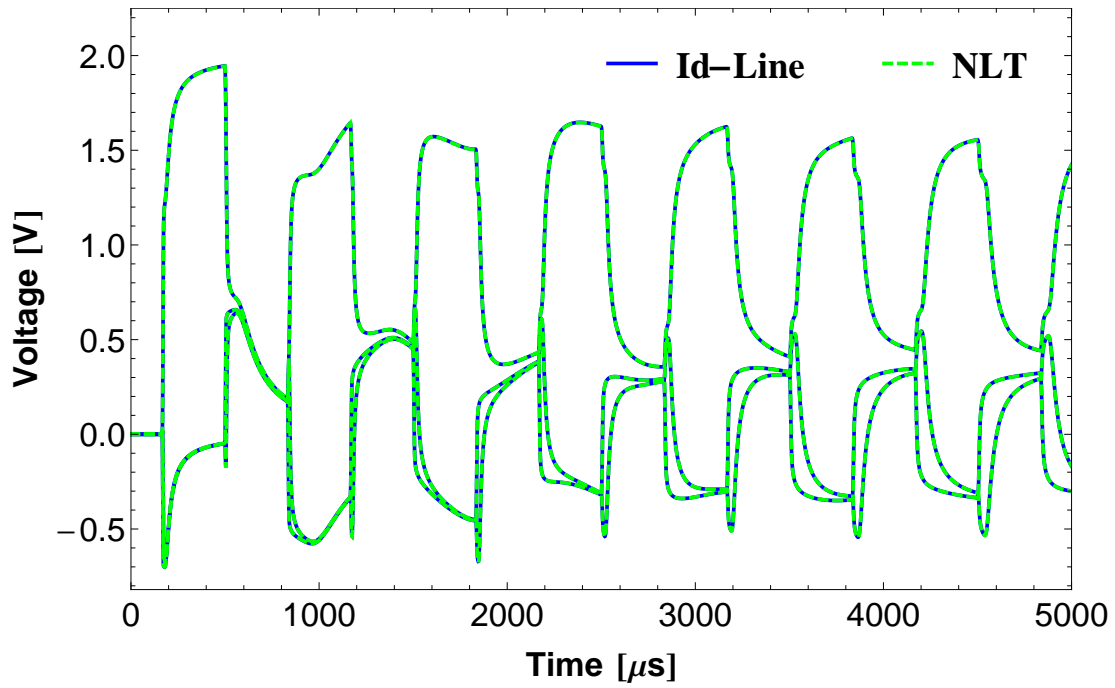


(a) Receiving end voltage simulation  $V_7$ .

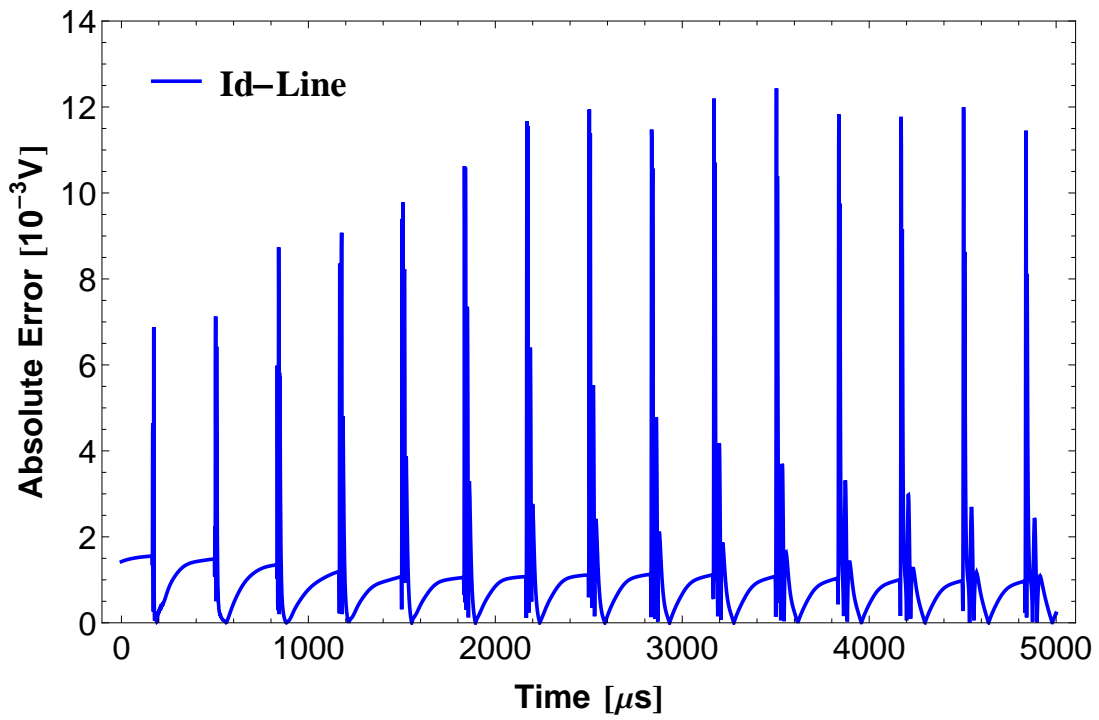


(b) Error from NLT results in  $V_7$ .

**Figure 2.24:** #1 - Time-domain simulations and error of the Idempotent Decomposition.

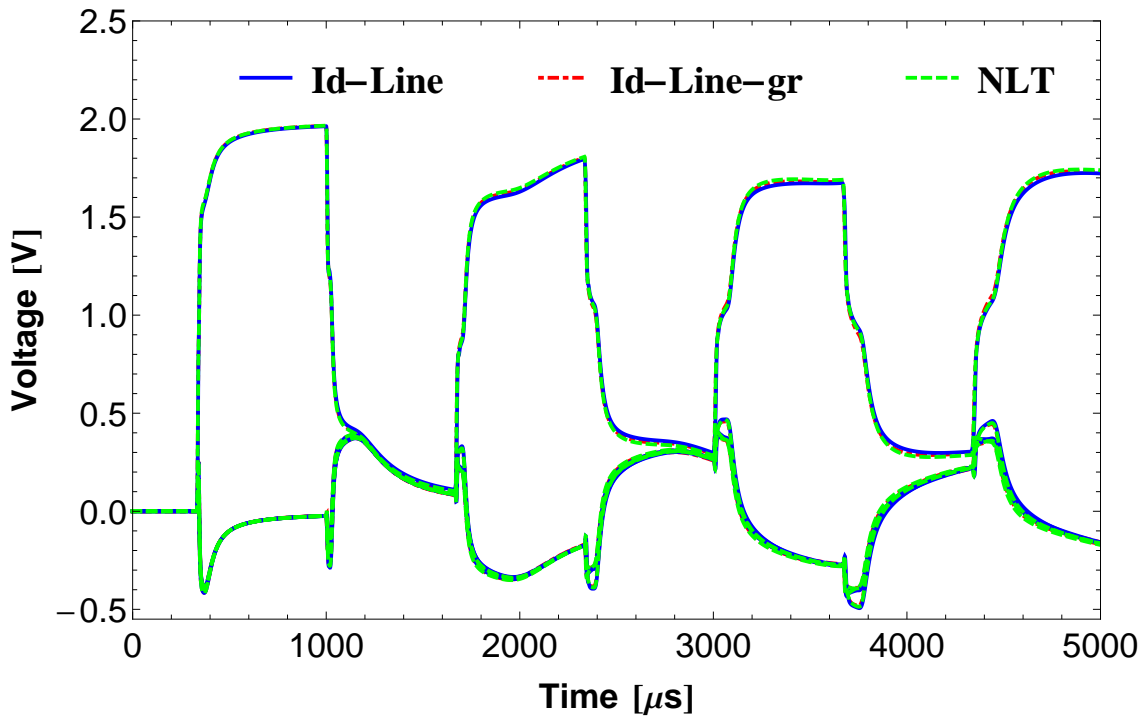


(a) Receiving end voltage simulation  $V_1$ ,  $V_2$  and  $V_3$ .

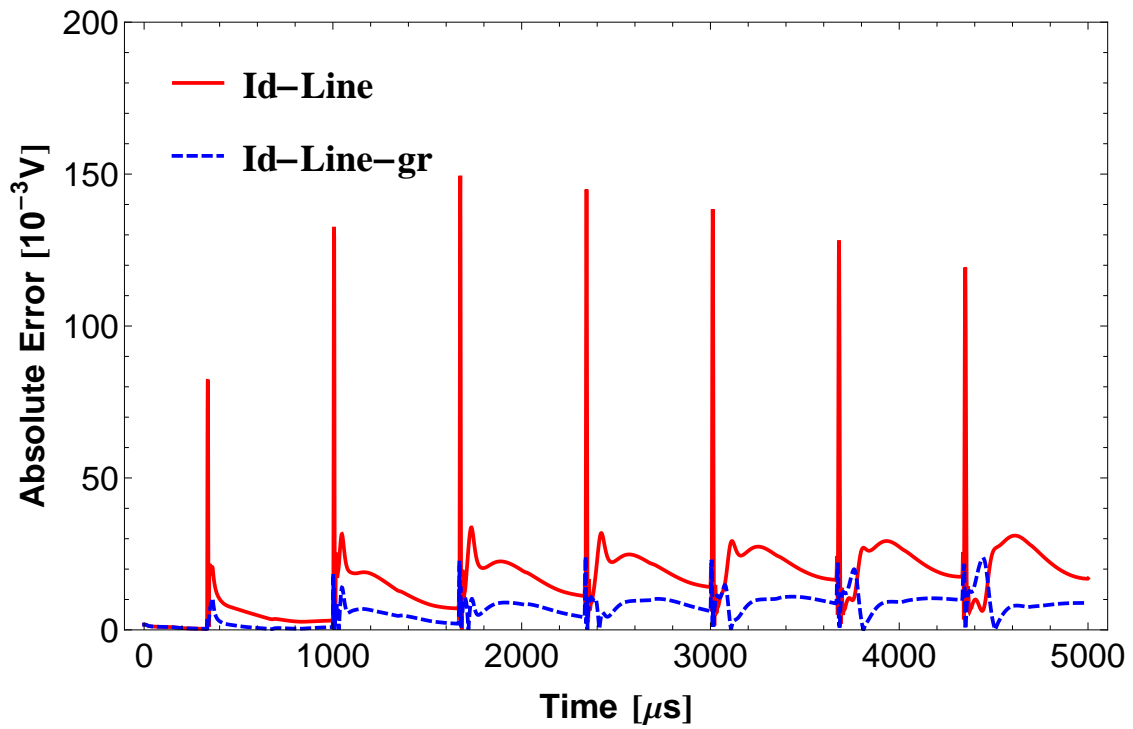


(b) Error from NLT results in  $V_1$ .

**Figure 2.25: #2 - Time domain simulations and error of the Idempotent Decomposition.**

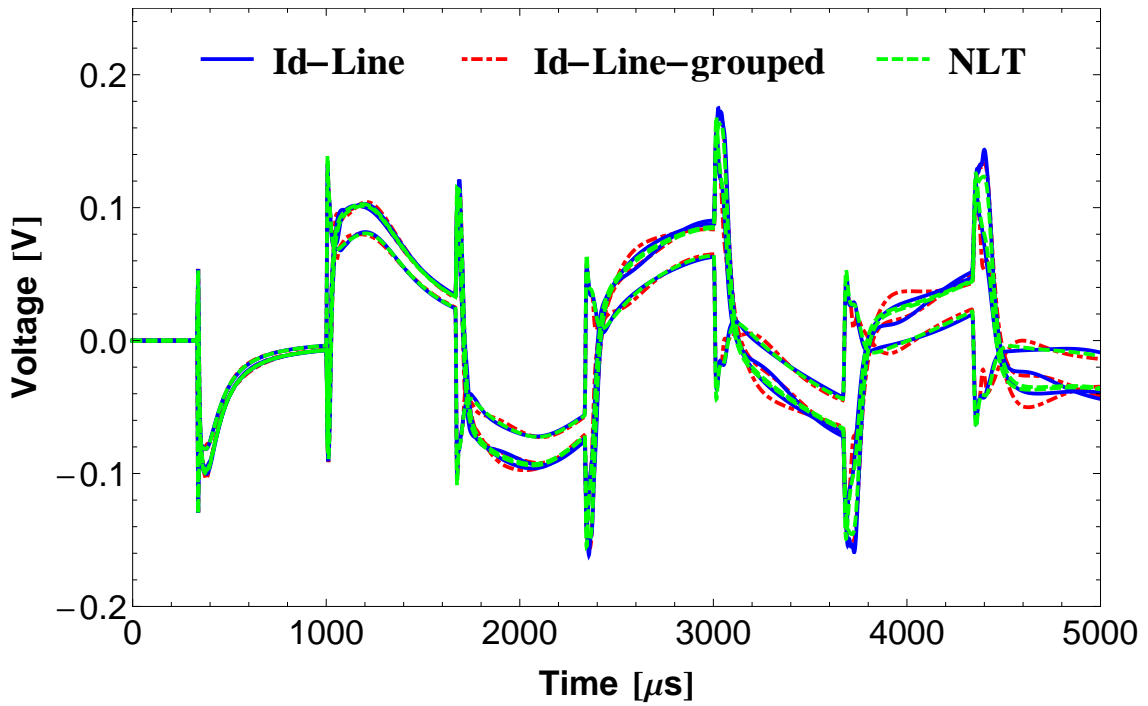


(a) Receiving end voltage simulation  $V_1$ ,  $V_4$ ,  $V_5$  and  $V_6$ .

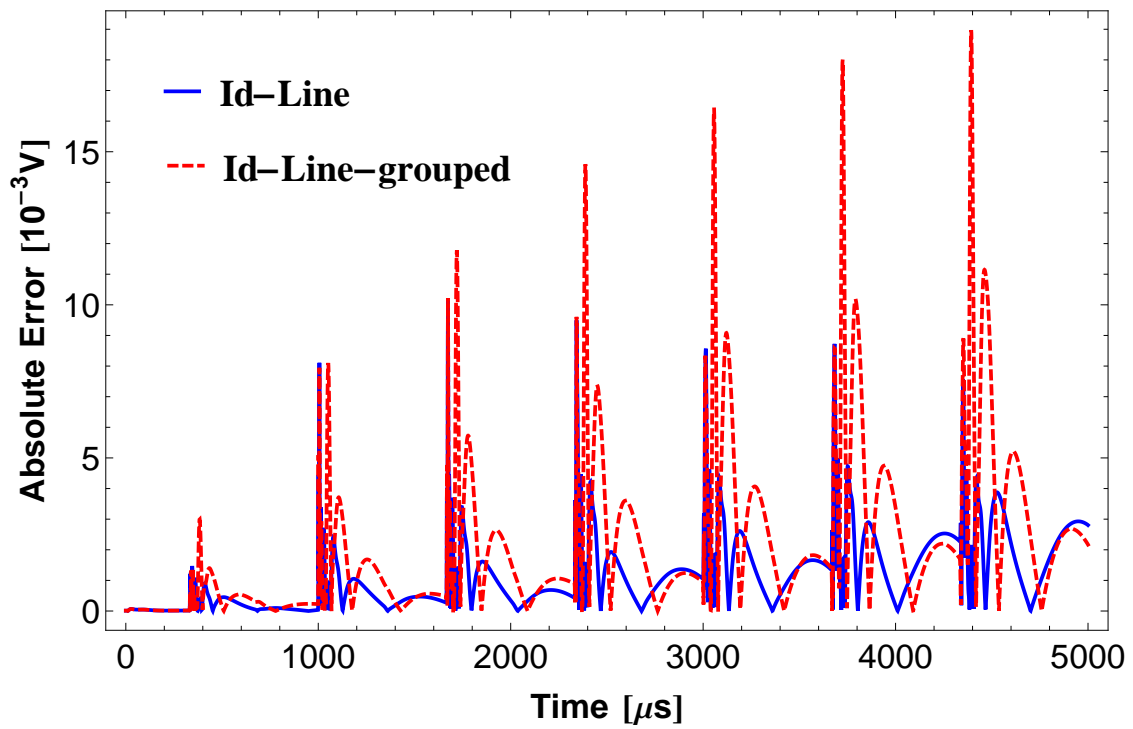


(b) Error from NLT results in  $V_4$ .

Figure 2.26: #3 - Time domain simulations and error of the Idempotent Decomposition.



(a) Receiving end voltage simulation  $V_4$ ,  $V_{15}$  and  $V_{18}$ .



(b) Error from NLT results in  $V_4$ .

**Figure 2.27:** #4 - Time-domain simulations and error of the Idempotent Decomposition.

Regardless of the test case, stable simulations were found using conventional and grouped idempotent decomposition when compared with the results obtained using NLT. With the exception of #4, accurate responses were obtained. The higher errors occurred near the steep fronts of the response. Small time-domain oscillations were found in both grouped and ungrouped idempotent modeling, the exception being the results of #4 where an increasing error with time was found.

It is worth mentioning that in spite of the inherently low accuracy involved in some of the Idempotent matrices for test case #4, a stable time-domain response was obtained using Idempotent modeling while the conventional ULM approach rendered unstable results as reported in [45]. This is due to the lower residue-pole ratio found in the rational modeling of  $\mathbf{H}$  using Idempotent decomposition as shown in Table 2.5. This table shows the results for the residue-pole ratio considering the Id-Line ( $\mathbf{H}_{M_i}$ ), Id-Line-gr ( $\mathbf{H}_{M_i-gr}$ ), ULM without lumping modes ( $\mathbf{H}_{ULM-ug}$ ) and conventional ULM ( $\mathbf{H}_{ULM}$ ). The idempotent modeling presented a considerably smaller residue-pole ratio when compared with the ULM. This result indicate the robustness of the idempotent decomposition when using a one-segment interpolation scheme.

**Table 2.5:** Residue-pole ratios of the propagation matrix  $\mathbf{H}$ .

Test Case	Residue-pole ratio (p.u.)			
	$\mathbf{H}_{ULM-ug}$	$\mathbf{H}_{ULM}$	$\mathbf{H}_{id}$	$\mathbf{H}_{id-gr}$
# 1	$2.52 \cdot 10^6$	69.00	8.09	8.09
# 2	0.53	—	0.40	—
# 3	38.58	1.20	2.49	9.56
# 4	$8.00 \cdot 10^3$	199.00	5.19	5.19

The total simulation times are shown in Table 2.6. The simulations were carried out in MATHEMATICA using a 2.4 GHz, Core i7-4700MQ computer with 12 GB of RAM.

**Table 2.6:** Total simulation time for Id-Line and ULM modeling.

Test Case	Simulation time (s)					
	One-segment interpolation scheme				Two-segment interpolation scheme	
	ULM-ug	ULM	Id-Line	Id-Line-gr	ULM-ug	ULM
# 1	3.64	1.38	4.60	3.12	6.09	2.23
# 2	10.37	—	33.71	—	35.59	—
# 3	40.75	34.57	157.64	138.33	111.48	102.99
# 4	728.70	152.08	2764.54	887.76	2908.08	656.51

Comparable simulation times were obtained for the Id-Line using a one-segment interpolation scheme and the ULM with a two-segment interpolation scheme.

## 2.8 Discussion

The application of the Idempotent decomposition for phase-domain modeling of underground cables and overhead transmission lines with a one-segment interpolation scheme was evaluated. Four test cases were considered: an underground single-core cable system without armor, a 800 kV three-phase overhead transmission line, two parallel lines of 500 kV and 138 kV and finally, a 230 kV overhead transmission line with 18-phases. Both the former and the latter cases were reported as highly unstable cases which presented unstable time-domain simulations using the ULM approach with a one-segment interpolation scheme [45]. Time-domain simulations were processed using the Numerical Laplace Transform and the Method of Characteristics approaches. Stable time responses are found in all the test cases even though only a one-segment interpolation scheme is used as a relatively small residue-pole ratio is found regardless of the circuit configuration.

For the underground single-core cable system, a very accurate fit of the Idempotent Matrices and an accurate time-domain response were obtained.

For the overhead transmission line cases studied, an unexpected behavior was found. The accuracy is dependent on the number of phases involved. As the number of phases increases, a decrease in the quality of the rational approximation of  $\mathbf{H}$  presents. This leads to small oscillations in the amplitude of the rational approximation of  $\mathbf{H}$  in the low frequency range, typically below 10 Hz. The inclusion of a diagonal shunt conductance matrix in the per-unit-length transmission line admittance is necessary to improve the accuracy of the fitting of the Idempotent matrices. However, as the number of phases increases this mitigation procedure ceased to be effective. To avoid the aforementioned oscillations, the value of the conductance would have to be considerably higher than the typical values found in the literature. Further tests of other rational fitting procedures such as matrix pencil or Levenberg-Marquadt to improve the rational approximation of  $\mathbf{H}$  in the low frequency range are also in order.

The viability of grouping Idempotent matrices with similar time-delays was also investigated. The speed gain attained was proportional to the number of grouped modes. The idempotent grouping slightly decreased the accuracy of the rational approximations. However, the test cases indicate that this grouping did not affect significantly the time-domain results with the exception being the 18-phases test case where both idempotent and idempotent grouping modelling did not provided accurate responses.

To assess the causes of the high fitting order of the Idempotent Matrices, a more detailed analysis of the phase coordinate modeling of the propagation matrix and the influence of the soil in these models is needed.

In the following chapters, the influence of the per-unit-length line parameters will be studied by comparing the results obtained using models with less simplifcative assumptions such as the Full-wave model, the quasi-TEM formulation and the Images method.

# Chapter 3

## Numerical Issues in Single-Phase Line Models

In the previous chapter, the Idempotent Decomposition was found to be a feasible alternative for phase-coordinate modeling of underground cables. Nonetheless, its application for overhead line models still merits future research work related to issues in the quality of the fitting of the Idempotent matrices when a large number of modes is considered.

We need to investigate whether the causes of the aforementioned application issues of the Idempotent Decomposition in phase coordinate modeling of overhead transmission lines are inherently related to the effect of physical inaccuracies in the formulation of the line parameters.

Therefore, in the present chapter, we evaluate the per-unit-length parameters considering a lossy ground in a wide frequency range, i.e., using both ground conduction currents and displacement currents. A simple configuration—a single-phase line—is modeled using a well established line model and two simplified models which originate from it: a Fullwave approach, which is the least simplified way to obtain the line parameters by the iterative calculus of the unknown propagation constant of the circuit, a quasi-TEM formulation, which includes simplified infinite integrals, and finally, the Image approximations, which uses closed-form expressions to consider the infinite integrals.

Although a complete full-wave model of an overhead line can circumvent the aforementioned limitations, it demands the solution of an integral equation involving an unknown propagation constant [72–74]. Pettersson [75] showed that both the fullwave model proposed by Kikuchi [72] and the one proposed by Wait [73] lead to an identical modal equation. No such comparison exists regarding the proposal made by Wedepohl and Efthymiadis [74, 76]. We show here that these two approaches lead to an identical propagation constant.

Results indicate that no passivity violations are found if either a full-wave model or quasi-TEM formulation are used. Accuracy and passivity issues in the Image approxima-

tions previously unreported in the technical literature were found. Technical difficulties related to the implementation of a multi-phase fullwave model are also addressed.

Time-domain responses based on the Numerical Laplace Transform and the Method of Characteristics were used to verify the accuracy and stability of the tested models. Tests were carried on using an input voltage including a small perturbation to excite the passivity violations found in the modeling using the Image approximations. The large number of complex-valued frequency samples hindered an efficient time-domain simulation of the full-wave model. While suitable responses were obtained for the quasi-TEM formulation, the image approximations model presented a loss of accuracy in its time-domain results due to the aforementioned passivity violations.

If the line length is increased, it was found that the image approximation can lead to a stable model in a frequency range up to 100 MHz as well. Therefore, besides the well-known limitations of the image approximation related to the ratio between conductor's height and diameter, there is a minimal length limitation to its applicability as a function of the frequency.

Furthermore, as an iterative solution based on a Newton-Raphson scheme is needed to solve the modal equation in the fullwave model, we show that instead of using a slightly perturbed air propagation constant as initial guess, it is possible to improve the numerical performance of the overall process if a distinct initial guess is considered. Some aspects related to a full-wave model based on the Method of Characteristics using rational fitting are also presented.

The chapter is organized as follows: Section 3.1 presents a brief introduction to the chapter. Section 3.2 briefly reviews the process of defining the modal equation and the root-finding scheme needed to solve it. Section 3.3 presents the basic formulation related to the definition of per-unit-length parameters considering a full-wave model, quasi-TEM approximations and image approximations. Section 3.4 shows the formulation of the nodal admittance matrix for a transmission line as well as the definition of its eigenvalues for the passivity violation assessment. Section 3.5 presents the frequency domain fitting results for a simple line considering a full wave model, a quasi-TEM formulation and Image approximations. This section also shows the time domain response tests of a slightly perturbed input voltage considering the Numerical Laplace Transform and the Method of Characteristics for the line modeling. Section 3.6 addresses the cause of the passivity violations by analyzing the accuracy of the simplified closed-form solution of the infinite integrals related to the quasi-TEM formulation. The main conclusions of this chapter are shown in Section 3.7.



### 3.1 Introduction

The relation between terminal voltages and injected currents in a thin wire above a lossy interface is one of the classical problems in electromagnetic field theory and it has a wide range of applications. Traditionally, power system transients studies on transmission lines or underground cables assume quasi-TEM (Transverse Electromagnetic) propagation and the ground to be a good conductor, i.e., neglecting displacement currents associated with the ground permittivity. This implies using either Carson's or Pollaczek's formulation [30–32] involving the solution of infinite integrals for the evaluation of the series impedance. To avoid dealing with the aforementioned infinite integrals, extensive research on simplified expressions has been carried out such as the ones in [33–36] to mention just a few. One of the most successful approximations is based on the image approach. This approach, also known as the complex-plane method, has been used to derive ground return impedances of overhead lines [34] and underground cables [37]. In the image method, the quasi-TEM formulation is further simplified, allowing closed-form formula based on logarithms.

More recent works related to approximations of line parameters [54, 75, 77] proposed image approximations that can deal with the inclusion of ground displacement currents. Unfortunately, as it is here shown, this approach might lead to small passivity violations in the high frequency range, typically above a few MHz. This frequency range might seem outside the usual bandwidth of interest for power system analysis. However, to improve frequency domain fitting, identification of time-delays and to evaluate the lightning performance of transmission circuits in time-domain modeling [39–41], a bandwidth with frequencies up to 10 MHz [20, 23, 42, 43] or 100 MHz [44, 45] might need to be considered.

It is important to mention that an assessment of a full wave line model considering either multi-phase conductors or frequency dependent ground parameters, as well as special cases like inclined or non-homogeneous lines which need to be evaluated using different calculation methods such as the discretization of the line [78], are outside of the scope of the present work and are left for future research.

### 3.2 Identification of the Propagation Constant

Consider an infinitely long conductor with radius  $r$  at a constant height  $h$  above a lossy ground as shown in Fig. 4.1. Both media are assumed to be air and ground, characterized by a permittivity  $\epsilon_i$ , conductivity  $\sigma_i$  and permeability  $\mu_i$ , where  $i = 1$  for air and  $i = 2$  for the ground, respectively. Time-dependence is assumed to be of the harmonic type, i.e.,

$e^{j\omega t}$ , and the propagation constant  $\gamma_i$  of each medium is given by

$$\gamma_i = \sqrt{j\omega\mu_i(\sigma_i + j\omega\epsilon_i)} \quad (3.1)$$

with the real part of the square root defined positive. The conductor current  $I$  propagates exponentially in the  $z$ -axis and has the form

$$I = I_0 e^{-\gamma z} \quad (3.2)$$

where  $I_0$  is the maximum amplitude and  $\gamma$  is the unknown propagation constant of the circuit. The expression for the electromagnetic field in both media can be obtained through

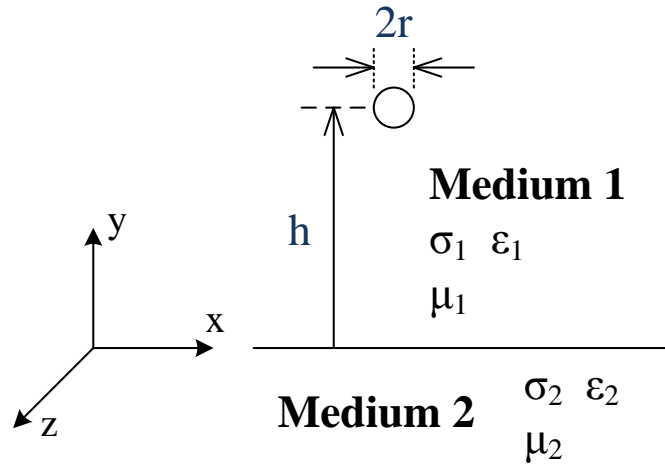


**Figure 3.1:** Single-phase conductor arrangement.

the use of the electric and magnetic Hertz vector,  $\Pi_{E_i}$  and  $\Pi_{M_i}$  respectively [79]. Both  $\Pi_{E_i}$  and  $\Pi_{M_i}$  have only a  $z$ -component. The general expressions of the electric field  $\mathbf{E}_i$  and the magnetic field  $\mathbf{H}_i$  are shown below.

$$\begin{aligned} \mathbf{E}_i &= \nabla \times \nabla \times \Pi_{E_i} - j\omega\mu_i \nabla \times \Pi_{M_i} \\ \mathbf{H}_i &= (\sigma_i + j\omega\epsilon_i) \nabla \times \Pi_{E_i} + \nabla \times \nabla \times \Pi_{M_i} \end{aligned} \quad (3.3)$$

A solution to (3.3) can be found using a double spatial Fourier Transform. The boundary condition at the conductor surface and at the interface between the two media are used to solve the field equations. An outline of this solution was first presented by Wait [73] and by D'Amore and Sarto in the appendix of [77] and it is summarized in Appendix C.

If the thin wire approximation [35, 77] is assumed, i.e., as long as  $\gamma_w \gg \gamma_1$ , where  $\gamma_w$  is the propagation constant of the wire, the evaluation of the electric field at  $x = 0, y = h - r$ , see Fig. 3.1, leads to the modal equation given by  $M$  below. Assuming equal ground and

air permeabilities,  $\mu_2 = \mu_1 = \mu_0$ , we have:

$$M = \frac{2\pi}{j\omega\mu_1} z_{int} + \left(1 - \frac{\gamma^2}{\gamma_1^2}\right) P + \left(S_1 - \frac{\gamma^2}{\gamma_1^2} S_2\right) \quad (3.4)$$

where  $z_{int}$  is the conductor internal impedance,  $P = K_0(r\eta_1) - K_0(d\eta_1)$ , being  $K_0$  the modified Bessel function of the second kind of order zero,  $d = \sqrt{4h^2 + r^2}$ ,  $\eta_1 = \sqrt{\gamma_1^2 - \gamma^2}$ , and  $S_1$  and  $S_2$  are the Sommerfeld integrals given by

$$S_1 = \int_{-\infty}^{\infty} \frac{e^{-2hu_1}}{u_1 + u_2} e^{-jr\lambda} d\lambda \quad (3.5)$$

$$S_2 = \int_{-\infty}^{\infty} \frac{e^{-2hu_1}}{n^2 u_1 + u_2} e^{-jr\lambda} d\lambda \quad (3.6)$$

where  $u_1 = \sqrt{\lambda^2 + \gamma_1^2 - \gamma^2}$ ,  $u_2 = \sqrt{\lambda^2 + \gamma_2^2 - \gamma^2}$ , and  $n = \gamma_2/\gamma_1$  is the refractive index of ground.

As pointed out in [75, 77] the numerical solution of (3.4) is not straightforward. Typically, we might use a Newton-Raphson (NR) scheme starting from a slightly perturbed  $\gamma_1$  as a starting point for the root finding process. This procedure can be expressed as follows

$$\gamma_{k+1} = \gamma_k - \frac{M}{M'} \quad (3.7)$$

where  $\gamma_{k+1}$  is the new value of the propagation constant obtained from the values of the  $k$ -th iteration,  $M'$  is the derivative of the modal equation with respect to  $\gamma$  given by

$$M' = \frac{\partial S_1}{\partial \gamma} + \frac{\partial P}{\partial \gamma} - \frac{\gamma^2}{\gamma_1^2} \left( \frac{\partial S_2}{\partial \gamma} + \frac{\partial P}{\partial \gamma} \right) - 2 \frac{\gamma}{\gamma_1^2} (S_2 + P) \quad (3.8)$$

where

$$\frac{\partial S_1}{\partial \gamma} = -\gamma \int_{-\infty}^{\infty} \left( \frac{1 + 2hu_2}{u_1^2 u_2 + u_1 u_2^2} \right) e^{-2hu_1 - j\lambda r} d\lambda \quad (3.9)$$

$$\frac{\partial S_2}{\partial \gamma} = -\gamma \int_{-\infty}^{\infty} \left( \frac{2hu_2 (u_2 + n^2 u_1) + n^2 u_2 + u_1}{u_1 u_2 (n^2 u_1 + u_2)^2} \right) e^{-2hu_1 - j\lambda r} d\lambda \quad (3.10)$$

$$\frac{\partial P}{\partial \gamma} = \frac{\gamma}{\eta_1} [dK_1(d\eta_1) - rK_1(r\eta_1)] \quad (3.11)$$

being  $K_1$  the modified Bessel function of the second kind of order one.

We found out that this process is rather slow in convergence and some numerical problems might occur as  $\eta_1$  tends to zero in  $P$ . Furthermore, the infinite integrals have a slow rate of convergence, even when specific integration algorithms such as Gauss-Kronrod (GK) quadrature are used. Both  $M$  and  $M'$  are evaluated using a GK quadrature as implemented in Mathematica, see Appendix D for some details. After the evaluation of  $M$  and  $M'$  the determination of the next guess of the propagation constant is straightforward. This process continues until

$$\left| \frac{\gamma_{k+1}}{\gamma_k} \right| \leq \delta \quad (3.12)$$

where  $\delta$  is a real number, here we considered  $\delta = 10^{-12}$ .

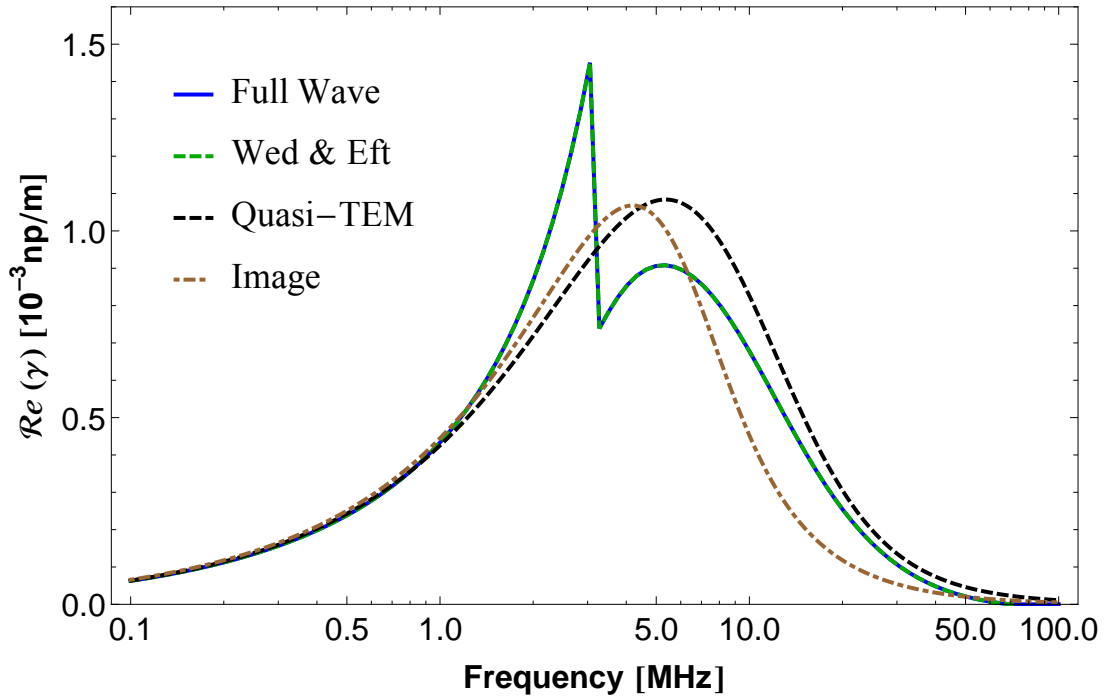
To improve the numerical evaluation of (3.7), several possible starting points for the NR algorithm were tested. We found that the use of an image approximation as a starting point significantly improves the numerical performance.

To illustrate this procedure, consider a single conductor at constant height  $h = 10$  m above ground, radius  $r = 1$  cm, conductivity  $\sigma_c = 64.96 \cdot 10^6$  S/m and length  $\ell = 500$  m. The ground parameters are  $\sigma_2 = 5$  mS/m,  $\epsilon_2 = 5 \epsilon_1$  with  $\epsilon_1 = \epsilon_0$  and  $\mu_1 = \mu_2 = \mu_0$ , air conductivity is null. This configuration is basically the same as in [77].

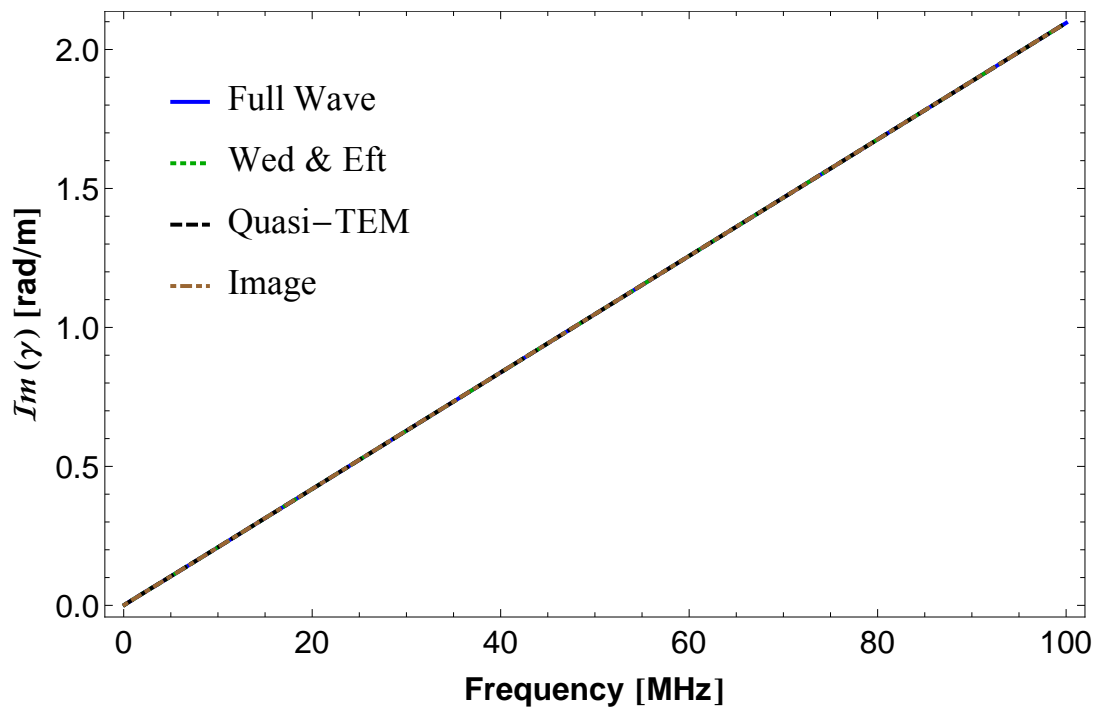
Fig. 3.2 shows the attenuation and phase constants of  $j\gamma$  for the full wave solution and the approximations. This result was obtained by solving the integral equation in a similar manner as done in [80]. In every case, the attenuation constant differs in 3 orders of magnitude to the phase constant. As reported in the literature [81, 82], there are two roots of the modal equation on the proper Riemann sheet, one is related to a fast wave (FW) mode with increasing damping and the other is a transmission line mode (TL) where the attenuation constant decreases in the high frequency range. Furthermore, as mentioned in [77], TL and FW are very close in the low frequency range. As TL mode starts to increase, its damping it is no longer a viable solution to the NR scheme, shifting from the TL mode to the FW one. This causes a discontinuity in the attenuation constant around 4 MHz.

Regardless of the original formulation, all methods provided identical results for the phase constant. If we compare the aforementioned figures with [77, Fig. 2a, Fig. 2b] a very good agreement is found. The main difference lies in the maximum value in the attenuation constant. For comparison, Fig. 3.2 also shows the values obtained using the full-wave model proposed by Wedepohl and Efthymiadis in [74, 76]. Unlike the previous model, this proposal is based on using magnetic and scalar vector potentials. We summarize this approach in Appendix E. It is worth mentioning that this formulation allows to evaluate the scenario of two media with different magnetic permeability, i.e.,  $\mu_1 \neq \mu_2$ .

For the starting point in the NR scheme of (3.7) we considered three possible initial



(a) Attenuation constant



(b) Phase constant

**Figure 3.2:** Behavior of  $\gamma$  for distinct approaches.

guesses: A perturbed air propagation constant  $\hat{\gamma}_k = \gamma_1(1 - j0.001)$ , a quasi-TEM approximation and an image approach. For the latter two, rearranging (3.4) and neglecting  $z_{int}$  it

follows that

$$\bar{\gamma}_k = \gamma_1 \sqrt{\frac{\bar{P} + \bar{S}_1}{\bar{P} + \bar{S}_2}} \quad \bar{\bar{\gamma}}_k = \gamma_1 \sqrt{\frac{\bar{P} + \bar{\bar{S}}_1}{\bar{P} + \bar{\bar{S}}_2}} \quad (3.13)$$

where  $\bar{P}$ ,  $\bar{S}_1$ ,  $\bar{S}_2$ ,  $\bar{\bar{S}}_1$  and  $\bar{\bar{S}}_2$  are given in (3.21) and (3.23).

Although a solution is reached using  $\hat{\gamma}_k$ , several convergence problems of the NR scheme arise. An improved convergence was achieved using  $\bar{\gamma}_k$  as it is closer to the actual solution. However, it demands the evaluation of infinite integrals in the frequency loop leading to a higher computational time. Finally,  $\bar{\bar{\gamma}}_k$  presents the best performance, with an improved convergence and minimal computational burden.

### 3.3 Evaluation of the Line Parameters

After the identification of  $\gamma$ , to define the propagation characteristics we must solve the well know wave equation

$$\frac{d^2 U}{dz^2} = Z(\gamma)Y(\gamma)U \quad \frac{d^2 I}{dz^2} = Y(\gamma)Z(\gamma)I \quad (3.14)$$

where  $Z(\gamma)$  and  $Y(\gamma)$  are the per-unit-length impedance and admittance, respectively,  $U$  is the wire voltage to ground and  $I$  is the line current.

The wire voltage to ground  $U$  can then be obtained by

$$U = - \int_0^{h-r} E_y(0, \xi) d\xi \quad (3.15)$$

for a conductor at a constant height  $h$  and centered at  $(0, h)$ . By using the magnetic vector potential  $\mathbf{A}$  and the electric scalar potentials  $\varphi$  it is possible to express  $U$  as

$$U = \varphi(0, h-r) - \varphi(0, 0) + j\omega \int_0^{h-r} A_y(0, \xi) d\xi \quad (3.16)$$

where  $A_y$  is the y-component of  $\mathbf{A}$ . Both  $\mathbf{A}$  and  $\varphi$  can be obtained in terms of the electric and magnetic Hertz vectors,  $\Pi_{E_i}$  and  $\Pi_{M_i}$  respectively, see (3.17) [79].

$$\mathbf{A} = \mu (\boldsymbol{\sigma} + j\omega\boldsymbol{\varepsilon}) \Pi_E + \mu \nabla \times \Pi_M \quad \varphi = -\nabla \cdot \Pi_E \quad (3.17)$$

Thus after obtaining  $\gamma$ , we calculate both  $\Pi_E$  and  $\Pi_M$  to define the line voltage, see Appendix C for details.

The per-unit-length line parameters, i.e., the line impedance  $Z$  and admittance  $Y$ , are

then given by

$$Z(\gamma) = z_{int} + \frac{j\omega\mu_1}{2\pi} \left[ P + S_1 - \left( \frac{\gamma}{\gamma_1} \right)^2 (T + S_2) \right] \quad (3.18)$$

$$Y(\gamma) = 2\pi(\sigma_1 + j\omega\epsilon_1) [P - T]^{-1}$$

where  $P$ ,  $S_1$ ,  $S_2$  are the same as before and  $T$  is an infinite integral accounting for the magnetic vector potential in the y-axis given by

$$T = \int_{-\infty}^{\infty} \frac{u_2}{u_1} \left( \frac{e^{-hu_1} - e^{-2hu_1}}{n^2u_1 + u_2} \right) e^{-jr\lambda} d\lambda \quad (3.19)$$

One disadvantage of using (3.18) for the evaluation of the line parameters is the need to first solve the modal equation, i.e., find a  $\gamma$  that leads to  $M = 0$  in (3.4), to calculate the infinite integrals. A possible simplification known as the quasi-TEM or small argument approximation consists in assuming  $\gamma = \gamma_1$  in  $P$ ,  $S_1$ ,  $S_2$  and  $T$ . Then, both the impedance and admittance per-unit-length become independent of the propagation constant. The resulting expressions for  $Z$  and  $Y$  considering these approximations are

$$Z = z_{int} + \frac{j\omega\mu_1}{2\pi} [\bar{P} + \bar{S}_1 - (\bar{T} + \bar{S}_2)] \quad (3.20)$$

$$Y = 2\pi(\sigma_1 + j\omega\epsilon_1) [\bar{P} - \bar{T}]^{-1}$$

where  $\bar{P} = \ln(2h/r)$  and the infinite integrals are given below

$$\bar{S}_1 = \int_{-\infty}^{\infty} \frac{e^{-2h\lambda}}{\lambda + \bar{u}} e^{-jr\lambda} d\lambda$$

$$\bar{S}_2 = \int_{-\infty}^{\infty} \frac{e^{-2h\lambda}}{n^2\lambda + \bar{u}} e^{-jr\lambda} d\lambda \quad (3.21)$$

$$\bar{T} = \int_{-\infty}^{\infty} \frac{\bar{u}}{\lambda} \left( \frac{e^{-h\lambda} - e^{-2h\lambda}}{n^2\lambda + \bar{u}} \right) e^{-jr\lambda} d\lambda$$

where  $\bar{u} = \sqrt{\lambda^2 + \gamma_2^2 - \gamma_1^2}$ .

Although the quasi-TEM approximation represents a simpler way to obtain the line parameters, infinite integrals are still involved. Extensive research has been carried out to approximate them, e.g., [81–84], or to avoid them, e.g., [33–36], just to mention a few. One of the most successful approximations is based on the image approach which can be considered as an extension of the case of a perfectly conducting ground plane. This approach is also known as the complex-plane method and has been used to derive ground

return impedances of overhead lines [34] and underground cables [37]. The resulting expressions for  $Z$  and  $Y$  are

$$\begin{aligned} Z &= z_{int} + \frac{j\omega\mu_1}{2\pi} \left[ \bar{P} + \bar{S}_1 - \left( \bar{T} + \bar{S}_2 \right) \right] \\ Y &= 2\pi(\sigma_1 + j\omega\epsilon_1) \left[ \bar{P} - \bar{T} \right]^{-1} \end{aligned} \quad (3.22)$$

where the infinite integrals are given by closed-form expressions based on logarithmic approximations given by

$$\begin{aligned} \bar{S}_1 &= \ln \left( 1 + \frac{2}{\beta\sqrt{4h^2 + r^2}} \right) \\ \bar{S}_2 &= \frac{2}{n^2 + 1} \ln \left( 1 + \frac{n^2 + 1}{\beta\sqrt{4h^2 + r^2}} \right) \\ \bar{T} &= 2\ln 2 + \frac{2n^2}{n^2 + 1} \ln \left( \frac{1 + \frac{n^2 + 1}{\beta\sqrt{4h^2 + r^2}}}{1 + \frac{2(n^2 + 1)}{\beta\sqrt{4h^2 + r^2}}} \right) \end{aligned} \quad (3.23)$$

with  $\beta = \sqrt{\gamma_2^2 - \gamma_1^2}$ . If the ground is assumed to be a good conductor, i.e.,  $\sigma_2 \gg \omega\epsilon_2$ , the following premises hold

$$\left| \bar{S}_1 \right| \gg \left| \bar{S}_2 + \bar{T} \right| \quad \text{and} \quad \left| \bar{S}_1 \right| \gg \left| \bar{S}_2 + \bar{T} \right| \quad (3.24)$$

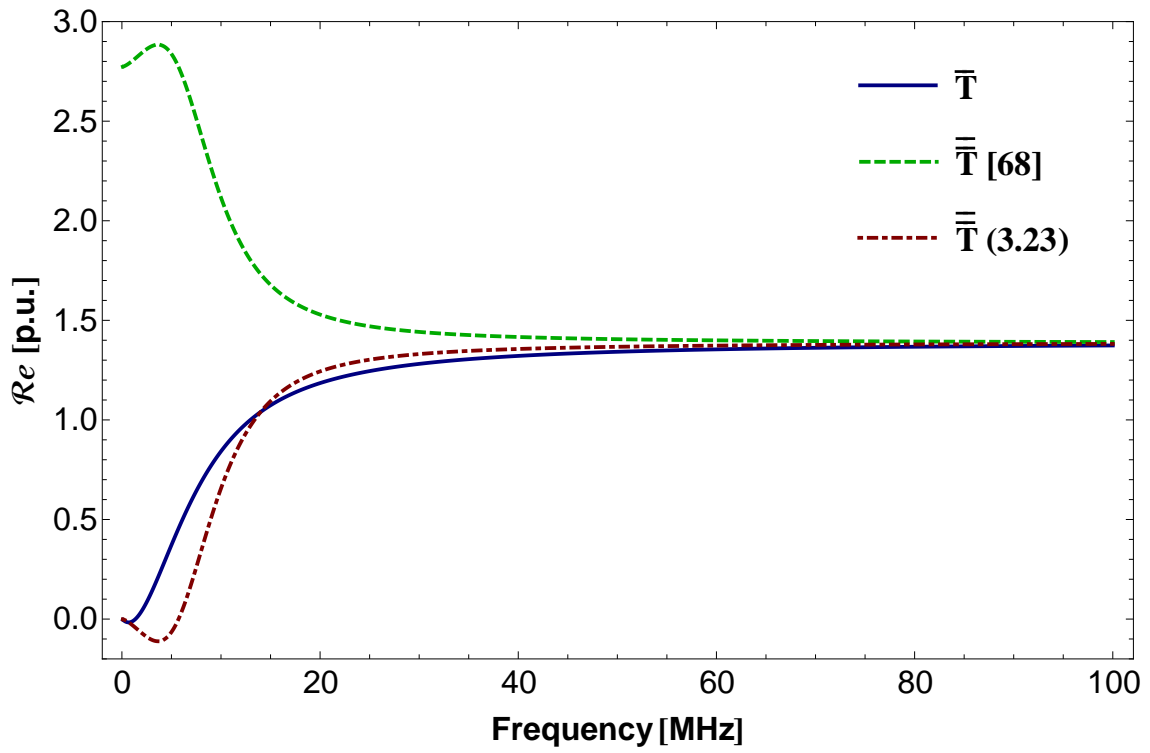
thus only the approximate expressions of  $S_1$  and  $P$  are needed in the evaluation of the line parameters. The expression for  $\bar{T}$  presented here is slightly different from the one reported in [75], this is due to a mismatch found in this expression with its corresponding infinite integral from the quasi-TEM formulation.

To clarify this finding in more detail, consider the single-phase line presented in Section 3.2. Fig. 3.3 shows the comparison for the real and imaginary part of  $\bar{T}$  and their approximated counterparts, i.e.,  $\bar{T}$  presented in [75] and  $\bar{T}$  using expression (3.23).

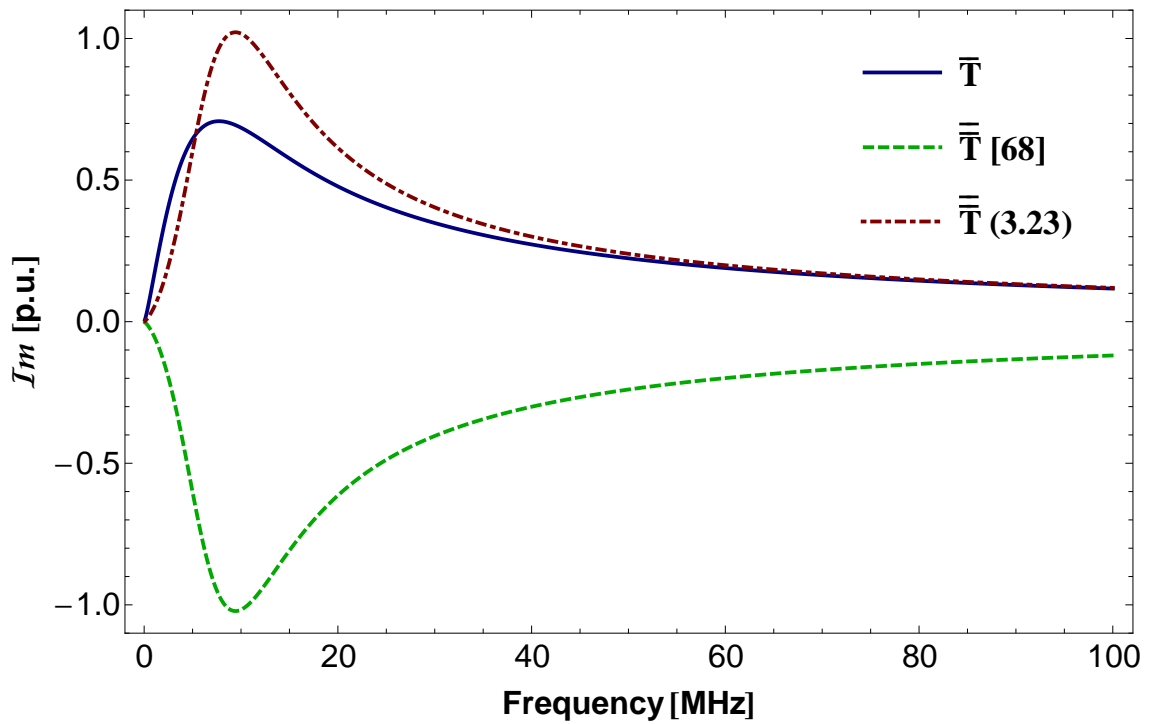
Besides of the large mismatch between  $\bar{T}$  and  $\bar{T}$  [24], and the increased magnitude of the passivity violations calculated using  $\bar{T}$  [24], due to inaccuracies inherent to the logarithmic approximation, the opposite phase in both real and imaginary values seem to indicate that it is possible there was a typo in such expression. Therefore, in the present work, we recommend to use the expression (3.23) instead of the one presented in [75].

Although deviations between  $\bar{T}$  and  $\bar{T}$  [24] are rather small when compared to the magnitudes of  $Z$  and  $Y$ , they create small deviations in both  $H$  and  $Y_c$ , thus increasing the existing passivity violations in the resulting nodal admittance matrix as presented in Fig. 3.4, see Section 3.4 for details.



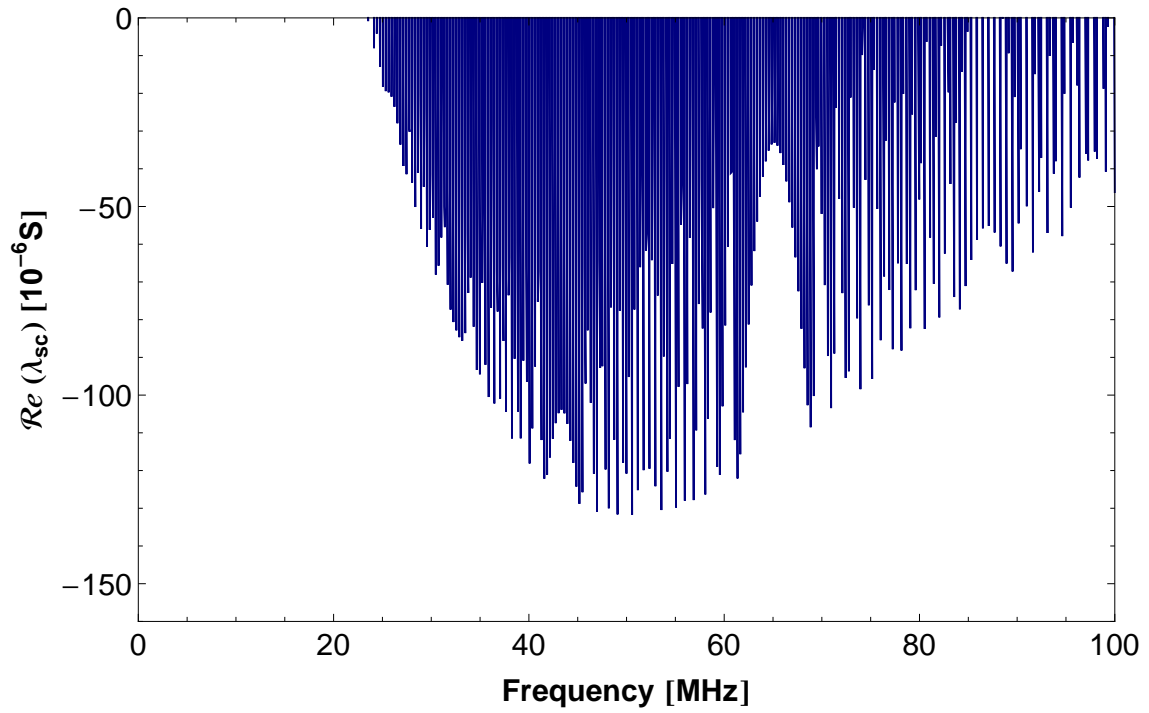


(a) Real Part

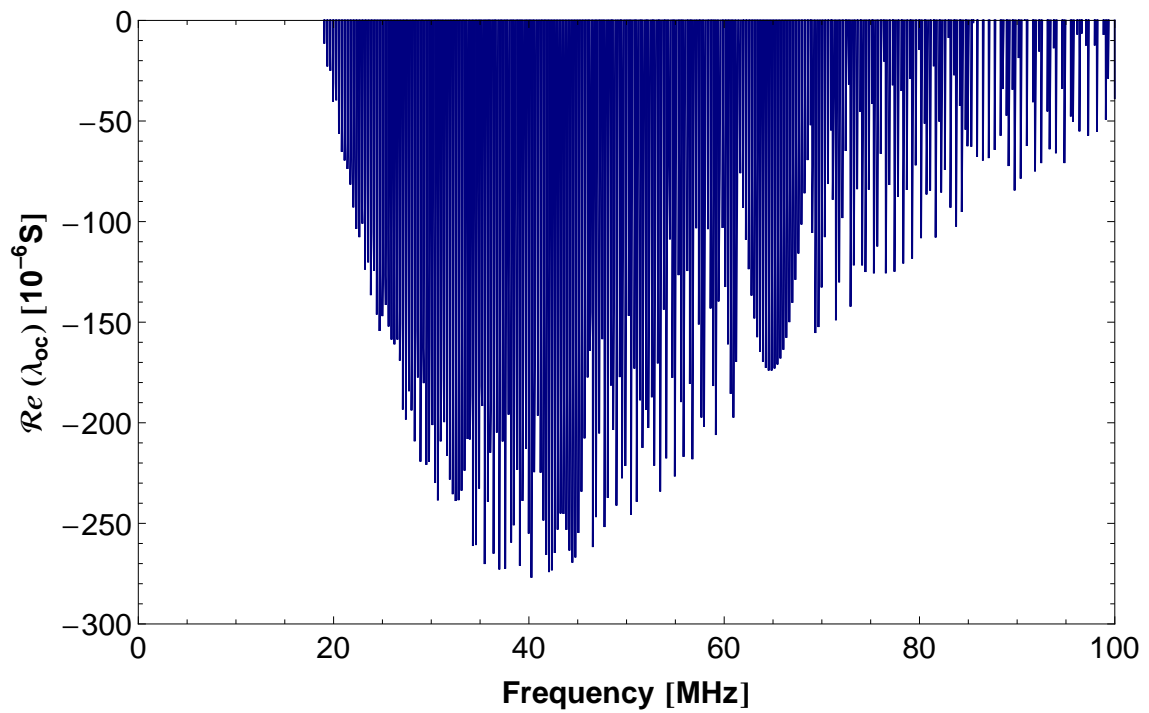


(b) Imaginary Part

**Figure 3.3:** Accuracy comparison of closed-form  $T$ .



(a)  $\bar{\bar{T}}$  using expression (3.23).



(b)  $\bar{\bar{T}}$  presented in [75]

**Figure 3.4:** Passivity violations in  $\mathbf{Y}$  using different closed-forms of  $T$ .

### 3.4 Numerical Stability of a Single-phase Line Model

Typically, the numerical stability of a transmission line model is analyzed using only the characteristic impedance  $Z_c$ , i.e., a line model is assumed stable as long as  $Z_c$  has a positive real part. However, this consideration alone might be insufficient to guarantee a passive line model, which can ensure stability throughout the whole frequency range.

A transmission line model can be represented in the frequency domain by its nodal admittance matrix, i.e.,

$$\mathbf{I} = \mathbf{Y} \cdot \mathbf{V} \quad (3.25)$$

with  $\mathbf{I}$  being the vector of injected currents,  $\mathbf{V}$  the vector of line terminal voltages and where the nodal admittance matrix  $\mathbf{Y}$  is given by

$$\mathbf{Y} = \mathbf{G} + j\mathbf{B} = \begin{bmatrix} Y_s & Y_m \\ Y_m & Y_s \end{bmatrix} \quad (3.26)$$

The power absorbed ( $P$ ) by this model for any complex vector  $\mathbf{V}$  is given by

$$P = \Re\{\mathbf{V}^* \mathbf{Y} \mathbf{V}\} = \mathbf{V}^* \mathbf{G} \mathbf{V} \quad (3.27)$$

where  $\mathbf{V}^*$  is the conjugate transpose of  $\mathbf{V}$ . Thus to verify the stability of any line model, a simple yet efficient procedure is to identify whether the real part of the eigenvalues of  $\bar{\mathbf{Y}}$  in (3.28) is positive. This means we must establish if  $\mathbf{Y}$  is positive definite, i.e.

$$\text{eig}(\bar{\mathbf{Y}}) = \text{eig}((\mathbf{Y} + \mathbf{Y}^H) / 2) \geq 0 \quad \forall(j\omega) \quad (3.28)$$

where  $\mathbf{Y}^H$  is the conjugate transpose of  $\mathbf{Y}$ .

Thus, identification of passivity violations can be carried out in the frequency domain. However, the maximum passivity violations could be difficult to identify as the global minimum of  $\text{eig}(\bar{\mathbf{Y}})$  may not be reached in the frequency sweep.

In a single-phase transmission line the elements of  $\mathbf{Y}$  in (3.26) are given by

$$Y_s = Y_c (1 + H^2) (1 - H^2)^{-1} \quad (3.29)$$

$$Y_m = -2Y_c H (1 - H^2)^{-1} \quad (3.30)$$

where  $Y_c = Z_c^{-1} = \sqrt{Y/Z}$  is the characteristic admittance,  $Z$  and  $Y$  are the per-unit-length line parameters, and  $H = \exp(-\ell\sqrt{ZY})$  for a line length  $\ell$ .

For the single conductor case considered here, the eigenvalues ( $\lambda_1, \lambda_2$ ) of the nodal admittance matrix are easily obtained, see (3.31), where  $\lambda_1$  is related to the short-circuit

current response and  $\lambda_2$  to the open circuit current response

$$\lambda_1 = Y_c \frac{1+H}{1-H} \quad \lambda_2 = Y_c \frac{1-H}{1+H} \quad (3.31)$$

Fig. 3.5 and Fig. 3.6 show the characteristic admittance and propagation matrix considering the full-wave model, the quasi-TEM approximation and the image approach. The discontinuity found in  $\gamma$  also leads to a discontinuity in both  $Y_c$  and  $H$ . Although all methods tend asymptotically to the same value, there is a large deviation in the absolute value of  $H$  in the high frequency range. As in the behavior of  $Y_c$  in the full-wave model,  $H$  also exhibits a discontinuity above a few MHz. These discontinuities in the full-wave approach will pose some challenges when we implement a time-domain model based on the method of characteristics as it will be shown in Section 3.5.

Using the expressions for  $Y_c$  and  $H$  in (3.31) and considering a frequency range from 1 MHz up to 100 MHz with 1500 logarithmic sampled frequency points we calculate  $\lambda_1$  and  $\lambda_2$  for the three models, i.e., Full-wave, quasi-TEM and image approximations. We have found that only the latter presents passivity violations. Table 3.1 summarizes these results, where *eig* denotes eigenvalue,  $\Omega$  stands for the frequency value at which the largest passivity violation occurs, *min* is the minima of  $\Re(\lambda_1(\Omega))$  and  $\Re(\lambda_2(\Omega))$  or the minima of  $\Re(\lambda_1)$ ,  $\Re(\lambda_2)$  in the frequency sweep if there are no passivity violations.

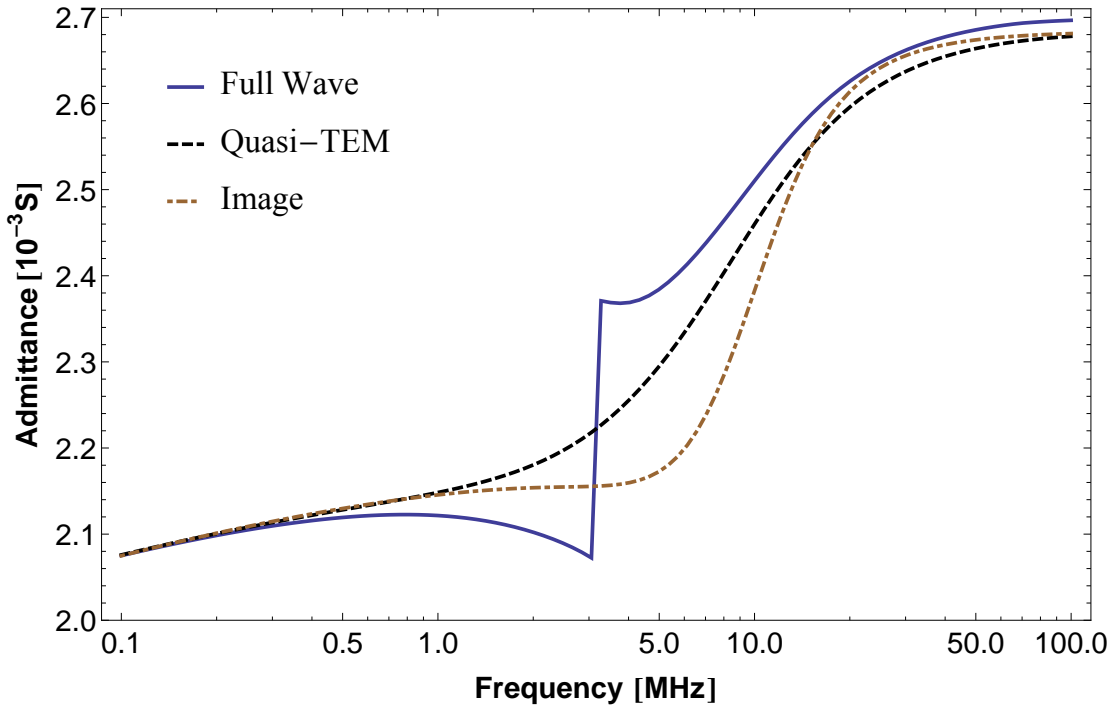
Passivity violations are considerably small and concentrated in the frequency range of  $20 \text{ MHz} \leq f \leq 60 \text{ MHz}$  for  $\lambda_1$  and just slightly larger for  $\lambda_2$ , with the most severe located around 33 MHz as shown in Fig. 3.7.

**Table 3.1:** Passivity violations and minima of  $\lambda_1$  and  $\lambda_2$ .

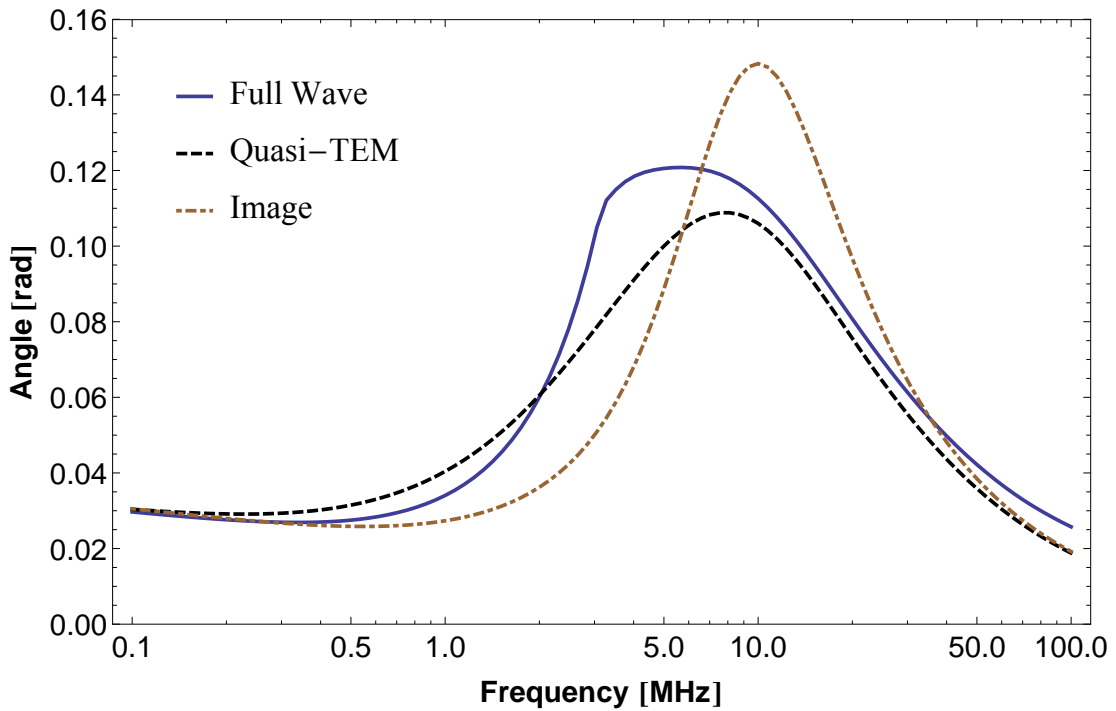
Model	<i>eig</i>	$\Omega$ (MHz)	<i>min</i> ( $10^{-6}$ )
Full-wave	$\lambda_1$	–	40.40
	$\lambda_2$	–	45.29
Quasi-TEM	$\lambda_1$	–	44.19
	$\lambda_2$	–	7.36
Image	$\lambda_1$	32.86	-29.07
	$\lambda_2$	33.76	-29.02

These results indicate that, besides the well-known limitations of the image approximation, it also has a maximum frequency limit to hold. To investigate which aspect of the approximation has a more profound effect on the passivity violations we carried out a small sensitivity analysis. First, we increased the line height  $h$ , then its radius  $r$  and finally we changed the line length  $\ell$ . Tables 3.2, 3.3 and 3.4 summarize these findings.

As expected, the increase in line height  $h$  increases the magnitude of the passivity violations, as the assumption  $\ell \gg h$  gets weaker. For the cases in Table 3.2, the frequency at which the most severe passivity violation occurs is inversely proportional to the value



(a) Module

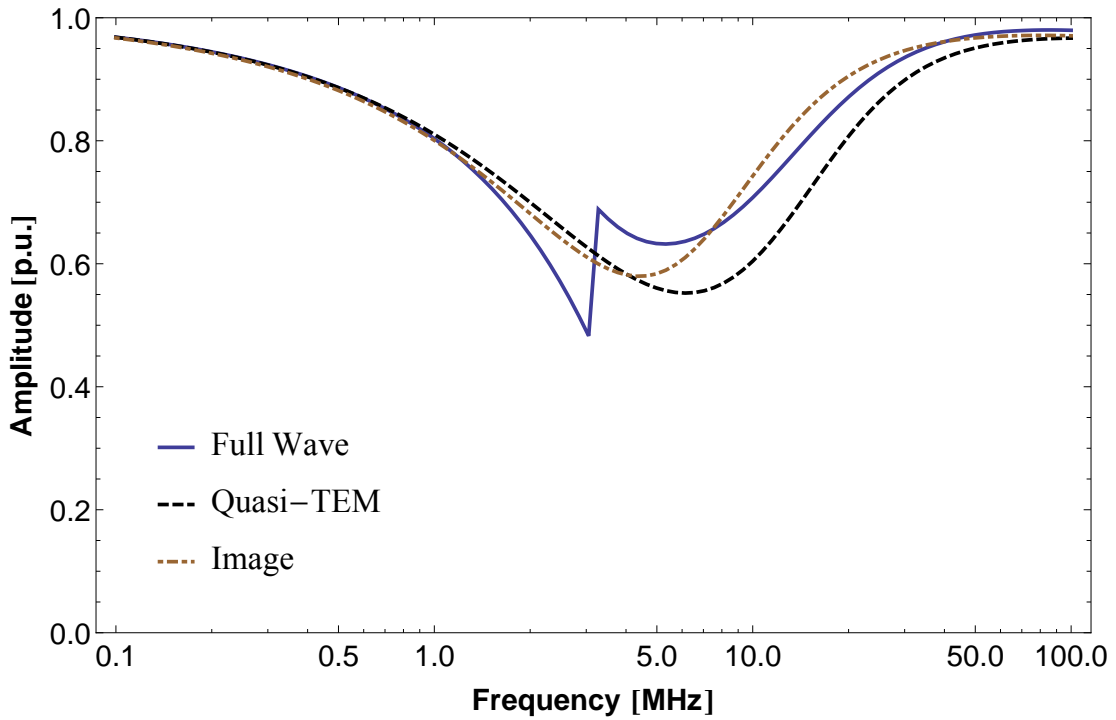


(b) Phase

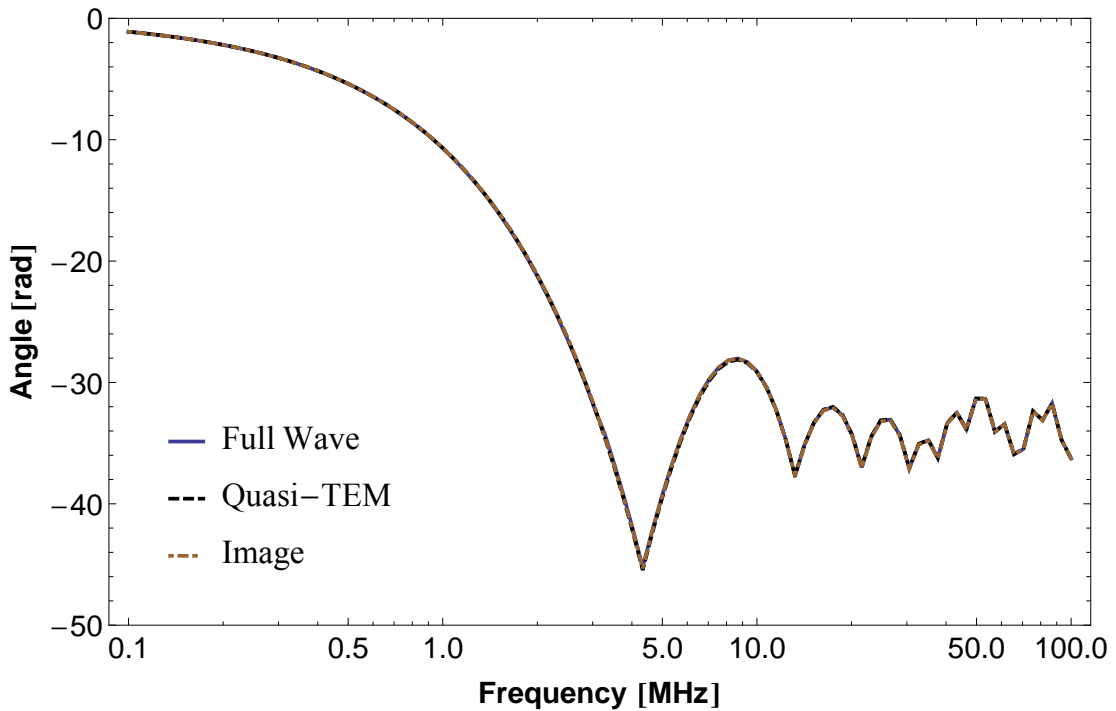
**Figure 3.5:** Behavior of  $Y_c$  for the three distinct approaches.

of  $h$ . Considering the range of conductor radius  $r$  in Table 3.3, we can see that it has very little effect in the passivity violations.

The most interesting finding is the influence of the line length  $\ell$  in passivity violations



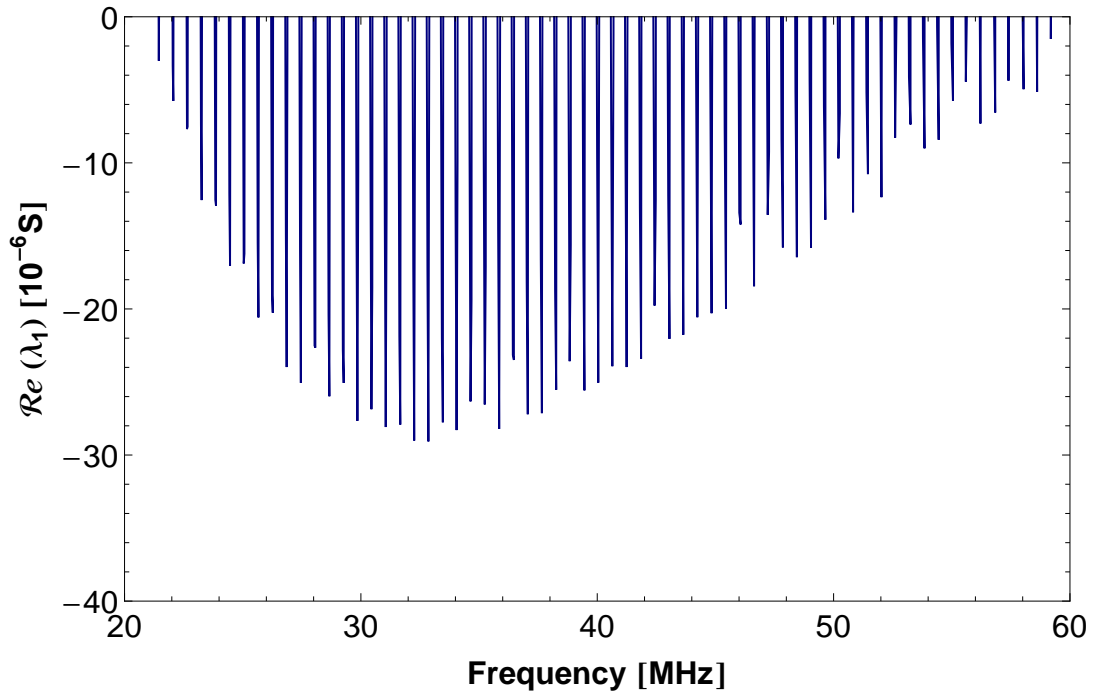
(a) Module



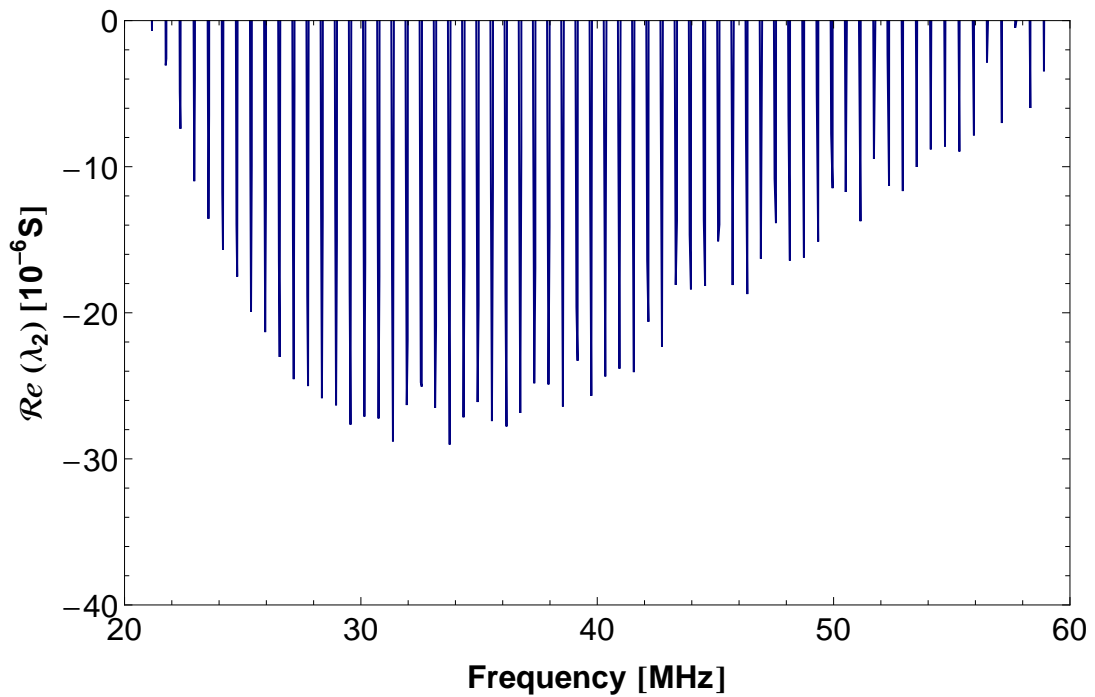
(b) Phase

**Figure 3.6:** Behavior of  $H$  for the three distinct approaches.

as shown in Table 3.4. For longer lines the passivity violations can be eliminated. This result indicates that the main cause of the passivity violations occurs in  $H$  as shorter lines will present higher oscillatory behavior. This behavior seems to stand to reason as shorter



(a)  $\lambda_1$



(b)  $\lambda_2$

**Figure 3.7:** Passivity violations in  $\lambda_1$  and  $\lambda_2$ .

lines are far from the infinite length in which the line parameters are defined.

The approximate expressions used here are based on a voltage-current relationship, thus the integration path is required. Another approach to the definition of approximate expressions, for instance based on a power-current formulation [85–87] might lead to other results regarding passivity violations. This topic is left for future research.

**Table 3.2:** Passivity violations as a function of  $h$ .

$h$ (m)	$eig$	$\Omega$ (MHz)	$min$ ( $10^{-6}$ )
20	$\lambda_1$	10.12	-234.80
	$\lambda_2$	10.50	-232.20
50	$\lambda_1$	4.17	-884.58
	$\lambda_2$	4.47	-901.49
100	$\lambda_1$	2.38	-1814.98
	$\lambda_2$	2.68	-1905.73

**Table 3.3:** Passivity violations as a function of  $r$ .

$r$ (cm)	$eig$	$\Omega$ (MHz)	$min$ ( $10^{-6}$ )
5	$\lambda_1$	33.84	-39.30
	$\lambda_2$	33.75	-39.20
10	$\lambda_1$	35.85	-43.74
	$\lambda_2$	38.55	-43.02

**Table 3.4:** Passivity violations as a function of  $\ell$ .

$\ell$ (m)	$eig$	$\Omega$ (MHz)	$min$ ( $10^{-6}$ )
50	$\lambda_1$	17.88	-1235.43
	$\lambda_2$	14.76	-1211.73
100	$\lambda_1$	17.80	-594.16
	$\lambda_2$	16.29	-590.82
1000	$\lambda_1$	–	58.74
	$\lambda_2$	–	58.65

### 3.5 Time and Frequency Domains Evaluation

At first it may seem that these rather small passivity violations in the high frequency range might not significantly affect time-domain simulations. To investigate their impact we consider the single-phase line presented in Section 3.2 excited by a slightly perturbed impulse voltage connected at the sending end of the single-phase line as depicted in Fig. 3.8. The input voltage  $v_{in}(t)$  is given by

$$v_{in}(t) = \exp(-10^{-6}t) - \exp(-10^{-7}t) + u_p(t) \quad (3.32)$$

where  $u_p(t) = 0.01 \cos(2\pi \cdot 33 \cdot 10^6 t)$  is a small harmonic perturbation chosen to study the effect of exciting the frequencies around these passivity violations.

To obtain the time-domain responses, we can use the Numerical Laplace Transform (NLT) [88–90]. We considered a total simulation time of  $40 \mu s$ . To ensure that the high frequency range where the passivity violations occur is correctly simulated, 16384 frequency samples were used. The large number of complex-valued frequency samples restricted an efficient simulation of the full-wave model. However, as both the full-wave



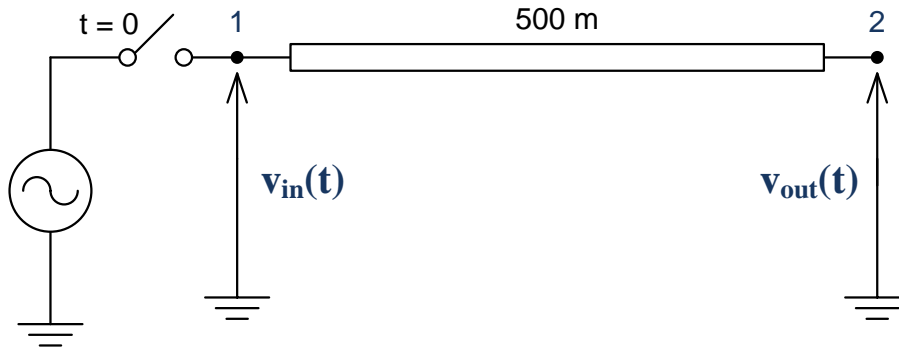


**Figure 3.8:** Single-phase circuit for time-domain test.

and the quasi-TEM approximations did not present any passivity violations, we can use the latter as a reference of suitable responses.

Fig. 3.9 depicts the output voltage  $v_{out}(t)$  considering the quasi-TEM formulation and the error of the image approximations solved using the NLT. There is an increasing error in the response of the image method due to the excitation of some of the passivity violations.

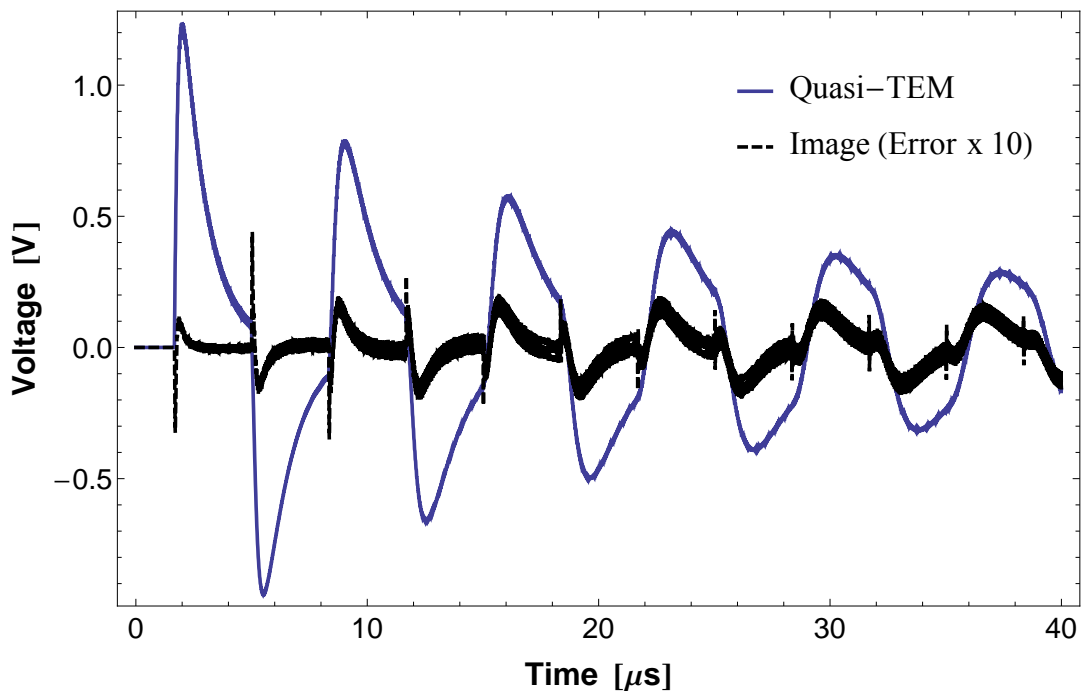


**Figure 3.9:** Impulse voltage response using NLT.

Purposely, another possibility is to use the Method of Characteristics (MoC). For efficient time domain simulation it is typical to represent both  $Y_c$  and  $H$  by rational functions, thus demanding a frequency domain fitting. This procedure allows for an efficient recur-

sive formulation of the convolutions [5, 23]. Therefore,  $Y_c$  is given by

$$Y_c \cong \sum_{n=1}^N \frac{r_n}{s - a_n} \quad (3.33)$$

where  $N$  is the fitting order,  $r_n$  are the residues and  $a_n$  are the poles of the rational approximation. Both can be real or come in complex conjugate pairs. Fig. 3.10 shows the absolute value of the fitting error for  $Y_c$  considering the full-wave model, quasi-TEM formulation and image approximations. While the latter two were accurately fitted using only 6 poles, due to the discontinuity the full-wave  $Y_c$  demanded a higher order fit, using 12 poles to achieve comparable accuracy.

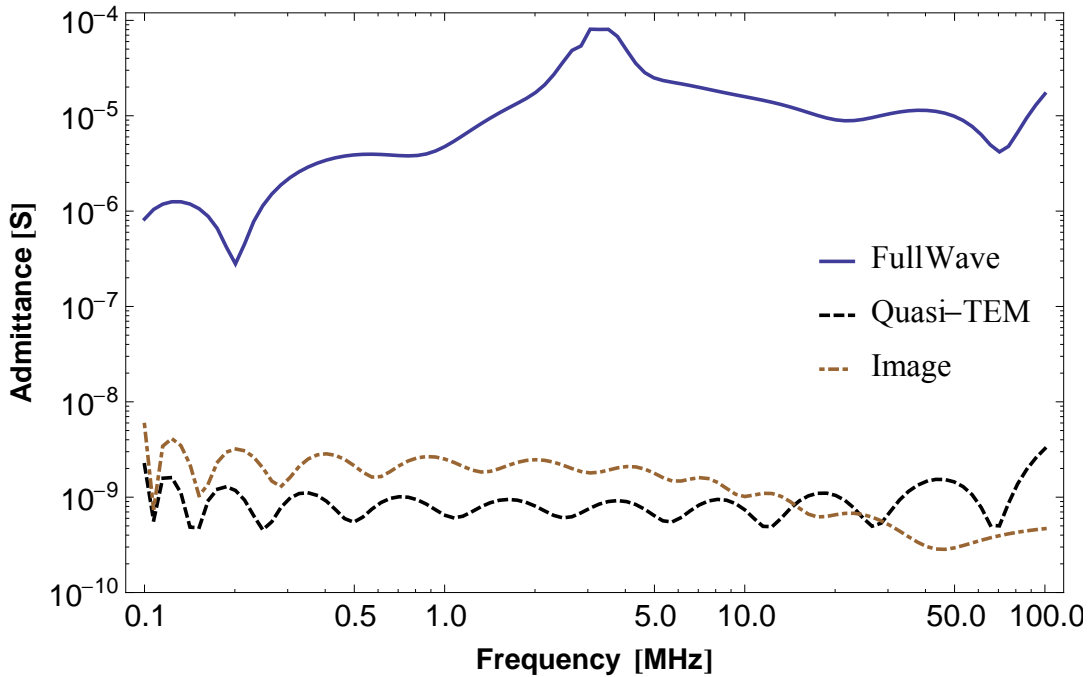


**Figure 3.10:** Fitting error of  $Y_c$  for the three distinct approaches.

To obtain a low order fitting of  $H$  first we need to extract its time-delay  $\tau$  so a minimum phase-shift function is obtained. Time-delay extraction was carried out as in [67]. Therefore, the approximation of  $H$  in the frequency domain is given by

$$H \cong \sum_{n=1}^N \frac{c_n}{s - p_n} \exp(-s\tau) \quad (3.34)$$

where  $c_n$  are the residues and  $p_n$  are the poles of the rational approximation. Both can be real or come in complex conjugate pairs. Fig. 3.11 shows the absolute value of the fitting error for  $H$ . Unlike the quasi-TEM formulation and image approximations, where a low order fit was possible using only 6 poles, the discontinuity in the full-wave model of  $H$  demanded a high order fit using 50 poles.

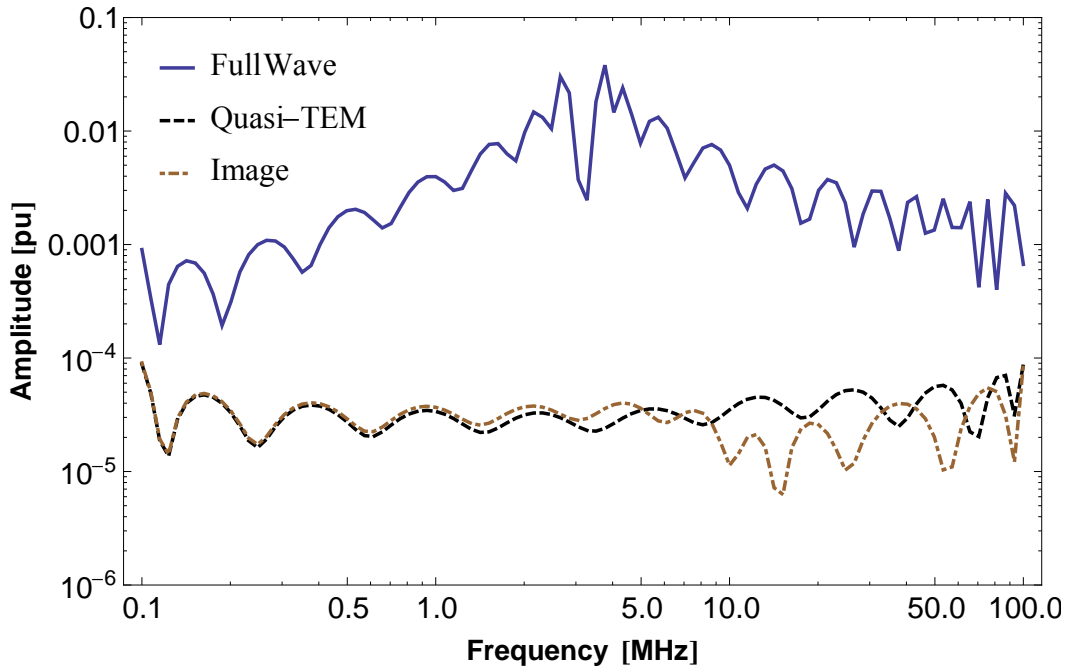


**Figure 3.11:** Fitting error of  $H$  for the three distinct approaches.

The magnitude of the passivity violations in  $\lambda_1$  and  $\lambda_2$  for the nodal admittance matrix calculated from the fit of  $Y_c$  and  $H$  in the method of images was very similar to the ones shown in Fig. 3.7 with negligible differences.

Fig. 3.12 depicts the output voltage  $v_{out}(t)$  considering the quasi-TEM formulation and the error of the image approximations using the MoC. There is a small but increasing time domain error in the response of the image method as in the case using the NLT.

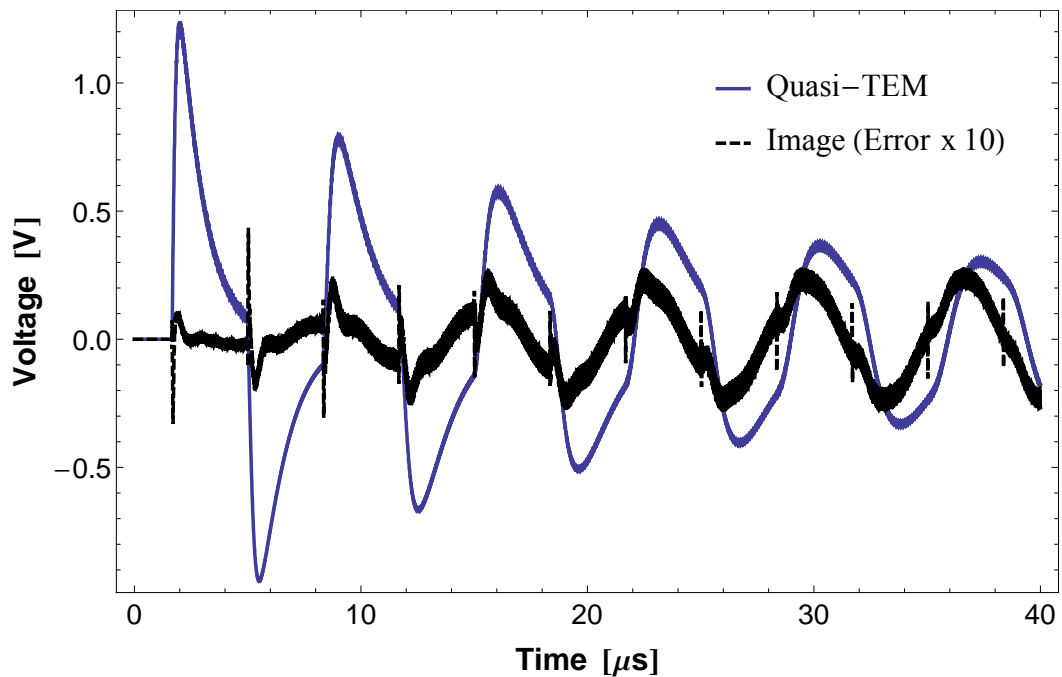


**Figure 3.12:** Impulse voltage response using MoC.

### 3.6 Causes of the Passivity violations

For a better understanding of the causes of the passivity violations, a numerical stability assessment for the single-phase line configuration presented in Section 3.2 is made here.

As  $\lambda_1$  and  $\lambda_2$  are intrinsic functions of the single-phase line parameters, both depend either of the infinite integrals terms  $S_1$ ,  $S_2$  and  $T$ , which are the single-phase counterparts of  $\mathbf{S}_1$ ,  $\mathbf{S}_2$  and  $\mathbf{T}$  depicted in (3.21) or of the closed-form image approximations  $\bar{S}_1$ ,  $\bar{S}_2$  and  $\bar{T}$ , which are the single-phase counterparts of  $\bar{\mathbf{S}}_1$ ,  $\bar{\mathbf{S}}_2$  and  $\bar{\mathbf{T}}$  presented in (3.23).

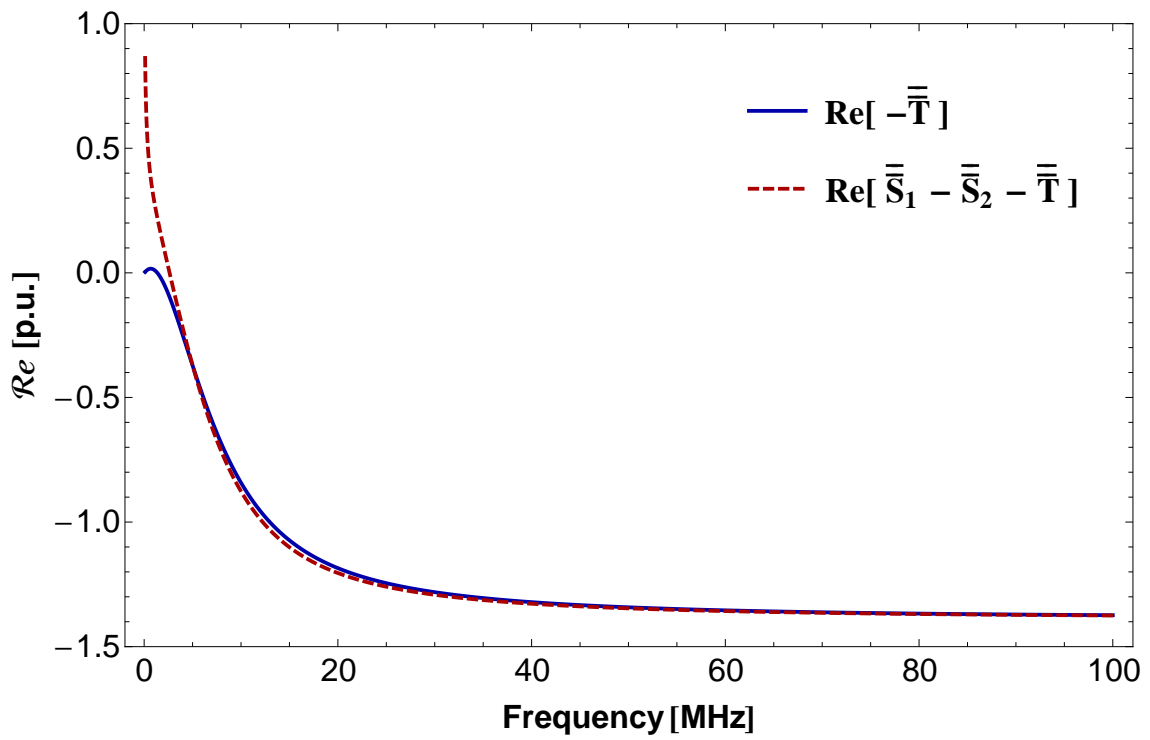
By inspection of the line parameters formulae, we can see that the shunt admittance is a function of the infinite integral  $\bar{T}$ . For a sensitivity assessment of the infinite integrals in the series impedance, we must analyze the effect of  $\bar{S}_1$ ,  $\bar{S}_2$  and  $\bar{T}$  in the frequency domain.

Fig. 3.13 shows the frequency spectrum for the variable part of  $Z$  and for the negative of  $\bar{T}$ . For frequencies over 20 MHz,  $\bar{T}$  becomes dominant with respect to  $\bar{S}_1$  and  $\bar{S}_2$ , as both the latter tend to mutually cancel in  $Z$ . Clearly, both the series impedance and the shunt admittance in the high frequency range become primarily functions of  $\bar{T}$ , and the error in the eigenvalues  $\lambda_1$  and  $\lambda_2$  tend to mainly depend on the error in the approximated closed-form expression  $\bar{T}$ .

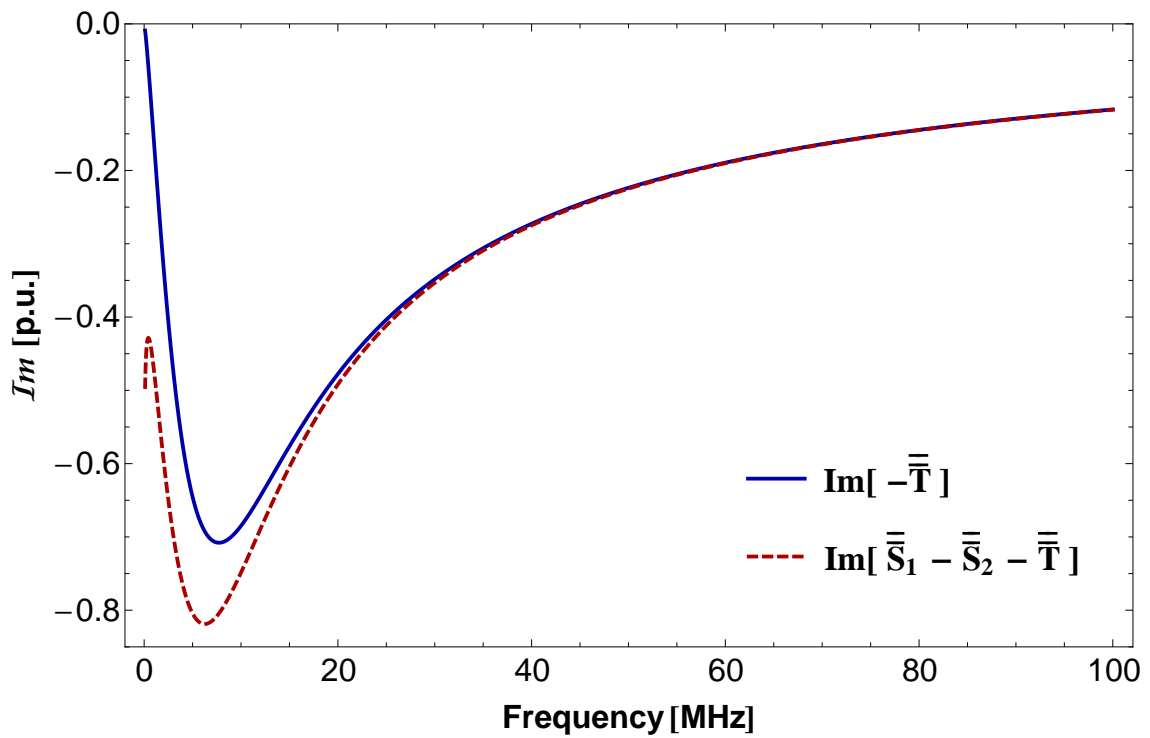
The absolute value of the mismatch found between the quasi-TEM infinite integrals and the closed-form image approximations is compared in Fig. 3.14.

Deviations in  $\bar{S}_1$  and  $\bar{S}_2$  from their infinite integral counterparts are negligible in the high frequency range. However, deviations in  $\bar{T}$  are larger and distributed throughout the entire frequency bandwidth, dominating the total error in both impedance and admittance.

These deviations are rather small when compared to the dominant magnitude of  $\bar{P}$  in the line parameters  $Z$  and  $Y$ , as they do not cause  $Y_c$  to have a negative real part. Nonetheless, they create small deviations in both  $H$  and  $Y_c$ , thus producing passivity violations in the resulting nodal admittance matrix.



(a) Real Part



(b) Imaginary Part

**Figure 3.13:** Sensitivity assessment of variables in  $Z$  and  $Y$ .

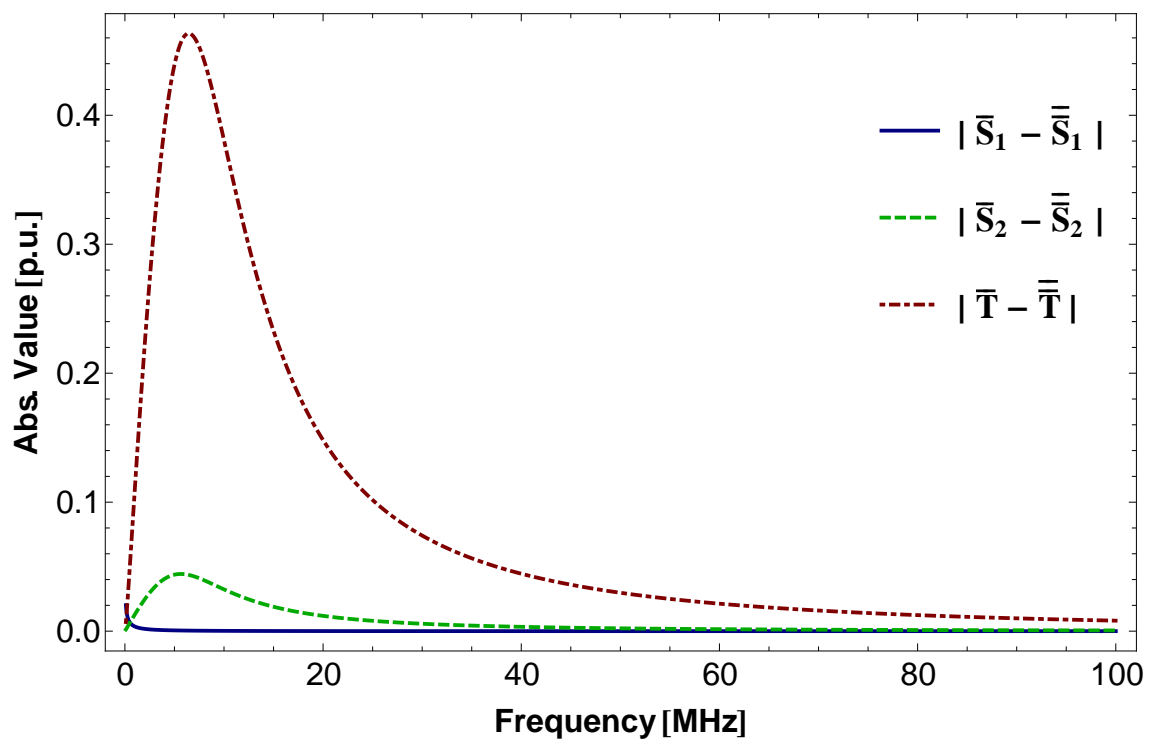


**Figure 3.14:** Deviation of quasi-TEM vs Image approximations.

### 3.7 Conclusions

In this chapter, we investigated the effect of including the displacement currents in the calculation of the line parameters for a single-phase conductor line model when a lossy ground is considered in a wide frequency range using a full-wave approach, a quasi-TEM formulation and image approximations.

We found that even though the increasing processing speed of computers facilitates the root finding scheme of the unknown propagation constant of the circuit, the implementation of a complete and efficient full-wave model for an single-phase line in frequency and time domain remains an issue. The large number of complex-valued frequency samples required for the transient simulation restricts the use of the Numerical Laplace Transform. A fitting of the line parameters with a high order rational function and some problems with the time-delay identification are originated by a discontinuity present in the solution roots of the unknown propagation function, which turns inefficient the use of the Method of Characteristics. Furthermore, for the full wave model, providing a suitable change in the initial guess in the root finding scheme, it is possible to improve the computational burden in the calculation of the unknown propagation constant. Also, a comparison of full-wave models not previously reported in the technical literature has also been made and represents a minor contribution of this work. It is important to point out that during the iterative calculation of the propagation constant, it is not yet possible to distinguish between the two possible roots until a large deviation between them occur.

As both the full-wave model and the quasi-TEM formulation did not present any passivity violations, we conclude that the stability problems with the Image approximations method are related to the simplificative hypotheses used to derive these formulae. Also, we can use the quasi-TEM formulation as a more precise reference model to avoid frequency domain passivity violations and to obtain stable and suitable time-domain responses. Also, both the quasi-TEM and Image approximations approaches gave an smooth fitting of the line parameters with low order rational functions. However, it was found that besides the well-known limitation of the method of images related to conductor height/radius ratio there is also an upper frequency limit as passivity violations were found. Although these are rather small, they cause a loss of accuracy in the time domain responses and might affect the accuracy of the results. As longer lines did not present any passivity violations, we found that the magnitude of these violations is related to the line length as the image approximation can lead to a stable model in a frequency range up to 100 MHz if the line length is increased.

Finally, we found that the inclusion of the ground displacement currents in the line model for a more sound representation of the soil model effectively affects the value of the line parameters. As this is a possible cause of the issues reported in the rational fitting of the Idempotent matrices presented in the previous chapter, further studies of the

inclusion of the ground displacement currents in a multi-phase overhead line system are conducted in the following chapters to evaluate how the aforementioned model limitations might affect more realistic line configurations such as three-phase power lines.

As severe limitations were found in the implementation of a single-phase full-wave line model, a multi-phase full-wave model is presently excluded as a viable option for time-domain simulations. Therefore, in the next chapter, further analysis of the accuracy in the calculation of line parameters will only involve the quasi-TEM formulation and image approximations.



# Chapter 4

## Numerical Issues in Multi-Phase Line Models

In the previous chapter, the use of closed form logarithmic image approximations for the evaluation of the per-unit-length line parameters of a single-phase transmission line model presented a frequency limit in terms of stability under a soil with constant ground parameters, as they may present passivity violations in the high frequency range when ground displacement currents are included.

In this chapter, the improvement of this frequency limit by the use of a soil model including a more physically consistent frequency dependence in the evaluation of the per-unit-length parameters of a multi-phase line is investigated.

We found that this frequency limit persists in spite of using a more sound soil model. Although time-domain simulations based on the Numerical Laplace Transform were stable, the use of the Method of Characteristics rendered unstable voltage responses in both soils models with constant and frequency dependent parameters.

The rational fitting of the propagation function and characteristic admittance is studied, along with the impact of the inclusion of frequency dependent ground parameters in the mitigation of the passivity violations of the Nodal admittance matrix in the frequency domain.

Comparative results of time domain simulations are presented for both perturbed and unperturbed voltage sources with constant and frequency dependent soil models.

The chapter is organized as follows: Section 4.1 presents a brief introduction to this chapter. Section 4.2 presents the basic formulations related to the definition of per-unit-length series impedance and shunt admittance matrices. Section 4.3 covers the mathematical formulation involving the modelling of frequency dependent soil models. Section 4.4 shows the numerical stability criteria used for the analysis of the nodal admittance matrix. Section 4.5 presents three multiphase overhead line test cases, along with results on the characteristic admittance, propagation function and passivity violations that arise in the modeling. Time-domain evaluation of the line performance is presented in Section 4.6.

An overview of possible mitigation techniques is treated in Section 4.7. An assessment of the Idempotent Decomposition improvement by the use of a quasi-TEM formulation is made in Section 4.8. Finally, a discussion of this chapter is presented in Section 4.9.

For the remainder of this chapter, whenever we mention impedance it is to be understood as impedance per unit of length, the same holds for the admittance.

## 4.1 Introduction

Over the last 50 years, there has been a considerable evolution in modeling the frequency dependence of overhead transmission lines and soil parameters of lossy grounds.

The frequency dependence in a wide frequency band of the ground and conductors can nowadays be more easily dealt with using computer-based transient analysis techniques. However, the calculation of the per-unit-length line parameters including both the ground displacement currents and the lossy nature of the soil parameters are still commonly neglected in power system analysis, originating inaccuracies in the time-domain simulation of high frequency excitations as lightning strokes.

The expressions for the per-unit-length impedance and admittance matrices associated to a general lossy soil model were independently developed by Pettersson [75] and by D'Amore [54], and are based in the works of Kikuchi [72] and Wait [73] respectively. Both works include a quasi-transverse electromagnetic formulation (quasi-TEM), which requires the time consuming numerical solution of highly oscillatory infinite integrals, and a set of closed-form logarithmic image approximations which involve a lesser computational burden.

Although some of these expressions have been proposed almost two decades ago, there has not been an assessment of neither the impact nor the stability of these approximate expressions in time-domain modeling.

Furthermore, although the study of frequency dependent soil models can be traced back to eight decades ago, with research on the soil behavior in frequencies from 100 Hz up to 200 MHz and beyond, little research has been done on its use for the evaluation of fast transients [38, 57].

## 4.2 Formulation of the Line Parameters

For typical power system analysis, the soil is assumed to be a good conductor and the expressions of the line parameters are well known, as they can be obtained considering the scalar electric potential identical to the line voltage.

To define the associated expressions under a general lossy ground, i.e., considering displacement currents for the wideband evaluation of impedance and admittance matri-

ces, a model which accounts for the variation of the propagation constant of the circuit in the high frequency range is required. As seen in the last chapter, the time-domain solution of a full-wave multiphase line model using either the Numerical Laplace Transform (NLT) or the Method of Characteristics (MoC) remains an issue which is beyond the scope of the present research. Therefore, we will use the quasi-TEM formulation and image approximations derived for a general voltage formulation as presented in [75]. Both simplified approaches sufficiently account for the variations of the propagation constant in the high frequency range.

Consider a system of  $n$  infinitely long conductors with radius  $r$  at a constant height  $h_n$  above a lossy ground as shown in Fig. 4.1. Both air and ground are characterized by a permittivity  $\epsilon_i$ , conductivity  $\sigma_i$  and permeability  $\mu_i$ , where  $i = 1$  for air and  $i = 2$  for the ground, respectively. The propagation constant  $\gamma_i$  of each medium is given by

$$\gamma_i = \sqrt{j\omega\mu_i(\sigma_i + j\omega\epsilon_i)} \quad (4.1)$$

with the real part of the square root defined positive.

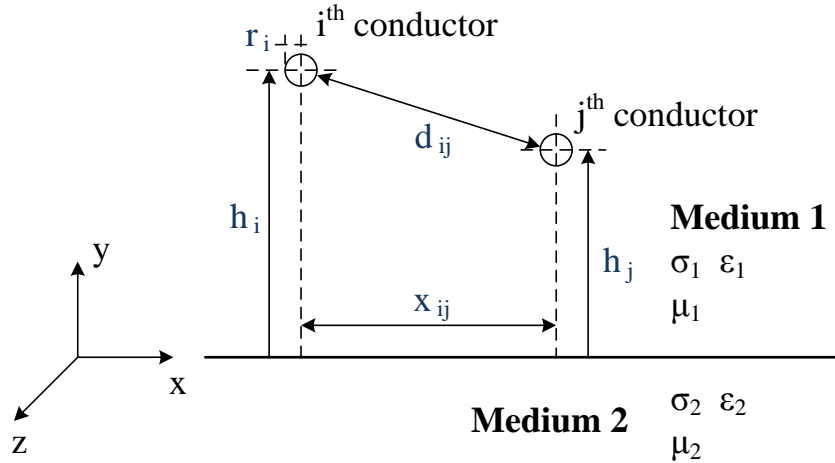


**Figure 4.1:** Multiphase conductor arrangement.

Each conductor has voltage  $U_n$ , electric scalar potential  $\varphi_n(x, y)$  and the magnetic vector potential is  $\mathbf{A}(x, y)$ . In this scenario, the scalar potential difference to ground is given by

$$V_n = \varphi_n(0, h_n - r) - \varphi_n(0, 0) \quad (4.2)$$

Using the wire voltage to ground to define the line parameters, the voltage  $U_n$  is given by

$$U_n = V_n + j\omega \int_0^{h_n - r} A_y(0, \xi) d\xi \quad (4.3)$$

where  $A_y$  is the y-component of  $\mathbf{A}$ .

### 4.2.1 Quasi-TEM Formulation

Considering a thin wire approximation [35, 77], we can derive from (4.3) the line parameters in function of the unknown propagation constant of the circuit  $\gamma$ , which needs to be calculated using iterative methods. An approximate solution requires to use a quasi-TEM approximation  $\gamma = \gamma_1$ . Assuming equal ground and air permeabilities,  $\mu_2 = \mu_1 = \mu_0$ , the per-unit length impedance and admittance matrices are then

$$\begin{aligned}\mathbf{Z} &= \mathbf{Z}_{int} + \frac{j\omega\mu_0}{2\pi} [P + \mathbf{S}_1 - (\mathbf{S}_2 + \mathbf{T})] \\ \mathbf{Y} &= 2\pi (j\omega\epsilon_0) [P - \mathbf{T}]^{-1}\end{aligned}\quad (4.4)$$

where  $\mathbf{Z}_{int}$  is the diagonal matrix with the internal impedance of each conductor. The matrix elements of  $P$  are given by

$$P_{ii} = \ln \frac{2h_i}{r_i} \quad P_{ij} = \ln \frac{D_{ij}}{d_{ij}} \quad (4.5)$$

with  $D_{ij} = \sqrt{\ell_{ij}^2 + x_{ij}^2}$ ,  $d_{ij} = \sqrt{(h_i - h_j)^2 + x_{ij}^2}$ ,  $\ell_{ij} = h_i + h_j$  and  $x_{ij}$  is the horizontal distance between conductors  $i$  and  $j$ . The elements of  $\mathbf{S}_1$ ,  $\mathbf{S}_2$  and  $\mathbf{T}$  are given by

$$\begin{aligned}S_{1ij} &= 2 \int_0^\infty \frac{e^{-\lambda\ell_{ij}}}{\lambda + \bar{u}} \cos(x_{ij}\lambda) d\lambda \\ S_{2ij} &= 2 \int_0^\infty \frac{e^{-\lambda\ell_{ij}}}{n^2\lambda + \bar{u}} \cos(x_{ij}\lambda) d\lambda \\ T_{ij} &= 2 \int_0^\infty \frac{\bar{u}}{\lambda} \left( \frac{e^{-\lambda\ell_{ij}/2} - e^{-\lambda\ell_{ij}}}{n^2\lambda + \bar{u}} \right) \cos(x_{ij}\lambda) d\lambda\end{aligned}\quad (4.6)$$

where  $\bar{u} = \sqrt{\lambda^2 + \gamma_2^2 - \gamma_1^2}$  and  $n = \gamma_2/\gamma_1$  is the refractive index of ground. If the ground is assumed to be a good conductor, i.e.,  $\sigma_2 \gg \omega\epsilon_2$ , it holds that the displacement currents can be neglected by assuming  $\mathbf{S}_2$  and  $\mathbf{T}$  tend to zero in (4.4). The resulting ground impedance is the same proposed by Carson in [31] where only  $\mathbf{S}_1$  is considered.

### 4.2.2 Image Approximation

In this approach, the quasi-TEM formulation can be simplified to allow a closed-form solution of the infinite integrals. The detailed procedure is shown in [75, Sec 3.2] and here we present a brief review. In all the infinite integrals the following approximation is

established

$$\left(a\lambda + \sqrt{\lambda^2 + \eta^2}\right)^{-1} \approx \frac{1}{\lambda} \frac{1}{1+a} \left[1 - \exp\left(-\lambda \frac{1+a}{\eta}\right)\right] \quad (4.7)$$

where  $\eta = \sqrt{\gamma_2^2 - \gamma_1^2}$ . Using this approximation with  $a = 1$  for  $\mathbf{S}_1$  and  $a = n^2$  for  $\mathbf{S}_2$  it is possible to write

$$\begin{aligned} \bar{\mathbf{Z}} &= \mathbf{Z}_{int} + \frac{j\omega\mu_0}{2\pi} [P + \bar{\mathbf{S}}_1 - (\bar{\mathbf{S}}_2 + \bar{\mathbf{T}})] \\ \bar{\mathbf{Y}} &= 2\pi(j\omega\epsilon_0) [P - \bar{\mathbf{T}}]^{-1} \end{aligned} \quad (4.8)$$

The closed-form solutions of the infinite integrals in (4.8) are the logarithmic image approximations, which are given by

$$\begin{aligned} \bar{S}_{1ij} &= \ln\left(1 + \frac{2}{\eta\sqrt{\ell_{ij}^2 + x_{ij}^2}}\right) \\ \bar{S}_{2ij} &= \frac{2}{n^2 + 1} \ln\left(1 + \frac{n^2 + 1}{\eta\sqrt{\ell_{ij}^2 + x_{ij}^2}}\right) \\ \bar{T}_{ij} &= 2\ln 2 + \frac{2n^2}{n^2 + 1} \ln\left(\frac{1 + \frac{n^2 + 1}{\eta\sqrt{\ell_{ij}^2 + x_{ij}^2}}}{1 + 2\frac{n^2 + 1}{\eta\sqrt{\ell_{ij}^2 + x_{ij}^2}}}\right) \end{aligned} \quad (4.9)$$

The expression for  $\bar{\mathbf{T}}$  presented here is slightly different from the one reported in [75], see Section 3.3 for details.

### 4.3 Inclusion of frequency dependent soil models

In this analysis, we consider three frequency dependent soil models chosen for their different obtention methods and validity ranges. Table 4.1 briefly presents their characteristics.

First, we evaluate the Portela soil model [91] expressed by

$$\sigma_2(\omega) \pm j\omega\epsilon_2(\omega) = \sigma_{100\text{ Hz}} + \Delta_i \left[\cot\left(\frac{\pi}{2}\alpha\right) \pm j\right] \left(\frac{\omega}{2\pi \cdot 10^6}\right)^\alpha \quad (4.10)$$

where  $\sigma_{100\text{ Hz}}$  is the soil conductivity measured at 100 Hz,  $\alpha = 0.706$  and  $\Delta_i = 11.71$  mS/m.

Next, we consider the Visacro-Alipio soil model [41], where the expressions for  $\sigma_2$

**Table 4.1:** Frequency dependent soil model characteristics.

Frequency dependent soil models	Frequency range model validity	Model obtention
Portela [91]	40 Hz - 2 MHz	Laboratory measurements
Visacro-Alipio [41]	100 Hz - 4 MHz	Field measurements
Smith-Longmire [92]	100 Hz - 200 MHz	Scott and Wilkenfeld's data

and  $\varepsilon_2$  are given by

$$\begin{aligned}\sigma_2(\omega) &= \sigma_{100\text{ Hz}} \left[ 1 + \frac{1.2 \cdot 10^{-6}}{\sigma_{100\text{ Hz}}^{0.73}} \left( \frac{\omega}{2\pi} - 100 \right)^{0.65} \right] \quad f \geq 100\text{ Hz} \\ \varepsilon_2(\omega) &= \varepsilon_0 \left[ 7.6 \cdot 10^3 \left( \frac{\omega}{2\pi} \right)^{-0.4} + 1.3 \right] \quad f \geq 10\text{ kHz}\end{aligned}\tag{4.11}$$

The value given by (4.11) at 10 kHz can be used to represent  $\varepsilon_2$  at frequencies below 10 kHz.

Finally, for the Smith-Longmire soil model [92] we have

$$\begin{aligned}\sigma_2(\omega) &= \sigma_{\text{DC}} + 2\pi\varepsilon_0 \sum_{i=1}^{13} a_i F_i \frac{\left(\frac{\omega}{F_i}\right)^2}{4\pi^2 + \left(\frac{\omega}{F_i}\right)^2} \\ \varepsilon_2(\omega) &= \varepsilon_0 \times \left[ 5 + \sum_{i=1}^{13} \frac{a_i}{1 + \left(\frac{\omega}{2\pi F_i}\right)^2} \right]\end{aligned}\tag{4.12}$$

with  $\sigma_{\text{DC}}$  as the DC soil conductivity,  $F_i = (125\sigma_{\text{DC}})^{0.8312} \times 10^{i-1}$  and the coefficients  $a_i$  are given in Table 4.2.

**Table 4.2:** Coefficients  $a_i$  for the Smith-Longmire soil model.

$i$	$a_i$	$i$	$a_i$	$i$	$a_i$
1	$3.40 \cdot 10^6$	6	$1.33 \cdot 10^2$	11	$9.80 \cdot 10^{-1}$
2	$2.74 \cdot 10^5$	7	$2.72 \cdot 10^1$	12	$3.92 \cdot 10^{-1}$
3	$2.58 \cdot 10^4$	8	$1.25 \cdot 10^1$	13	$1.73 \cdot 10^{-1}$
4	$3.38 \cdot 10^3$	9	$4.80 \cdot 10^0$		
5	$5.26 \cdot 10^2$	10	$2.17 \cdot 10^0$		

For a comprehensive work regarding frequency dependent soil models in grounding systems, the reader can refer to [57].

## 4.4 Numerical stability of a multiphase line model

Typically, the numerical stability of a multiphase transmission line model is verified using only the characteristic impedance  $\mathbf{Z}_c$ , i.e., a line model is assumed stable as long as  $\mathbf{Z}_c$  has a positive real part. However, this consideration alone might be insufficient to guarantee a passive line model throughout the whole frequency range.

A transmission line model can be represented in the frequency domain by its nodal admittance matrix given by

$$\mathbf{Y}_n = \begin{bmatrix} \mathbf{A} & \mathbf{B} \\ \mathbf{B} & \mathbf{A} \end{bmatrix} \quad (4.13)$$

To analyze the stability of the line model, a simple yet efficient procedure is to verify whether the model absorbs power by corroborating that  $\mathbf{Y}_H$  in (4.14) has the real part of all its eigenvalues positive. This means we must establish if  $\mathbf{Y}_n$  is positive definite, i.e.

$$\text{eig}(\mathbf{Y}_H) = \text{eig}[(\mathbf{Y}_n + \mathbf{Y}_n^H)/2] \geq 0 \quad \forall(j\omega) \quad (4.14)$$

where  $\mathbf{Y}_n^H$  is the conjugate transpose of  $\mathbf{Y}_n$ .

In a multiphase transmission line, the elements of  $\mathbf{Y}_n$  in (4.13) are given by

$$\begin{aligned} \mathbf{A} &= \mathbf{Y}_c (\mathbf{I}_n + \mathbf{H}^2) (\mathbf{I}_n - \mathbf{H}^2)^{-1} \\ \mathbf{B} &= -2\mathbf{Y}_c \mathbf{H} (\mathbf{I}_n + \mathbf{H}^2)^{-1} \end{aligned} \quad (4.15)$$

where  $\mathbf{I}_n$  is the  $n \times n$  identity matrix,  $\mathbf{Y}_c = \mathbf{Z}^{-1} \sqrt{\mathbf{Z}\bar{\mathbf{Y}}}$  is the characteristic admittance and  $\mathbf{H} = \exp(-\ell \sqrt{\mathbf{Z}\bar{\mathbf{Y}}})$  the propagation function for a line length  $\ell$ . Due to the lower computational burden associated with the image approximations of the infinite integrals involved, it is custom to reformulate these expressions using the per-unit-length line parameters  $\bar{\mathbf{Z}}$  and  $\bar{\mathbf{Y}}$  given in (4.8).

For a comparison of the magnitude of the passivity violations calculated using the rational fitting of  $\mathbf{Y}_c$  and  $\mathbf{H}$  with the original data calculated from the use of the closed-form image approximations, rational approximations of both  $\mathbf{Y}_c$  and  $\mathbf{H}$  are needed. Here, we use the pole relocation method known as Vector Fitting for the frequency-domain rational approximation [24, 26, 58]. Therefore,  $\mathbf{Y}_c$  is given by

$$\mathbf{Y}_c \cong \sum_{n=1}^N \frac{\mathbf{R}_n}{s - a_n} \quad (4.16)$$

where  $\mathbf{R}_n$  are the matrices of residues and  $a_n$  are the poles of the rational approximation. Both can be real or come in complex conjugate pairs. To obtain a low order rational fitting of  $\mathbf{H}$ , each modal time-delay  $\tau_i$  must first be extracted so a minimum phase-shift function

is obtained for each mode as shown in Section 2.4. Each mode  $h_i$  is approximated in the frequency domain by

$$h_i \cong \sum_{n=1}^{N_i} \frac{c_{i,n}}{s - p_{i,n}} \exp(-s\tau_i) \quad (4.17)$$

where  $c_{i,n}$  are the residues and  $p_{i,n}$  are the poles. Both can be real or come in complex conjugate pairs. Modes with similar time-delays are lumped together. The rational approximation of  $\mathbf{H}$  is given by a linear combination of poles, residues and time delays as

$$\mathbf{H} = \exp(-\ell\sqrt{\mathbf{Y}\mathbf{Z}}) \cong \sum_{i=1}^G \left( \sum_{n=1}^{N_i} \frac{\mathbf{C}_{i,n}}{s - p_{i,n}} \right) \exp(-s\tau_i) \quad (4.18)$$

where  $\mathbf{C}_{i,n}$  are the matrices of residues, whose elements can be real or come in complex conjugate pairs and  $G$  is the number of lumped modes.

## 4.5 Test Cases

For the evaluation of the impact of the image approximations on the numerical stability of the line model, we consider 3 test case circuits of three-phase lines with two ground wires as shown in Fig. 4.2: a vertical 138 kV line, a horizontal 230 kV line and a compact 500 kV line.

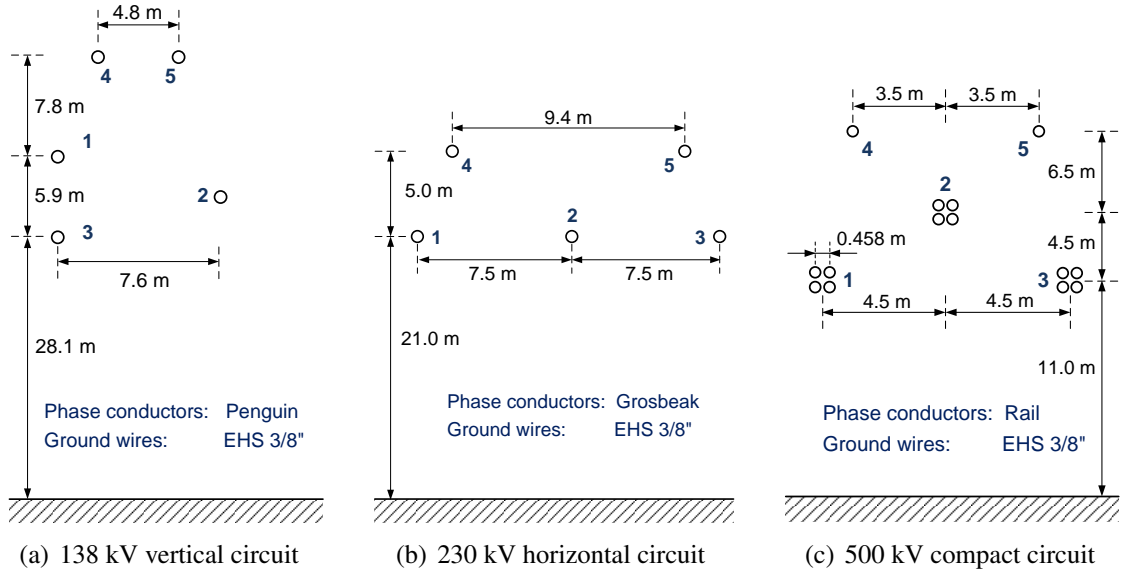


**Figure 4.2:** Test cases configurations.

The per-unit-length line parameters were calculated considering 1500 log-spaced samples in the frequency loop from 0.01 Hz to 100 MHz. To avoid artificial eigenvalues



switchover, a switch-back procedure as described in [93] was implemented. A 2.4 GHz Core i7-4700MQ computer with 12 GB of RAM was used for the calculations.

First, we evaluate the eigenvalues  $\lambda$  of the nodal admittance matrix using the per-unit-length line parameters defined in (4.4) for the quasi-TEM formulation. Numerical integration problems evaluating the infinite integrals were prevented using the Gauss-Kronrod quadrature scheme as in [38, 94].

To evaluate the eigenvalues  $\lambda$  of the nodal admittance matrix using the closed-form logarithmic image approximations, we use the expressions given for the line parameters in (4.8). Table 4.3 presents the processing times employed by both the quasi-TEM formulation and the image approximations for line lengths of 300 m and 1000 m.

**Table 4.3:** Computational processing times of quasi-TEM and image approximations.

Line Model	Length (m)	Test Circuit (kV)		
		138	230	500
Images	300	15.31	15.42	29.89
	1000	15.39	15.44	30.19
quasi-TEM	300	451.32	645.87	3608.23
	1000	459.65	665.47	4940.22

As expected, the calculation of the highly oscillatory infinite integrals took significantly greater processing times than the simplified image approximations. No significant variations in the processing times were obtained by using soils either with constant or frequency dependent ground parameters. As in the single-phase case presented in Chapter 3, no passivity violations were found for both soil models with constant and frequency dependent parameters, independently of the line length considered.

The findings regarding the passivity violations for the test case configurations using constant and frequency dependent soil models with different parameters are summarized next.

#### 4.5.1 Constant ground parameters soil models

Table 4.4 shows the passivity violations for the three test case configurations evaluated using a constant ground parameters soil model with a line length of  $\ell = 300$  m, chosen for being a typical value for extra high voltage circuits, where  $\epsilon_r$  is the relative permittivity of the soil,  $\sigma_s$  is the ground conductivity,  $\Omega$  stands for the frequency value at which the largest passivity violation arises, and  $\min$  stands for the minima of  $\Re(\lambda(\Omega))$ .

For all the scenarios tested, even though a positive definite  $\mathbf{Y}_c$  is calculated throughout the whole frequency band considered, which is an intrinsic numerical stability requirement of the line model, passivity violations arise when image approximations are used along with constant parameter soil models. Furthermore, these results indicate that higher values of  $\sigma_s$  increase the magnitude of the passivity violations, with typical values of  $\Omega$

**Table 4.4:** Frequency of largest passivity violations and minima of  $\lambda$  for  $\ell = 300$  m.

Line circuit		138 kV		230 kV		500 kV	
$\varepsilon_r$ (p.u.)	$\sigma_s$ (S/m)	$\Omega$ (MHz)	$min$ ( $10^{-6}$ )	$\Omega$ (MHz)	$min$ ( $10^{-6}$ )	$\Omega$ (MHz)	$min$ ( $10^{-6}$ )
5	$10^{-4}$	12.40	-347.34	30.88	-358.68	45.90	-246.97
	$10^{-3}$	11.90	-403.16	30.88	-374.31	45.90	-251.52
	0.01	10.41	-1234.92	17.36	-850.03	30.88	-337.50
	0.05	18.95	-2420.25	26.40	-2112.65	29.90	-927.38
10	$10^{-4}$	14.91	-505.26	31.89	-560.98	59.41	-366.775
	$10^{-3}$	13.91	-539.12	31.89	-575.04	59.41	-369.64
	0.01	11.41	-1083.89	22.87	-807.68	47.40	-418.33
	0.05	18.95	-2252.88	27.90	-1928.08	33.40	-855.20
100	$10^{-4}$	32.94	-1062.24	59.41	-1518.76	92.89	-1057.50
	$10^{-3}$	32.94	-1066.52	59.41	-1521.54	92.89	-1058.36
	0.01	32.94	1110.27	59.41	-1549.64	82.40	-1068.15
	0.05	25.45	-1345.73	59.41	-1682.15	82.40	-1116.43

starting around 10 MHz. As for a fixed permittivity, the largest violations  $min$  arise for the maximum conductivity  $\sigma_s$  considered.

As seen in Chapter 3, for a single-phase line under a soil with constant ground parameters, its length  $\ell$  is a key parameter regarding the numerical stability when closed-form image approximations are considered. To evaluate whether passivity violations in three-phase lines also depend of the line length  $\ell$  as occurs in the case of single-phase lines, we calculate the eigenvalues of the 138 kV, 230 kV and 500 kV lines considering a value of  $\sigma_s = 0.05$  and  $\varepsilon_r = 5$  for line lengths of  $\ell = 300$  m and  $\ell = 1$  km. The magnitude of the resulting passivity violations are shown in Fig. 4.3 to Fig. 4.5.

In the three cases, it can be seen that there is a sensible reduction in the magnitude of the passivity violations as the line length  $\ell$  increases. For the 138 kV and the 230 kV lines, as the line length  $\ell$  increases, the frequency band where the passivity violations arise gets narrower. The 500 kV lines presents a slightly different characteristic, as when the line length  $\ell$  increases, the frequency band of the “bell-shaped” distribution of the passivity violations is displaced to the higher frequencies. For the compact 500 kV circuit the line length significantly affects the frequency band where the largest passivity violations occur.

For the geometrical configurations of the three lines considered here, the minimal lengths where no passivity violations arise are 992 m for the 138 kV vertical circuit, 763 m for the 230 kV horizontal circuit and 1083 m for the 500 kV compact circuit.

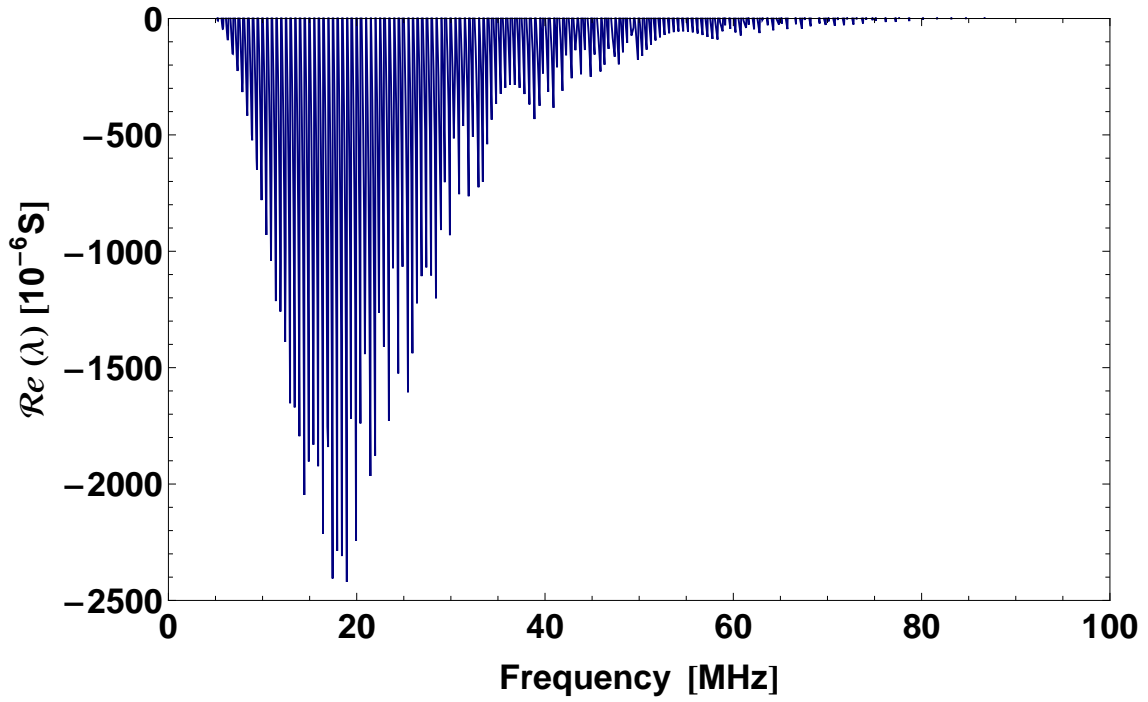
Fig. 4.6 depicts the results of the absolute value of the rational approximations of both  $\mathbf{Y}_c$  and  $\mathbf{H}$  compared together with their respective original frequency domain data for the 138 kV circuit with a line length of  $\ell = 300$  m. A very good agreement is found as a

maximum absolute deviation of  $0.35 \cdot 10^{-3}$  p.u. was obtained for  $\mathbf{H}$  while for  $\mathbf{Y}_c$  it was  $2.4 \cdot 10^{-6}$  S.

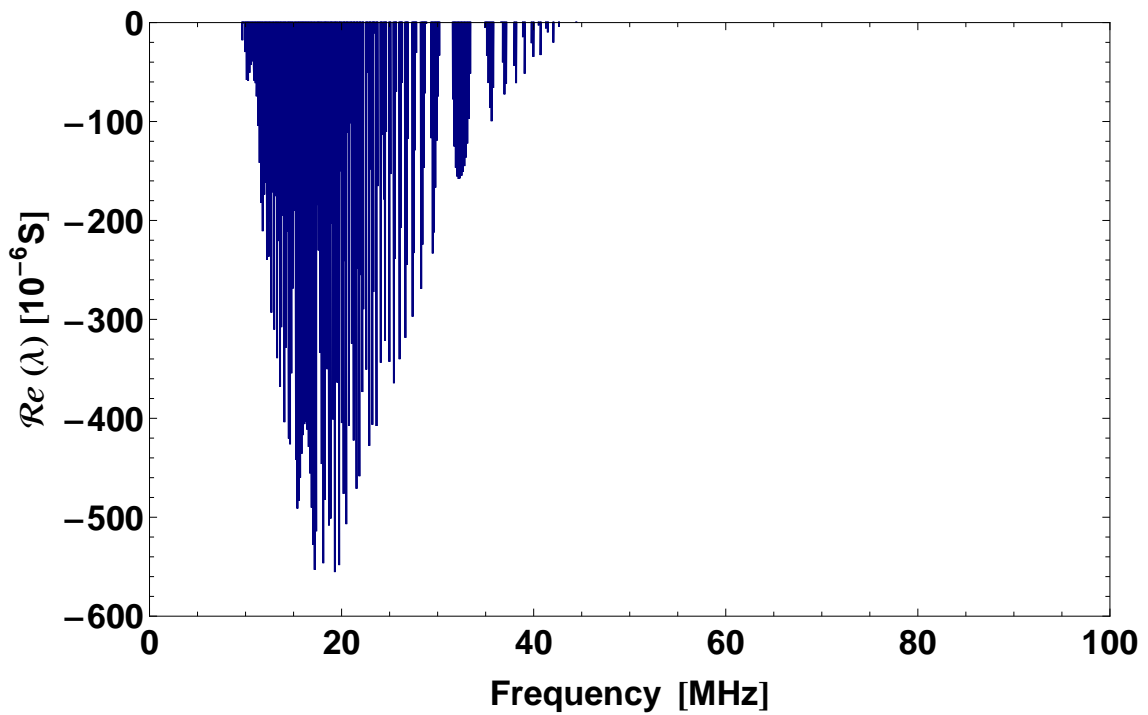
It is necessary to investigate the value of the passivity violations using the rational approximations. The fitted counterparts of  $\mathbf{Y}_c$  and  $\mathbf{H}$  are used in (4.13) and then the eigenvalues  $\lambda$  are determined using (4.14).

Fig. 4.7 shows respectively the absolute value of the fitting error for  $\mathbf{Y}_c$  and of each mode  $h_i$  considering the image approximations for a soil model with constant ground parameters for the 138 kV circuit. For the rational approximation of the characteristic admittance a minimum fit order of 12 poles is obtained. It is also worth mentioning that from the fitting of  $\mathbf{Y}_c$  a positive definite matrix was also calculated for all the frequencies involved. For each mode  $h_i$  of the propagation function, a successful time delay extraction was achieved and a low order fit was possible using only 6 poles per mode.

Fig. 4.8 depicts the behavior of the eigenvalues with the largest passivity violations using both the calculated values of  $\mathbf{Y}_n$  and the rational approximations of  $\mathbf{Y}_c$  and  $\mathbf{H}$  for the 138 kV circuit. As it can be seen, the magnitude of the passivity violations calculated using the original data of  $\mathbf{Y}_n$  and the rational approximations of  $\mathbf{H}$  and  $\mathbf{Y}_c$  with closed-form image approximations match with negligible differences, as the use of the rational approximations did not affect significantly the behavior of the passivity violations. Nonetheless, it is important to point out that errors associated with the rational approximations may normally lead to larger passivity violations.

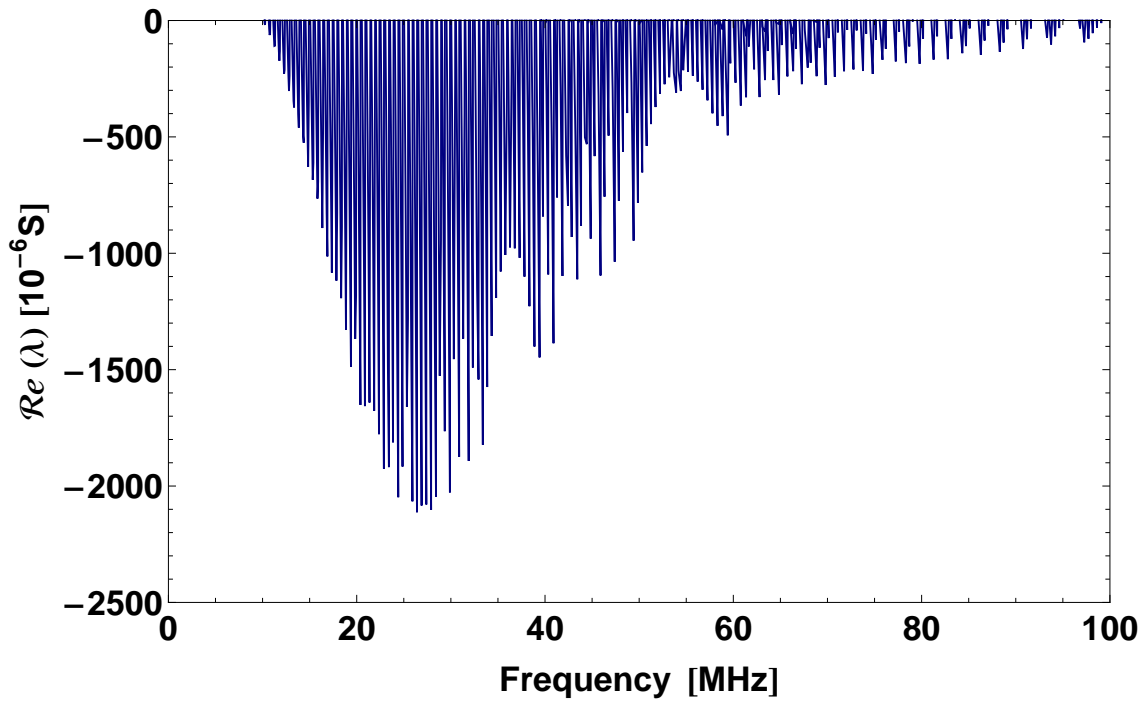


(a)  $\ell = 300$  m

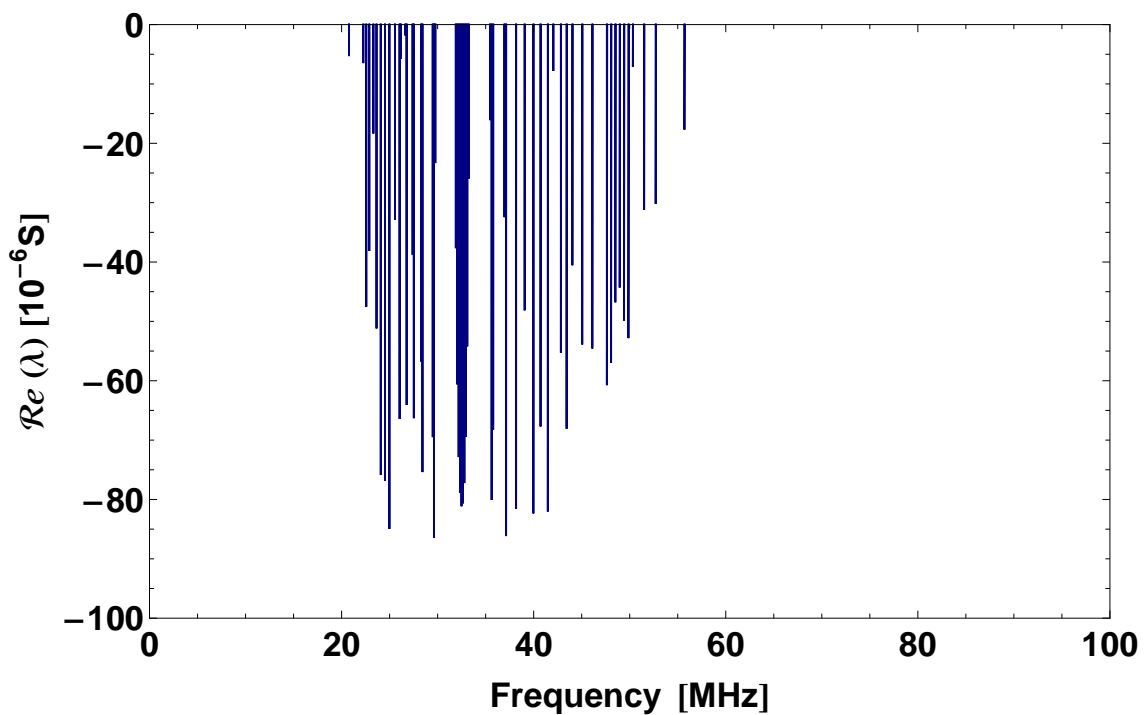


(b)  $\ell = 1000$  m

**Figure 4.3:** Passivity violations of the 138 kV circuit - Constant ground parameters.

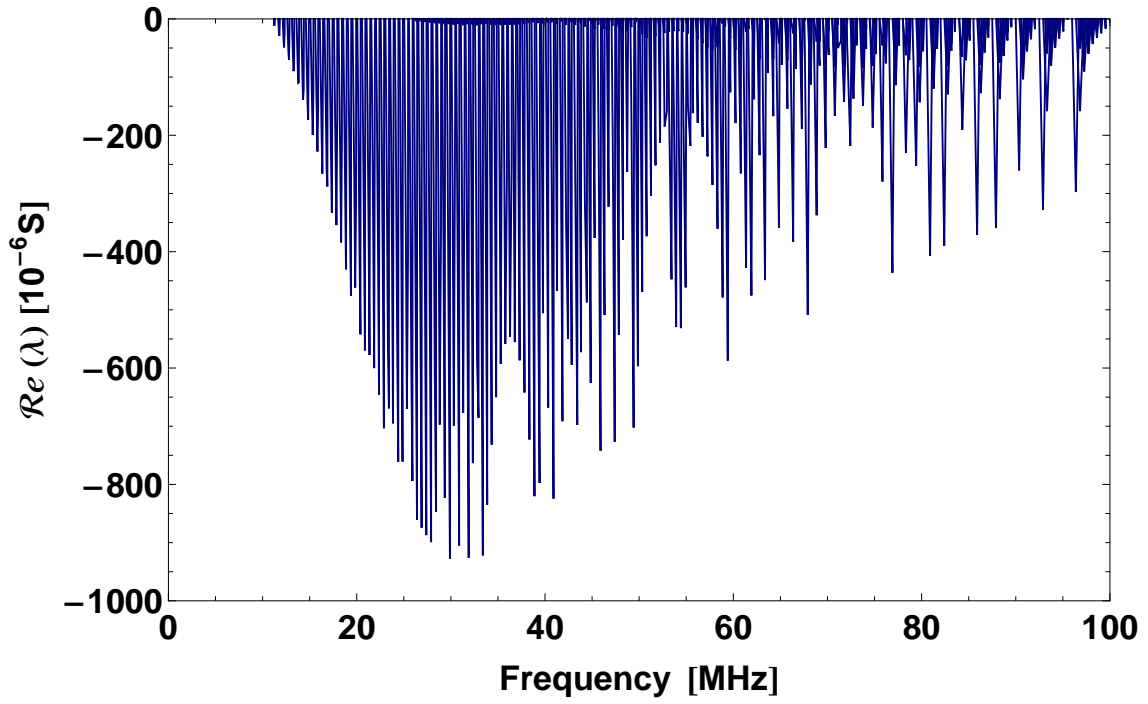


(a)  $\ell = 300$  m

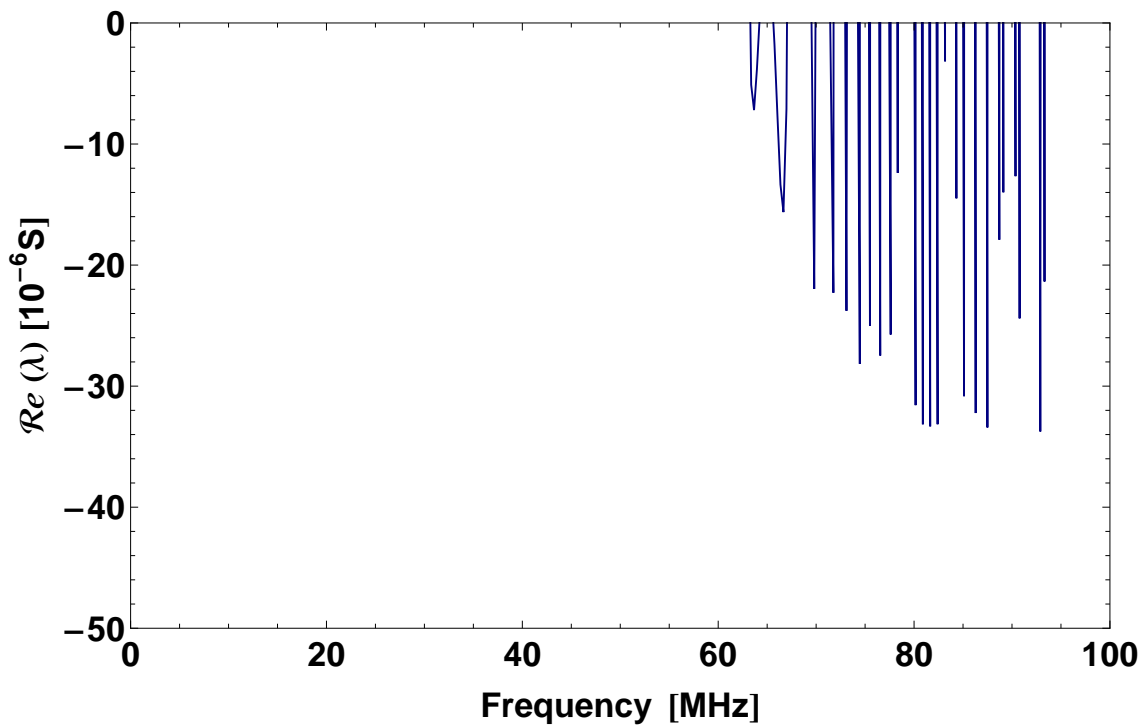


(b)  $\ell = 1000$  m

**Figure 4.4:** Passivity violations of the 230 kV circuit - Constant ground parameters.

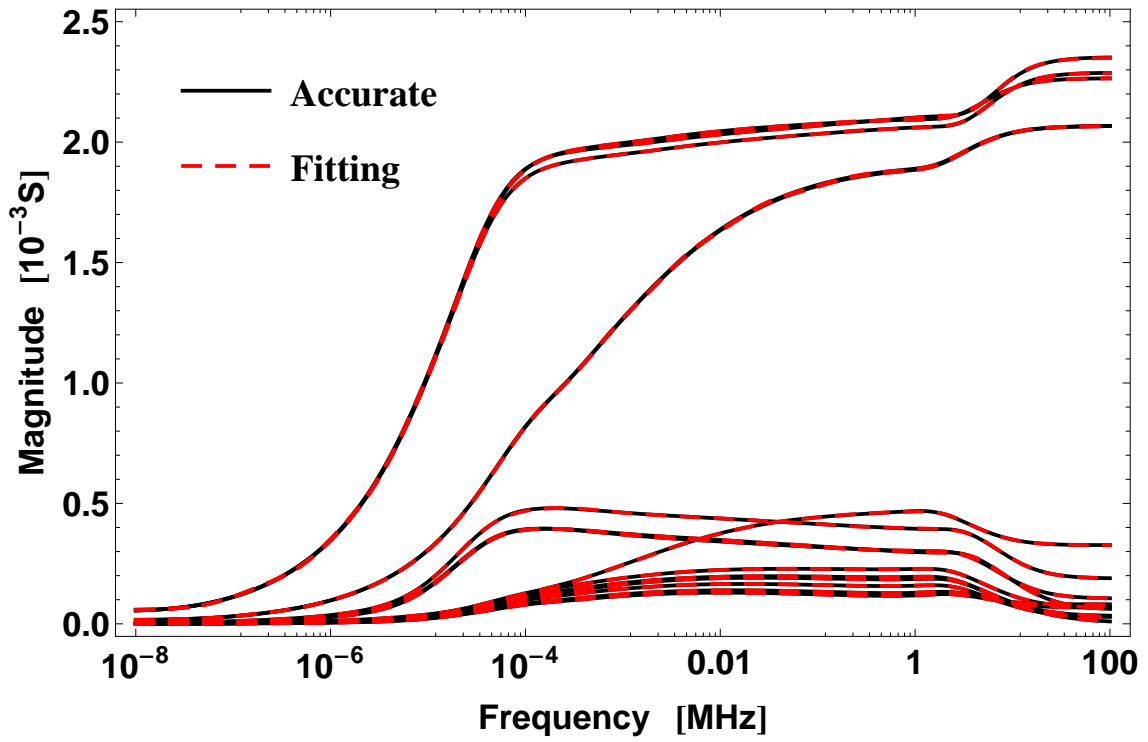


(a)  $\ell = 300$  m

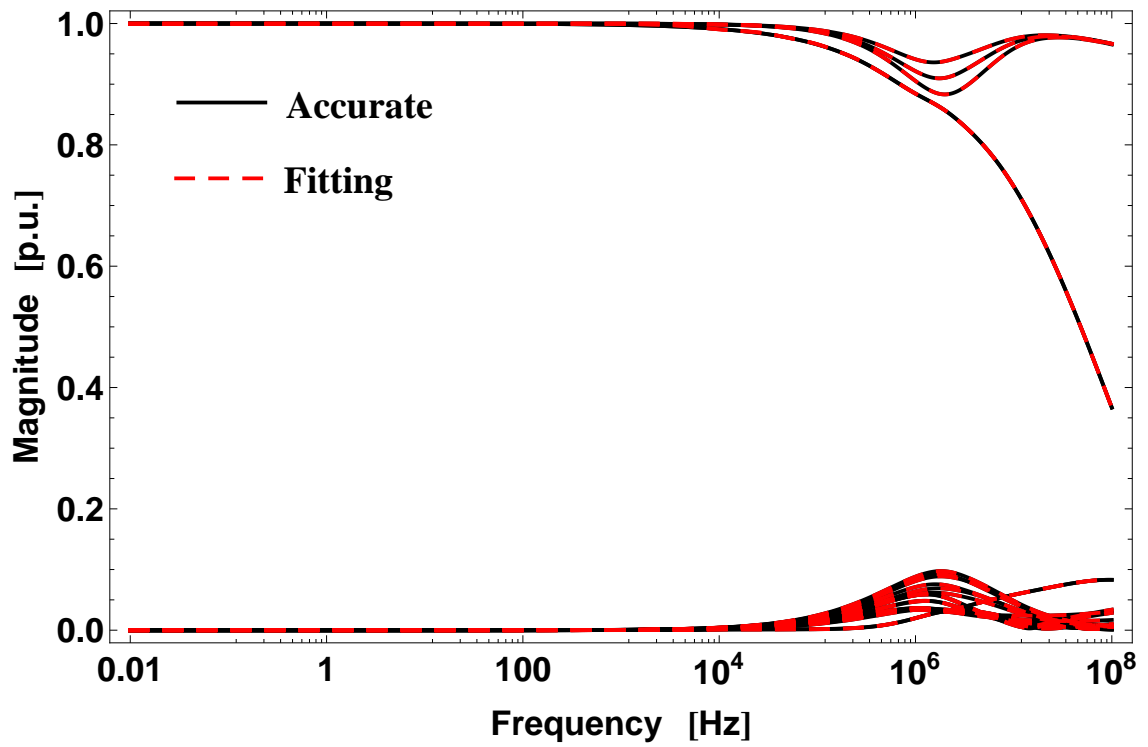


(b)  $\ell = 1000$  m

**Figure 4.5:** Passivity violations of the 500 kV circuit - Constant ground parameters.

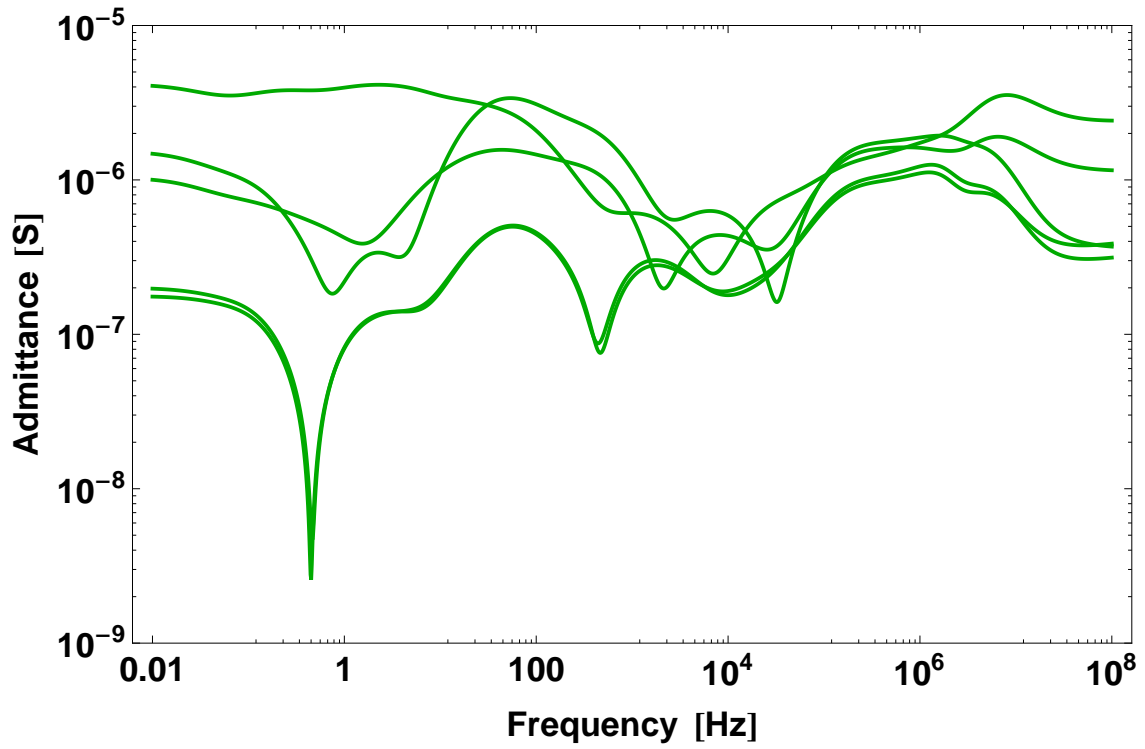


(a) Fitting of  $Y_c$

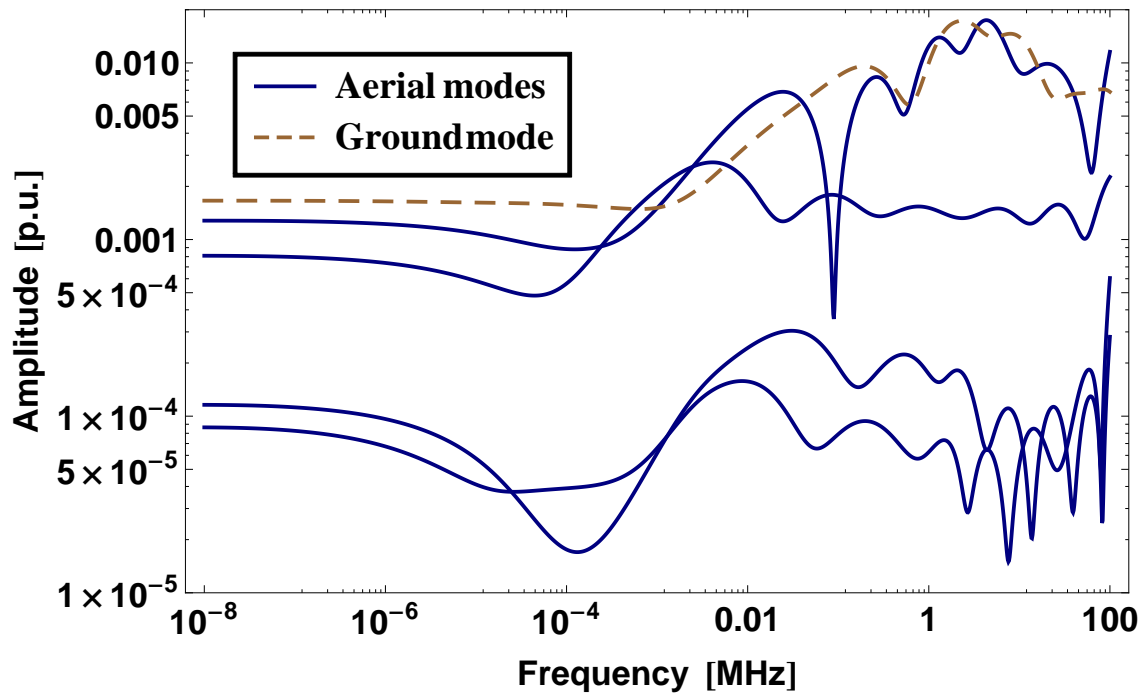


(b) Fitting of  $H$

Figure 4.6: Rational fitting of  $Y_c$  and  $H$  - 138 kV circuit.



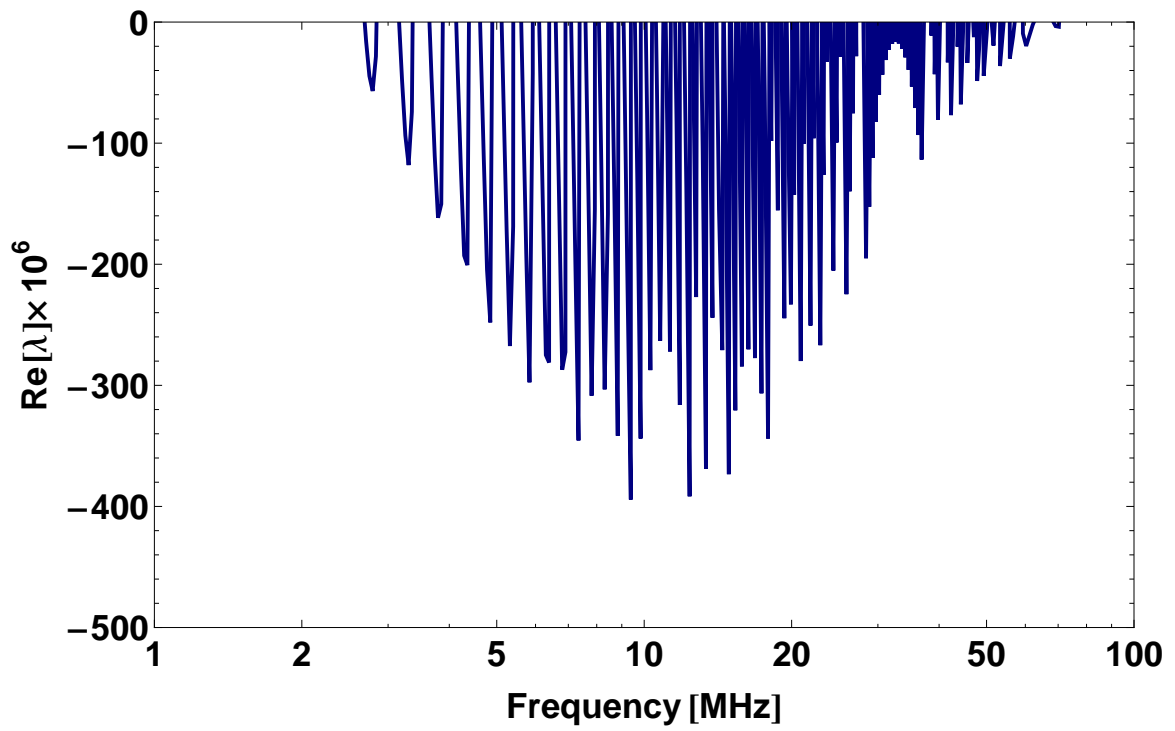
(a) Fitting error of  $Y_c$ .



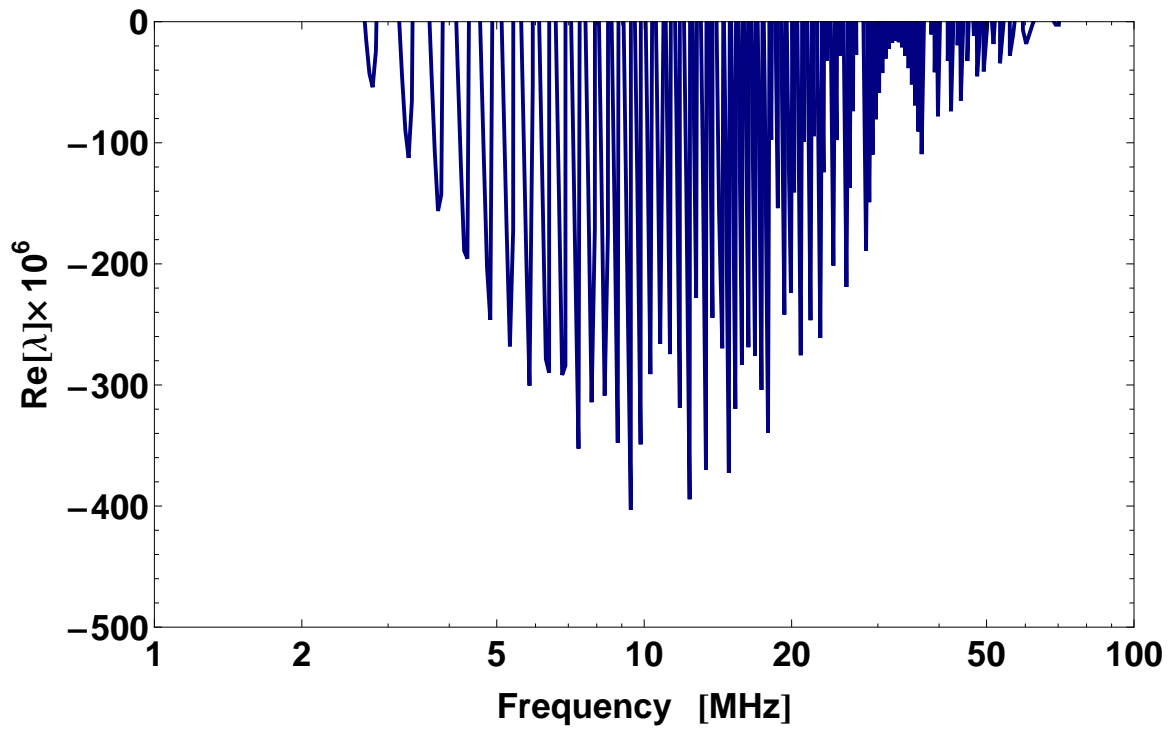
(b) Fitting error of the modes  $h_i$ .

**Figure 4.7:** Absolute fitting error of  $Y_c$  and  $h_i$  - 138 kV circuit.





(a) Using the calculated values of  $\mathbf{Y}_n$



(b) Using the rational approximations of  $\mathbf{Y}_c$  and  $\mathbf{H}$

**Figure 4.8:** Passivity violations in  $\mathbf{Y}_n$  - 138 kV circuit.

## 4.5.2 Frequency dependent ground parameters soil models

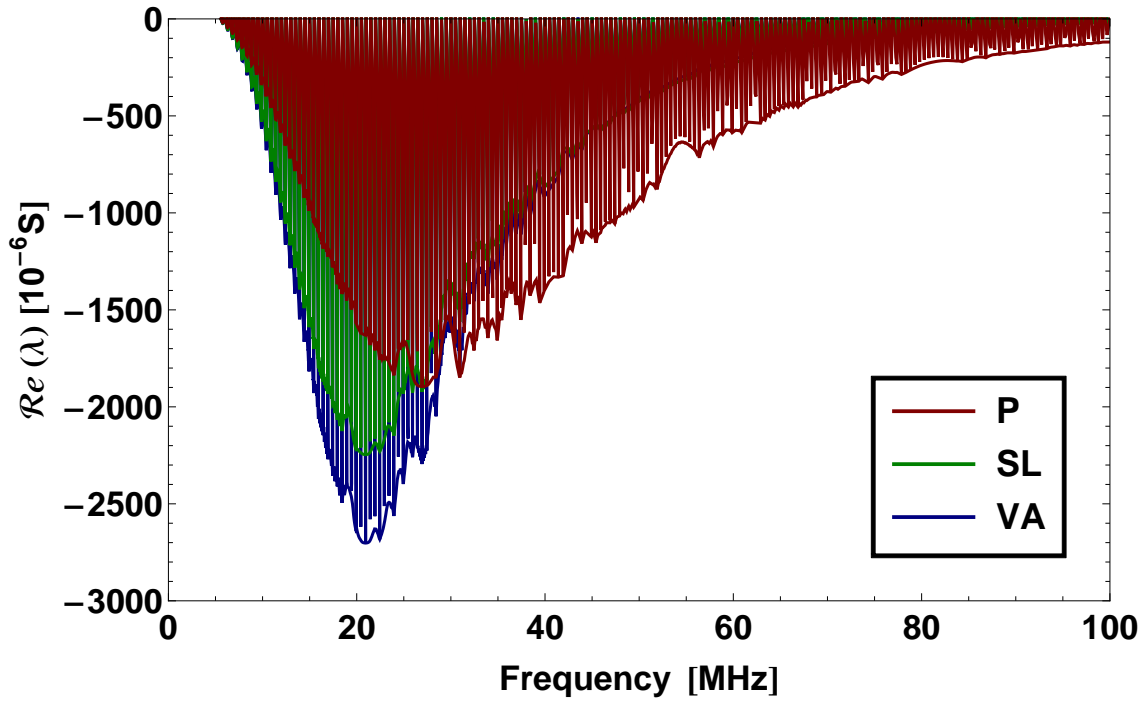
Table 4.5 summarises the findings regarding the eigenvalues  $\lambda$  for the test case configurations evaluated with frequency dependent soil models using image approximations for a line length of  $\ell = 300$  m, where  $\sigma = \sigma_{DC} = \sigma_{100\text{ Hz}}$  is the low frequency soil conductivity in S/m,  $\Omega$  is the frequency value in MHz at which the largest passivity violation arises and  $min$  is the minima of  $\Re(\lambda(\Omega))$ .

**Table 4.5:** Passivity violations and minima of  $\lambda$  for a line length of  $\ell = 300$  m.

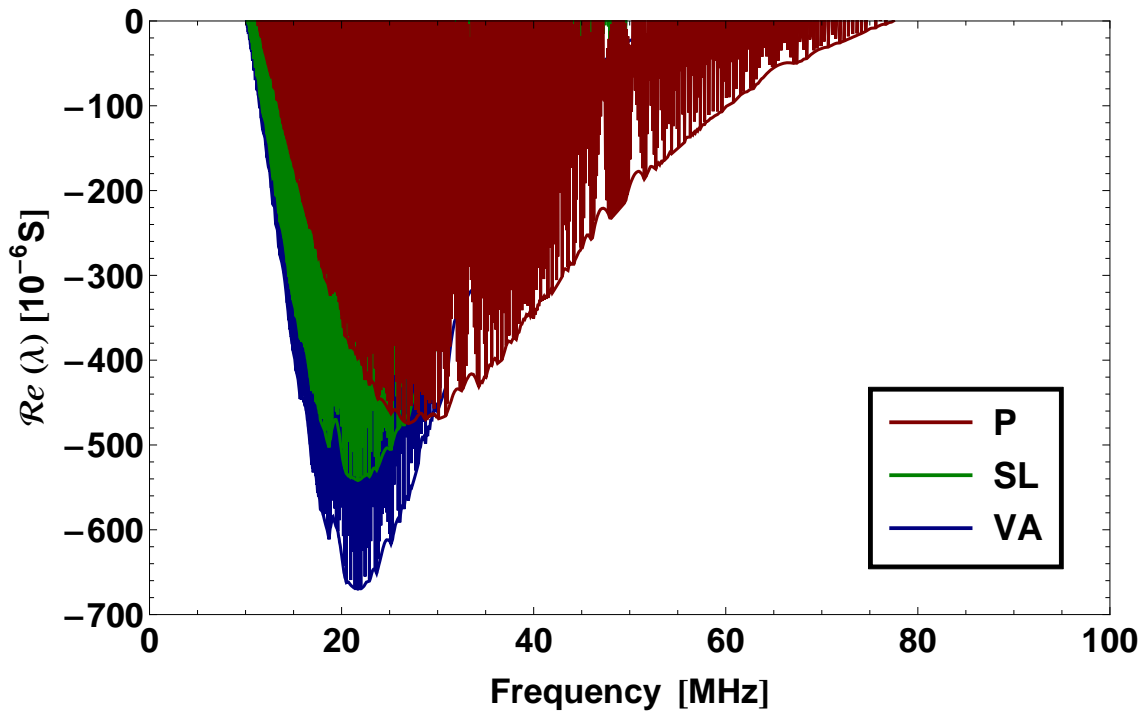
Line Circuit		Portela		Smith Longmire		Visacro Alipio	
kV	$\sigma$ (S/m)	$\Omega$ (MHz)	$min$ ( $10^{-6}$ )	$\Omega$ (MHz)	$min$ ( $10^{-6}$ )	$\Omega$ (MHz)	$min$ ( $10^{-6}$ )
138	$10^{-4}$	28.43	-1472.49	12.91	-540.38	13.42	-730.75
	$10^{-3}$	28.43	-1479.34	13.42	-751.48	13.92	-977.53
	0.01	28.43	-1547.97	15.43	-1350.89	15.94	-1693.38
	0.05	26.95	-1895.49	20.95	-2246.24	20.95	-2702.24
230	$10^{-4}$	51.91	-1815.48	28.39	-528.09	28.39	-688.38
	$10^{-3}$	51.91	-1820.76	28.39	-703.97	25.89	-907.50
	0.01	50.42	-1875.21	27.40	-1193.84	26.90	-1557.89
	0.05	50.42	-2130.50	35.41	-2094.14	35.41	-2583.11
500	$10^{-4}$	76.91	-1107.01	48.89	-321.32	46.40	-375.68
	$10^{-3}$	76.91	-1108.98	46.40	-393.83	38.89	-457.93
	0.01	76.91	-1128.81	42.91	-586.38	34.40	-728.29
	0.05	76.91	-1219.83	43.91	-1014.07	42.91	-1221.19

As in the case with soil models using constant ground parameters, even though a positive definite  $\mathbf{Y}_c$  is calculated throughout the frequency band considered, passivity violations arise when image approximations are used along with frequency dependent soil models. Higher values of  $\sigma$  also increase the magnitude of these passivity violations, with typical values of  $\Omega$  starting around 10 MHz. For the Portela soil model, variations in the value of  $\sigma$  have little incidence in the resulting value of  $\Omega$ . As for the Visacro-Alipio and Smith-Longmire soil models, for a fixed  $\sigma$  similar values of  $\Omega$  are calculated.

As in the case of soil models with constant parameters, we evaluate whether passivity violations in three-phase lines depend of the line length  $\ell$  when the frequency dependent soil models of Portela (P), Smith-Longmire (SL) and Visacro-Alipio (VA) are used. We calculate the eigenvalues  $\lambda$  of the 138 kV, 230 kV and 500 kV test case lines considering a value of  $\sigma = 0.05$  S/m for line lengths of  $\ell = 300$  m and  $\ell = 1$  km. Figs. 4.9 to 4.11 show the resulting passivity violations.

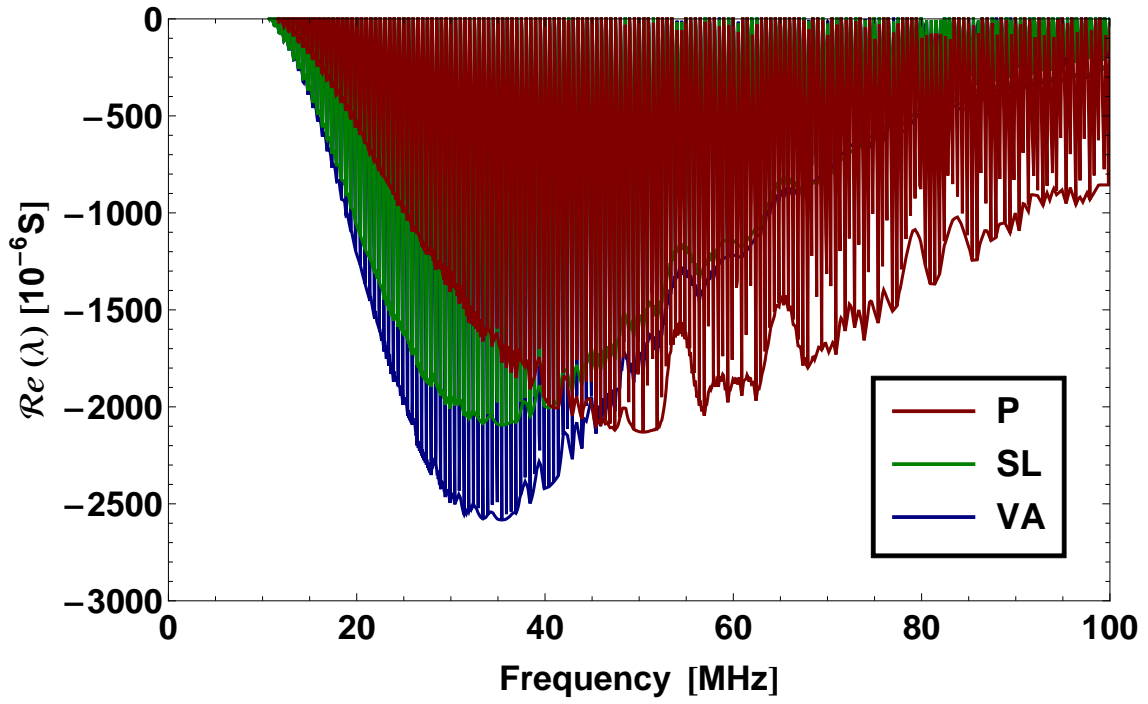


(a)  $\ell = 300$  m.

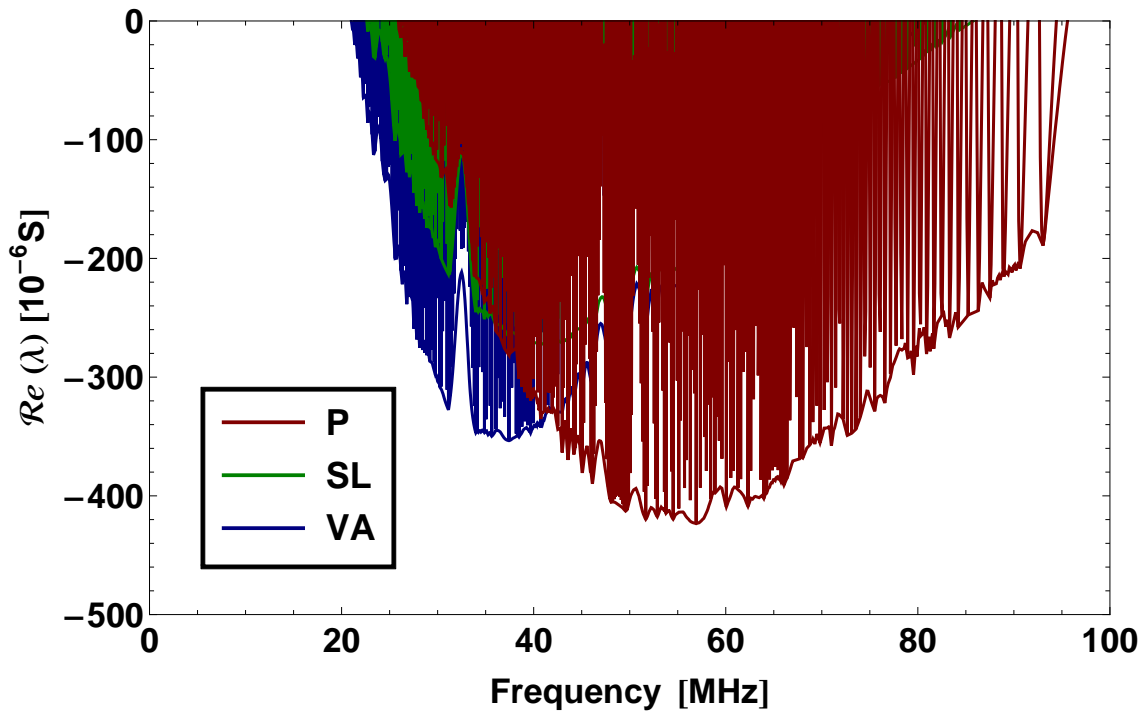


(b)  $\ell = 1$  km.

**Figure 4.9:** Passivity violations of the 138 kV circuit - Frequency dependent soils.

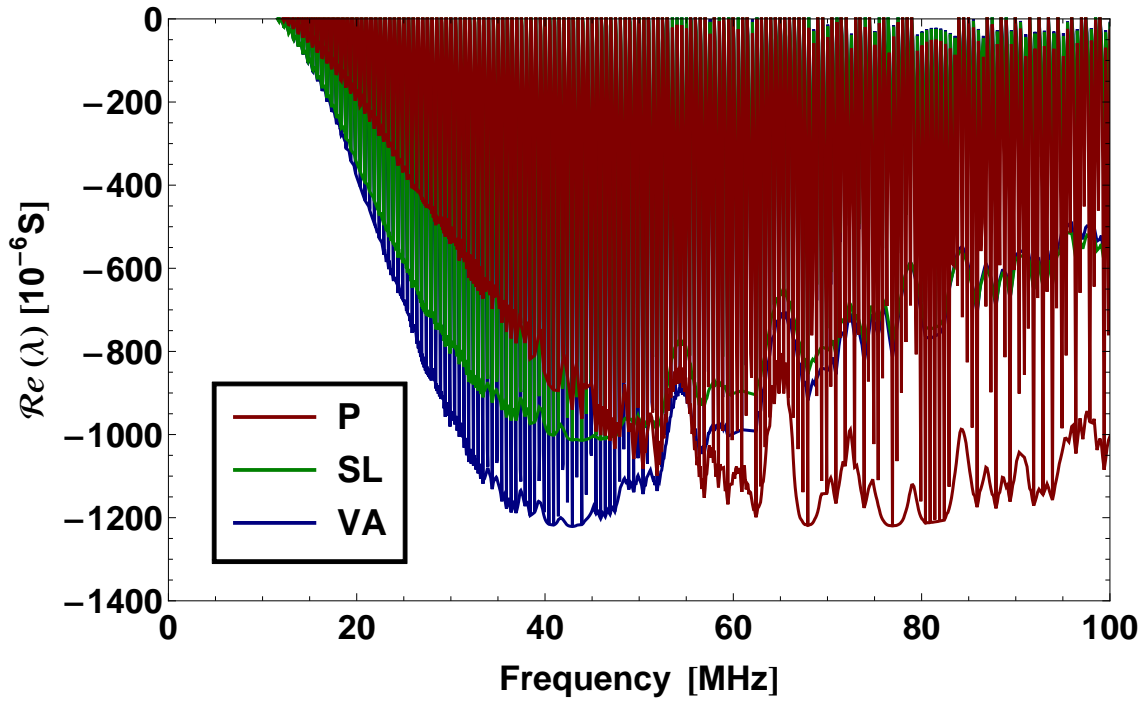


(a)  $\ell = 300$  m.

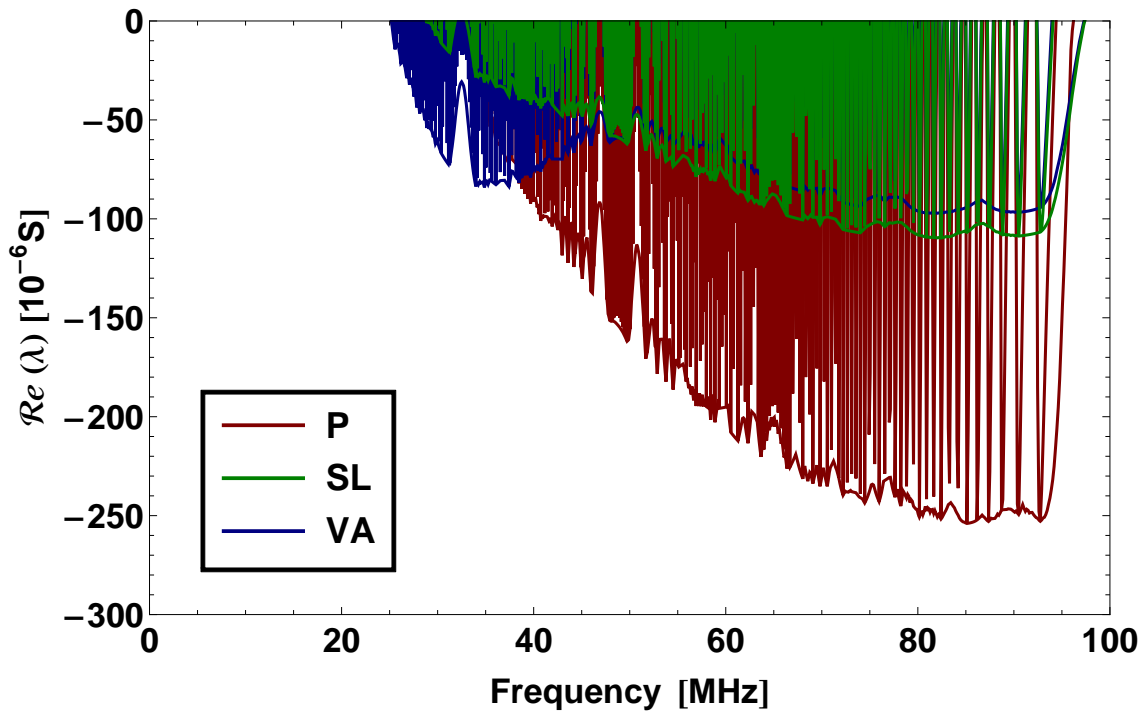


(b)  $\ell = 1$  km.

**Figure 4.10:** Passivity violations of the 230 kV circuit - Frequency dependent soils.



(a)  $\ell = 300$  m.



(b)  $\ell = 1$  km.

**Figure 4.11:** Passivity violations of the 500 kV circuit - Frequency dependent soils.

In all cases, as the line length  $\ell$  increases, the magnitude of the passivity violations decrease. For the 138 kV line, the frequency band where the passivity violations arise is trimmed in the higher frequencies. For the 230 kV and 500 kV lines, the frequency band of the “bell-shaped” distribution of the passivity violations is displaced to the higher frequencies.

The magnitude of the passivity violations calculated using the rational fitting of  $\mathbf{Y}_c$  and  $\mathbf{H}$  with closed-form image approximations and frequency dependent soil models matches those presented in Fig. 4.9 to Fig. 4.11 with negligible differences.

Table 4.6 shows the minimum line lengths  $\ell$  in function of  $\sigma$  for which the test case circuits present no passivity violations.

**Table 4.6:** Minimum line length  $\ell$  for test cases (m).

Line circuit	$\sigma$ (S/m)	Portela	Visacro Alipio	Smith Longmire
138 kV	$10^{-4}$	2169	1288	1152
	$10^{-3}$	2175	1405	1304
	0.01	2214	1731	1644
	0.05	2396	2337	2220
230 kV	$10^{-4}$	1641	907	853
	$10^{-3}$	1643	960	935
	0.01	1656	1100	1097
	0.05	1716	1361	1364
500 kV	$10^{-4}$	1788	1156	1157
	$10^{-3}$	1785	1185	1225
	0.01	1785	1256	1321
	0.05	1796	1358	1447

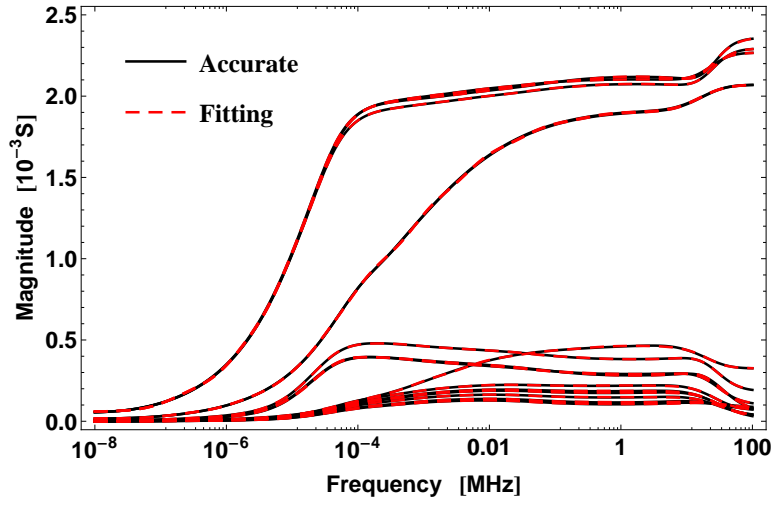
We can see that as the value of  $\sigma$  increases, the minimum line length is also increased. For the Portela soil model, a limited incidence of  $\sigma$  in the minimum line length can be observed. The Visacro-Alipio and Smith-Longmire soil models present as well a distinct characteristic: as  $\sigma$  increases, the minimum length is significantly increased as compared to the Portela soil model.

Fig. 4.12 and Fig. 4.13 depicts the results of the absolute value of the rational approximations of both  $\mathbf{Y}_c$  and  $\mathbf{H}$  compared together with their respective original frequency domain data for the 138 kV circuit using frequency dependent soil models with a line length of  $\ell = 300$  m. A very good agreement is found for the Portela, Smith-Longmire and Visacro-Alipio frequency dependent soil models as a maximum absolute deviation of  $1.99 \cdot 10^{-3}$  p.u.,  $2.19 \cdot 10^{-3}$  p.u. and  $2.13 \cdot 10^{-3}$  p.u. is obtained for  $\mathbf{H}$  while for  $\mathbf{Y}_c$  it was  $7.48 \cdot 10^{-6}$  S,  $6.72 \cdot 10^{-6}$  S and  $1.03 \cdot 10^{-5}$  S.

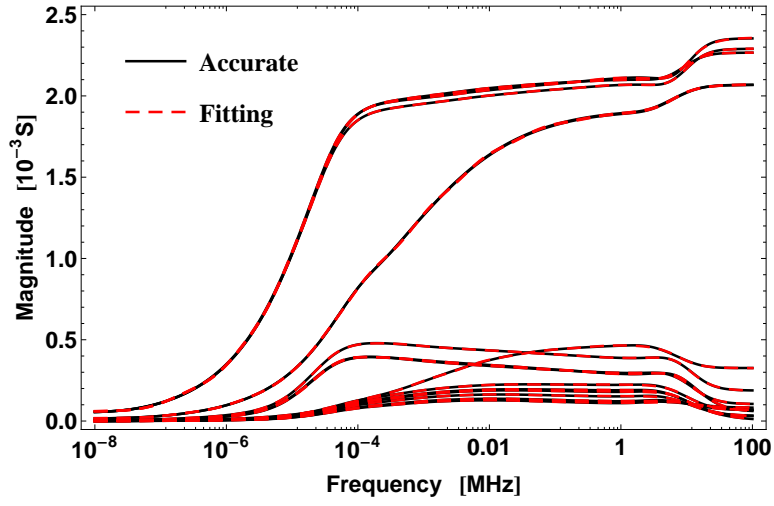
As in the case of soils with constant ground parameters, the fitted counterparts of  $\mathbf{Y}_c$  and  $\mathbf{H}$  are used in (4.13) and then the eigenvalues  $\lambda$  are determined using (4.14).

Fig. 4.14 and Fig. 4.15 show respectively the absolute value of the fitting error for  $\mathbf{Y}_c$  and of each mode  $h_i$  considering the image approximations for a soil model with constant ground parameters for the 138 kV circuit. For the rational approximation of the characteristic admittance a minimum fit order of 12 poles is obtained. As with the case of soils with constant ground parameters, it is also worth mentioning that from the fitting of  $\mathbf{Y}_c$  a positive definite matrix was also calculated for all the frequencies involved. For each mode  $h_i$  of the propagation function, a successful time delay extraction was achieved and a low order fit was possible using only 6 poles per mode.

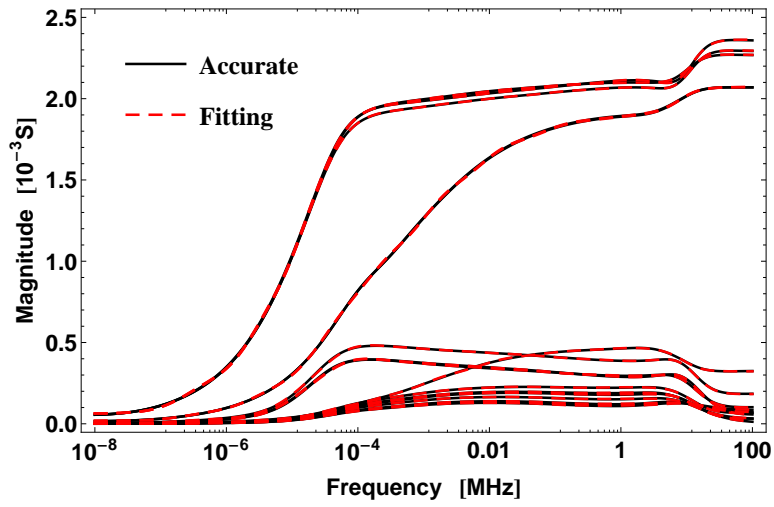
Fig. 4.16 and Fig. 4.17 depicts the behavior of the eigenvalues with the largest passivity violations using both the calculated values of  $\mathbf{Y}_n$  and the rational approximations of  $\mathbf{Y}_c$  and  $\mathbf{H}$  for the 138 kV circuit with frequency dependent soil models. As took place in the case of soils with constant ground parameters, the magnitude of the passivity violations calculated using the original data of  $\mathbf{Y}_n$  and the rational approximations of  $\mathbf{H}$  and  $\mathbf{Y}_c$  with closed-form image approximations match with negligible differences, as the use of the rational approximations did not affect significantly the behavior of the passivity violations.



(a) Portela.



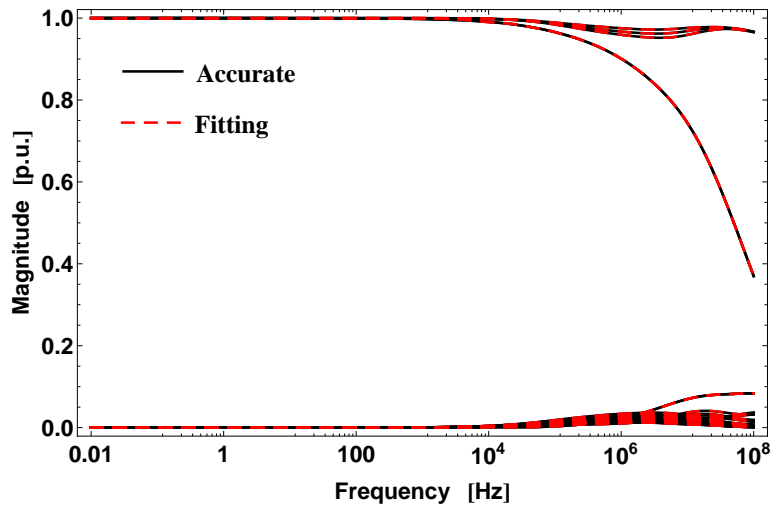
(b) Smith-Longmire.



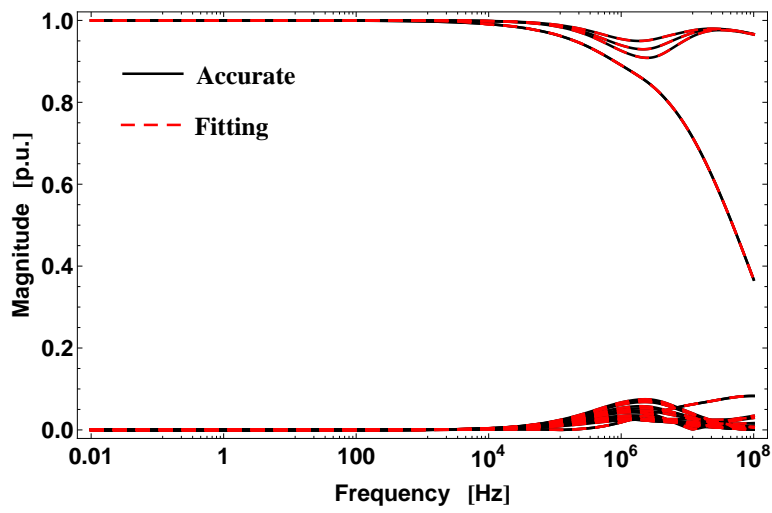
(c) Visacro-Alipio.

**Figure 4.12:** Rational fitting of  $Y_c$  - 138 kV circuit.

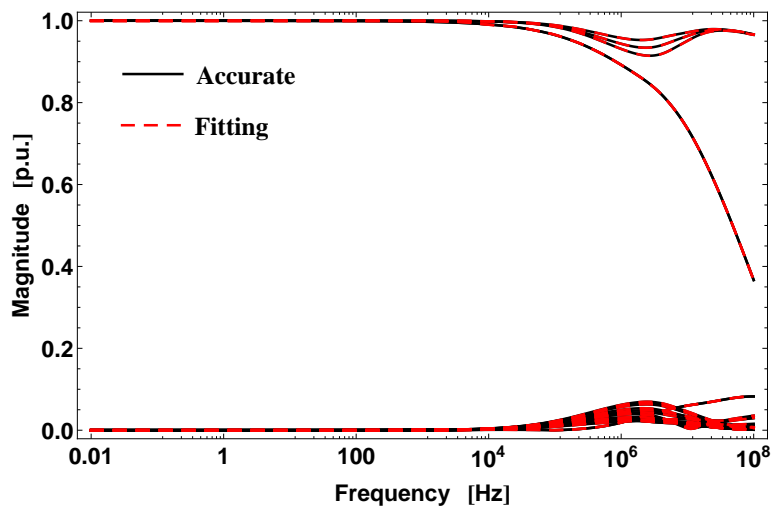




(a) Portela.

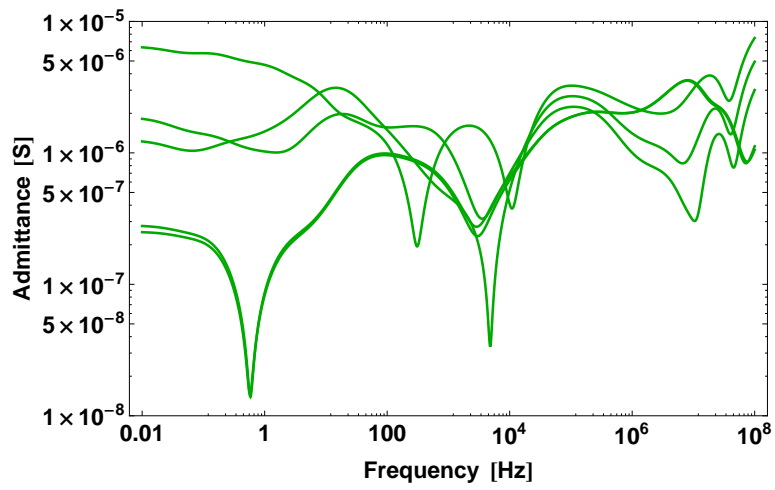


(b) Smith-Longmire.

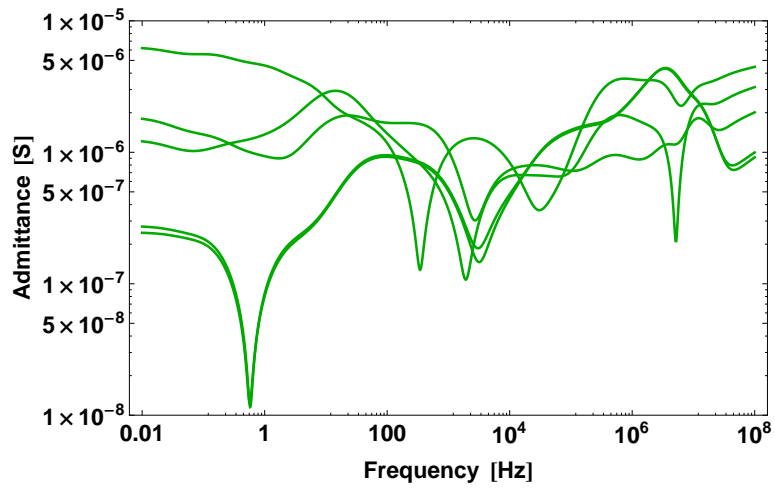


(c) Visacro-Alipio.

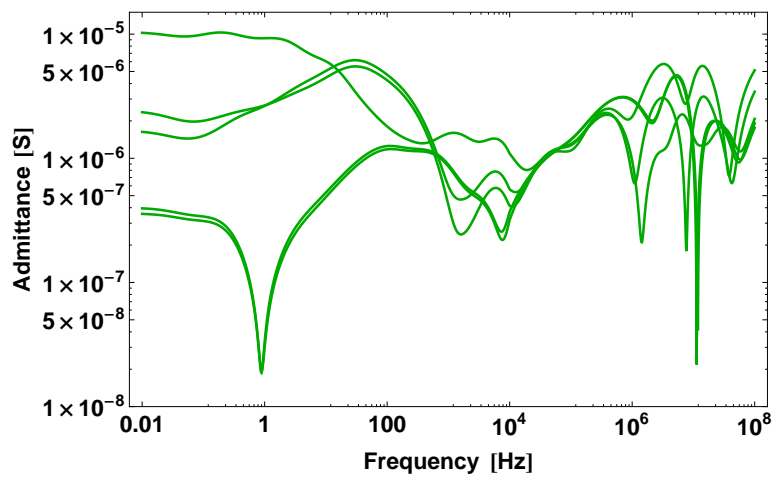
**Figure 4.13:** Rational fitting of  $\mathbf{H}$  - 138 kV circuit.



(a) Portela.

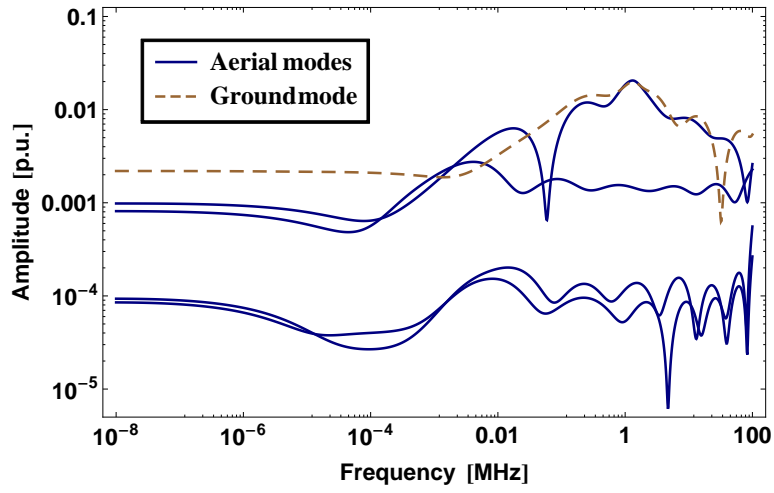


(b) Smith-Longmire.

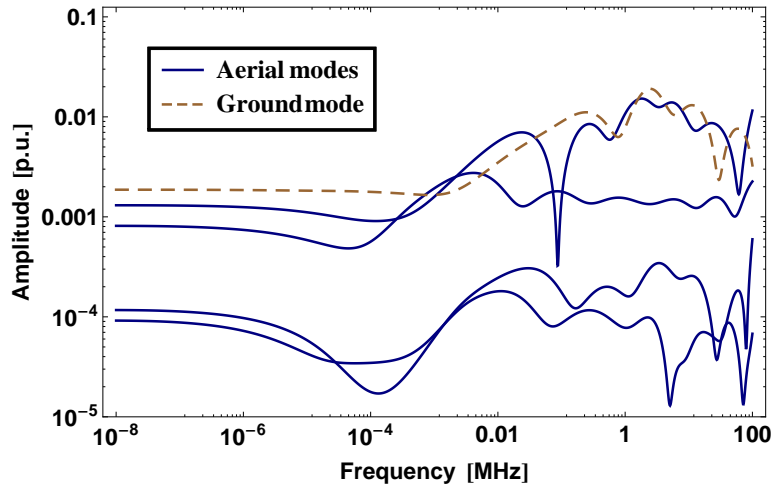


(c) Visacro-Alipio.

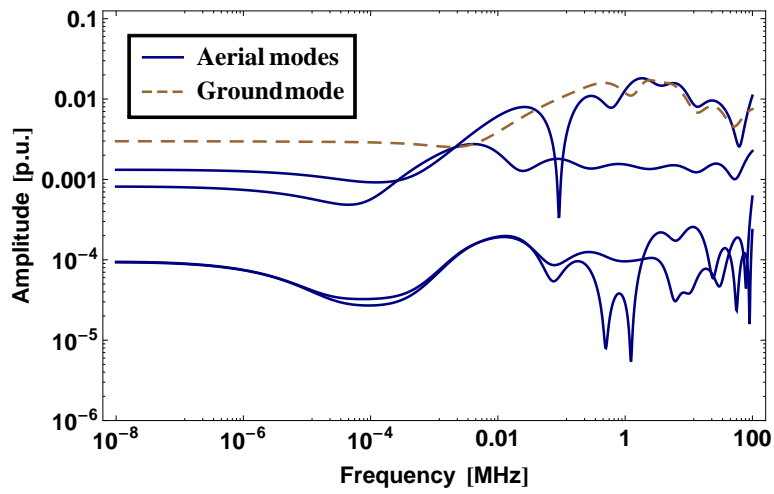
**Figure 4.14:** Absolute fitting error of  $Y_c$  - 138 kV circuit.



(a) Portela.

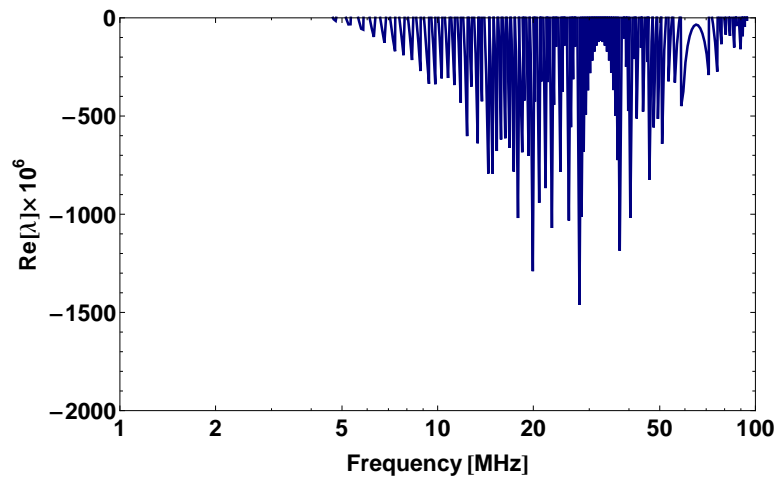


(b) Smith-Longmire.

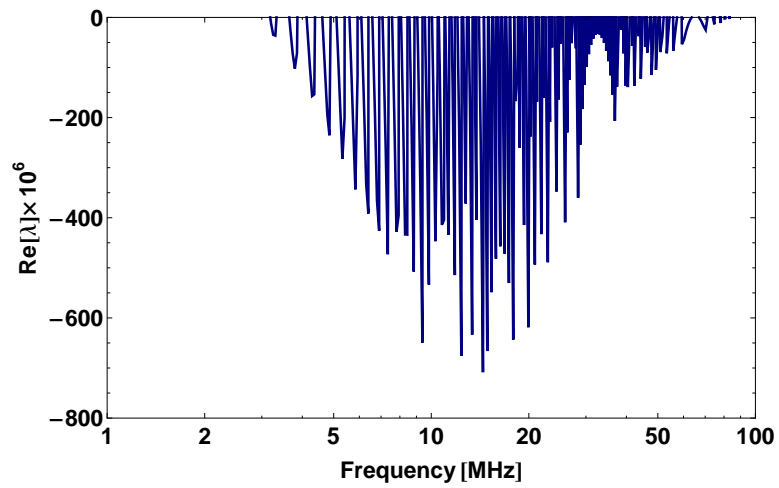


(c) Visacro-Alipio.

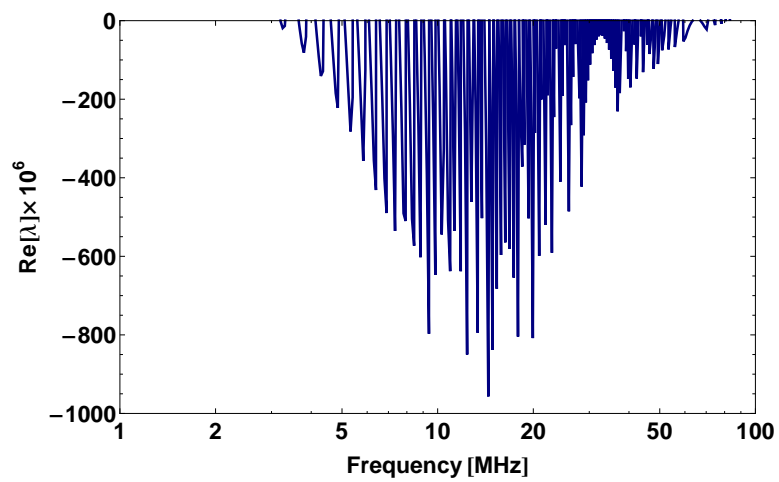
**Figure 4.15:** Absolute fitting error of  $h_i$  - 138 kV circuit.



(a) Using the calculated values of  $\mathbf{Y}_n$

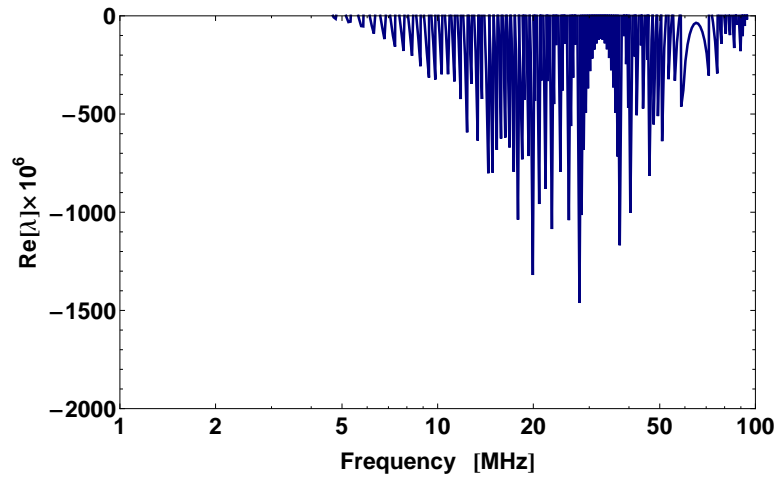


(b) Using the calculated values of  $\mathbf{Y}_n$

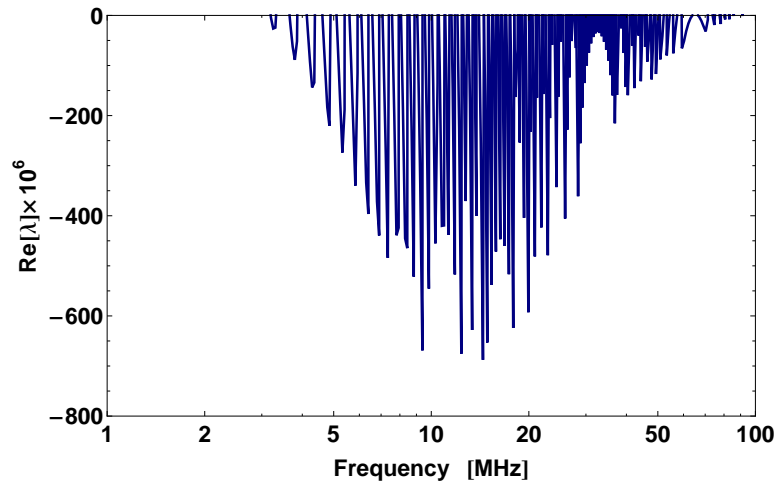


(c) Using the calculated values of  $\mathbf{Y}_n$

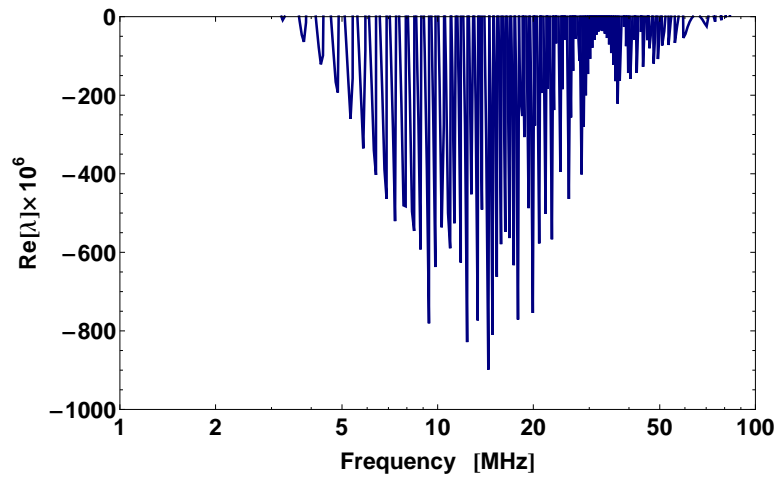
**Figure 4.16:** Passivity violations in  $\mathbf{Y}_n$  from original data - 138 kV circuit.



(a) Using the rational approximations of  $\mathbf{Y}_c$  and  $\mathbf{H}$



(b) Using the rational approximations of  $\mathbf{Y}_c$  and  $\mathbf{H}$



(c) Using the rational approximations of  $\mathbf{Y}_c$  and  $\mathbf{H}$

**Figure 4.17:** Passivity violations in  $\mathbf{Y}_n$  from fitted  $\mathbf{Y}_c$  and  $\mathbf{H}$  - 138 kV circuit.

## 4.6 Time and Frequency Domain Evaluation

To assess whether the rather small passivity violations affect time-domain simulations, we consider the 138 kV circuit test case presented in Fig. 4.2(a) using a value of  $\sigma = 10^{-3}$  S/m and a span length of 300 m for soils with both constant and frequency dependent parameters. A slightly perturbed impulse source voltage is connected at one phase of the sending end while the other phases are directly grounded to earth, with all the receiving ends open. The input voltage  $v_{in}(t)$  is given by

$$v_{in}(t) = \exp(-10^{-6}t) - \exp(-10^{-7}t) + u_p(t) \quad (4.19)$$

where  $u_p(t) = 0.01 \cos(2\pi \cdot \Omega \cdot 10^6 \cdot t)$  is a small perturbation around the respective frequency  $\Omega$  where the passivity violations occur presented in Table 4.5 and  $v_{out}(t)$  is the output voltage at the end of the line. The time-domain evaluation circuit is shown in Fig. 4.18.

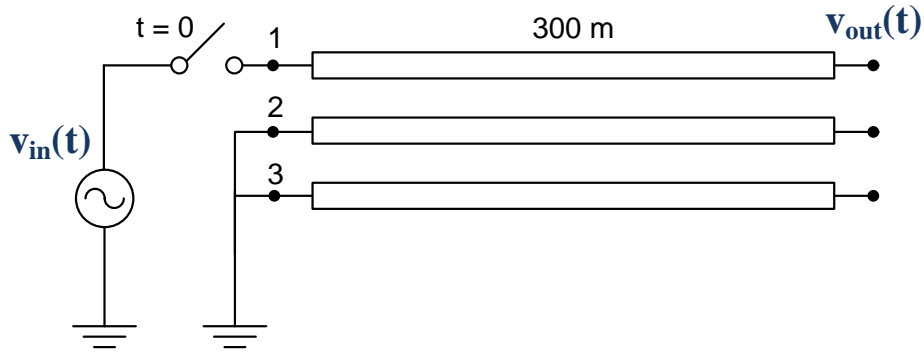


**Figure 4.18:** Multiphase circuit for time-domain test.

To obtain the time-domain simulation responses, we consider two approaches. The first one is the Numerical Laplace Transform (NLT) [88–90], based on a frequency-domain analysis. The second one is the Method of Characteristics (MoC) [5, 23], based on a time-domain approach. An alternative modeling approach consists to use the rational approximation of the nodal admittance matrix based on a Folded line equivalent [95]. However, in this case the passivity violations could be eliminated by passivity enforcement as shown in [64]. It is important to use the MoC to assess the behavior of the transmission line model against passivity violations that are not directly identified.

For the MoC simulation we adopt the formulation based on the so-called Universal Line Model (ULM) [20] using a two-segment interpolation scheme to avoid instabilities related to large residue-pole ratios in the rational approximation of  $\mathbf{H}$  [45].

For the NLT simulation we consider a complex frequency  $s = c + j\omega$  with a constant  $c = -\ln(0.001)/T_{max}$  and a maximum observation time of  $T_{max} = 40 \mu\text{s}$ . To ensure that the high frequency range where the passivity violations occur is correctly simulated, 31774 frequency samples are used.

Comparison between NLT and MoC results is carried out using sample interpolation between consecutive frequencies.

Even though passivity violations are present in the high frequency range, the NLT results show a stable voltage response. This stability robustness of the NLT algorithm is related to the damping effect of using a complex axis  $s = c + j\omega$  instead of the imaginary axis  $s = j\omega$  in which the passivity violations are calculated. This is an important finding as it illustrates that a frequency-domain based transient simulation is robust regarding inaccuracies in the evaluation of line parameters. Furthermore, the results from the NLT can be treated as a benchmark for the expected line behavior.

#### 4.6.1 Constant ground parameters soil models

Fig. 4.19 shows the time-domain output voltage response  $v_{out}(t)$  for the perturbed input voltage  $v_{in}(t)$  using the NLT and the MoC approaches in the 138 kV circuit.

Fig. 4.19(a) shows the results using image approximations. From  $0 \mu s$  to  $7 \mu s$  some spikes are present in the voltage; after that, oscillations increase up to  $10 \mu s$ , from which point, the result from the MoC is completely unstable.

Fig. 4.19(b) shows the results when a quasi-TEM formulation is considered instead. Both the NLT and MoC methods present very similar responses and are free of numerical oscillations or instabilities when using a quasi-TEM formulation for the latter case.

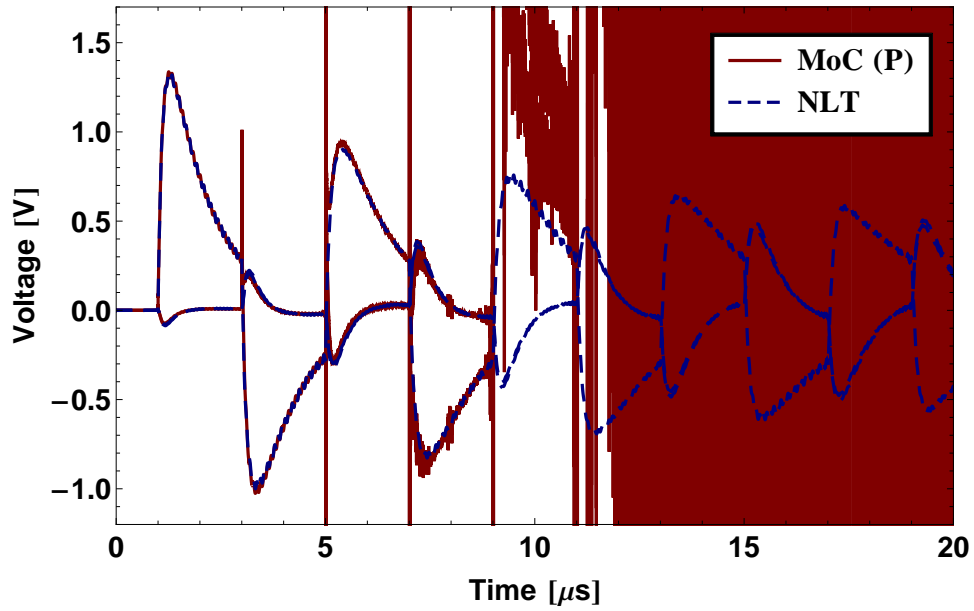
#### 4.6.2 Frequency dependent ground parameters soil models

Fig. 4.20 shows the output voltage  $v_{out}(t)$  using the image approximations with the NLT and the MoC approaches for the three frequency-dependent soil models in the 138 kV circuit.

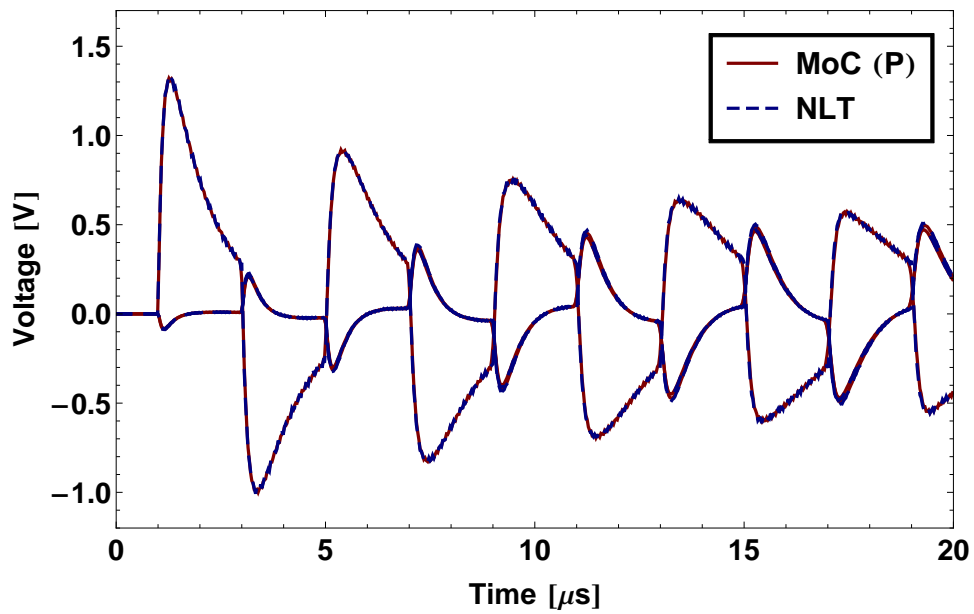
As passivity violations in the high frequency range are excited, unstable simulations are obtained for the Portela, Smith-Longmire and Visacro-Alipio soil models in all the test cases evaluated using the MoC approach.

For the Portela and Smith-Longmire soil models, although stable time-domain simulations are apparently attained, a small yet stable mismatch appears can be observed.

Finally, we found stable time-domain results using the quasi-TEM formulation with both the MoC and NLT approaches that match those obtained using the image approximations with the NLT approach. These findings enforce the idea that the cause of the numerical instabilities reported here in the use of the image approximations is related to the deviations of the closed-form terms in (4.9) from their infinite integral counterparts in (4.6).



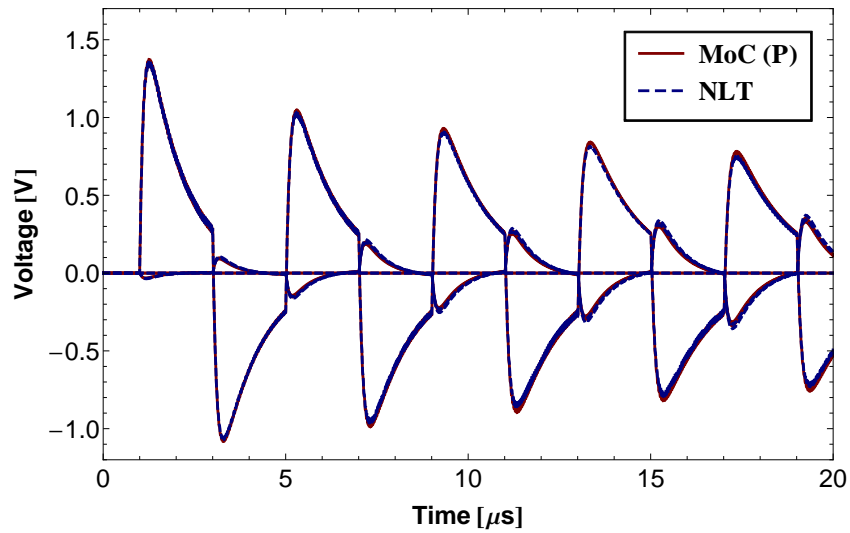
(a) Using image approximation



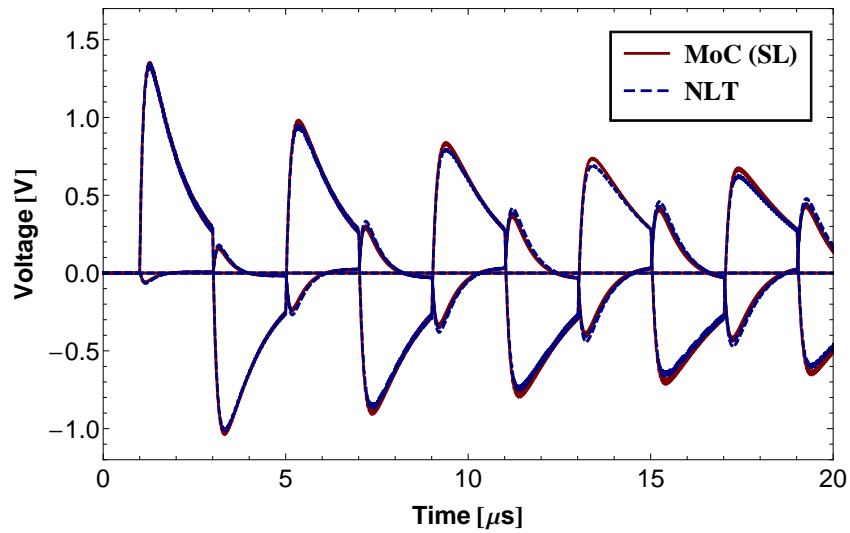
(b) Using quasi-TEM approximation

**Figure 4.19:** Time-domain results in 138 kV circuit - Constant ground parameters.

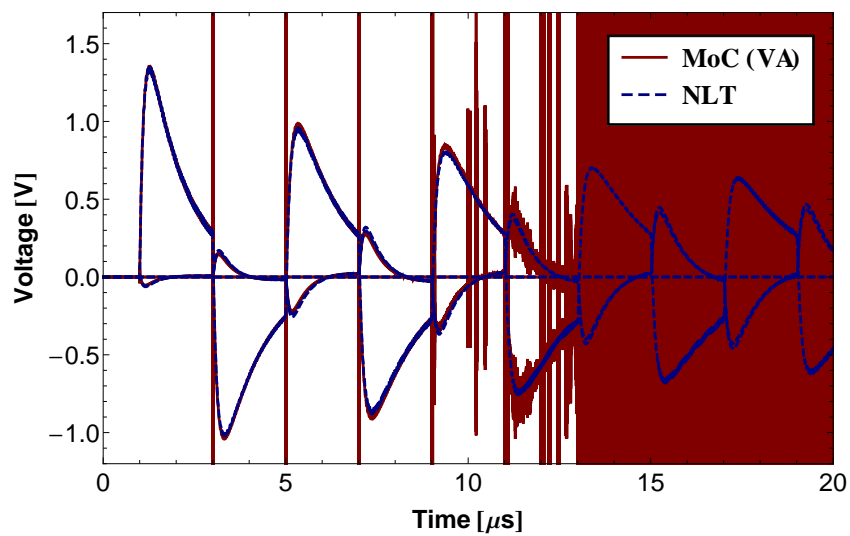




(a) Portela.



(b) Smith-Longmire.



(c) Visacro-Alipio.

**Figure 4.20:** Time-domain results in 138 kV circuit - Frequency dependent soils.

## 4.7 Mitigation Techniques

To avoid the unstable simulations obtained when the image approximations are used along with the Method of Characteristics, besides the increase in the minimal line length, a possibility is to mitigate these unexpected numerical instabilities using the quasi-TEM formulation. This solution implies a greater computational burden as a time-consuming and accurate numerical integration scheme is required to deal with highly oscillatory infinite integrals. One way to avoid dealing with such integrals is to develop closed-form approximations using integral transformation techniques [33] or asymptotic expansions [36]. This approach is left for future research. Here we propose to use a slightly modified expression of the per-unit-length parameters to avoid the passivity violations. So, instead of using the actual line voltage to define the per-unit-length line parameters, we use the electric scalar potential definition, then

$$\begin{aligned}\mathbf{Z} &= \mathbf{Z}_{int} + \frac{j\omega\mu_0}{2\pi} [\mathbf{P} + \mathbf{S}_1] \\ \mathbf{Y} &= 2\pi(j\omega\epsilon_0) [\mathbf{P} + \mathbf{S}_2]^{-1}\end{aligned}\tag{4.20}$$

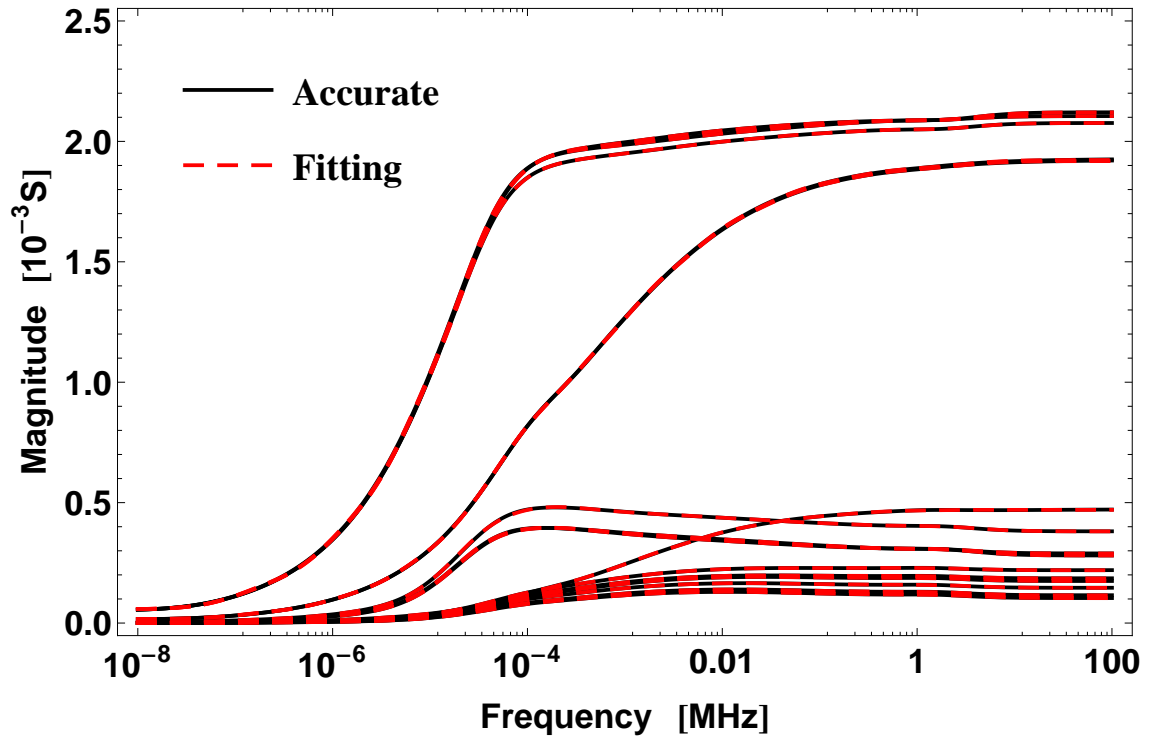
where  $\mathbf{P}$ ,  $\mathbf{S}_1$  and  $\mathbf{S}_2$  are the same as before, see [75] for details on how to determine the per-unit-length line parameters as a function of different formulations.

Using the expressions in (4.20) does not significantly change the behaviour of both the characteristic admittance and the propagation function in the lower frequency range. However, for frequencies higher than 1 MHz there is a more noticeable change in the characteristic admittance as shown in Fig. 4.21. This figure also shows the results of the rational approximation of both  $\mathbf{Y}_c$  and  $\mathbf{H}$  using  $\mathbf{Z}$  and  $\mathbf{Y}$  as defined in (4.20). The fitting errors are  $2.2 \cdot 10^{-6}$  S for  $\mathbf{Y}_c$  and  $0.35 \cdot 10^{-3}$  p.u. for  $\mathbf{H}$ .

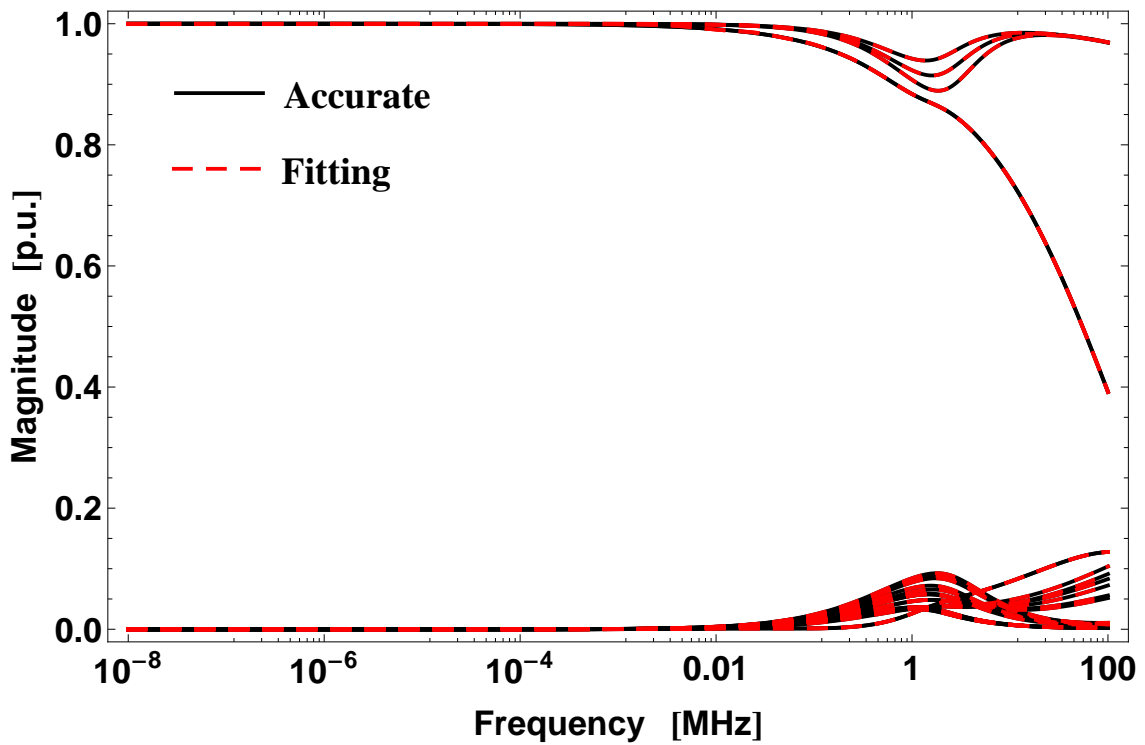
Fig. 4.22 depicts the behavior of the real part of the eigenvalues  $\lambda$  calculated using the original frequency-domain data or either both rational approximations of  $\mathbf{Y}_c$  and  $\mathbf{H}$ . The change in the high frequency behaviour did not change the accuracy of the results. However, it did affect the value of the passivity violations, as for this scenario their mitigation has been accomplished. The model is now stable as the real part of all the eigenvalues is now positive.

The time-domain response obtained using the MoC for the 138 kV line model using the expressions in (4.20) is shown in Fig. 4.23. It can be seen that the results are closer to the ones obtained using NLT and to the one from the previous section using MoC with a quasi-TEM formulation. A closer comparison of the results indicates a small deviation in the results using (4.20) from the ones obtained using (4.8) compared with a quasi-TEM formulation.

Another possibility is to modify the expressions for the closed form approximated expressions to avoid the passivity violations considering  $\eta = \gamma_2$  in the definition of the

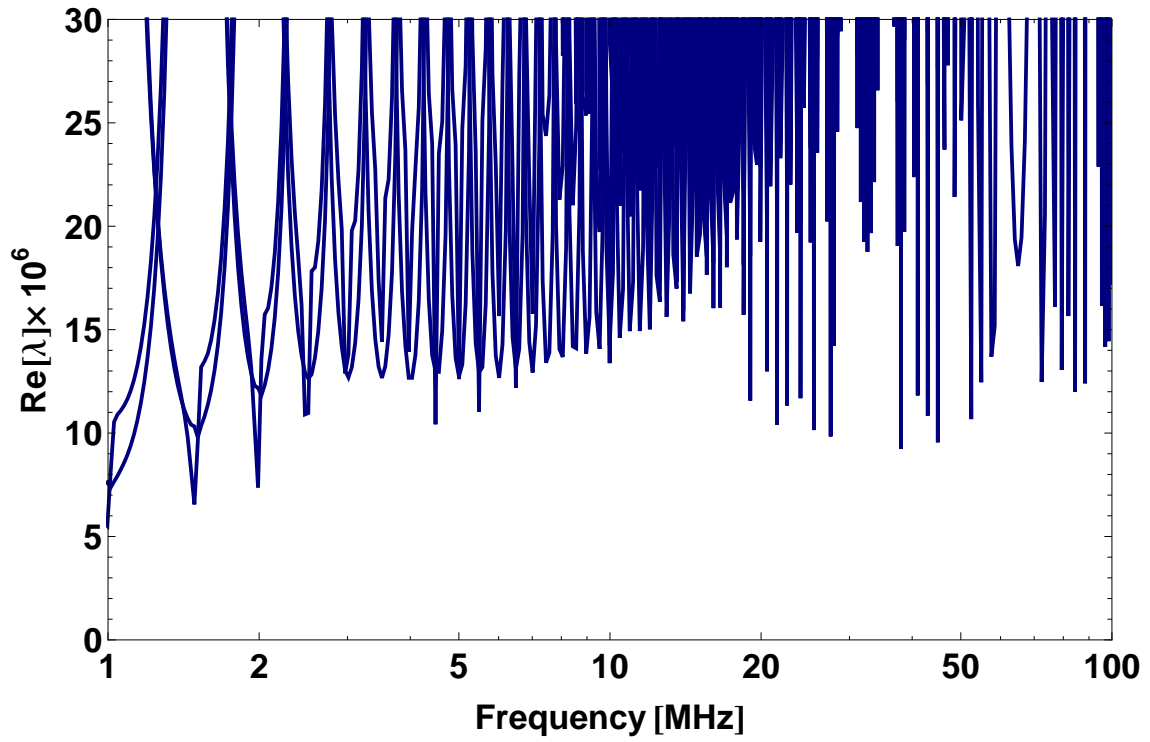


(a) Fitting of  $Y_c$

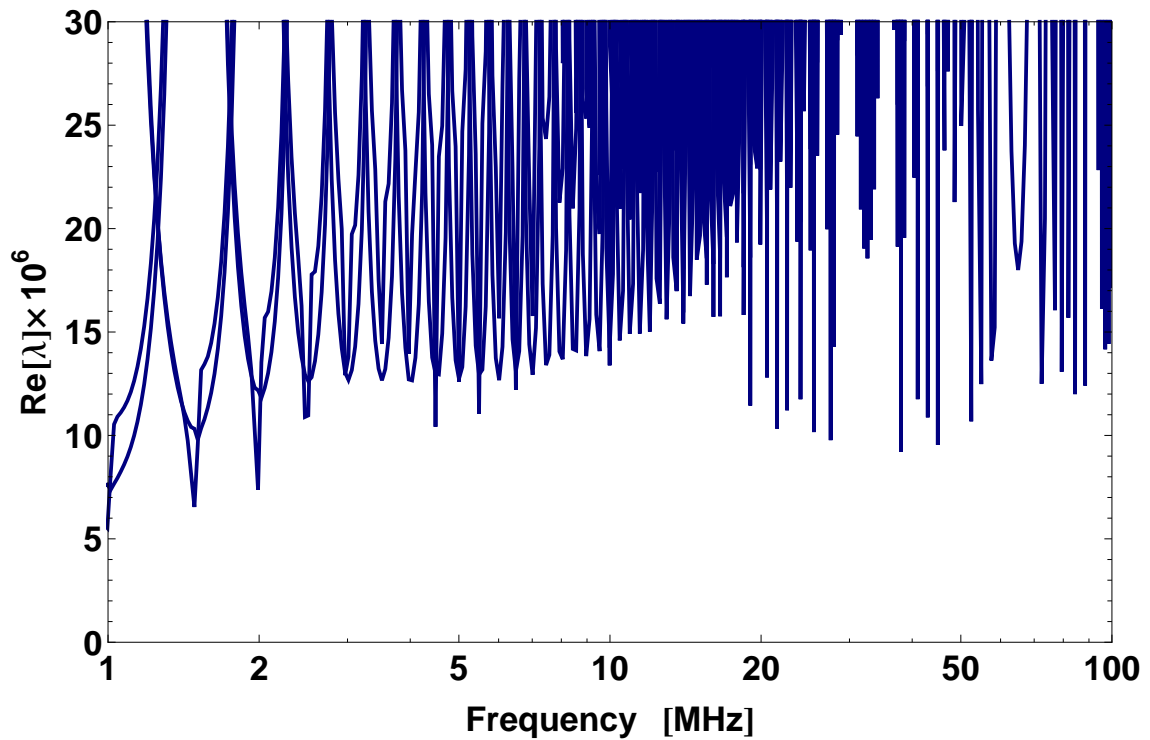


(b) Fitting of  $H$

Figure 4.21: Rational fitting of  $Y_c$  and  $H$  for 138 kV circuit - scalar potential definition



(a) Using the calculated values of  $\mathbf{Y}_n$



(b) Using the rational approximations of  $\mathbf{Y}_c$  and  $\mathbf{H}$

**Figure 4.22:** Passivity violations for 138 kV circuit - scalar potential definition

image approximations of  $\bar{\mathbf{S}}_1$ ,  $\bar{\mathbf{S}}_2$  and  $\bar{\mathbf{T}}$  in (4.9).

The fitting results for both  $\mathbf{Y}_c$  and  $\mathbf{H}$  are depicted in Fig. 4.24.

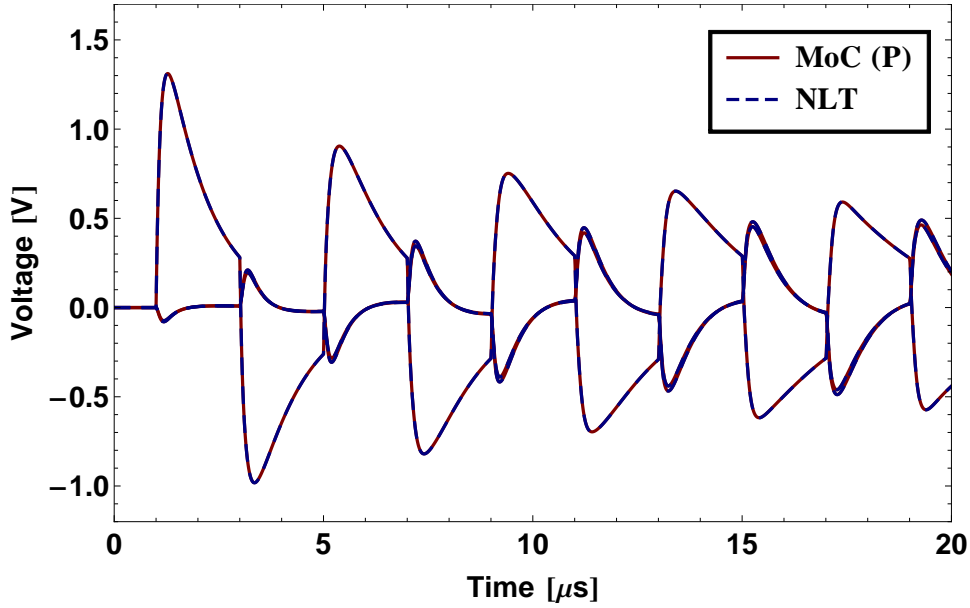
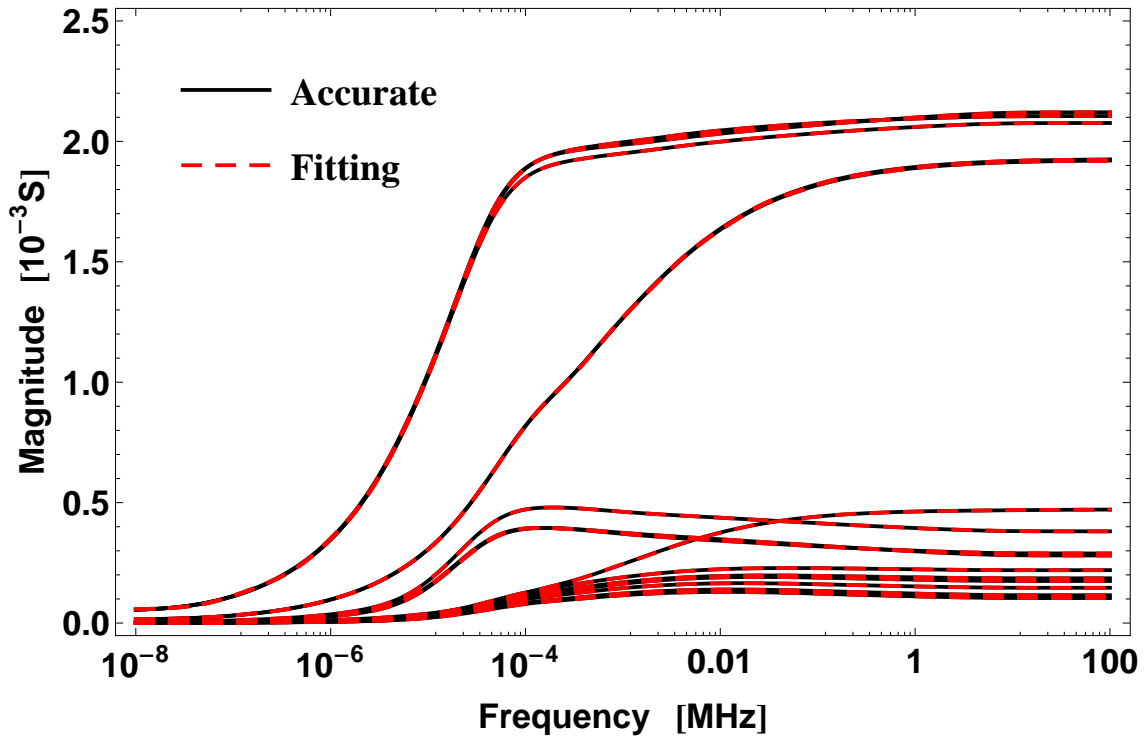


**Figure 4.23:** Time-domain results in 138 kV circuit - scalar potential definition

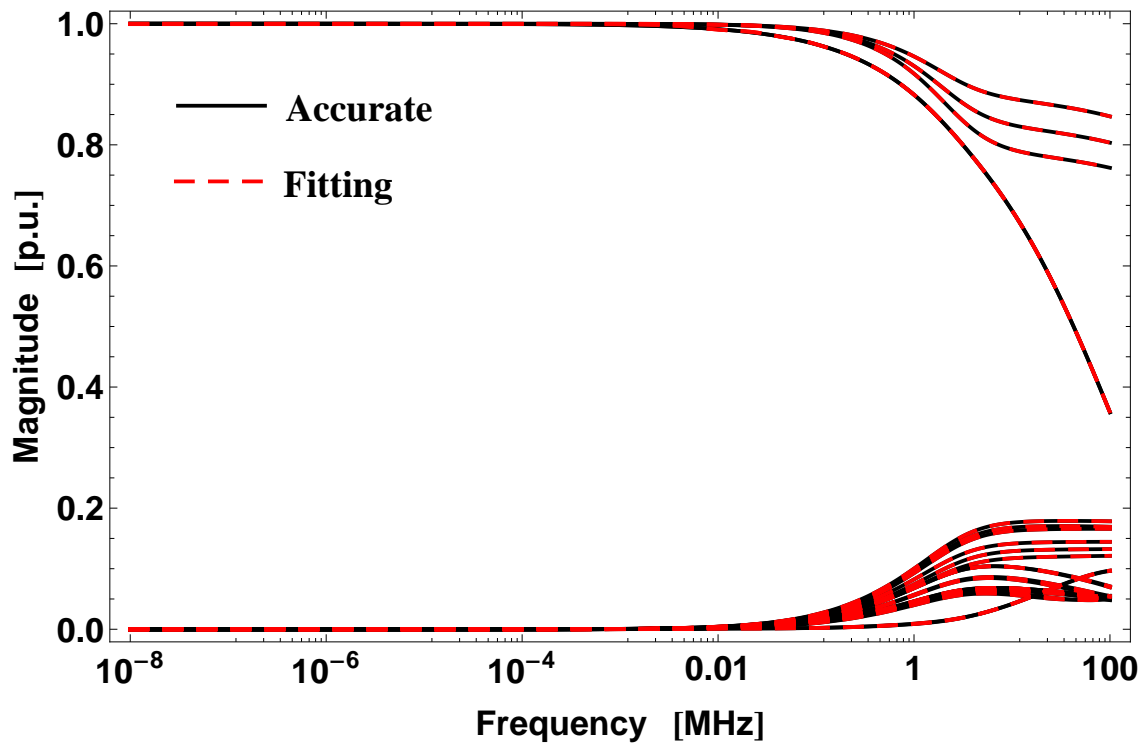
As it can be seen, the behavior of both functions in the frequency-domain is rather similar to the one shown in Fig. 4.21. The main differences are in the fitting results. Using the modified expressions, i.e. with  $\eta = \gamma_2$  the overall error was smaller than using only the electric scalar potential to define the per unit length parameters. The fitting errors are  $1.9 \cdot 10^{-6}$  S for  $\mathbf{Y}_c$  and  $0.2 \cdot 10^{-3}$  p.u. for  $\mathbf{H}$ .

It was also found that the stability of the eigenvalues  $\lambda$  is further increased when the original frequency-domain data or either both rational approximations of  $\mathbf{Y}_c$  and  $\mathbf{H}$  are used for their calculation, as presented in Fig. 4.25.

The corresponding time-domain response obtained using this latter mitigation procedure is shown in Fig. 4.26. For this case, stable results were also attained.

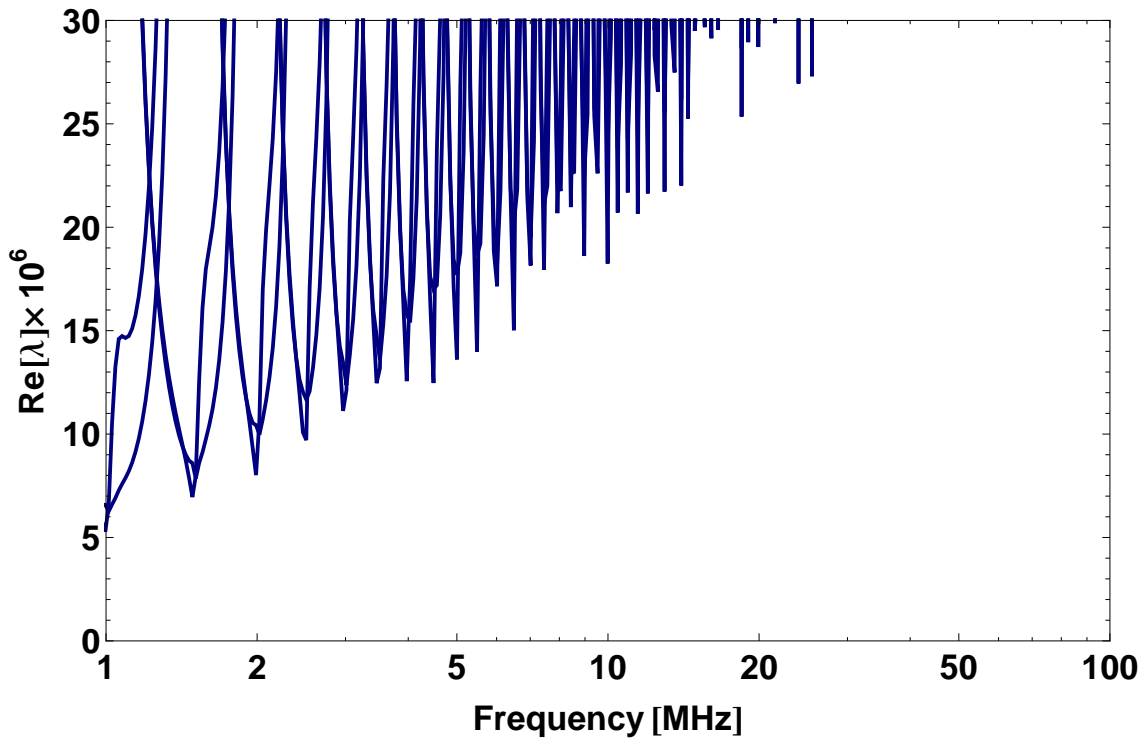


(a) Fitting of  $Y_c$

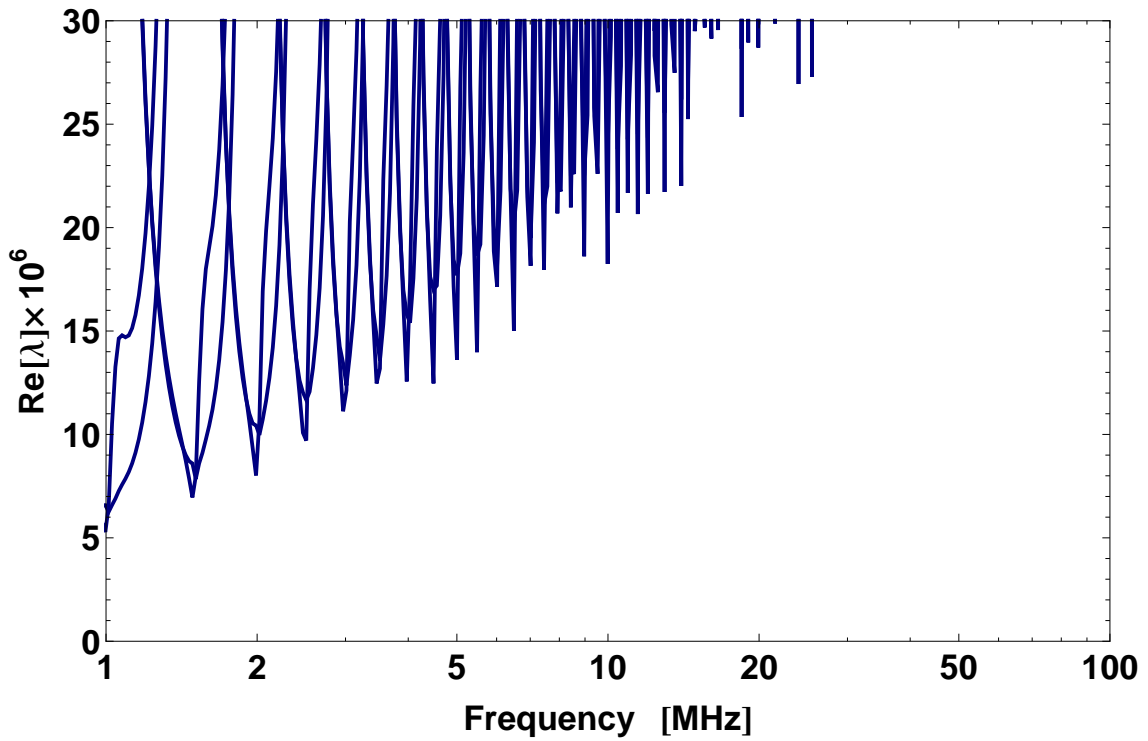


(b) Fitting of  $H$

Figure 4.24: Fitting of  $Y_c$  and  $H$  for 138 kV circuit - scalar potential definition ( $\eta = \gamma_2$ )



(a) Using the calculated values of  $Y_n$



(b) Using the rational approximations of  $Y_c$  and  $H$

**Figure 4.25:** Passivity violations for 138 kV circuit - scalar potential definition ( $\eta = \gamma_2$ )

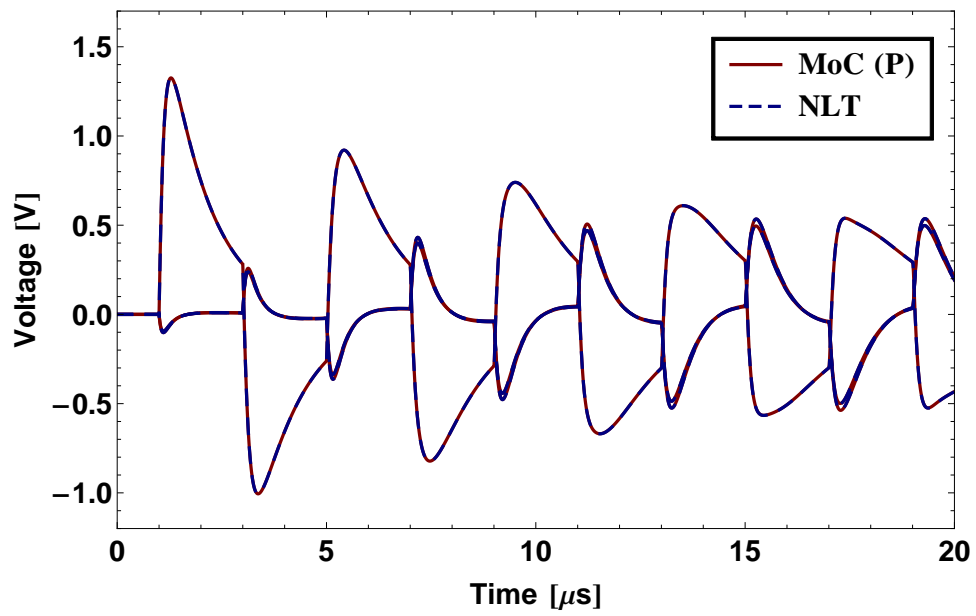


**Figure 4.26:** Time responses for 138 kV circuit - scalar potential definition ( $\eta = \gamma_2$ )



## **4.8 Assessment of Idempotent Decomposition improvement by the use of a quasi-TEM formulation**

We have shown that the use of the so-called image approximations in multi-phase transmission line models for the evaluation of the per-unit-length line parameters might cause numerical instabilities in the high frequency range when ground displacement currents are included in soils with both constant and frequency dependent ground parameters.

To investigate whether the reported issues in the rational fitting of the Idempotent matrices are related to the low accuracy in the evaluation of the per-unit-length line parameters, we calculate these line parameters using a quasi-TEM formulation for the overhead transmission line test cases previously presented in the former chapters:

1. #1: A 500 kV line with 2 ground wires and 3-phases.
2. #2: A 800 kV line with 2 ground wires and 3-phases.
3. #3: A 500 kV line in parallel with a 138 kV line with a total of 6-phases.
4. #4: A 230 kV line with 18-phases.

To calculate the Idempotent matrices from the per-unit-length transmission system parameters using the quasi-TEM formulation, a user defined routine was written in MATHEMATICA.

## 4.8.1 System Geometry and data

The four test case system geometries are presented in Fig. 4.27.

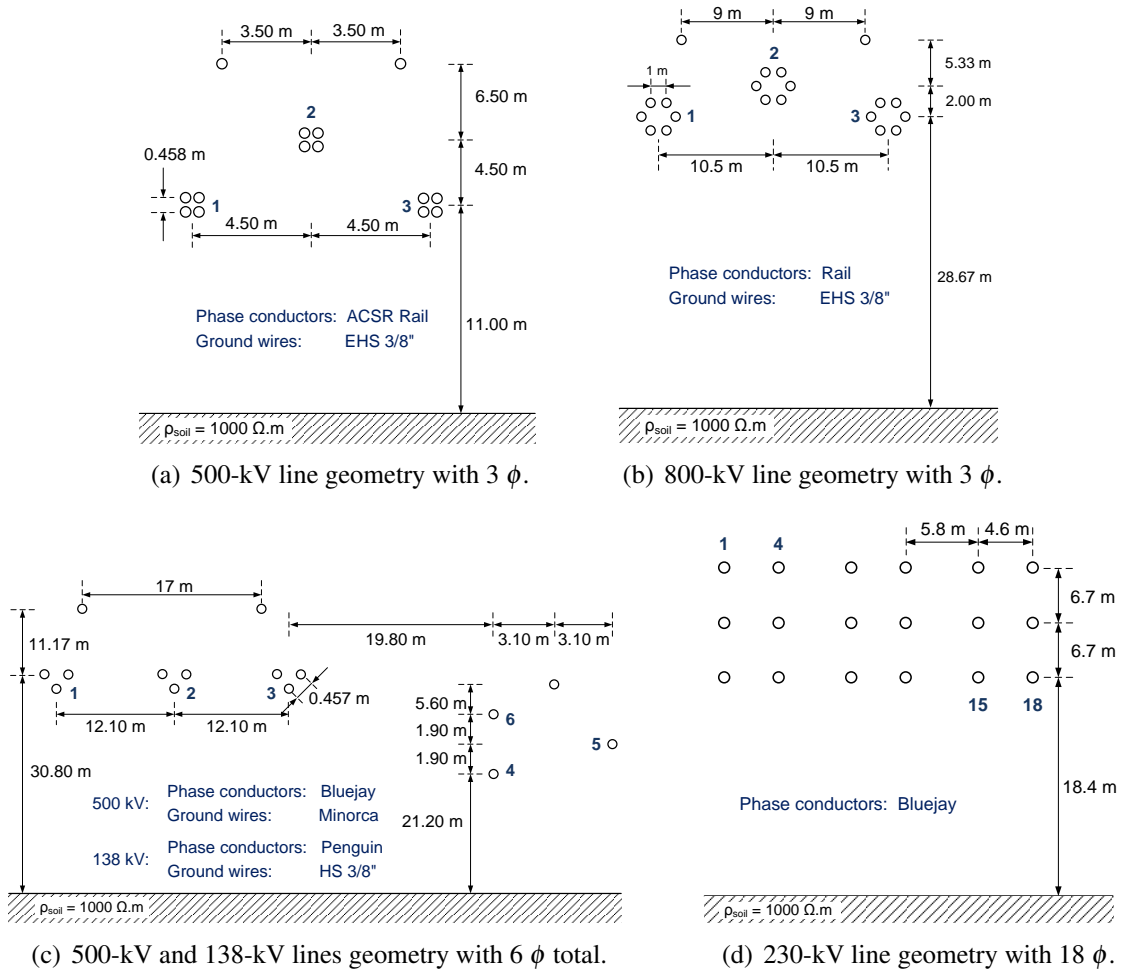


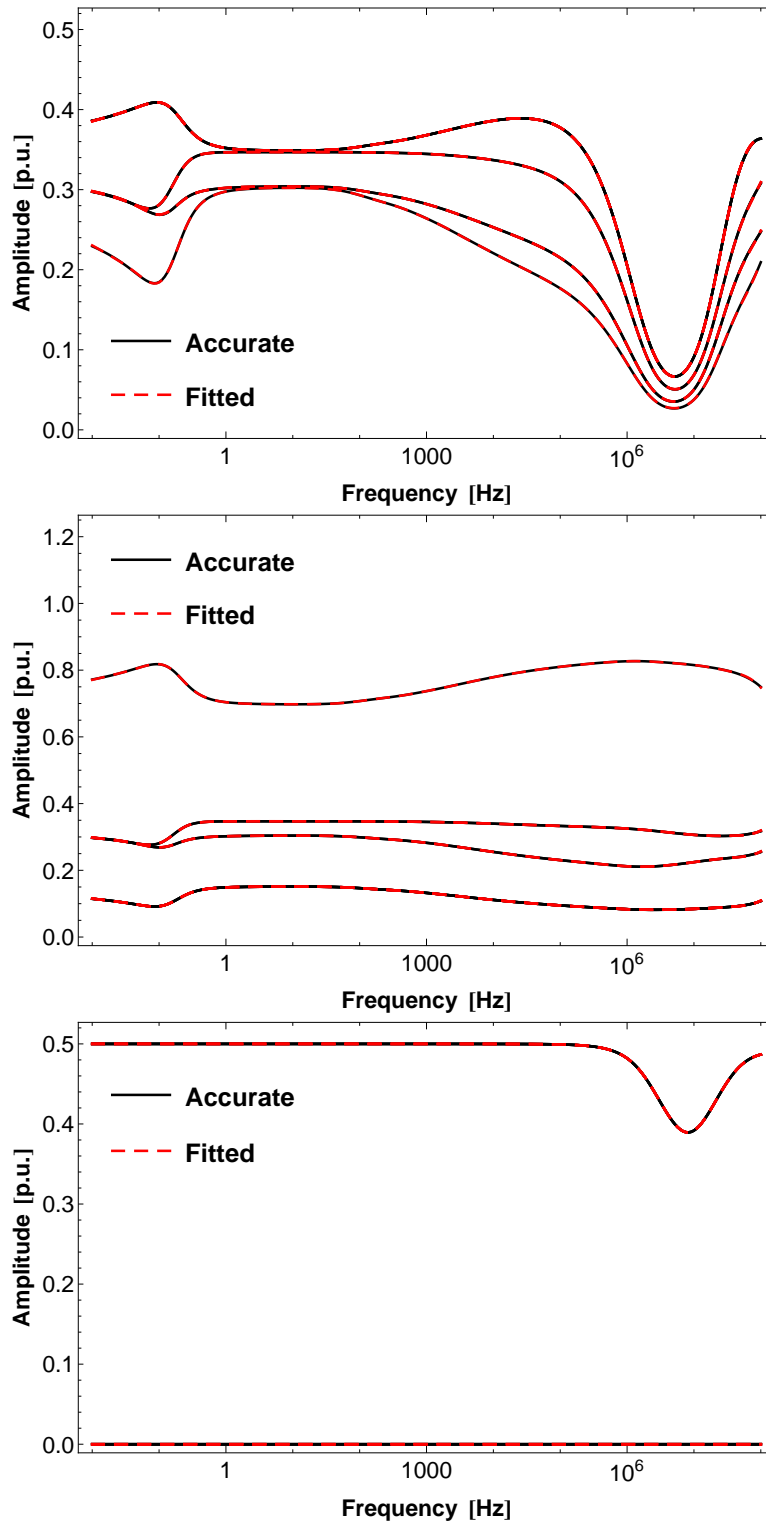
**Figure 4.27:** System geometry of each case.

In all cases, soils with constant ground parameters were considered with a soil relative permittivity of  $\epsilon_2 = 5\epsilon_0$ .

To decrease the dimension of the line parameters matrices, all the ground wires in the overhead transmission lines test cases were represented implicitly using a matrix reduction process.

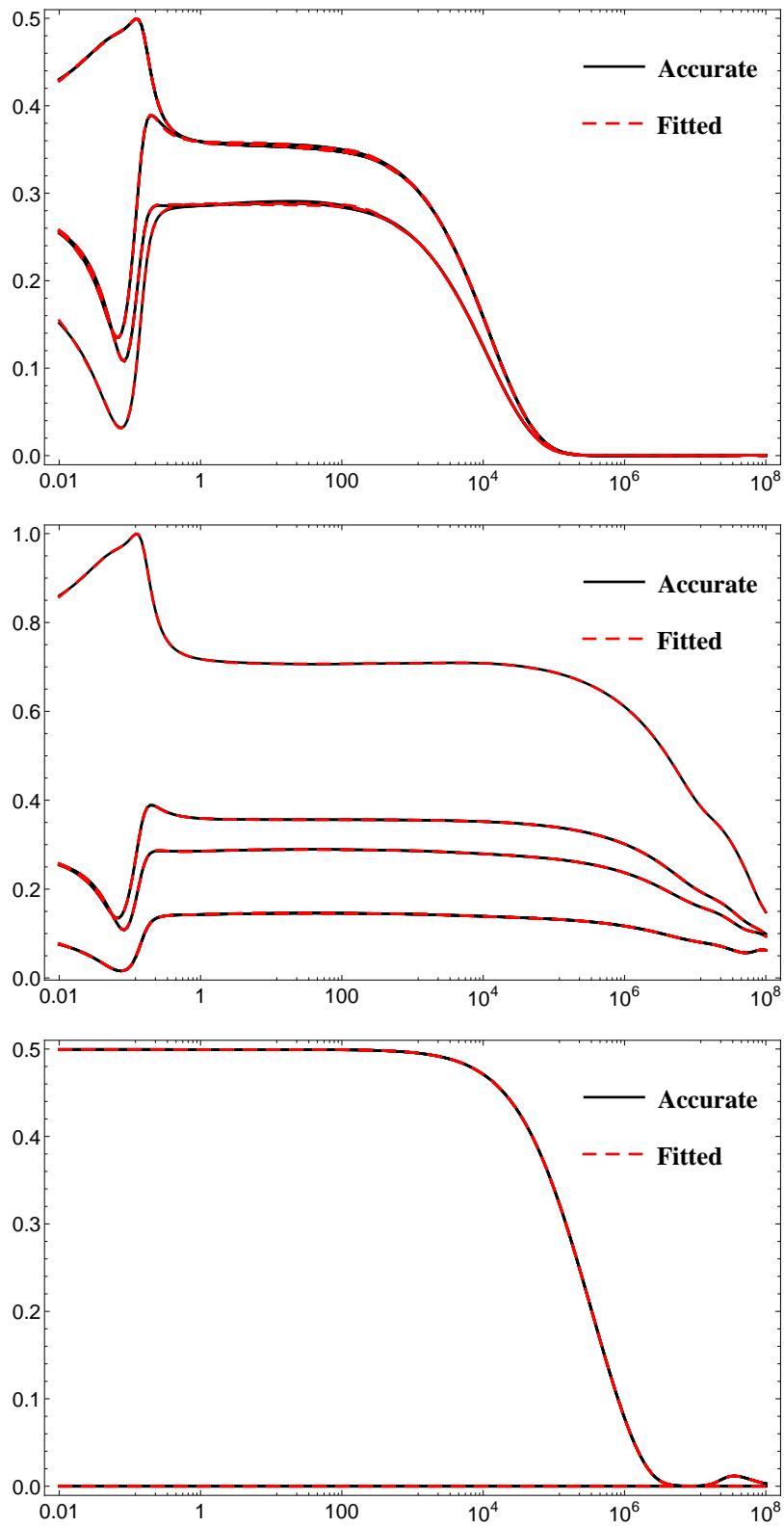
## 4.8.2 Fitting of $\bar{M}_i$

Fig. 4.28 shows the results for the fitting of the elements of the Idempotent matrices  $\bar{M}_i$  for #1.



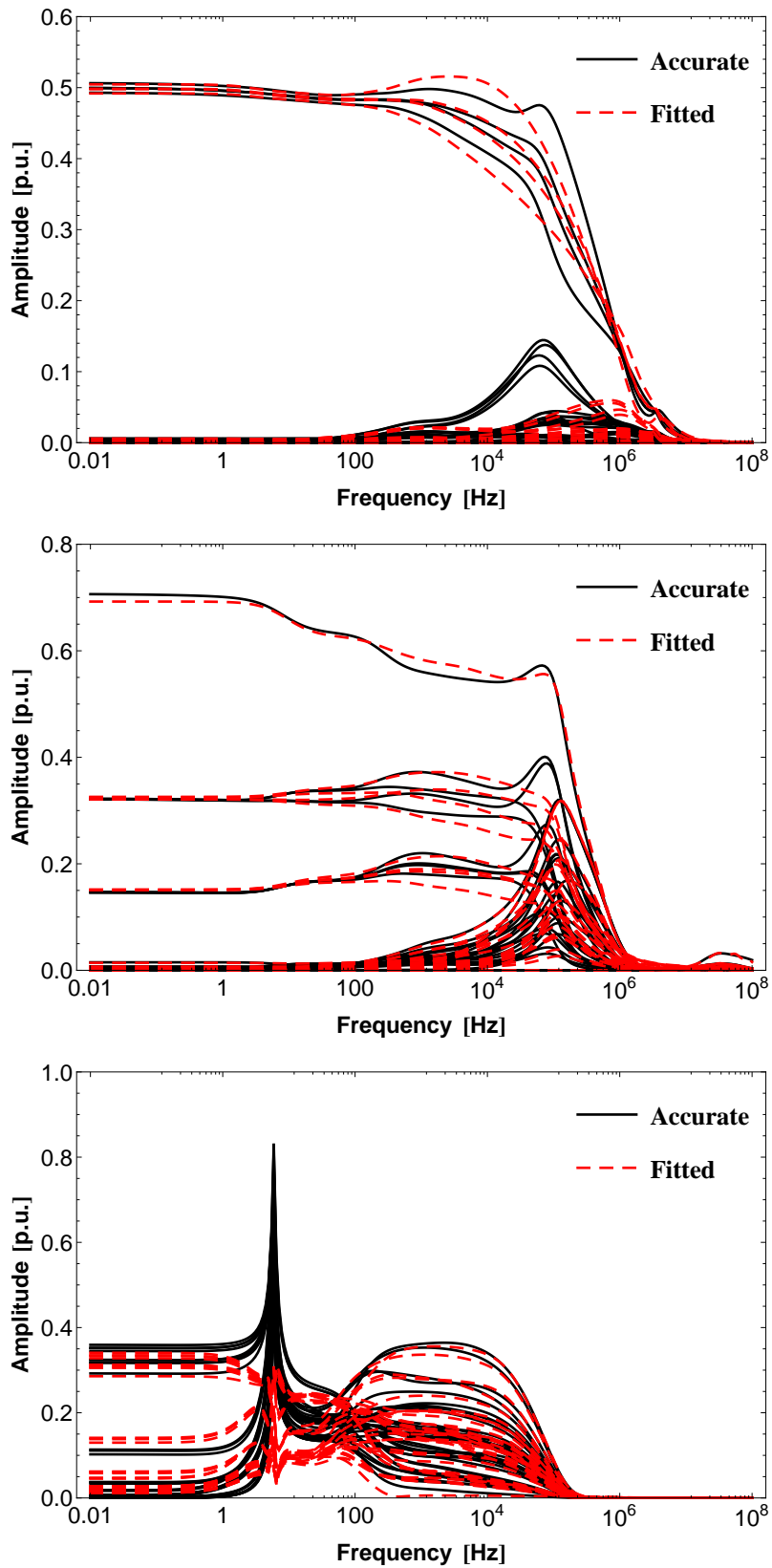
**Figure 4.28:** Rational Fitting of  $\bar{M}_1$ ,  $\bar{M}_2$  and  $\bar{M}_3$  for #1.

Fig. 4.29 shows the results for the fitting of the elements of the Idempotent matrices  $\bar{\mathbf{M}}_i$  for #2.



**Figure 4.29:** Rational Fitting of  $\bar{\mathbf{M}}_1$ ,  $\bar{\mathbf{M}}_2$  and  $\bar{\mathbf{M}}_3$  for #2.

Fig. 4.30 to Fig. 4.31 shows the results for the fitting of the elements of the Idempotent matrices  $\bar{\mathbf{M}}_i$  for #3.



**Figure 4.30:** Rational Fitting of  $\bar{\mathbf{M}}_1$ ,  $\bar{\mathbf{M}}_2$  and  $\bar{\mathbf{M}}_3$  for #3.

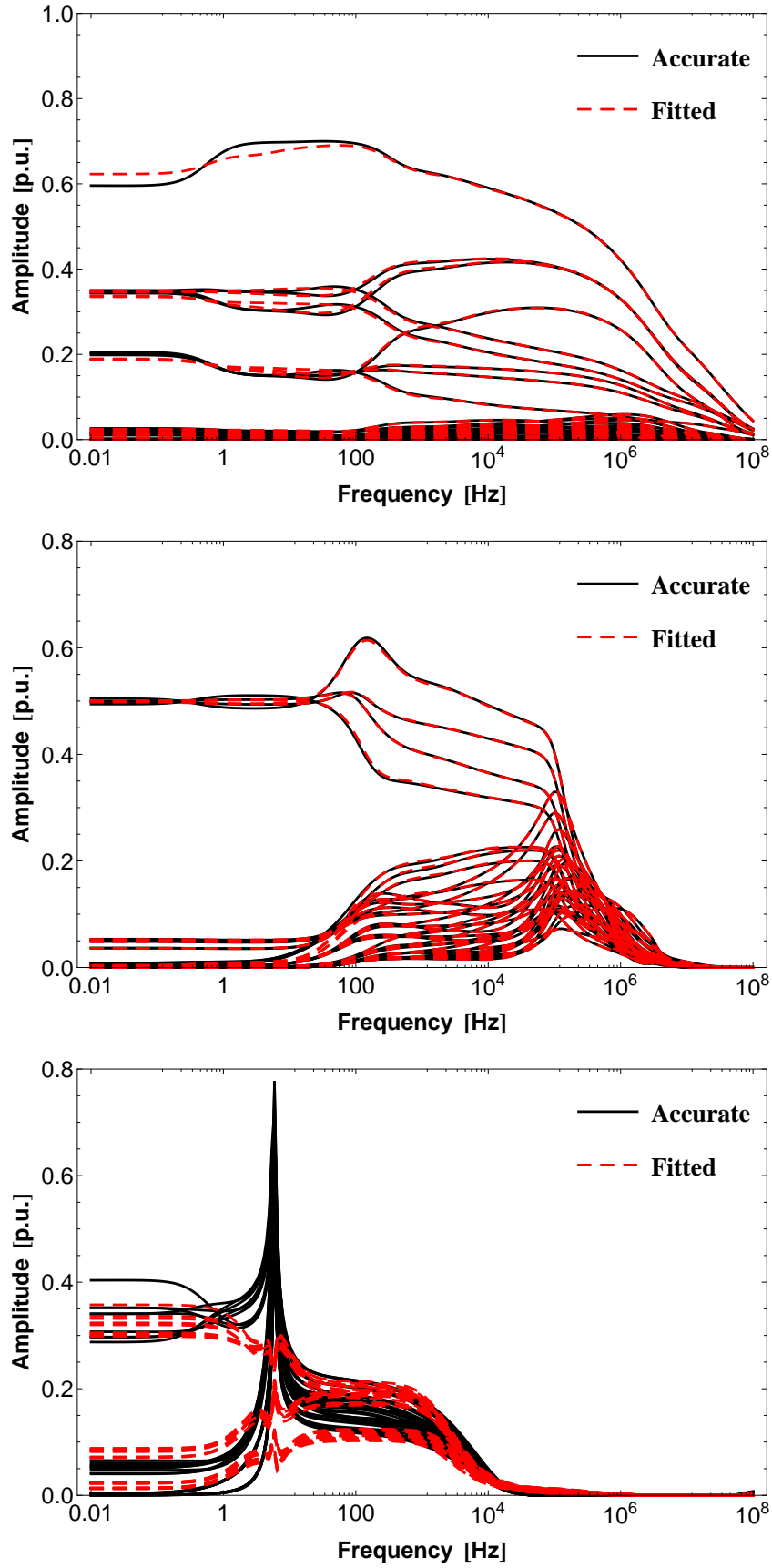
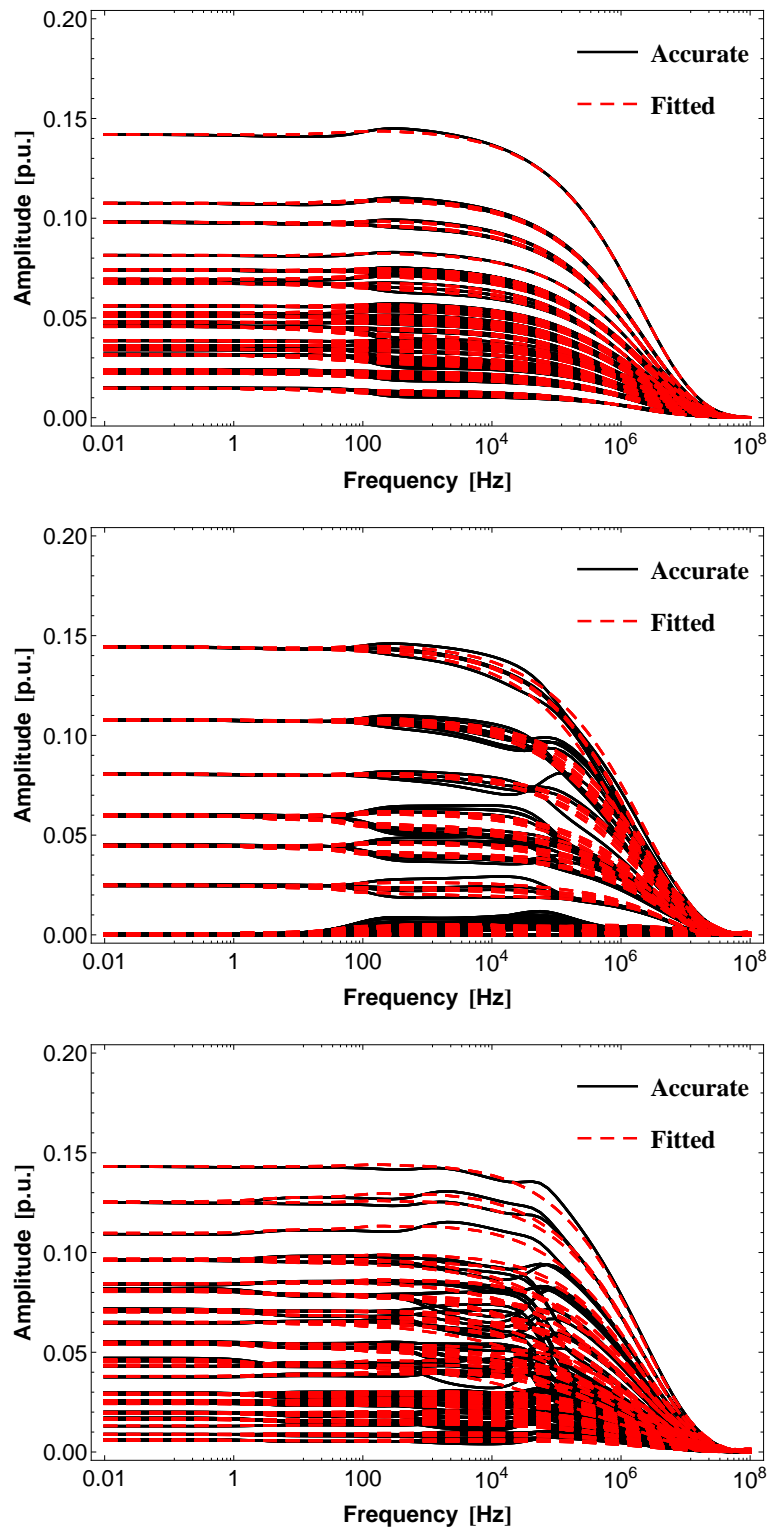


Figure 4.31: Rational Fitting of  $\bar{M}_4$ ,  $\bar{M}_5$  and  $\bar{M}_6$  for #3.

Fig. 4.32 to Fig. 4.37 shows the results for the fitting of the elements of the Idempotent matrices  $\bar{\mathbf{M}}_i$  for #4.



**Figure 4.32:** Rational Fitting of  $\bar{\mathbf{M}}_1$ ,  $\bar{\mathbf{M}}_2$  and  $\bar{\mathbf{M}}_3$  for #4.

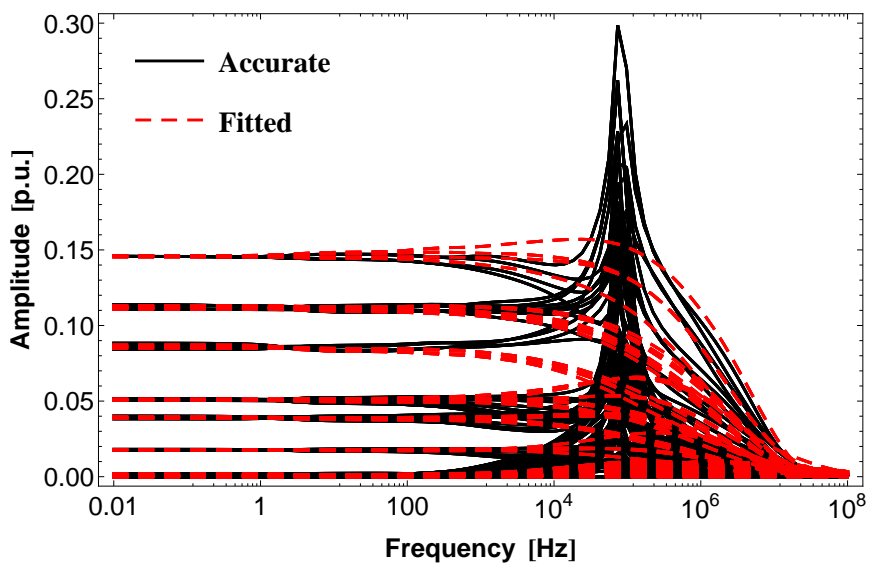
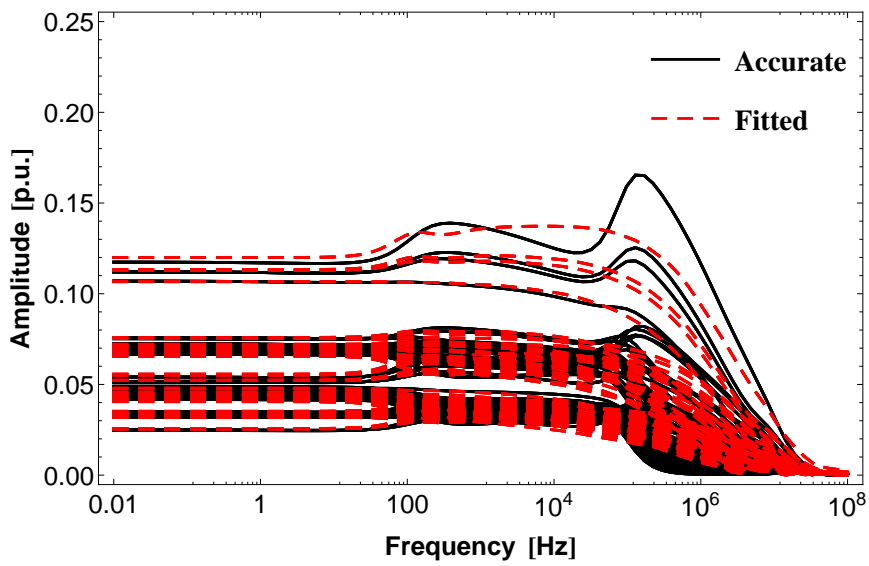
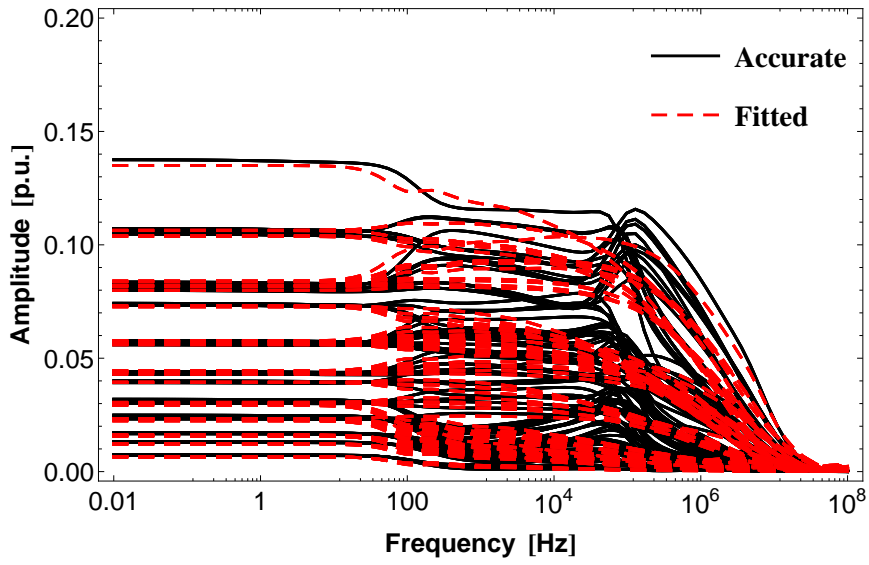


Figure 4.33: Rational Fitting of  $\bar{M}_4$ ,  $\bar{M}_5$  and  $\bar{M}_6$  for #4.



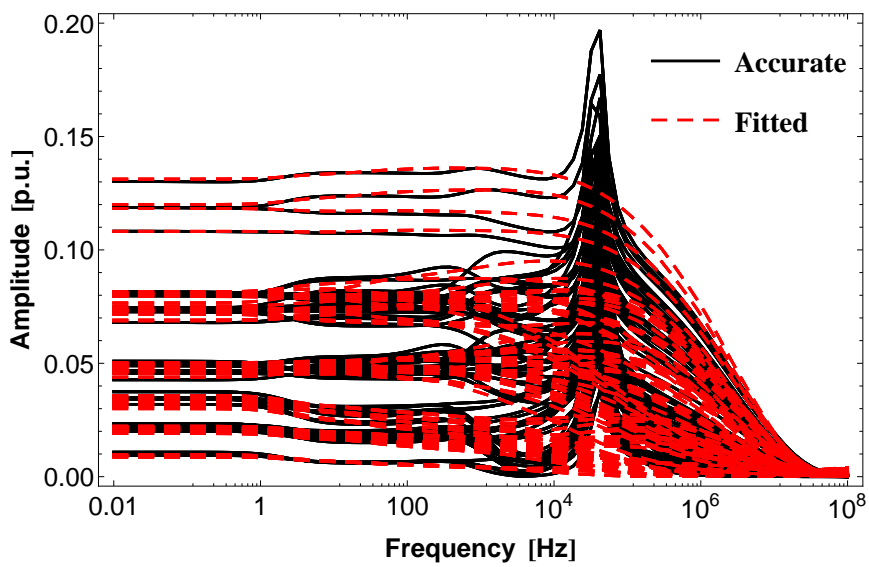
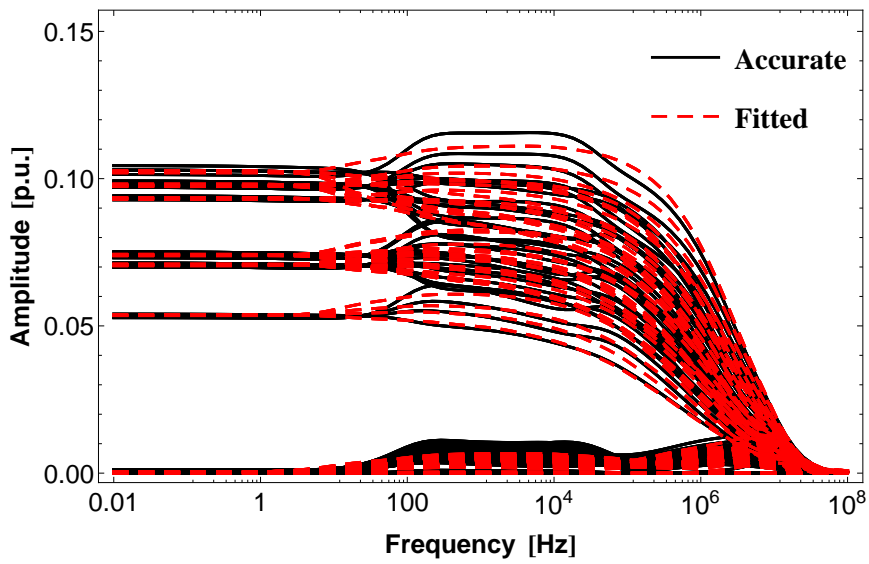
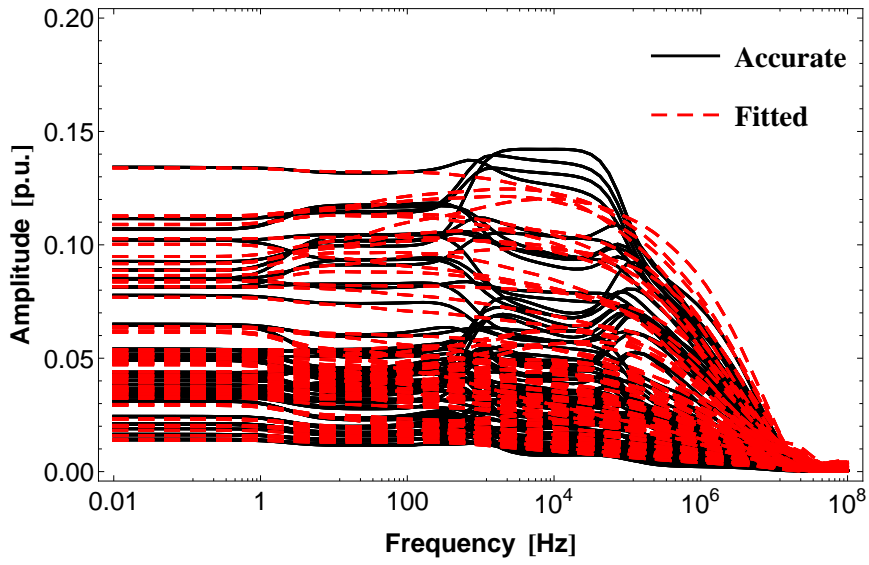


Figure 4.34: Rational Fitting of  $\bar{M}_7$ ,  $\bar{M}_8$  and  $\bar{M}_9$  for #4.

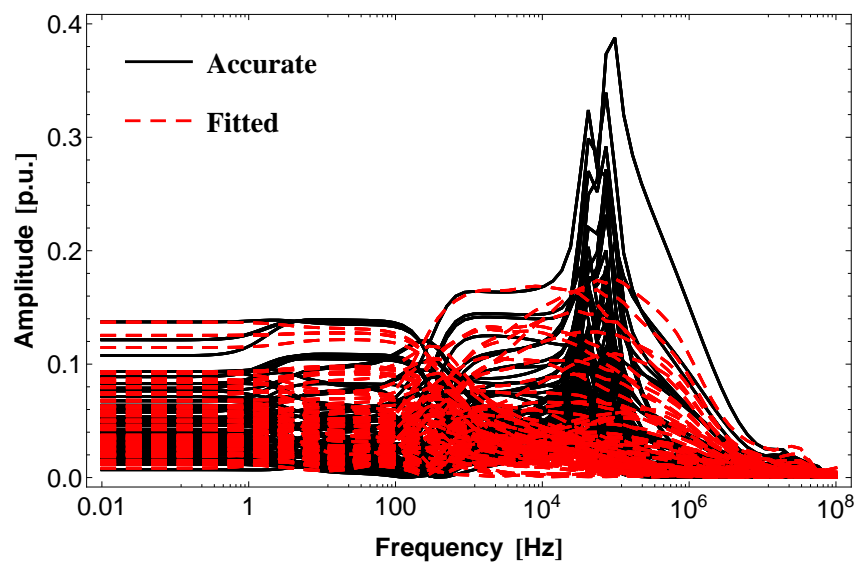
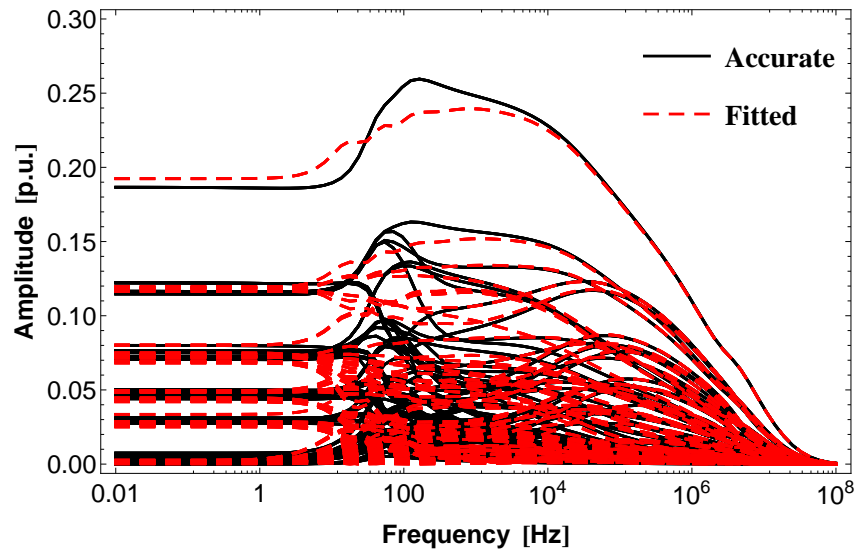
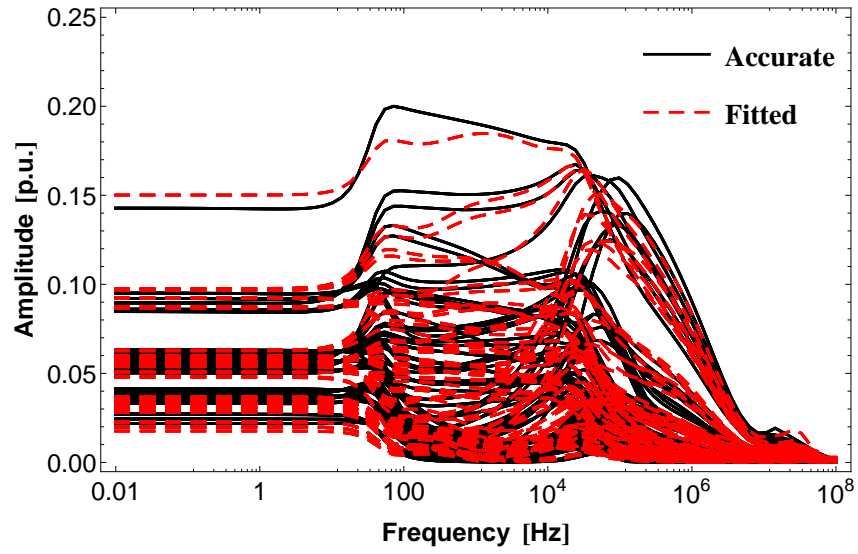


Figure 4.35: Rational Fitting of  $\bar{M}_{10}$ ,  $\bar{M}_{11}$  and  $\bar{M}_{12}$  for #4.

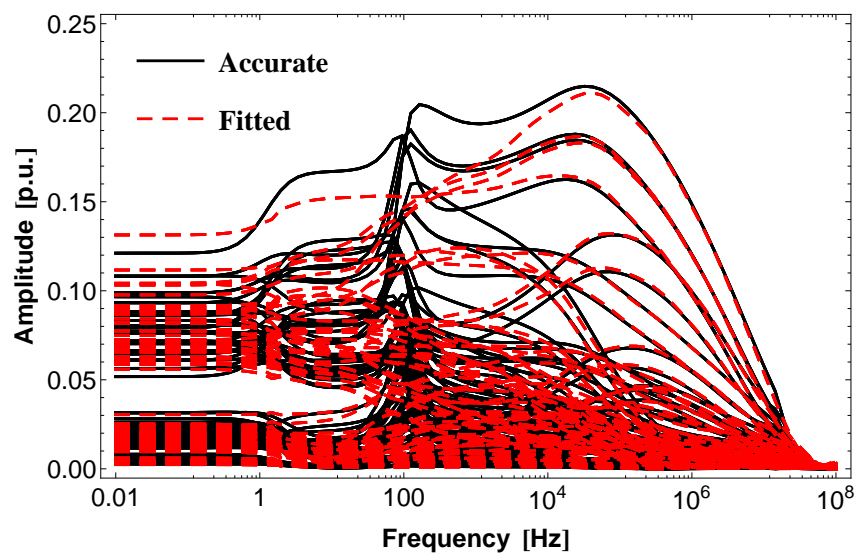
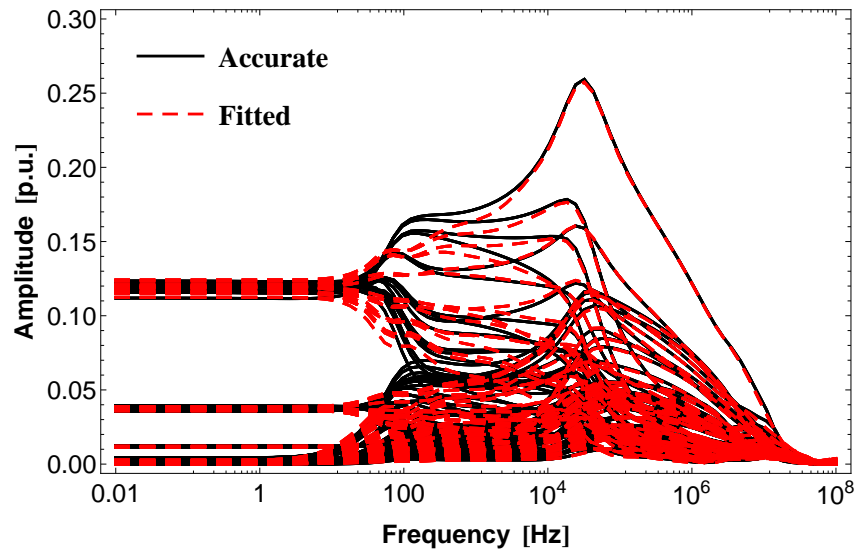
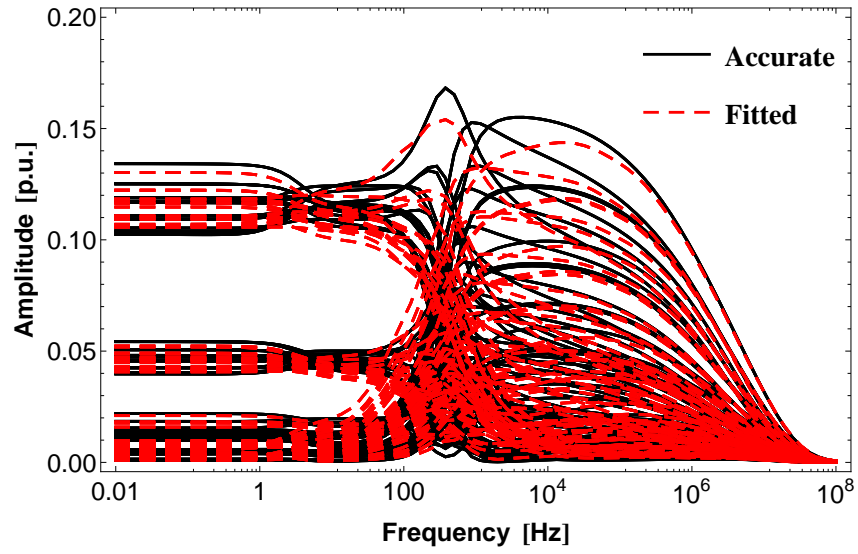


Figure 4.36: Rational Fitting of  $\bar{M}_{13}$ ,  $\bar{M}_{14}$  and  $\bar{M}_{15}$  for #4.

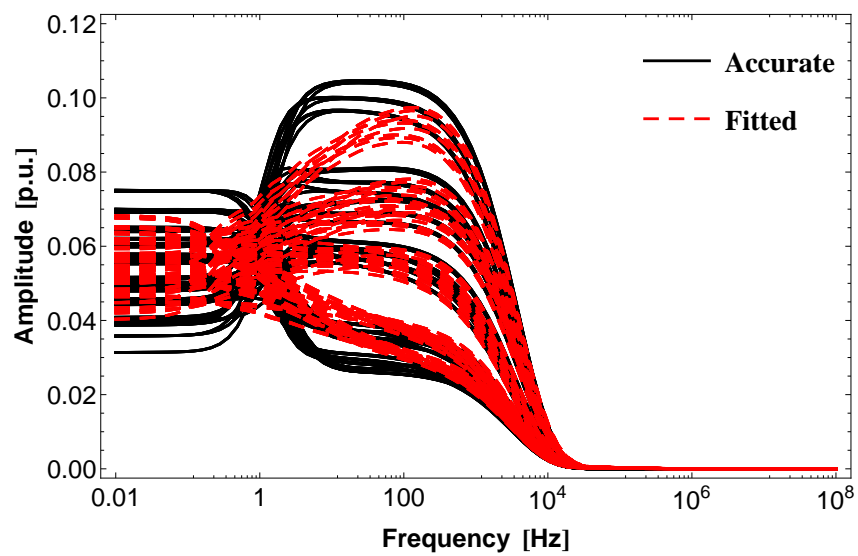
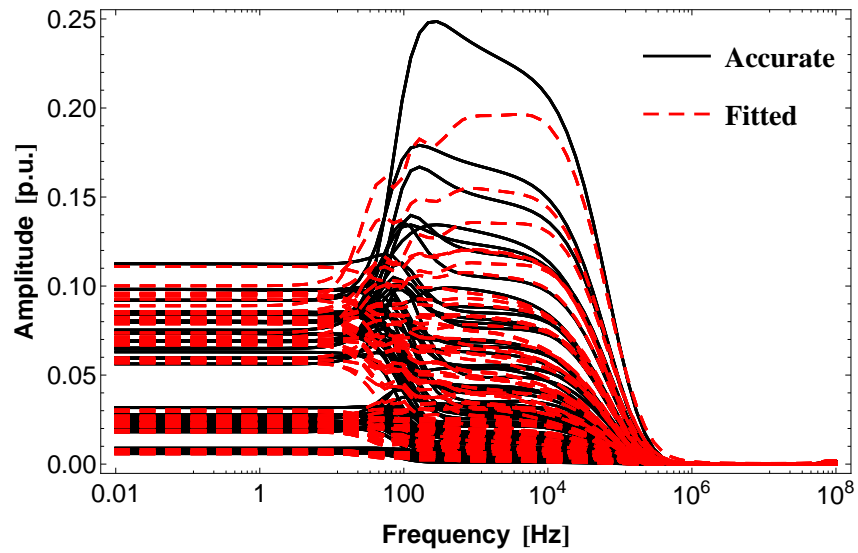
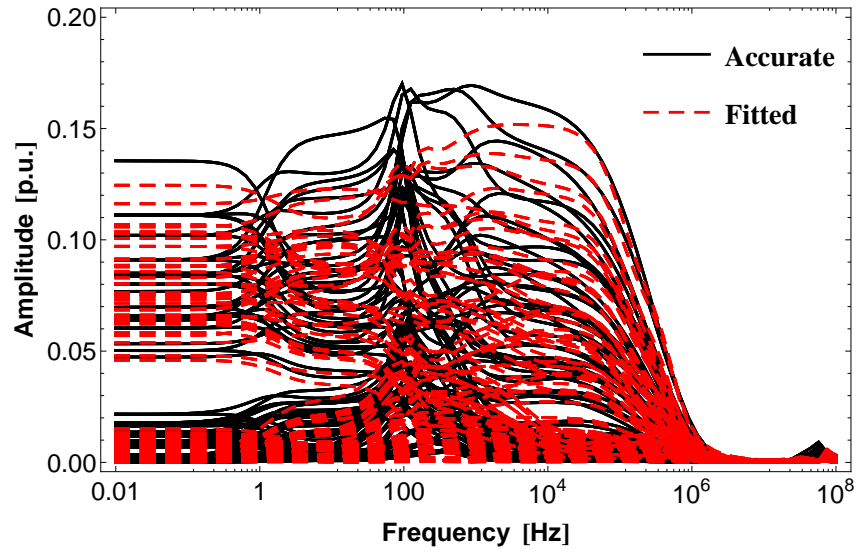


Figure 4.37: Rational Fitting of  $\bar{M}_{16}$ ,  $\bar{M}_{17}$  and  $\bar{M}_{18}$  for #4.

In #1 and #2, despite using a quasi-TEM approach to calculate the Idempotent matrices, the inclusion of a diagonal matrix shunt conductance  $\mathbf{G}$  with value  $3 \cdot 10^{-11}$  S/m to the per-unit-length transmission line admittance was still necessary to avoid low frequency oscillations in the fitting of the Idempotent matrices  $\overline{\mathbf{M}}_i$ . Furthermore, for #3 and #4, the use of a quasi-TEM formulation rendered no improvement in the fitting of the Idempotent matrices was noted, as an inaccurate fitting is still attained.

No significant accuracy improvement in the fitting of the Idempotent matrices was obtained in the test cases considered.

## 4.9 Discussion

In this chapter, we investigated some numerical issues related to the multiphase transmission line model when image approximations are used to include ground displacement currents considering soils with both constant and frequency dependent ground parameters.

For three test case examples of 138 kV, 230 kV and 500 kV multiphase overhead lines, it was found that the use of the image approximations originates small passivity violations in the high frequency range of the Nodal Admittance Matrix, starting typically around 10 MHz for both soils with constant and frequency dependent parameters. These instabilities are mainly related to the error in the image approximation of the infinite integral term present in both the per-unit-length series impedance and the shunt admittance. Furthermore, as reported in Chapter 3 for a single-phase line with constant ground parameters, an upper frequency limit of the images approximations was also found, as the magnitude of passivity violations is related to the line length. A smooth low order fit was found for the modes of the propagation function and for the characteristic admittance, with the latter being positive definite throughout the frequency range considered.

Time-domain responses obtained using the Method of Characteristics with a slightly perturbed impulse voltage to excite the passivity violations found using Image approximations were inaccurate. Nonetheless, a stable behavior was obtained using the Numerical Laplace Transform due to the damping effect of the complex frequencies used in its processing algorithm.

Two mitigation procedures were considered where an image approximation is still possible. The expressions used can be seen as a further simplification from the actual expressions of impedance and admittance matrices. The time-domain responses for both scenarios indicate the viability of both procedures.

It is important to stress that if a quasi-TEM formulation is used or the ground permittivity is neglected, the passivity violations reported here for soil models with both constant and frequency dependent ground parameters do not occur. It is the inclusion of the ground displacement currents in the line model using the image approximations that leads to the aforementioned numerical instabilities reported here. Further research is still needed to improve the quality of the image approximations.

Finally, an Idempotent line model based on a quasi-TEM formulation of the per-unit-length line parameters is tested to verify if the cause of the poor quality fit of the Idempotent Matrices reported in the examples of Chapter 2 is related to the low accuracy of the image approximations. No significant accuracy improvement in the rational fitting of the Idempotent Matrices is observed for any of the test-cases presented here, still requiring the inclusion of a diagonal matrix shunt conductance to the per-unit-length transmission line admittance to avoid low frequency oscillations in the fitting of the Idempotent matrices in spite of using a more precise quasi-TEM formulation line model.

# Chapter 5

## Conclusions

### 5.1 Final Conclusions

In the preceding chapters we presented the research carried out during this doctorate project. It concerns mainly with the applicability, limitations, numerical stability and precision of rational modeling in transmission lines. The following conclusions were obtained:

- The inaccuracies in the rational approximation of the Idempotent matrices when idempotent modeling in overhead lines is used are not related to the precision of the calculation of the per-unit-length line parameters. This was verified by evaluating the idempotent modeling considering a quasi-TEM formulation of such parameters. No improvement of the rational approximations involved in the Idempotent modeling was observed.
- The Idempotent line model can be used as a feasible alternative to the ULM approach for phase coordinate modeling of Single-Core underground cables.
- Although stable time-domain simulations can be achieved using the idempotent modeling for overhead transmission line models, the accuracy is reduced as the fitting order of the rational approximations increase with the number of phases involved. This issue merits future work to evaluate how to improve the rational fitting procedure to obtain a better approximation of the Idempotent Matrices.
- The implementation of a multiphase full-wave line model for time-domain simulation presented the following issues:
  - The existence of a pronounced discontinuity in both the propagation function and the characteristic admittance, which leads to difficulties in the frequency domain fitting, causing high order rational functions and some problems with the time-delay identification required for the Method of Characteristics.

- The large number of complex-valued frequency samples required for an efficient simulation using the Numerical Laplace Transform remains as an issue, even though the increasing processing speed of computers facilitates the root finding scheme of the unknown propagation constant of the circuit.
- Through a suitable change in the initial guess in the root finding scheme of the full wave model, the computational burden in the calculation of the unknown propagation constant can be improved.
- Frequency domain modeling of multiphase overhead lines using the so-called image approximations for the evaluation of the per-unit-length parameters when ground displacement currents are considered presented passivity violations in the range of 10 MHz to 100 MHz. This was verified using a simpler configuration: a single-phase transmission line.
- Time-domain modeling based on the rational fitting of the aforementioned frequency domain models led to a numerically unstable behavior when a small harmonic perturbation in the range of 10 MHz to 100 MHz was added to the input voltage. While both the characteristic admittance and the propagation function present a smooth behavior, allowing a low order fitting, the nodal admittance matrix still presented passivity violations in the high frequency range over 10 MHz, which led to numerically unstable impulse response simulations.
- The modeling of the line using a quasi-TEM formulation instead of the conventional closed-form expressions prevents the aforementioned numerical instabilities. Although successful, it has the disadvantage of dealing with infinite integrals that may pose some challenges in the numerical evaluation.
- For the three frequency dependent soil models evaluated, the inclusion of frequency dependent soil parameters was unsuccessful to overcome the numerical instabilities issue, even considering a soil model associated with physical coherent ground parameter data valid up to 200 MHz.
- Two mitigation procedures were considered where an image approximation is still possible. The expressions used can be seen as a further simplification from the actual expressions of impedance and admittance matrices. The time-domain responses for both scenarios indicates the viability of both procedures.
- It was found that longer lines are not subject to passivity violations. In fact, as the line length increases, the mismatch between the values found in the infinite integrals and in the image approximation formulas decreases.



- The time-domain responses indicate that there is a minimal length for the realization of transmission line models based on the image approximations. The inclusion of frequency dependent soil parameters which represents an increase in the model accuracy did not overcome this limitation.

The principal contributions of the present work are:

- The suitability of Idempotent line model as a feasible alternative to the ULM approach for phase coordinate modeling of underground cables has been determined.
- A novel time-domain implementation of the idempotent modeling using the Method of Characteristics for Single-Core underground cables as an alternative to the Universal Line Model has been successfully achieved.
- A limitation to the number of phases an Idempotent Line model can accurately represent in transmission lines has been found. Although issues with Idempotent modeling have been previously reported in the technical literature, no specific details were given.
- An Idempotent grouping process analogue to the one used in the Universal Line Model was implemented.
- Previously unreported accuracy issues in the image approximations for the calculation of per-unit-length line parameters have been found.
- Issues concerning the implementation of a multiphase full-wave line model using both the Method of Characteristics and the Numerical Laplace Transform have been clearly identified and described.
- A procedure to improve the computational burden in the calculation of the unknown propagation constant in the full-wave model has been determined.

## 5.2 Future Research

The rational modeling of frequency dependent functions for the simulation of electromagnetic transients is still a theme with multiple research possibilities. To continue this line of work we suggest the following:

- Research the causes of the accuracy loss in the fitting of the Idempotent Matrices in overhead transmission line modeling when the number of phases involved is increased by a revision of the mathematical formulation of the Idempotent Line model.

- As the suitability of the Idempotent model for Single-Core cables was determined, further research on the accuracy of the Idempotent Line model for Trifoil and Pipe-Type cables is in order, as well as their implementation in EMTP type programs.
- Evaluate the rational approximations associated with the idempotent modeling using other techniques such as matrix pencil, Levenberg-Marquadt or others.
- An assessment of a full wave line model considering either multi-phase conductors, frequency dependent ground parameters and non-homogeneous lines, evaluated using different calculation methods such as the discretization of the line, as well as time-domain simulation of such models using either the Numerical Laplace Transform or the Method of Characteristics.
- Development of alternative closed-form expressions to calculate the per-unit-length parameters that might present an improved numerical stability when compared with the image approximation formulas.
- An assessment of the frequency range of validity of frequency-dependent soil models for very fast transients.

# Bibliography

- [1] WEDEPOHL, L. “Application of matrix methods to the solution of travelling-wave phenomena in polyphase systems”, *Electrical Engineers, Proceedings of the Institution of*, v. 110, n. 12, pp. 2200–2212, Dec. 1963. ISSN: 0020-3270. doi: 10.1049/piee.1963.0314.
- [2] FOR BPA), H. W. D. P. *ElectroMagnetic Transients Program Reference Manual (EMTP Theory Book)*. Branch of System Engineering - Bonneville Power Administration, 1995.
- [3] PRIKLER, L., HOIDALEN, H. K. *ATPDraw version 3.5 for Windows 9x/NT/2000/XP User’s Manual*. SINTEF Energy Research, out. 2002.
- [4] HOIDALEN, H. K. “User manual supplements - New features in ATPDraw v5”. Nov. 2007.
- [5] SEMLYEN, A., DABULEANU, A. “Fast and accurate switching transient calculations on transmission lines with ground return using recursive convolutions”, *IEEE Trans. on Power Apparatus and Systems*, v. 94, n. 2, pp. 561–571, Mar. 1975. ISSN: 0018-9510. doi: 10.1109/T-PAS.1975.31884.
- [6] MARTI, J. “Accurate Modelling of Frequency-Dependent Transmission Lines in Electromagnetic Transient Simulations”, *IEEE Trans. on Power Apparatus and Systems*, v. PAS-101, n. 1, pp. 147–157, Jan. 1982. ISSN: 0018-9510. doi: 10.1109/TPAS.1982.317332.
- [7] NODA, T., NAGAOKA, N., AMETANI, A. “Phase domain modeling of frequency-dependent transmission lines by means of an ARMA model”, *IEEE Trans. on Power Delivery*, v. 11, n. 1, pp. 401–411, Jan. 1996. ISSN: 0885-8977. doi: 10.1109/61.484040.
- [8] HEDMAN, D. E. “Propagation on Overhead Transmission Lines I-Theory of Modal Analysis”, *IEEE Trans. on Power Apparatus and Systems*, v. 84, n. 3, pp. 200–205, Mar. 1965. ISSN: 0018-9510. doi: 10.1109/TPAS.1965.4766176.

- [9] WEDEPOHL, L. *The theory of Natural Modes in Multiconductor Transmission Systems*. Relatório técnico, The University of British Columbia, Sep. 1997.
- [10] SEMLYEN, A. “Contributions to the Theory of Calculation of Electromagnetic Transients on Transmission Lines with Frequency Dependent Parameters”, *IEEE Trans. on Power Apparatus and Systems*, v. PAS-100, n. 2, pp. 848–856, Feb. 1981. ISSN: 0018-9510. doi: 10.1109/TPAS.1981.316943.
- [11] SEMLYEN, A., ABDEL-RAHMAN, M. “Transmission line modeling by rational transfer functions”, *IEEE Trans. on Power Apparatus and Systems*, v. PAS-101, n. 9, pp. 3576–3584, Sep. 1982.
- [12] GOMEZ, P. “Validation of ATP Transmission Line Models for a Monte Carlo Study of Switching Transients”. In: *Power Symposium, 2007. NAPS '07. 39th North American*, pp. 124 –129, Oct. 2007. doi: 10.1109/NAPS.2007.4402298.
- [13] HEVIA, O. P. “Comparación de los modelos de línea del ATP”, *Revista Iberoamericana del ATP*, v. 1, n. 1, pp. 1–11, Mar. 1999.
- [14] ANGELIDIS, G., SEMLYEN, A. “Direct phase-domain calculation of transmission line transients using two-sided recursions”, *IEEE Trans. on Power Delivery*, v. 10, n. 2, pp. 941–949, Apr. 1995.
- [15] GUSTAVSEN, B., SLETBAK, J., HENRIKSEN, T. “Calculation of the electromagnetic transients in transmission cables and lines taking frequency dependent effects accurately account”, *IEEE Trans. on Power Delivery*, v. 10, n. 2, pp. 1076–1084, Apr. 1995.
- [16] NODA, T., NAGAOKA, N., AMETANI, A. “Further Improvements to a Phase-Domain ARMA Line Model in Terms of Convolution, Steady-State Initialization, and Stability”, *IEEE Trans. on Power Delivery*, v. 12, n. 3, pp. 1327–1334, Jul. 1997.
- [17] NGUYEN, H., DOMMEL, H., MARTI, J. “Direct phase-domain modelling of frequency-dependent overhead transmission lines”, *IEEE Trans. on Power Delivery*, v. 12, n. 3, pp. 916–921, Jul. 1997.
- [18] CASTELLANOS, F., MARTI, J. “Full Frequency-Dependent Phase-Domain Transmission Line Model”, *IEEE Trans. on Power Systems*, v. 12, n. 3, pp. 1331–1339, Aug. 1997.
- [19] CASTELLANOS, F., MARTI, J., MARCANO, F. “Phase-domain multiphase transmission line models”, *International Journal of Electrical Power & Energy*

*Systems*, v. 19, n. 4, pp. 241–248, 1997. ISSN: 0142-0615. doi: [http://dx.doi.org/10.1016/S0142-0615\(96\)00039-7](http://dx.doi.org/10.1016/S0142-0615(96)00039-7). Power Systems Transients.

- [20] MORCHED, A., GUSTAVSEN, B., TARTIBI, M. “A universal model for accurate calculation of electromagnetic transients on overhead lines and underground cables”, *IEEE Trans. on Power Delivery*, v. 14, n. 3, pp. 1032–1038, Jul. 1999. ISSN: 0885-8977. doi: 10.1109/61.772350.
- [21] YU, T.-C., MARTI, J. R. “A robust phase-coordinates frequency-dependent underground cable model (zCable) for the EMTP”, *IEEE Trans. on Power Delivery*, v. 18, n. 1, pp. 189–194, Jan. 2003. ISSN: 0885-8977. doi: 10.1109/TPWRD.2002.807749.
- [22] HENDRICKX, W., DHAENE, T. “A discussion of "Rational approximation of frequency domain responses by vector fitting"”, *IEEE Transactions on Power Systems*, v. 21, n. 1, pp. 441–443, Feb. 2006. ISSN: 0885-8950. doi: 10.1109/TPWRS.2005.860905.
- [23] GUSTAVSEN, B., SEMLYEN, A. “Simulation of Transmission Line Transients using Vector Fitting and Modal Decomposition”, *IEEE Trans. on Power Delivery*, v. 13, n. 2, pp. 605–614, Apr. 1998. ISSN: 0885-8977. doi: 10.1109/61.660941.
- [24] GUSTAVSEN, B., SEMLYEN, A. “Rational approximation of frequency domain responses by vector fitting”, *IEEE Trans. on Power Delivery*, v. 14, n. 3, pp. 1052–1061, Jul. 1999. ISSN: 0885-8977. doi: 10.1109/61.772353.
- [25] GUSTAVSEN, B. “Relaxed Vector Fitting Algorithm for Rational Approximation of Frequency Domain Responses”. In: *IEEE Workshop on Signal Propagation on Interconnects*, pp. 97–100, May 2006. doi: 10.1109/SPI.2006.289202.
- [26] GUSTAVSEN, B. “Improving the pole relocating properties of vector fitting”, *IEEE Trans. on Power Delivery*, v. 21, n. 3, pp. 1587–1592, Jul. 2006. ISSN: 0885-8977. doi: 10.1109/TPWRD.2005.860281.
- [27] DESCHRIJVER, D., HAEGEMAN, B., DHAENE, T. “Orthonormal Vector Fitting: A Robust Macromodeling Tool for Rational Approximation of Frequency Domain Responses”, *Advanced Packaging, IEEE Transactions on*, v. 30, n. 2, pp. 216–225, May 2007. ISSN: 1521-3323. doi: 10.1109/TADVP.2006.879429.
- [28] DESCHRIJVER, D., GUSTAVSEN, B., DHAENE, T. “Advancements in Iterative Methods for Rational Approximation in the Frequency Domain”, *IEEE Trans.*

*on Power Delivery*, v. 22, n. 3, pp. 1633–1642, Jul. 2007. ISSN: 0885-8977. doi: 10.1109/TPWRD.2007.899584.

- [29] GUSTAVSEN, B. “Computer code for rational approximation of frequency dependent admittance matrices”, *IEEE Trans. on Power Delivery*, v. 17, n. 4, pp. 1093–1098, Oct. 2002. ISSN: 0885-8977. doi: 10.1109/TPWRD.2002.803829.
- [30] POLLACZEK, F. “On the field produced by an infinitely long wire carrying alternating current (in German)”, *Elektrische Nachrichten Technik*, v. 3, pp. 339–360, 1926.
- [31] CARSON, J. R. “Wave propagation in overhead wires with ground return”, *Bell Syst. Tech. Journal*, v. 5, pp. 539–554, Oct. 1926.
- [32] CARSON, J. R. “Ground Return Impedance: Underground Wire with Earth Return”, *Bell System Technical Journal*, v. 8, n. 1, pp. 94–98, 1929.
- [33] WEDEPOHL, L. M., WILCOX, D. J. “Transient analysis of underground power-transmission system – System model and wave propagation characteristics”, *Proceedings of the Institution of Electrical Engineers*, v. 120, n. 2, pp. 253–260, Feb. 1973.
- [34] DERI, A., TEVAN, G., SEMLYEN, A., et al. “The Complex Ground Return Plane - A Simplified Model for Homogeneous and Multi-Layer Earth Return”, *IEEE Trans. on Power Apparatus and Systems*, v. PAS-100, n. 8, pp. 3686–3693, Aug. 1981. ISSN: 0018-9510. doi: 10.1109/TPAS.1981.317011.
- [35] OLSEN, R., YOUNG, J., CHANG, D. “Electromagnetic wave propagation on a thin wire above earth”, *IEEE Trans. on Antennas and Propagation*, v. 48, n. 9, pp. 1413–1419, Sep. 2000. ISSN: 0018-926X. doi: 10.1109/8.898775.
- [36] LIMA, A. C. S., PORTELA, C. “Closed-form expressions for ground return impedances of overhead lines and underground cables”, *International Journal of Electrical Power & Energy Systems*, v. 38, n. 1, pp. 20–26, 2012. ISSN: 0142-0615. doi: 10.1016/j.ijepes.2011.12.016.
- [37] SAAD, O., GABA, G., GIROUX, M. “A closed-form approximation for ground return impedance of underground cables”, *IEEE Trans. on Power Delivery*, v. 11, n. 3, pp. 1536–1545, Jul. 1996. ISSN: 0885-8977. doi: 10.1109/61.517514.

- [38] LIMA, A. C. S., PORTELA, C. “Inclusion of Frequency-Dependent Soil Parameters in Transmission-Line Modeling”, *IEEE Trans. on Power Delivery*, v. 22, n. 1, pp. 492–499, Jan. 2007.
- [39] SALARI, J. C. *Efeito das Descargas Atmosféricas no desempenho de Linhas de Transmissão - Modelagens nos Domínios do Tempo e da Frequência*. Tese de Doutorado, Universidade Federal do Rio de Janeiro, COPPE/UFRJ, Dec. 2006.
- [40] VISACRO, S., ALIPIO, R. “Frequency Dependence of Soil Parameters: Experimental Results, Predicting Formula and Influence on the Lightning Response of Grounding Electrodes”, *IEEE Trans. on Power Delivery*, v. 27, n. 2, pp. 927–935, Apr. 2012. ISSN: 0885-8977. doi: 10.1109/TPWRD.2011.2179070.
- [41] ALIPIO, R., VISACRO, S. “Frequency Dependence of Soil Parameters: Effect on the Lightning Response of Grounding Electrodes”, *IEEE Trans. on Electromagnetic Compatibility*, v. 55, n. 1, pp. 132–139, 2013. ISSN: 0018-9375. doi: 10.1109/TEMC.2012.2210227.
- [42] GUSTAVSEN, B., MAHSEREDJIAN, J. “Simulation of Internal Overvoltages on Transmission Lines by an Extended Method of Characteristics Approach”, *IEEE Trans. on Power Delivery*, v. 22, n. 3, pp. 1736–1742, Jul. 2007. ISSN: 0885-8977. doi: 10.1109/TPWRD.2007.899614.
- [43] GUSTAVSEN, B. “Passivity Enforcement for Transmission Line Models Based on the Method of Characteristics”, *IEEE Trans. on Power Delivery*, v. 23, n. 4, pp. 2286–2293, Oct. 2008. ISSN: 0885-8977. doi: 10.1109/TPWRD.2008.919034.
- [44] RAMOS-LEANOS, O., NAREDO, J., MAHSEREDJIAN, J., et al. “A Wideband Line/Cable Model for Real-Time Simulations of Power System Transients”, *IEEE Trans. on Power Delivery*, v. 27, n. 4, pp. 2211–2218, Oct. 2012. ISSN: 0885-8977. doi: 10.1109/TPWRD.2012.2206833.
- [45] GUSTAVSEN, B. “Avoiding Numerical Instabilities in the Universal Line Model by a Two-Segment Interpolation Scheme”, *IEEE Trans. on Power Delivery*, v. 28, n. 3, pp. 1643–1651, Jul. 2013.
- [46] GUSTAVSEN, B., NORDSTROM, J. “Pole Identification for The Universal Line Model Based on Trace Fitting”, *IEEE Trans. on Power Delivery*, v. 23, n. 1, pp. 472–479, Jan. 2008. ISSN: 0885-8977. doi: 10.1109/TPWRD.2007.911186.

- [47] KOCAR, L., MAHSEREDJIAN, J., OLIVIER, G. “Improvement of Numerical Stability for the Computation of Transients in Lines and Cables”, *IEEE Trans. on Power Delivery*, v. 25, n. 2, pp. 1104–1111, Apr. 2010. ISSN: 0885-8977. doi: 10.1109/TPWRD.2009.2037633.
- [48] MARTINS, T. D. F. R. D. *Modelagem de Linhas de Transmissão a partir de Modos Exponenciais e Coeficientes Equivalentes*. Tese de Doutorado, Universidade Federal do Rio de Janeiro - UFRJ, 2010.
- [49] GUSTAVSEN, B., SEMLYEN, A. “Calculation of transmission line transients using polar decomposition”, *IEEE Trans. on Power Delivery*, v. 13, n. 3, pp. 855–862, Jul. 1998. ISSN: 0885-8977. doi: 10.1109/61.686984.
- [50] CASTELLANOS, F., MARTI, J. “Phase-domain multiphase transmission line models”, *Proceeding of IPST’95 – International Conference on Power Systems Transients*, v. 1, pp. 17–22, Sep. 1995. Lisbon.
- [51] MARCANO, F., MARTI, J. “Idempotent Line Model: Case Studies”. In: *Proceedings of IPST’97 - International Conference on Power Systems Transients*, pp. 67–72, 1997.
- [52] GUSTAVSEN, B., IRWIN, G., MANGELROD, R., et al. “Transmission Line Models for the Simulation of Interaction Phenomena between parallel AC and DC overhead lines”. In: *IPST 99 - International Conference on Power System Transients*, 1999.
- [53] PETTERSSON, P. “Image representation of wave propagation on wires above, on and under ground”, *IEEE Trans. on Power Delivery*, v. 9, n. 2, pp. 1049–1055, Apr. 1994. ISSN: 0885-8977. doi: 10.1109/61.296290.
- [54] D’AMORE, M., SARTO, M. “Simulation models of a dissipative transmission line above a lossy ground for a wide-frequency range, part 2, Multiconductor configuration”, *IEEE Trans. on Electromagnetic Compatibility*, v. 38, n. 2, pp. 139–149, May 1996. ISSN: 0018-9375. doi: 10.1109/15.494616.
- [55] D’AMORE, M., SARTO, M. “A new formulation of lossy ground return parameters for transient analysis of multiconductor dissipative lines”, *IEEE Trans. on Power Delivery*, v. 12, n. 1, pp. 303–314, Jan. 1997.
- [56] PETRACHE, E., RACHIDI, F., PAOLONE, M., et al. “Lightning induced disturbances in buried cables, part 1, theory”, *IEEE Trans. on Electromagnetic Compatibility*, v. 47, n. 3, pp. 498–508, Aug. 2005.



- [57] CAVKA, D., MORA, N., RACHIDI, F. “A Comparison of Frequency-Dependent Soil Models: Application to the Analysis of Grounding Systems”, *IEEE Trans. Electromagnetic Compatibility*, v. 56, n. 1, pp. 177–187, 2014.
- [58] DESCHRIJVER, D., MROZOWSKI, M., DHAENE, T., et al. “Macromodeling of Multiport Systems Using a Fast Implementation of the Vector Fitting Method”, *IEEE Microwave and Wireless Components Letters*, v. 18, n. 6, pp. 383–385, Jun. 2008. ISSN: 1531-1309. doi: 10.1109/LMWC.2008.922585.
- [59] WILCOX, D. J. “Numerical Laplace Transformation and Inversion”, *International Journal Elect. Eng.*, v. 15, pp. 247–265, 1978.
- [60] URIBE, F. A., NAREDO, J. L., MORENO, P., et al. “Electromagnetic transients in underground transmission systems through the numerical Laplace transform”, *Elsevier Electrical Power & Energy Systems*, v. 24, pp. 215–221, 2002.
- [61] MORENO, P., RAMIREZ, A. “Implementation of the Numerical Laplace Transform: A review task force on frequency domain methods for EMT studies”, *IEEE Trans. on Power Delivery*, v. 23, n. 4, pp. 2599–2609, Oct. 2008.
- [62] DIAS, R., DE LIMA, A. C. S., PORTELA, C., et al. “Extra Long-Distance Bulk Power Transmission”, *IEEE Trans. on Power Delivery*, v. 26, n. 3, pp. 1440–1448, Jul. 2011. ISSN: 0885-8977. doi: 10.1109/TPWRD.2011.2126610.
- [63] DOS SANTOS, M. L., JARDINI, J. A., CASOLARI, R. P., et al. “Power Transmission Over Long Distances: Economic Comparison Between HVDC and Half-Wavelength Line”, *IEEE Trans. on Power Delivery*, v. 29, n. 2, pp. 502–509, Apr. 2014. ISSN: 0885-8977. doi: 10.1109/TPWRD.2013.2274333.
- [64] GUSTAVSEN, B. “Fast Passivity Enforcement for Pole-Residue Models by Perturbation of Residue Matrix Eigenvalues”, *IEEE Trans. on Power Delivery*, v. 23, n. 4, pp. 2278–2285, Oct. 2008. ISSN: 0885-8977. doi: 10.1109/TPWRD.2008.919027.
- [65] TOMASEVICH, M. Y. *Modelos de Linhas de Transmissão usando Representação Racional da Matriz de Admitancia Nodal e Decomposição Idempotente*. Tese de Mestrado, PEE/UFRJ, Nov. 2011.
- [66] BODE, H. W. *Network analysis and feedback amplifier design*. New York, D. Van Nostrand, 1945.
- [67] GUSTAVSEN, B. “Time delay identification for transmission line modeling”. In: *Signal Propagation on Interconnects, 2004. Proceedings. 8th IEEE Workshop on*, pp. 103–106, May 2004. doi: 10.1109/SPI.2004.1409018.

- [68] FERNANDES, A., NEVES, W., COSTA, E., et al. “Transmission line shunt conductance from measurements”, *IEEE Trans. on Power Delivery*, v. 19, n. 2, pp. 722–728, Apr. 2004. ISSN: 0885-8977. doi: 10.1109/TPWRD.2003.822526.
- [69] TROTT, M. *The Mathematica Guidebook for Programming*. <http://www.MathematicaGuideBooks.org>, Springer, 2004.
- [70] MAHSEREDJIAN, J., ALVARADO, F. “Creating an Electromagnetic Transients Program in MATLAB: MatEMTP”, *IEEE Trans. on Power Delivery*, v. 12, n. 1, pp. 380–388, Jan. 1997. ISSN: 0885-8977. doi: 10.1109/61.568262.
- [71] WEDEPOHL, L. M. “Power system transients: Errors incurred in the numerical inversion of the Laplace transform”. In: *26th Midwest Symp. Circuits and Syst.*, pp. 174–178, Aug. 1983.
- [72] KIKUCHI, H. “Wave Propagation Along an Infinite Wire Above Ground at High Frequencies”, *Eletrotech. J. Japan*, v. 2, pp. 73–78, 1956.
- [73] WAIT, J. R. “Theory of wave propagation along a thin wire parallel to an interface”, *Radio Sci.*, v. 7, pp. 675–679, Jun. 1972.
- [74] WEDEPOHL, L., EFTHYMIADIS, A. “Wave propagation in transmission lines over lossy ground: a new, complete field solution”, *Proceedings of the Institution of Electrical Engineers*, v. 125, n. 6, pp. 505–510, Jun. 1978. ISSN: 0020-3270. doi: 10.1049/piee.1978.0123.
- [75] PETTERSSON, P. “Propagation of waves on a wire above a lossy ground - Different formulations with approximations”, *IEEE Trans. on Power Delivery*, v. 14, n. 3, pp. 1173–1180, Jul. 1999. ISSN: 0885-8977. doi: 10.1109/61.772389.
- [76] EFTHYMIADIS, A., WEDEPOHL, L. “Propagation characteristics of infinitely-long single-conductor lines by the complete field solution method”, *Proceedings of the Institution of Electrical Engineers*, v. 125, n. 6, pp. 511–517, Jun. 1978. ISSN: 0020-3270. doi: 10.1049/piee.1978.0124.
- [77] D’AMORE, M., SARTO, M. “Simulation models of a dissipative transmission line above a lossy ground for a wide-frequency range, part 1, Single conductor configuration”, *IEEE Trans. on Electromagnetic Compatibility*, v. 38, n. 2, pp. 127–138, May 1996. ISSN: 0018-9375. doi: 10.1109/15.494615.
- [78] SALARI FILHO, J., PORTELA, C. “A Methodology for Electromagnetic Transients Calculation – An Application for the Calculation of Lightning Propagation in

Transmission Lines”, *IEEE Trans. on Power Delivery*, v. 22, n. 01, pp. 527–536, Jan. 2007.

- [79] STRATTON, J. A. *ElectroMagnetic Theory*. McGraw Hill Book Company, 1941.
- [80] ROCHA, P. D. *Redução da Instabilidade Numérica em Modelos de Linhas de Transmissão*. Tese de Doutorado, Universidade Federal do Rio de Janeiro, Jul. 2013.
- [81] KUSTER, E. F., CHANG, D. C., OLSEN, R. G. “Modal theory of long horizontal wire structures above the earth, part 1, excitation”, *Radio Sci.*, v. 13, n. 4, pp. 605–613, Jul.-Aug. 1978.
- [82] KUSTER, E. F., CHANG, D. C., OLSEN, R. G. “Modal theory of long horizontal wire structures above the earth, part 2, properties of discrete modes”, *Radio Sci.*, v. 13, n. 4, pp. 615–623, Jul.-Aug. 1978.
- [83] POGORZELSKI, R., CHANG, D. “On the validity of the thin wire approximation in Analysis of wave propagation along wire over a ground”, *Radio Science Journal*, v. 12, n. 5, pp. 699–707, Sep.-Oct. 1977.
- [84] CHANG, D. C., PLATE, S. W. “Electromagnetic wave propagation along horizontal wire systems in or near a layered earth”, *Electromagnetics*, v. 1, pp. 243–265, 1981.
- [85] OLYSLAGER, F., ZUTTER, D. D. “High frequency transmission line models for a thin wire above a conducting ground”, *IEEE Trans. on Electromagnetic Compatibility*, v. 37, pp. 234–240, May 1995.
- [86] RODRIGUEZ-BERRAL, R., MESA, F., JACKSON, D. R. “A high-frequency circuit model for the Gap Excitation of a microstrip line”, *IEEE Trans. on Microwave Theory and Techniques*, v. 54, pp. 4100–4110, 2006.
- [87] BRIDGES, G. E. “Definition of the high frequency characteristic impedance of an overhead conductor”, *Electronic Letters*, v. 26, pp. 2079–2081, Dec. 1990.
- [88] WEDEPOHL, L., MOHAMED, S. E. T. “Multiconductor transmission lines. Theory of natural modes and Fourier integral applied to transient analysis”, *Proceedings of the Institution of Electrical Engineers*, v. 116, n. 9, pp. 1553–1563, Sep. 1969. ISSN: 0020-3270. doi: 10.1049/piee.1969.0281.
- [89] GOMEZ, P., URIBE, F. A. “The Numerical Laplace Transform: An accurate technique for analyzing electromagnetic transients on power system devices”, *International Journal of Electrical Power & Energy Systems*, v. 31, n. 2-3, pp. 116–123, 2009. ISSN: 0142-0615. doi: 10.1016/j.ijepes.2008.10.

006. Available at: <<http://www.sciencedirect.com/science/article/pii/S0142061508001002>>.

- [90] GUSTAVSEN, B. “Validation of Frequency Dependent Transmission Line Models”, *IEEE Trans. on Power Delivery*, v. 20, n. 2, pp. 925–933, Apr. 2005.
- [91] PORTELA, C. M., TAVARES, M. C., PISSOLATO, J. “Influence of a more accurate soil representation in electromagnetic transient phenomena”. In: *Power System Technology, 2002. Proceedings. PowerCon 2002. International Conference on*, pp. 1426 – 1431, 2002.
- [92] SMITH, K. S., LONGMIRE, C. L. *A universal impedance for soils*. Defense Nuclear Agency, Alexandria, VA, USA, jul. 1975. Topical Report for Period, 1 July 1975 - 30 September 1975.
- [93] WEDEPOHL, L., NGUYEN, H., IRWIN, G. “Frequency-dependent transformation matrices for untransposed transmission lines using Newton-Raphson method”, *IEEE Trans. on Power Systems*, v. 11, n. 3, pp. 1538–1546, Aug. 1996. ISSN: 0885-8950. doi: 10.1109/59.535695.
- [94] DE FARIA ROCHA DOURADO MARTINS, T., DE LIMA, A. C. S., CARNEIRO, S. “Effect of approximate impedance formulae on the accuracy of transmission line modelling”, *Generation, Transmission & Distribution, IET*, v. 1, n. 4, pp. 534–539, Jul. 2007. ISSN: 1751-8695. doi: 10.1049/iet-gtd:20060289.
- [95] GUSTAVSEN, B., SEMLYEN, A. “Admittance-Based Modeling of Transmission Lines by a Folded Line Equivalent”, *Power Delivery, IEEE Transactions on*, v. 24, n. 1, pp. 231–239, Jan. 2009. ISSN: 0885-8977. doi: 10.1109/TPWRD.2008.2002960.
- [96] KRONROD, A. S. “On a line integral”, *Doklady Akad*, v. 154, pp. 283–286, 1964.
- [97] PRESS, W., TEUKOLSKY, S., VETTERING, W., et al. *Numerical Recipes in Fortran 77*. <http://www.nr.com/>, Cambridge University Press, 1996.
- [98] KRONROD, A. S. *Nodes and Weights for Quadrature Formulae. Sixteen-Place Tables*. Consultants Bureau, 1965.
- [99] AMMAR, G. S., CALVETTI, D., REICHEL, L. “Computation of Gauss-Kronrod Quadrature Rules with non-positive weights”, *Electronic Trans. Numerical Analysis*, v. 9, pp. 26–38, 1999.
- [100] LAURIE, D. P. “Calculation of Gauss-Kronrod Quadrature Rules”, *Mathematics of Computation*, v. 219, pp. 1133–1145, Jul. 1997.

- [101] GAUTSCHI, W. *Numerical Methods and Approximation Theory III*. Niš, 1987.
- [102] PIESSENS, R., BRANDERS, M. “A note on the optimal addition of abscissas to quadrature formulas of Gauss and Lobatto type”, *Mathematics of Computation*, v. 28, pp. 135–139, 1974.

# Appendix A

## State Space Formulation of Overhead Lines and Underground Cable Parameters

An efficient time-domain evaluation of transmission systems requires to represent both  $\mathbf{Y}_c$  and  $\mathbf{H}$  by rational functions in the frequency domain [5, 23], which allows to implement a recursive formulation of the convolutions.

To illustrate the numerical evaluation involved, a first order pole-residue model will be presented for both cases. This procedure can be readily extended to the more general  $n$ th order multi-phase transmission system case.

For the Characteristic Admittance  $\mathbf{Y}_c$ , we assume a proper rational model with input  $u$ , output  $y$  and constant term  $d$ . In the frequency domain we may write

$$y = \left( \frac{r}{s-a} + d \right) u \quad (\text{A.1})$$

thus, a continuous time-domain representation of (A.1) can be written as

$$\begin{aligned} \dot{x} &= ax + ru \\ y &= x + du \end{aligned} \quad (\text{A.2})$$

A discrete time-domain model of (A.2) can be obtained using either trapezoidal rule integration or recursive convolutions. The resulting expressions are shown in (A.3).

$$\begin{aligned} x(n) &= \alpha x(n-1) + (\alpha\lambda + \mu) u(n-1) \\ y(n) &= x(n) + (\lambda + d) u(n) \end{aligned} \quad (\text{A.3})$$

If the trapezoidal integration rule is applied, the coefficients  $\alpha$ ,  $\lambda$  and  $\mu$  are given by

$$\alpha = \frac{2 + a\Delta t}{2 - a\Delta t} \quad \lambda = \mu = \frac{r\Delta t}{2 - a\Delta t} \quad (\text{A.4})$$

and in the case recursive convolutions are used, we have

$$\alpha = \exp(a\Delta t) \quad \lambda = -\frac{r}{a} \left( 1 + \frac{1 - \alpha}{a\Delta t} \right) \quad \mu = \frac{r}{a} \left( \alpha + \frac{1 - \alpha}{a\Delta t} \right) \quad . \quad (\text{A.5})$$

For the Propagation Matrix  $\mathbf{H}$ , we assume a strictly proper first order pole-residue rational model multiplied by an exponential function of a time-delay  $\tau$  with input  $u$  and output  $y$ . In the frequency domain we may write

$$y = \exp(-s\tau_k) \left( \frac{r}{s - a} \right) u \quad (\text{A.6})$$

thus, the continuous time-domain representation of (A.6) can be written as

$$\begin{aligned} \dot{x} &= ax + ru_{(t-\tau_k)} \\ y &= x \end{aligned} \quad . \quad (\text{A.7})$$

A discrete time-domain model of (A.7) can be obtained using either trapezoidal rule integration or recursive convolutions. The resulting expressions are shown in (A.8).

$$\begin{aligned} x(n) &= \alpha x(n-1) + \lambda u_{(t-\tau)} + \mu u_{(t-\tau-\Delta t)} \\ y(n) &= x(n) \end{aligned} \quad . \quad (\text{A.8})$$

The expressions for the coefficients depend whether trapezoidal integration or recursive convolution is used. For the latter,  $\alpha$ ,  $\lambda$  and  $\mu$  are given by (A.5) while for the former (A.4) should be used.

# Appendix B

## Numerical Laplace Transform

During the development of the present research work, it was necessary to validate the time-domain results obtained using the fitting of the line parameters and either trapezoidal integration or recursive convolutions.

Therefore, a different modeling approach such as to solve all the equations in the frequency-domain, can be safely used to compare the results of the model tested. To convert the answer to the time-domain, a transformation routine such as the Fast Fourier Transform or the Numerical Laplace Transform is generally used, with the latter being preferred for its improved numerical stability and easiness of implementation.

For a causal function  $f(t)$  and  $F(s)$  its image in the Laplace domain, the analytical inverse of  $F(s)$  is given by:

$$F(s) = \mathcal{L}\{f(t)\} = \int_0^{\infty} e^{-st} f(t) dt \quad (\text{B.1})$$

$$f(t) = \frac{1}{2\pi j} \int_{\sigma-j\infty}^{\sigma+j\infty} F(s) e^{st} ds \quad (\text{B.2})$$

Considering a finite integration range, we have:

$$F(c + j\omega) = \int_0^T [f(t) e^{-ct}] e^{-j\omega t} dt \quad (\text{B.3})$$

$$f(t) = \Re e \left[ \frac{e^{ct}}{\pi} \int_0^{\Omega} F(c + j\omega) e^{j\omega t} d\omega \right] \quad (\text{B.4})$$

where  $\omega$  is the angular frequency,  $c$  is the stability constant,  $\sigma(j\omega)$  is a window function to reduce truncation errors,  $T$  is the observation time and  $\Omega$  is the maximum frequency.

The discretization of equations (B.3) and (B.4) that allows for the use of the Fast



Fourier Transform (FFT) are as follows

$$F_m = \Delta t \sum_{n=0}^{N-1} f_n D_n^{-1} \exp(-j2\pi mn/N) \quad (\text{B.5})$$

$$f_n = \frac{2\Delta\omega}{\pi} \Re \left\{ D_n \sum_{m=0}^{N-1} f_m \sigma_m \exp(j2\pi mn/N) \right\} \quad (\text{B.6})$$

where

$$F_m = F [c + j(2m + 1) \Delta\omega] \quad (\text{B.7})$$

$$f_n = f(n\Delta t) \quad (\text{B.8})$$

$$D_n = \exp(cn\Delta t + j\pi n/N) \quad (\text{B.9})$$

$$\sigma_m = \sigma [(2m + 1) \Delta\omega] \quad (\text{B.10})$$

$$\Delta t = T/N \quad (\text{B.11})$$

$$\Delta\omega = 2\pi/T = 2\pi/(N\Delta t) \quad (\text{B.12})$$

$$\Omega = 2\pi/\Delta t \quad (\text{B.13})$$

being  $N$  the number of frequency samples.

To reduce the effect of Gibbs oscillations, there are different options for the window function, being the most common the Hanning and Blackman windows, which are respectively given by

$$\begin{aligned} \sigma(\omega) &= 0.5 - 0.5\cos(\pi\omega/\Omega) \\ \sigma(\omega) &= 0.42 - 0.5\cos(\pi\omega/\Omega) + 0.08\cos(2\pi\omega/\Omega) \end{aligned} \quad (\text{B.14})$$

For the factor  $c$ , the most used approaches are the ones given by Wilcox and Wedepohl, which are respectively

$$\begin{aligned}c &= 2\Delta\omega \\c &= \ln(N^2)/T\end{aligned}\tag{B.15}$$

Alternatively, another value of  $c$  most frequently used is

$$c = -\ln(0.001)/T\tag{B.16}$$

# Appendix C

## Formulation of Modal Equation Using Hertz Vectors

The Hertz vector of electric and magnetic type that can define the electromagnetic field at a generic point  $(x, y, z)$  associated with a thin wire of infinite length parallel to a lossy ground are given below. In air, the expressions are

$$\begin{aligned}\Pi_{E_1} &= M_0 \int_{-\infty}^{\infty} \frac{\left( e^{-u_1|y-h|} + R_E(\lambda) e^{-u_1|y+h|} \right)}{u_1} e^{-jx\lambda} d\lambda \\ \Pi_{M_1} &= M_0 \int_{-\infty}^{\infty} \frac{R_H(\lambda) e^{-u_1|y+h|}}{u_1} e^{-jx\lambda} d\lambda\end{aligned}\tag{C.1}$$

For the ground we have

$$\begin{aligned}\Pi_{E_2} &= M_0 \int_{-\infty}^{\infty} \frac{T_E(\lambda) e^{-u_1 h + u_2 y}}{u_1} e^{-jx\lambda} d\lambda \\ \Pi_{M_2} &= M_0 \int_{-\infty}^{\infty} \frac{T_M(\lambda) e^{-u_1 h + u_2 y}}{u_1} e^{-jx\lambda} d\lambda\end{aligned}\tag{C.2}$$

where  $M_0 = -\frac{j\omega\mu_1}{4\pi k_1^2} I_0 e^{-j\gamma z}$ . To determine  $R_E$ ,  $R_H$ ,  $T_E$  and  $T_H$  we must enforce the continuity of tangential components in  $\mathbf{E}$  and  $\mathbf{H}$  at the air-ground interface. Thus,

$$\begin{aligned}
R_E(\lambda) &= -1 + u_1 \frac{2k_1^2}{k_1^2 - \gamma^2} \left( \frac{1}{u_1 + u_2} - \frac{\gamma^2}{k_2^2 u_1 + k_1^2 u_2} \right) \\
R_H(\lambda) &= -\frac{2k_1^2 \gamma \lambda}{j\omega\mu_1(k_1^2 - \gamma^2)} \left( \frac{1}{u_1 + u_2} - \frac{k_1^2}{k_2^2 u_1 + k_1^2 u_2} \right) \\
T_E(\lambda) &= u_1 \frac{2k_1^2}{k_2^2 - \gamma^2} \left( \frac{1}{u_1 + u_2} - \frac{\gamma^2}{k_2^2 u_1 + k_1^2 u_2} \right) \\
T_H(\lambda) &= -\frac{2\gamma\lambda k_1^2}{j\omega\mu_1(k_2^2 - \gamma^2)} \left( \frac{1}{u_1 + u_2} - \frac{k_1^2}{k_2^2 u_1 + k_1^2 u_2} \right)
\end{aligned} \tag{C.3}$$

where  $\gamma$ ,  $k_1$ ,  $k_2$ ,  $u_1$  and  $u_2$  are the same given in Section 3.2.

# Appendix D

## Numerical Integration

Although trapezoidal rule integration is a powerful tool for solving large systems of Ordinary Differential Equations, it is not well suited when highly oscillatory functions are involved as the number of samples tend to be excessive. One way to overcome this limitation is to use an adaptive integration scheme based on the so-called Gaussian quadrature. Gauss observed that a polynomial having a degree of less than or equal to  $2n - 1$  could be integrated exactly by finding  $n$  special abscissas, also called nodes. Integrals of non-polynomial functions and polynomial functions of greater degree are approximated very well. Kronrod [96] proposed a method to choose the nodes optimally from the Legendre-Gauss quadrature. These points are known as Kronrod points [97].

The Gaussian quadrature consists to transform the function to be integrated,  $f(x)$ , into a new function,  $g(x)$ , integrable from  $x = -1$  to  $x = 1$  while preserving the original area. The integral is calculated by summing the product of the new function values  $g(n_i)$  times a weighting factor  $w_i$  specific for each node.

$$\int_a^b f(x)dx = \int_{-1}^1 g(x)dx \approx \sum_{i=1}^n w_i g(n_i) \quad (\text{D.1})$$

where

$$w_i = \frac{2(1-x_i^2)}{(n+1)^2 P_{n+1}(x_i)^2} \quad (\text{D.2})$$

and  $P_n(x)$  is a Legendre polynomial of order  $n$ . The nodes are the roots of the  $P_n(x_i)$ . The roots of the Legendre polynomials are unique, thus no nodes are common to any pair of Legendre polynomials except the midpoint  $x = 0$ . Some illustrative examples of Gaussian quadrature are located at <http://demonstrations.wolfram.com/GaussianQuadrature/>.

Error determination in (D.1) is based on the difference between the integral estimates obtained from two Gaussian quadrature rules of different orders [98–100]. Instead of a simple difference between estimates a more complex error estimation can be used based

on the Quadpack package (available at <http://www.netlib.org/quadpack/>). Thus error determination has a high computational burden which is the main responsible for a slow convergence in the numerical integration.

A Gauss-Kronrod scheme can also be used with the so-called Lobatto integration rule, which uses the original integration interval adding new sampling “Kronrod points” in between those given by the Lobatto rule. This gives a higher order rule that reuses the Lobatto rule integrand evaluations.

A thorough survey of the history, existence and other theoretical properties, as well as computational aspects of Gauss-Kronrod rules and their generalizations is given by Gautschi [101]. Further description and details regarding Gauss-Lobatto rules are presented in [102]. Several numerical analysis programs have implemented these integration schemes as highly efficient and optimized routines such as `NIntegrate` in MATHEMATICA and `quadgk` and `quadl` in MATLAB.

# Appendix E

## Formulation of Modal Equation Using Magnetic and Electric Vector Potentials

In this approach, the wave propagation is decomposed in Transverse Magnetic (TM) and Transverse Electric (TE) modes, using the magnetic and the electric vector potentials, respectively. An important detail: in [74], the definition of the magnetic vector potential as  $\mathbf{H} = \nabla \times \mathbf{A}$  was adopted instead of the conventional approach. In this formulation, the current has the form  $I = I_0 e^{-\gamma z}$ . The Lorentz gauge is used to relate the electric scalar potential in TM modes. Also, in the same reference, the electric vector potential  $\mathbf{F}$  is defined by  $\mathbf{E} = \nabla \times \mathbf{F}$ . Using these definitions for TM modes in the air and bellow ground surface, the respective expressions are

$$\begin{aligned}\nabla^2 \mathbf{A}_1 + (\gamma^2 - k_1^2) \mathbf{A}_1 &= I \delta(x - x_c) \delta(y - h) \\ \nabla^2 \mathbf{A}_2 + (\gamma^2 - k_2^2) \mathbf{A}_2 &= 0\end{aligned}\tag{E.1}$$

where  $(x_c, h)$  are the conductor center coordinates and  $\delta$  is the Dirac delta impulse function. For TE modes we have

$$\begin{aligned}\nabla^2 \mathbf{F}_1 + (\gamma^2 - k_1^2) \mathbf{F}_1 &= 0 \\ \nabla^2 \mathbf{F}_2 + (\gamma^2 - k_2^2) \mathbf{F}_2 &= 0\end{aligned}\tag{E.2}$$

Similarly to the case using Hertz vectors, by enforcing the continuity of components  $E_x$  and  $E_z$  of the electric field and  $H_x$  and  $H_z$  of the magnetic field at the ground surface, i.e.,  $y = 0$ , it is possible to obtain an integral equation for the electromagnetic field in the air and in the ground. The modal equation in this formulation can be written as

$$M = (\gamma^2 - k_1^2) \left[ K_0(\eta r) - K_0(2h\eta) + \int_{-\infty}^{\infty} \frac{e^{-2hu_1}}{g(\lambda)} d\lambda \right]\tag{E.3}$$

where  $g(\lambda)$  is given by

$$g(\lambda) = u_1 + u_2 n^2 \frac{\gamma^2 - k_1^2}{\gamma^2 - k_2^2} + \frac{\lambda^2 \gamma^2 \mu_1 (k_1^2 - k_2^2)^2}{k_1^2 (\gamma^2 - k_2^2) [u_2 \mu_2 (\gamma^2 - k_1^2) + u_1 \mu_1 (\gamma^2 - k_2^2)]} \quad (E.4)$$

Despite the differences in the expression shown in (E.4), the results presented here indicate that a similar propagation constant is obtained regardless of the formulation.